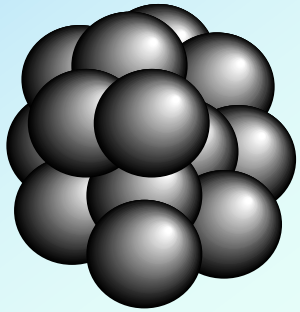

物理化学特論IV
クラスターの科学
第三部

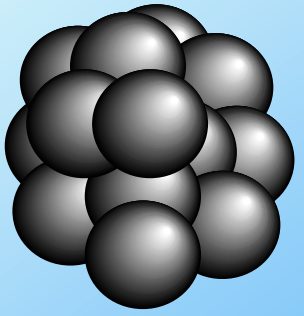

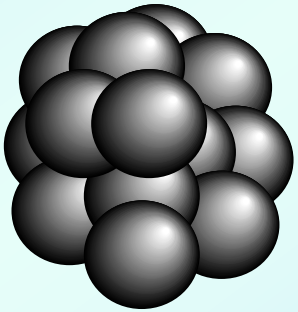

講義内容(予定)

クラスターとは？

1. 金属クラスターの電子構造1；水銀クラスター, 金属ー非金属相転移
2. 金属クラスターの電子構造2；アルカリ金属クラスター，電子殻模型と魔法数, 原子核とクラスターとの類似性と異質性
3. 分子クラスターの反応とダイナミクス；$I_2^-(CO_2)_n$，光解離と再結合, 微視的な溶媒効果
4. 遷移金属クラスターと気体分子との反応
5. クラスターの衝突反応
6. タンパク質のフォールディング;Levinthalのパラドックス
7. 気相タンパク質イオンの立体構造の変化;イオン移動度の測定
8. 生体分子の質量分析における新技術
9. 孤立状態において生体分子を研究する; Angiotensin Iイオンと気体分子の温度変化によるプロトン移動反応

講義内容(予定)

クラスターとは？

1. 金属クラスターの電子構造1；水銀クラスター, 金属ー非金属相転移
2. 金属クラスターの電子構造2；アルカリ金属クラスター，電子殻模型と魔法数, 原子核とクラスターとの類似性と異質性
3. 分子クラスターの反応とダイナミクス；$I_2^-(CO_2)_n$，光解離と再結合，微視的な溶媒効果
4. 遷移金属クラスターと気体分子との反応
5. クラスターの衝突反応
6. タンパク質のフォールディング;Levinthalのパラドックス
7. 気相タンパク質イオンの立体構造の変化;イオン移動度の測定
8. 生体分子の質量分析における新技術
9. 孤立状態において生体分子を研究する；Angiotensin Iイオンと気体分子の温度変化によるプロトン移動反応

♣ タンパク質のフォールディング

フォールディング

- フォールディングとは、タンパク質が特定の立体構造に折りたたまれる現象
- 細胞内で翻訳されたタンパク質は、すぐにそのアミノ酸配列に応じて固有の立体構造に折りたたまれ、機能を有するようになる。この状態を天然状態(native state)という。
- この天然状態の構造を熱や変性剤で崩して機能を失わせたものを、変性状態(denatured state)という。
- タンパク質はアミノ酸の複数結合した直鎖状の分子で、可能な立体構造は無数に存在するが、細胞内ではそれぞれ特定の立体構造をとる。
- クリスチャン・アンフィンセンが、リボヌクレアーゼが試験管内において変性状態から天然状態に変化することを示し、「タンパク質は自発的に、熱力学的に最も安定な立体構造をとる」とした。これをアンフィンセンのドグマと言う。

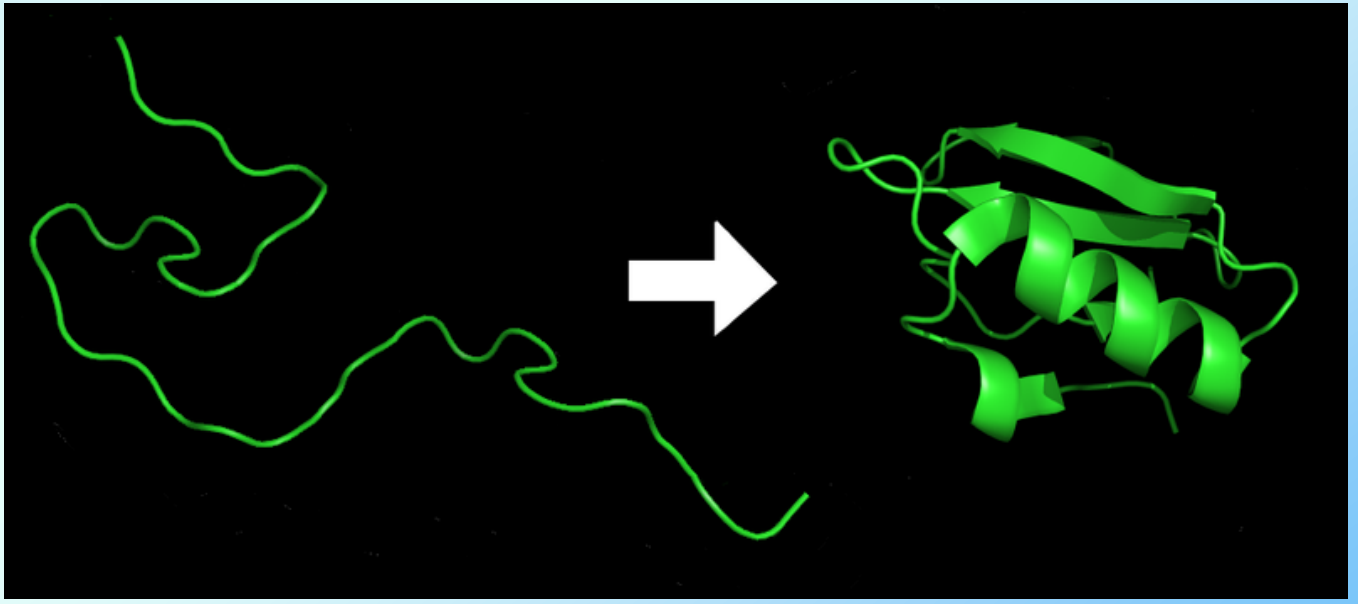

フォールディングの経路

- n残基のタンパク質はおよそ10^n通りの構造が可能であり、タンパク質が最安定構造を網羅的に探すことは現実的に不可能である（レヴィンタールのパラドクス）。このため、フォールディングには特定の経路が存在する。
- 100残基以下の小型タンパク質に関しては、変性状態と天然状態の二状態いずれかしか観測されず、中間的な構造はほとんど存在しないことが分かっている。このため、小型タンパク質のフォールディングは協同的(cooperative)であるとされる。これは、進化の過程でタンパク質が高速にフォールディングできるアミノ酸配列を獲得したことによると考えられる。実際、ランダムにアミノ酸を並べたポリペプチドでは多くの準安定な中間状態が存在し、フォールディングは遅い。
- 100残基以上の大型タンパク質においては、フォールディングの過程はジスルフィド結合の形成などを含むため複雑で、中間体が見られるものも多い。
- なお生体内ではタンパク質の翻訳とフォールディングが並行して起こるため、フォールディングの過程は試験管内と必ずしも同じではない。通常はフォールディングは翻訳よりも速いため、先に翻訳されたN末端側から順次フォールディングが行われる。

※ウィキペディア　フォールディングより

Levinthal's paradox

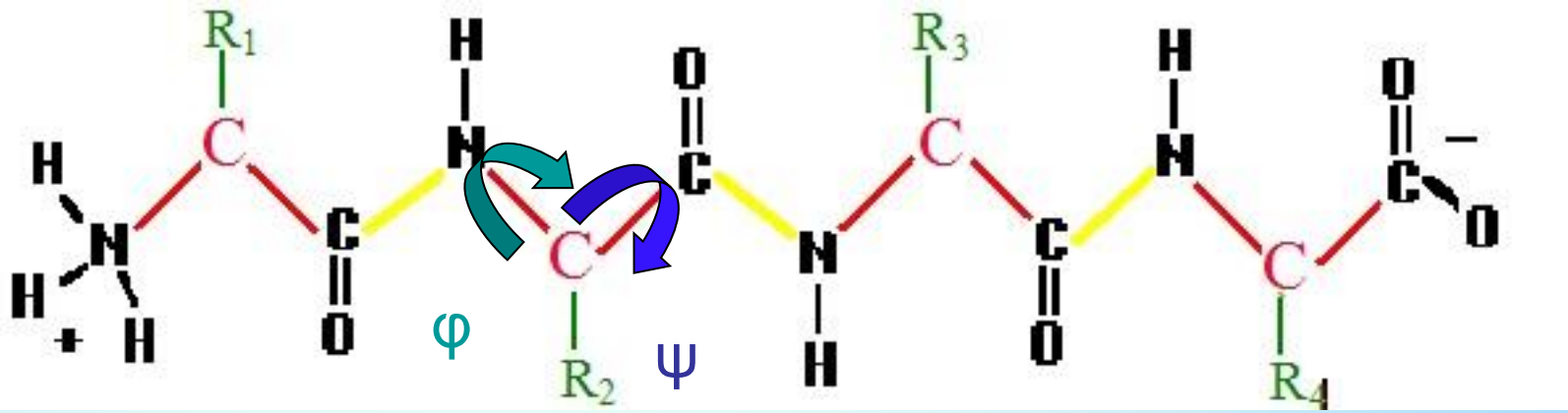

Cyrus Levinthal (1969)
A thought experiment, constituting a self-reference in the theory of protein folding.

assume a 50 aa polypeptide

assume each aa can have 3 main chain rotations (in φ and ψ) – a very conservative assumption

number of structures is then $3^{100} = 5 \times 10^{47}$

typically, rotations take ~ 10^{-13} sec, so a search of all conformations takes

~ $5 \times 10^{47} \times 10^{-13}$ sec = 1.6×10^{27} years

g must follow limited pathways

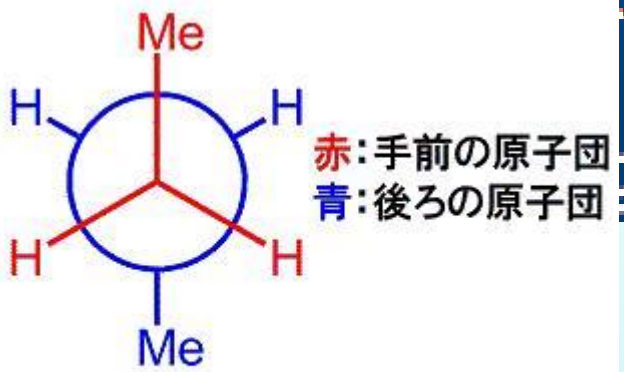

※ 宇宙の年代 200億年（2×10^{10}年）

If a protein were to attain its correctly folded configuration by sequentially sampling all the possible conformations, it would require a time longer than the age of the universe to arrive at its correct native conformation.

This is true even if conformations are sampled at rapid (picosecond) rates.

The "paradox" is that most small proteins fold spontaneously on a millisecond or even microsecond time scale.

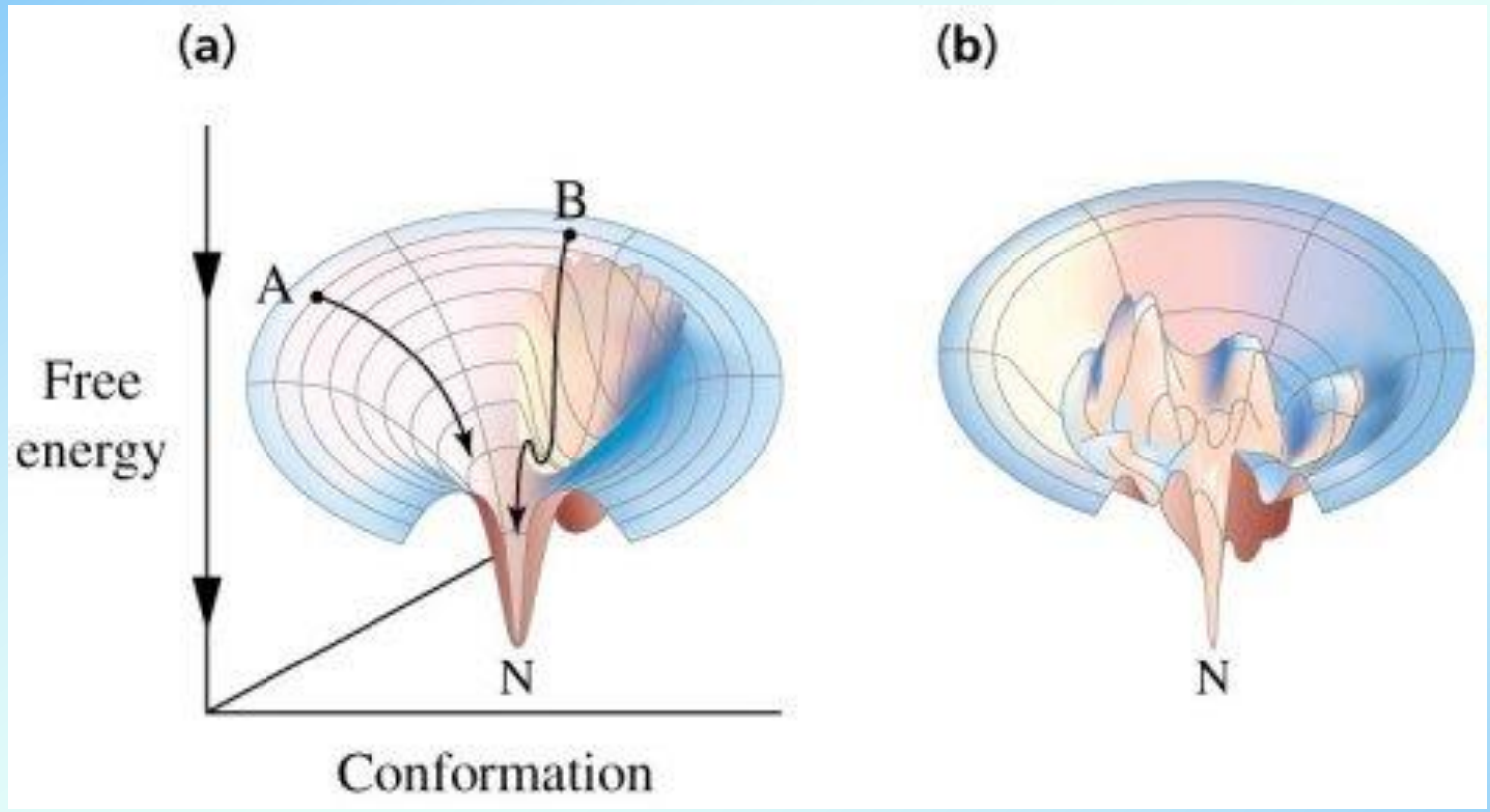
(a)
(b)
B
A
Free
energy
N
N
Conformation

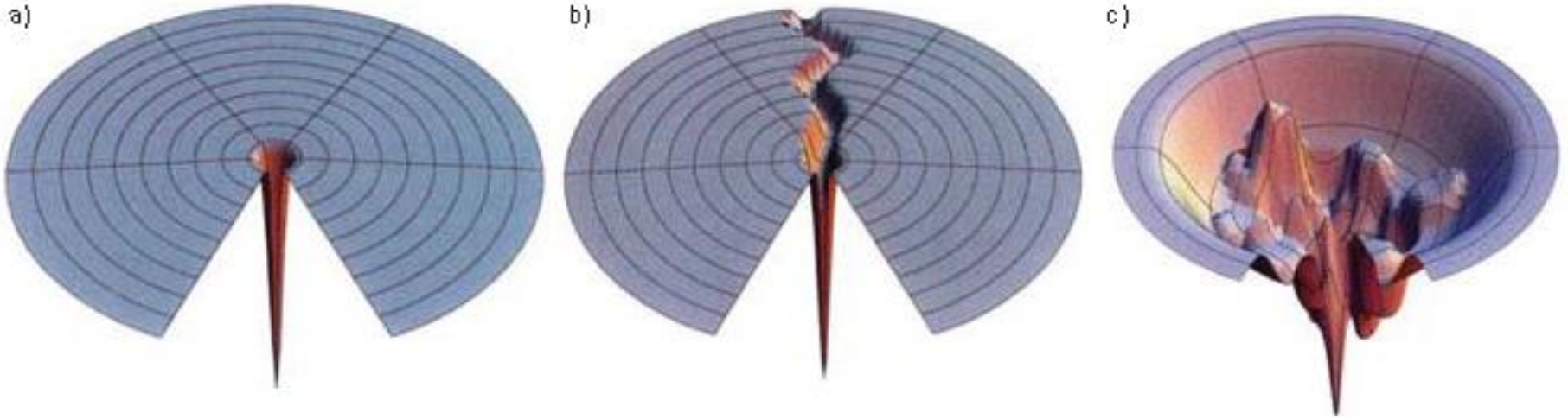
a)
b)
c)

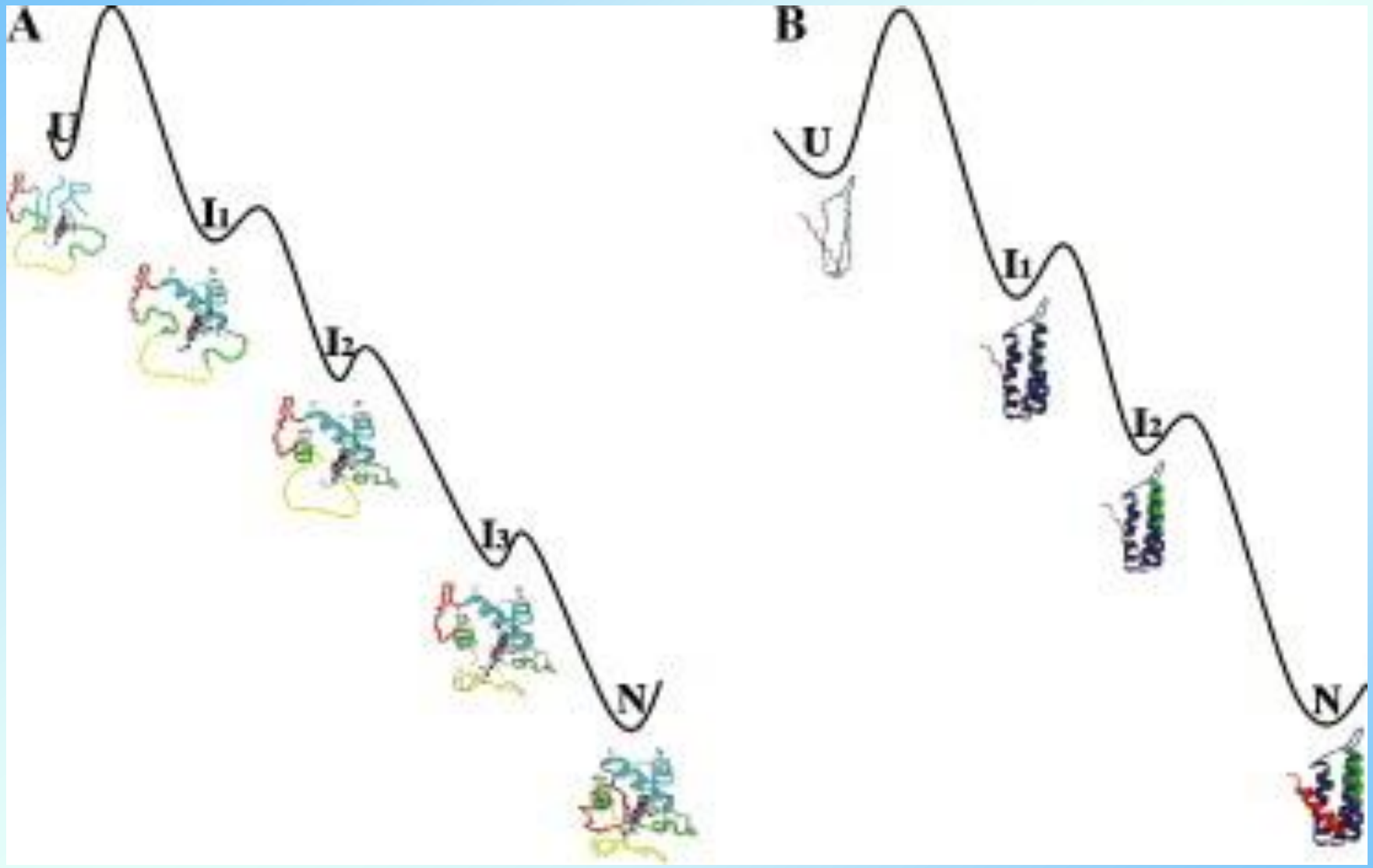
A
U
I1
I2
I3
N
B
U
I1
I2
N

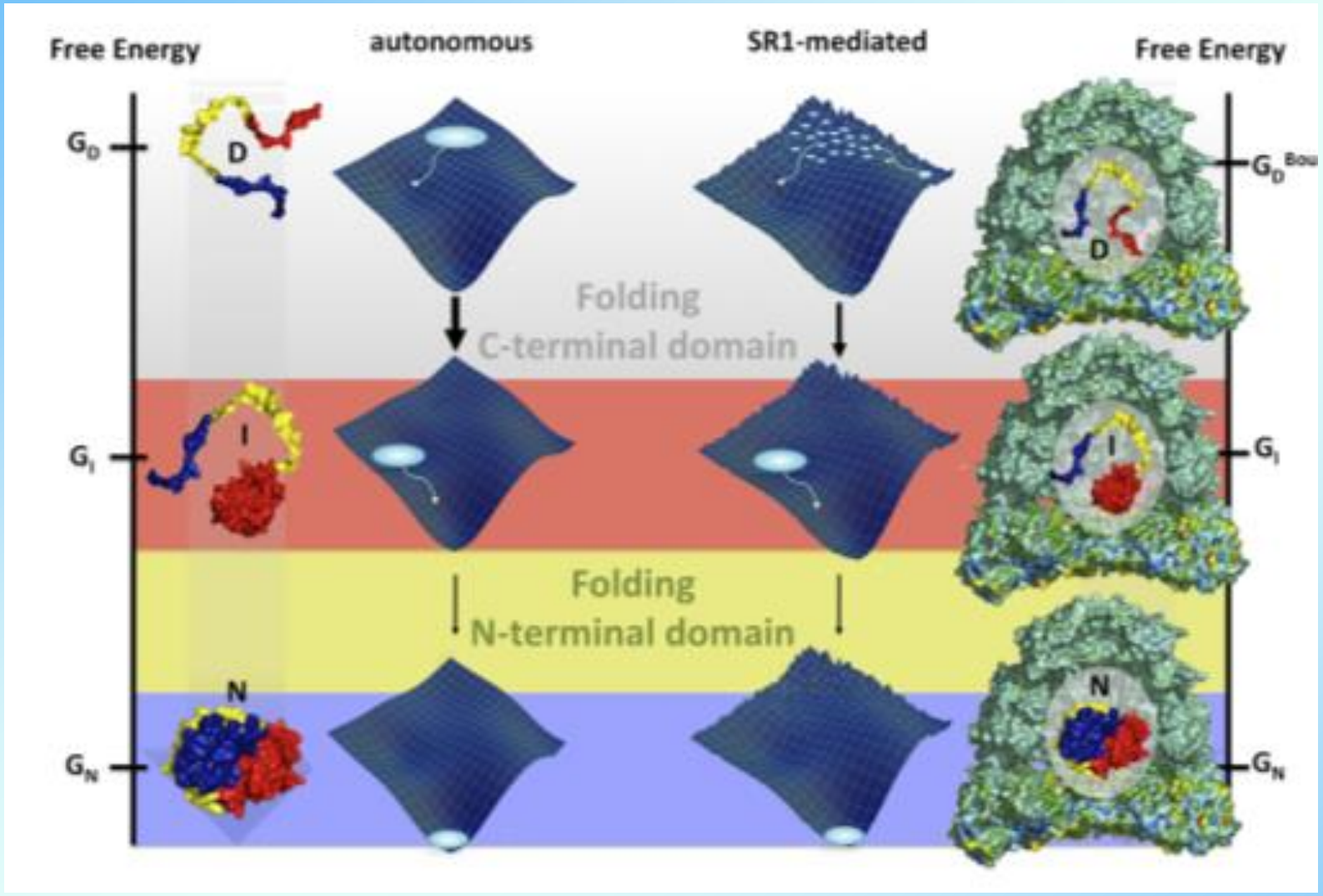

Energy landscape for the folding of the protein Rhodanese. The landscape on the left shows is the landscape for folding in solution, while the landscape on the right shows the landscape for folding mediated by SR1. Note that the lowest energy corresponds to the fully folded state.

Figure taken from wikipedia “Levinthal's Paradox – soft matter”..

Anfinsen's dogma

- At least for small globular proteins, the native structure is determined only by the protein's amino acid sequence.
- Folding occurs, the native structure is a unique, stable and kinetically accessible minimum of the free energy.

- **Uniqueness:** requires that the sequence does not have any other configuration with a comparable free energy. Hence the free energy minimum must be unchallenged.

- **Stability:** small changes in the surrounding environment cannot give rise to changes in the minimum configuration. This can be pictured as a free energy surface that looks more like a funnel (with the native state in the bottom of it) rather than like a soup plate (with several closely related low-energy states); the free energy surface around the native state must be rather steep and high, in order to provide stability.

- **Kinetic accessibility:** means that the path in the free energy surface from the unfolded to the folded state must be reasonably smooth or, in other words, that the folding of the chain must not involve highly complex changes in the shape (like knots or other high order conformations).

Anfinsen's dogma

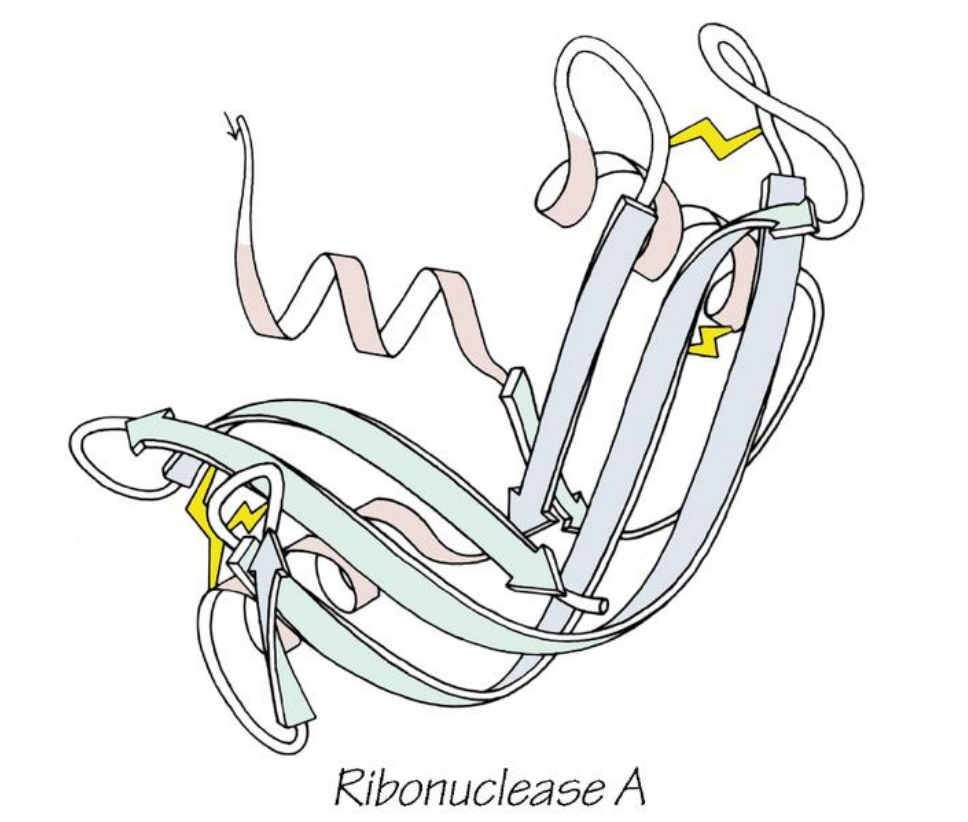

Ribonuclease could be refolded after denaturation while preserving enzyme activity. Thereby, it is suggested that all the information required by protein to adopt its final conformation is encoded in its amino-acid sequence.

The Anfinsen Experiment in Protein Folding

Disulfide bridges can be disrupted by treating a protein with 2-mercaptoethanol ($HS\text{-}CH_2\text{-}CHOH$). The bond between the two sulfurs in the protein is broken.

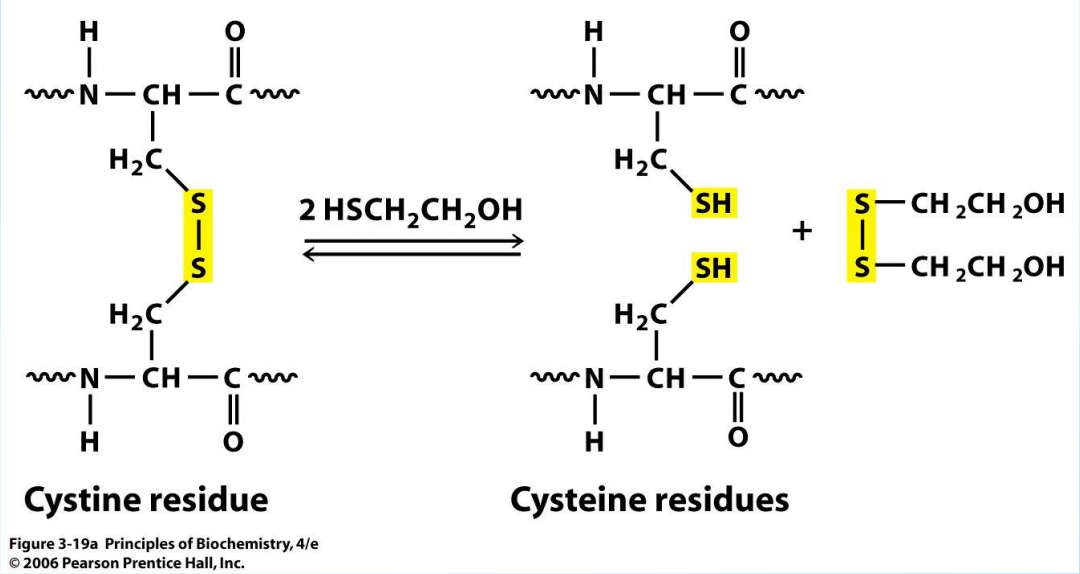

Figure 3-19a Principles of Biochemistry, 4/e

Anfinsen wanted to show that the information for protein folding resided entirely within the amino acid sequence of the protein. He choose ribonuclease A as his model for folding but he couldn't completely denature the protein unless he treated it with the denaturant urea plus 2ME to break the disulfide bridges.

Under those conditions, the protein unfolded. It would refold spontaneously once he removed urea and 2ME from the folding solution. Ribonuclease A regained biological activity under those conditions. This demonstrated that refolding could take place in vitro.

Anfinsen discovered that removing 2ME but not urea led to recovery of 1% of the activity. This is attributed to the formation of random disulfide bridges between the 8 cysteines present in the protein. There are 105 different possibilities (7x5x3x1) so the 1% recovery makes sense. It also shows that the correct three-dimensional conformation must be achieved fairly rapidly when urea is removed since most of the protein under those conditions becomes active.

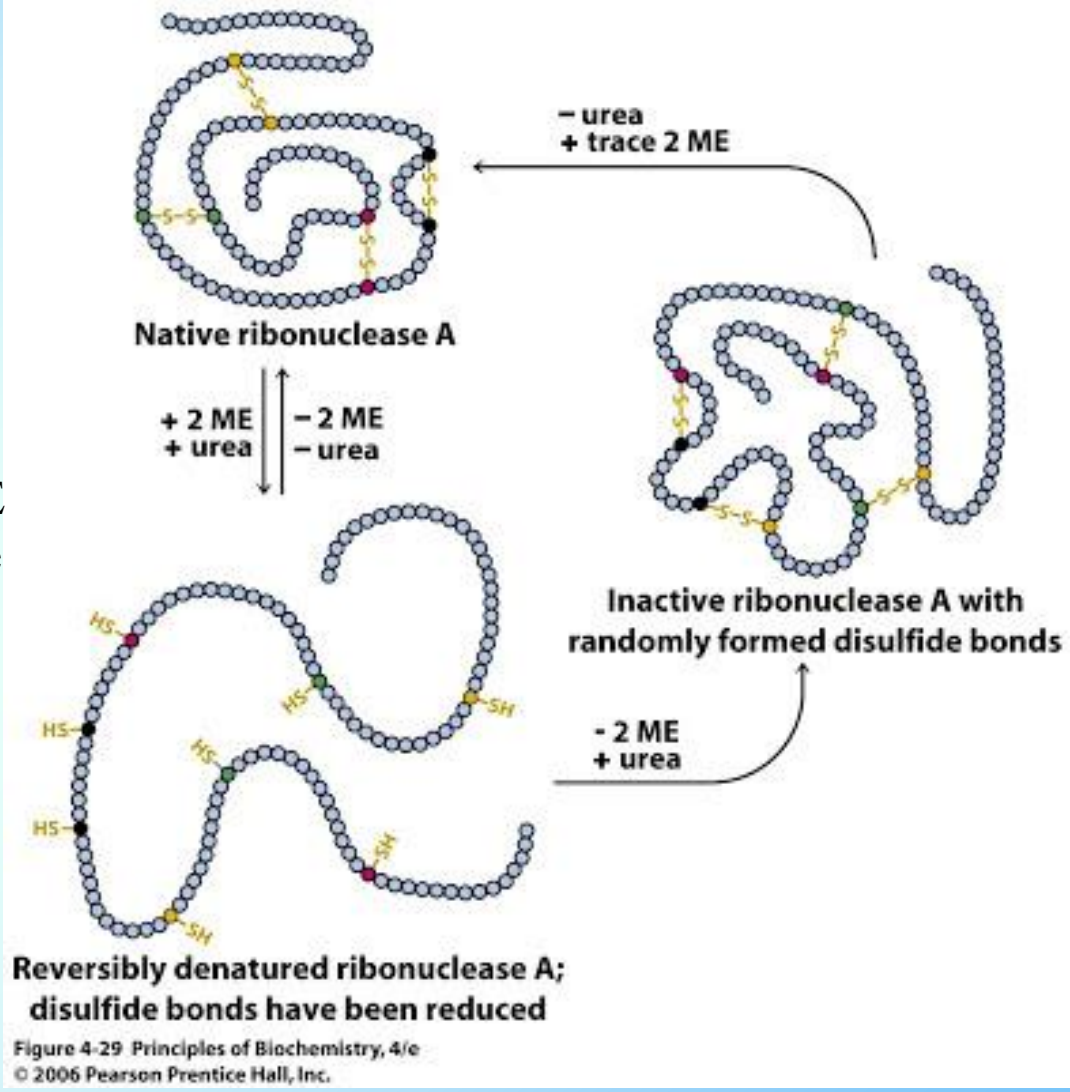

Figure 4-29 Principles of Biochemistry, 4/e

Christian Boehmer Anfinsen, Jr. (1916 –1995)
1972 Nobel Prize in Chemistry

Protein Folding: A Perspective from Theory and Experiment

Christopher M. Dobson,* Andrej Šali, and Martin Karplus*

Angew. Chem. Int. Ed. **1998**, *37*, 868 – 893

C. M. Dobson

A. Šali

M. Karplus

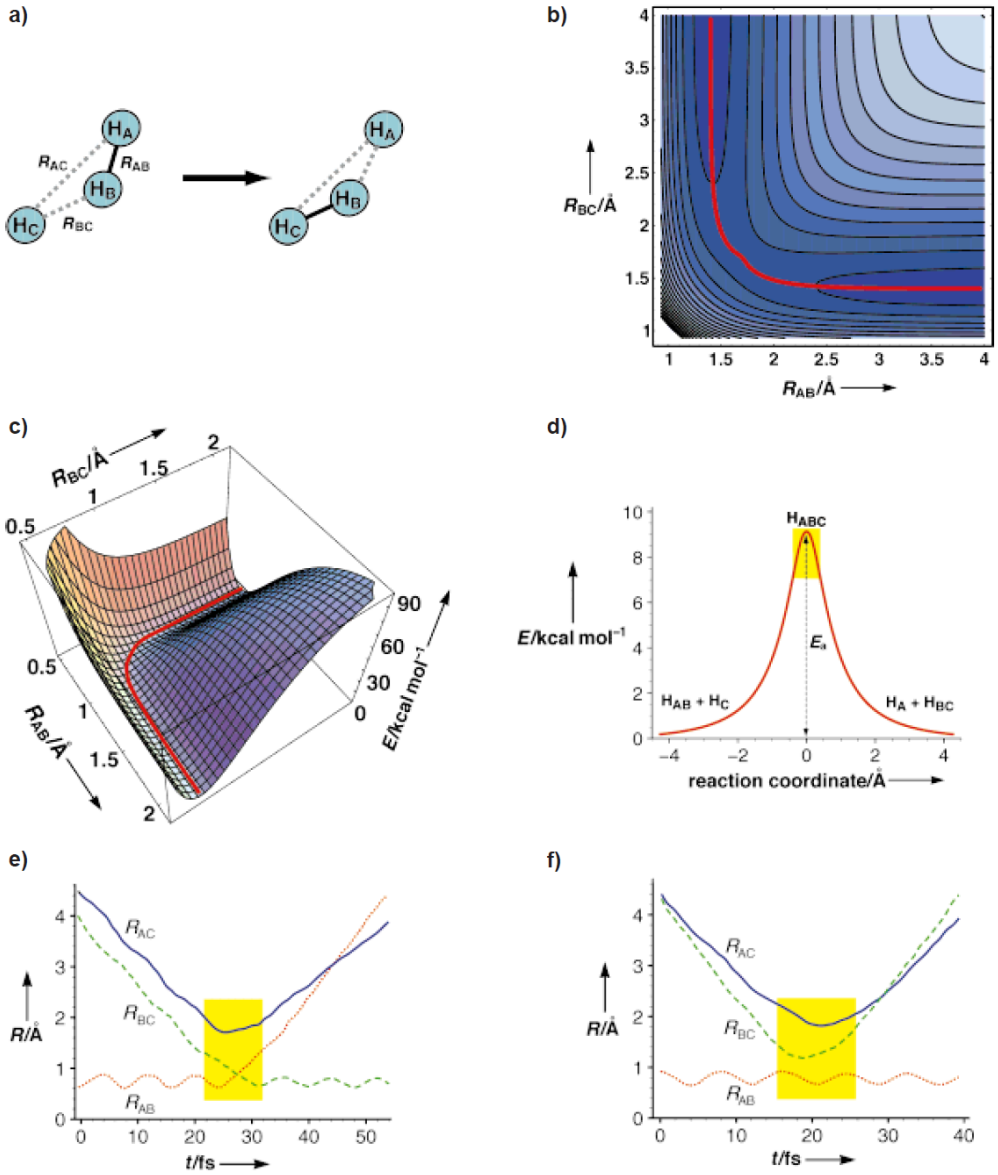

Figure 2. The exchange reaction between a hydrogen atom and a hydrogen molecule. a) Schematic representation of the reaction with definitions for the distances R_{AB}, R_{AC}, and R_{BC}. b) Contour plot of the potential energy surface for a linear collision as a function of the distances R_{AB} and R_{BC} with $R_{AC} = R_{AB} + R_{BC}$; the minimum-energy path is shown in red. c) Same as b), but in a three-dimensional representation. d) Energy along the reaction coordinate corresponding to the minimum-energy path in b) and c); the transition state is indicated in yellow. e) A typical trajectory for the reactive, three-dimensional collision; the three distances R_{AB}, R_{AC}, and R_{BC} are represented as a function of time. f) A typical trajectory for the nonreactive collision; shown as in e). In both e) and f) the interactions between the three atoms are limited to a very short time period (yellow background); this mirrors the narrow potential energy barrier in d). The results are adapted from references [13, 19].

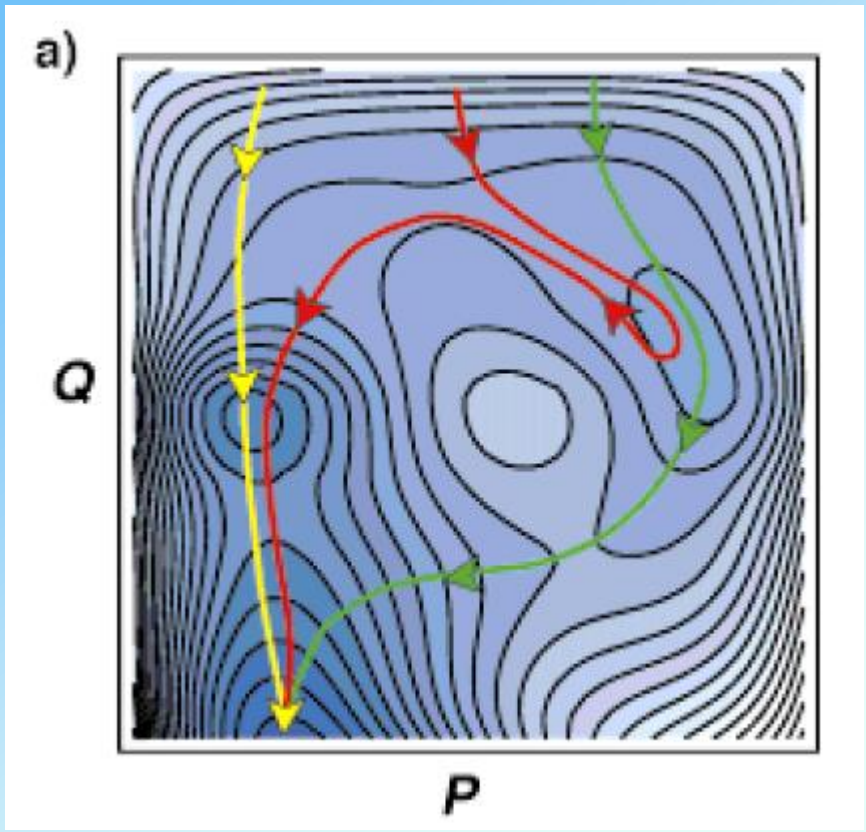

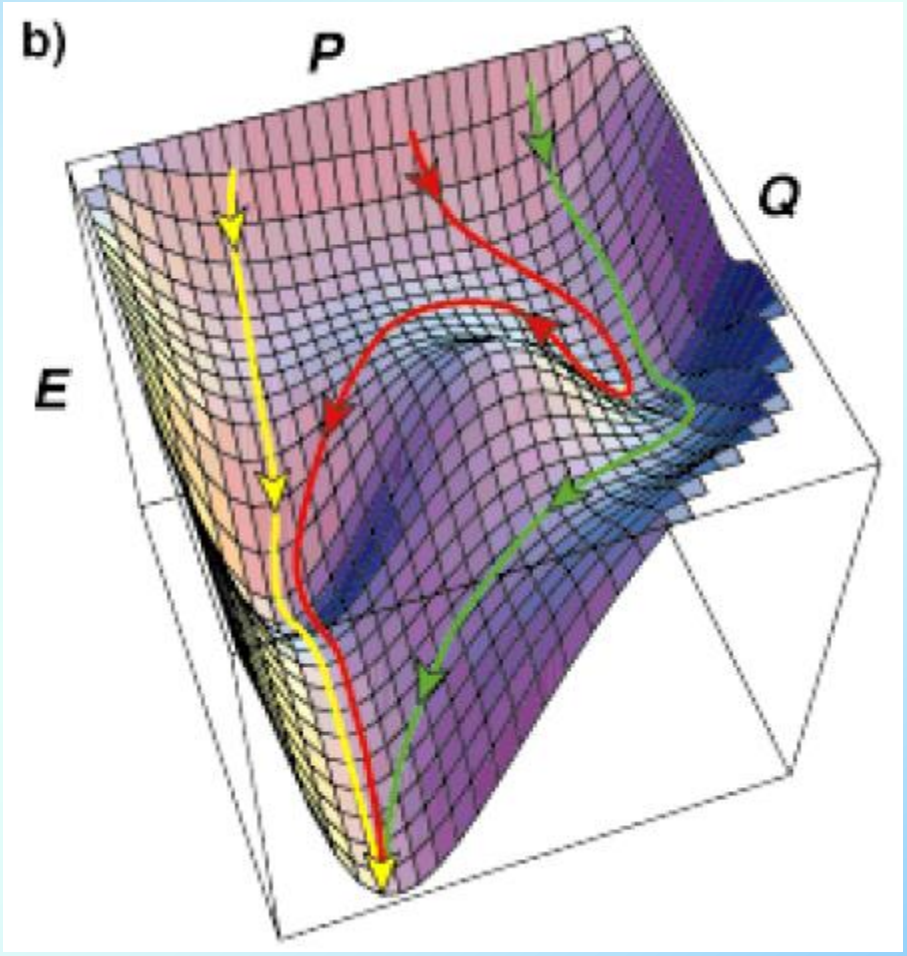

Figure 12. Averaged effective energy surface based on experimental data for the folding of lysozyme (see text, Appendix 2, and Figure 10) illustrated as a) a contour plot and b) a three-dimensional surface. Several possible folding trajectories are shown: a trajectory for fast folding (yellow); a trajectory for slow folding that crosses the high energy barrier (green); a trajectory for slow folding (red) that returns to a less folded state and then follows the valley corresponding to the trajectory for fast folding.

Schematic representation of a funneled energy landscape.

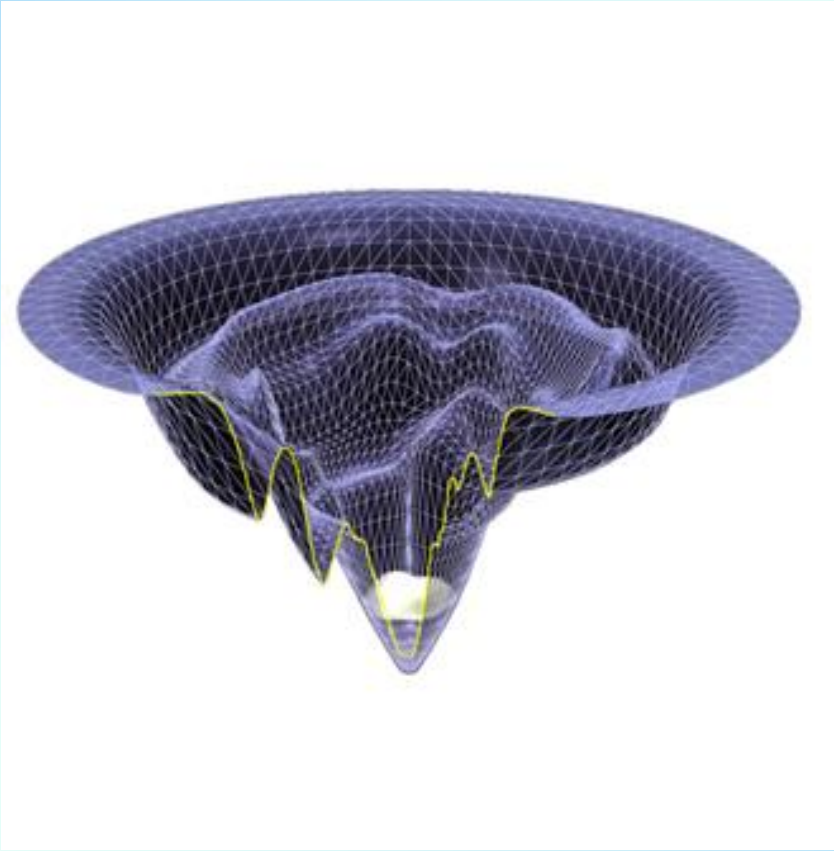

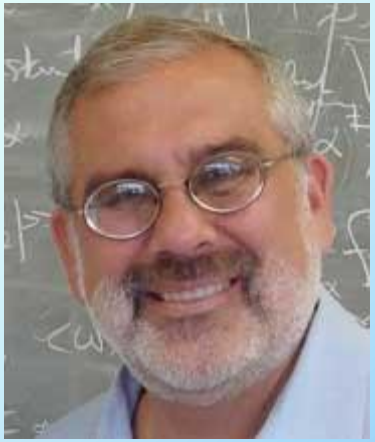

Prof. Peter G. Wolynes

Center for Theoretical Biological Physics and Departments of Physics and *Chemistry and Biochemistry, University of California at San Diego

Minimally frustrated
"Natural protein"

High Temperature

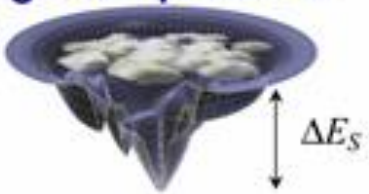

Below T_F

$T_F \propto \Delta E_S / (S_C / k_B)$

Much below T_F

Highly frustrated
Random sequence

High Temperature

At T_G

$T_G = \delta E / \sqrt{S_C / k_B}$

Much below T_G

For fast reliable folding must have $T_F > T_G$

Principle of Minimal Frustration

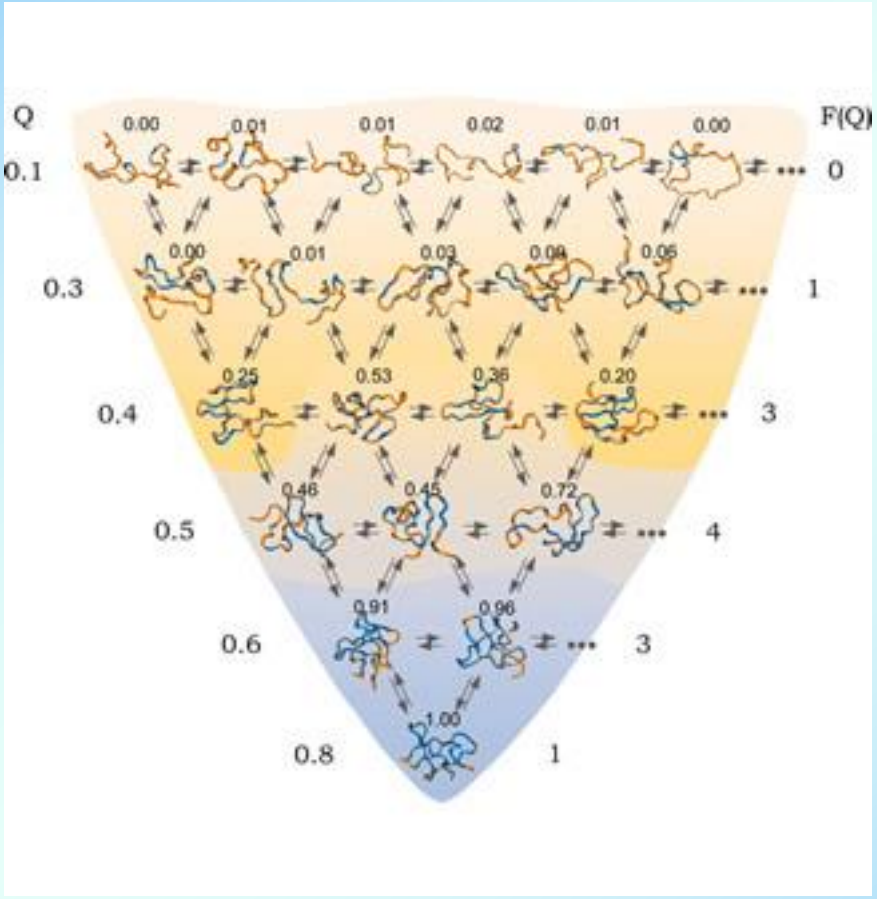

Protein structures in a funneled energy landscape with order parameter Q and P_{fold} shown.

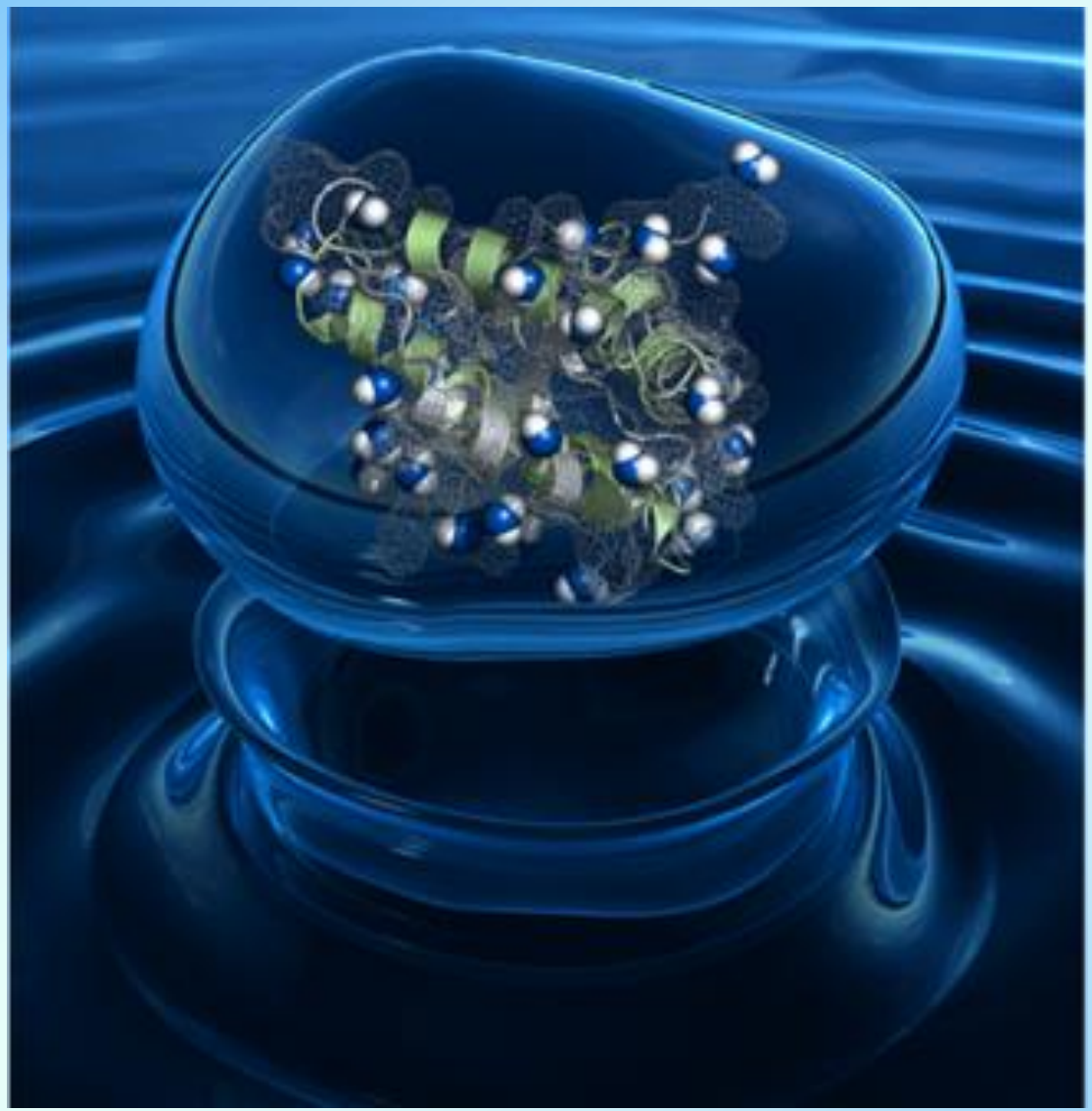

Water-mediated interactions in protein folding.

問. Levinthalのパラドックスについて、簡単に説明しなさい。また、10個のアミノ酸から構成されるポリペプチド鎖が全てのコンフォーメーションを探索するのにかかる時間を求めなさい。

ただし、各々のアミノ酸の結合角φとψがとりうる配置はそれぞれ3とおりとする。また、コンフォーメーション探索の一回の試行に要する時間は10^{-13}秒とする。

♣ 気相タンパク質イオンの立体構造の変化; イオン移動度の測定

Ion mobility mass spectrometry

Collision cross section (Ω), which represents the orientationally averaged shape of the ion, can be calculated from an ion's drift time according to the following equation

$$\Omega = \frac{(18\pi)^{1/2}}{16} \frac{ze}{(k_b T)^{1/2}} \left[\frac{1}{m_I} + \frac{1}{m_B}\right]^{1/2} \frac{t_D E}{L} \frac{760}{P} \frac{T}{273.2} \frac{1}{N}$$

where k_b is Boltzmann's constant, T is temperature, m_I is the mass of the ion, m_B is the mass of the buffer gas (typically He or N_2), t_D is the ion drift time, E is the electric field, L is the length of the drift region, P is the pressure, and N is the number density of the gas at STP.

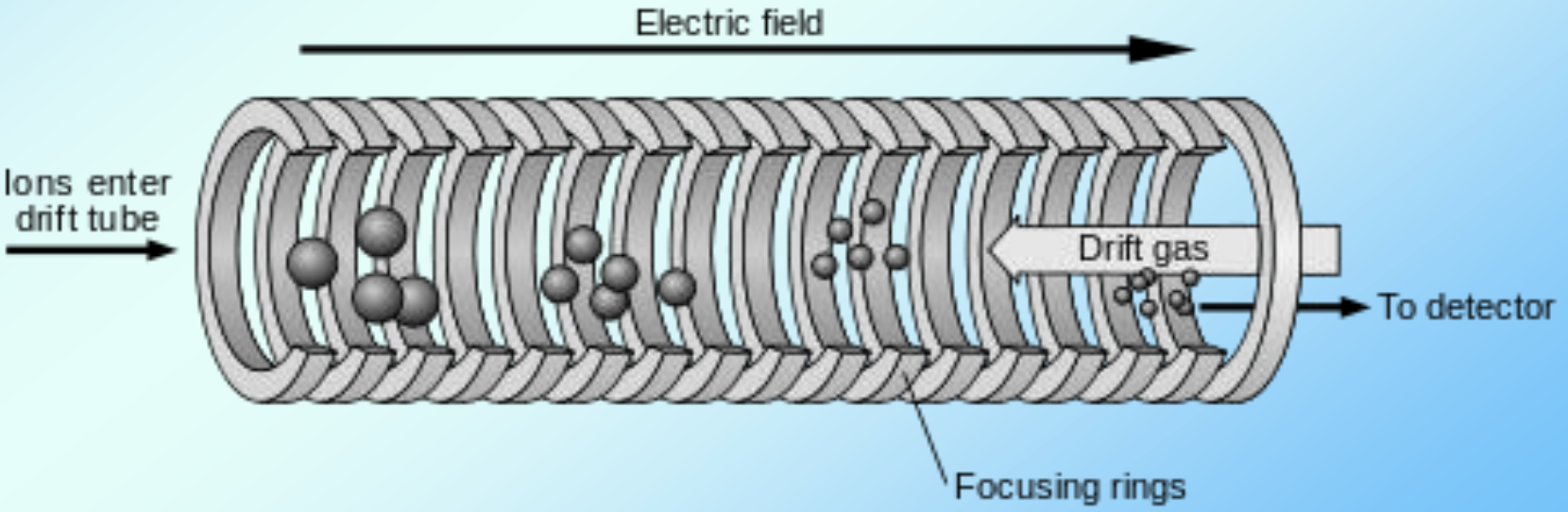

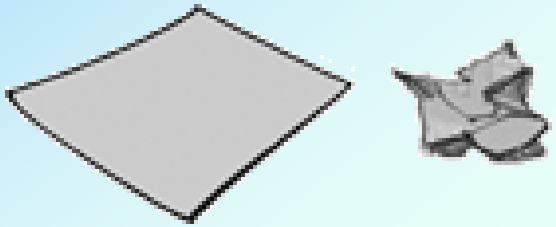

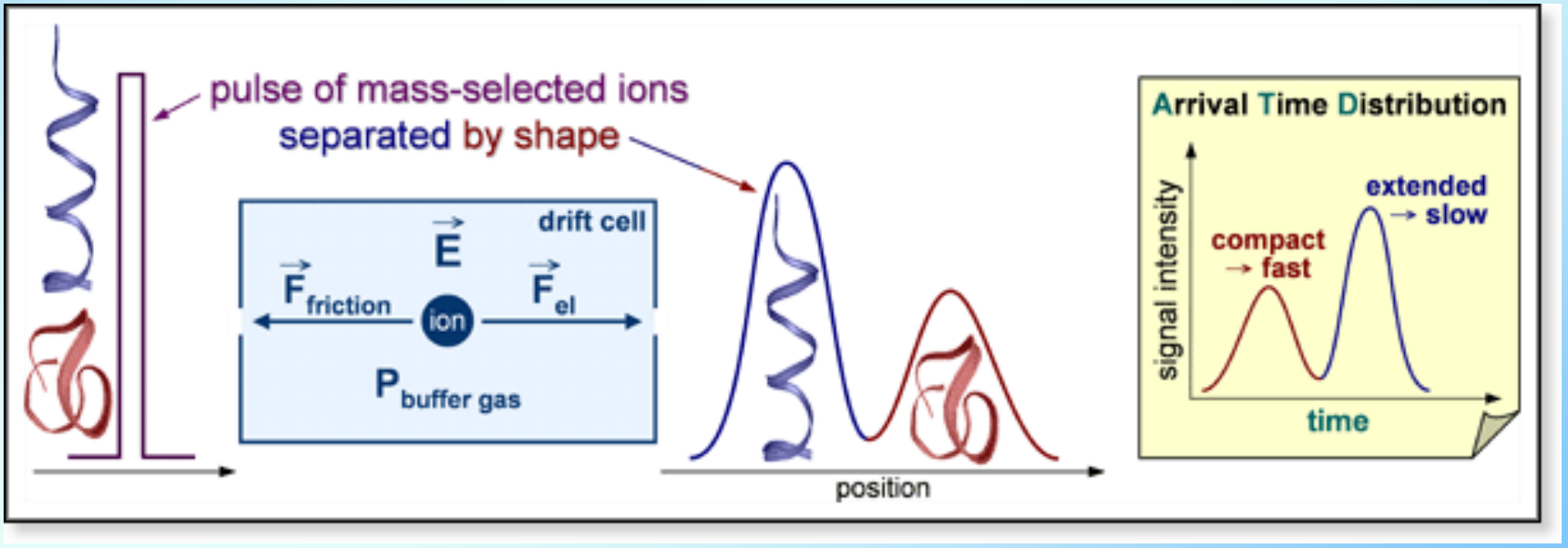
pulse of mass-selected ions
separated by shape
drift cell
E
F friction
F el
ion
P buffer gas
position
Arrival Time Distribution
signal intensity
compact
→ fast
extended
→ slow
time

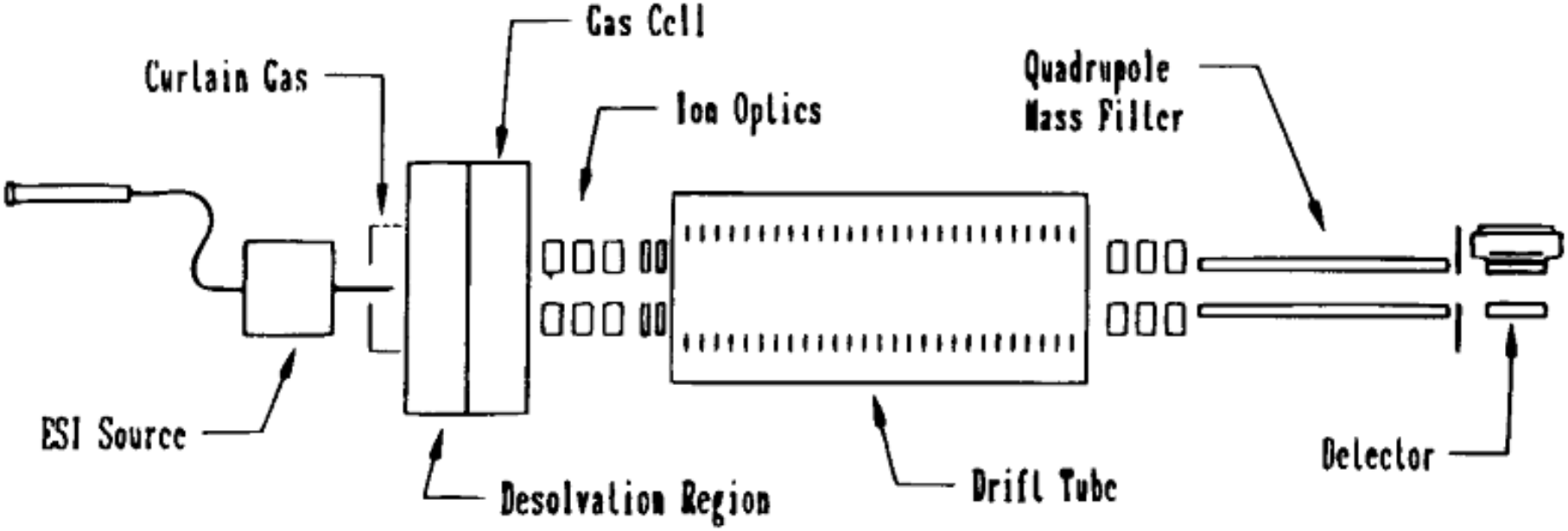

Figure 1. Schematic diagram of injected ion drift tube apparatus at the University of Indiana.

JOURNAL OF MASS SPECTROMETRY, VOL. 32, 577–592 (1997)

Cytochrome c とは・・

- **シトクロム*c***（cytochrome *c*）は、ミトコンドリアの内膜に弱く結合しているヘム蛋白質の一種である。ミトコンドリア内で電子伝達系の構成要素を成す。
- 分子量は1個あたり約12,000である。
- シトクロム*c*は高度に保存されたタンパク質で、動物、植物、単細胞生物など非常に多様な生物で確認されている。

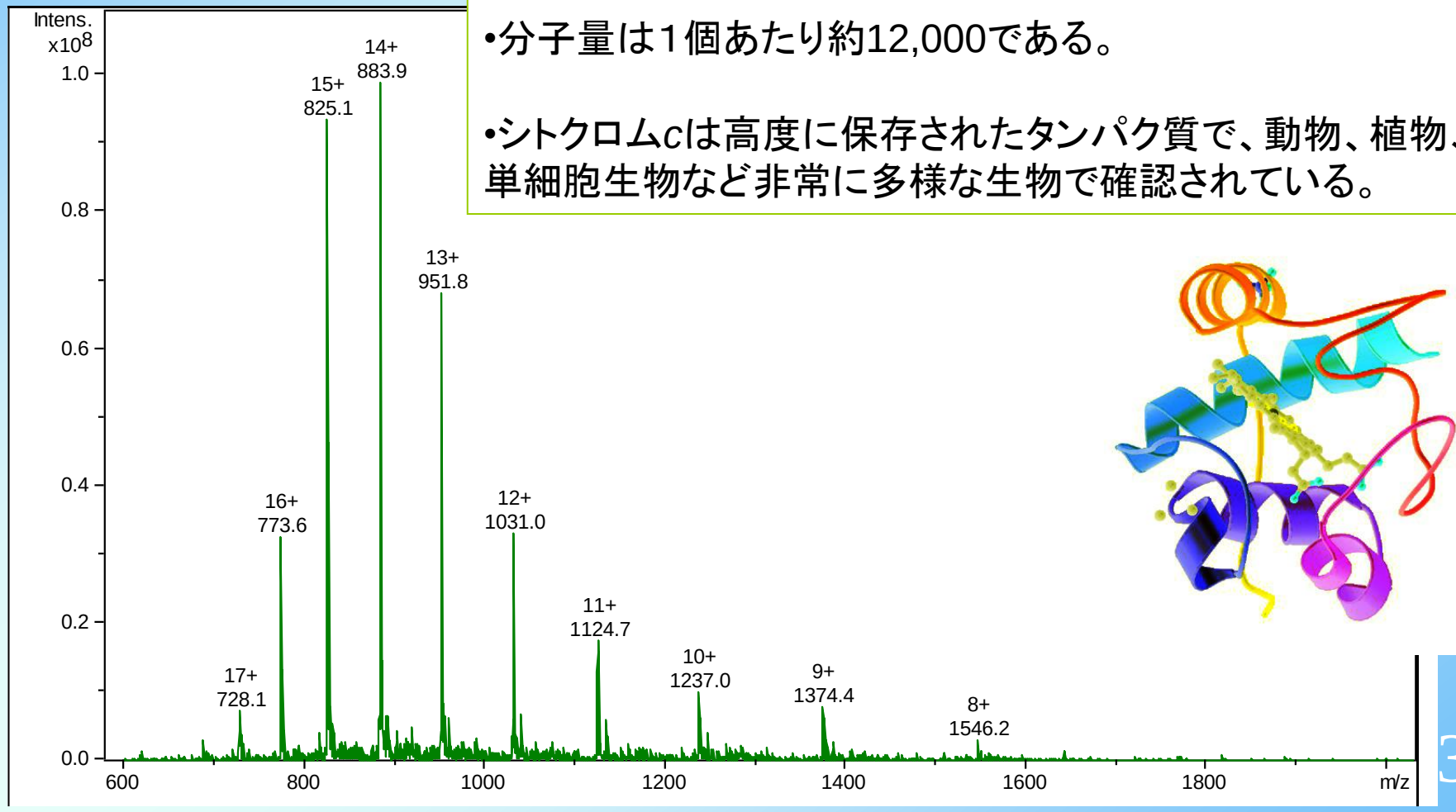

Chain Sequence of Cytochrome c

Basic Residues;
Lysine;K, Arginine;R, Histidine;H

104 residues
GDVEKGKKIFVQKCAQCHTVEKGGKHKTGPN
LHGLFGRKTGQAPGFTYTDANKNKGITWKEET
LMEYLENPKKYIPGTKMIFAGIKKKTEREDLIA
YLKKATNE

PEPTIDES AND PROTEINS IN THE VAPOR PHASE

Martin F. Jarrold
Department of Chemistry, Northwestern University, Evanston, Illinois 60208;
e-mail: mfj@nwu.edu

Annu. Rev. Phys. Chem. 2000. 51:179–207

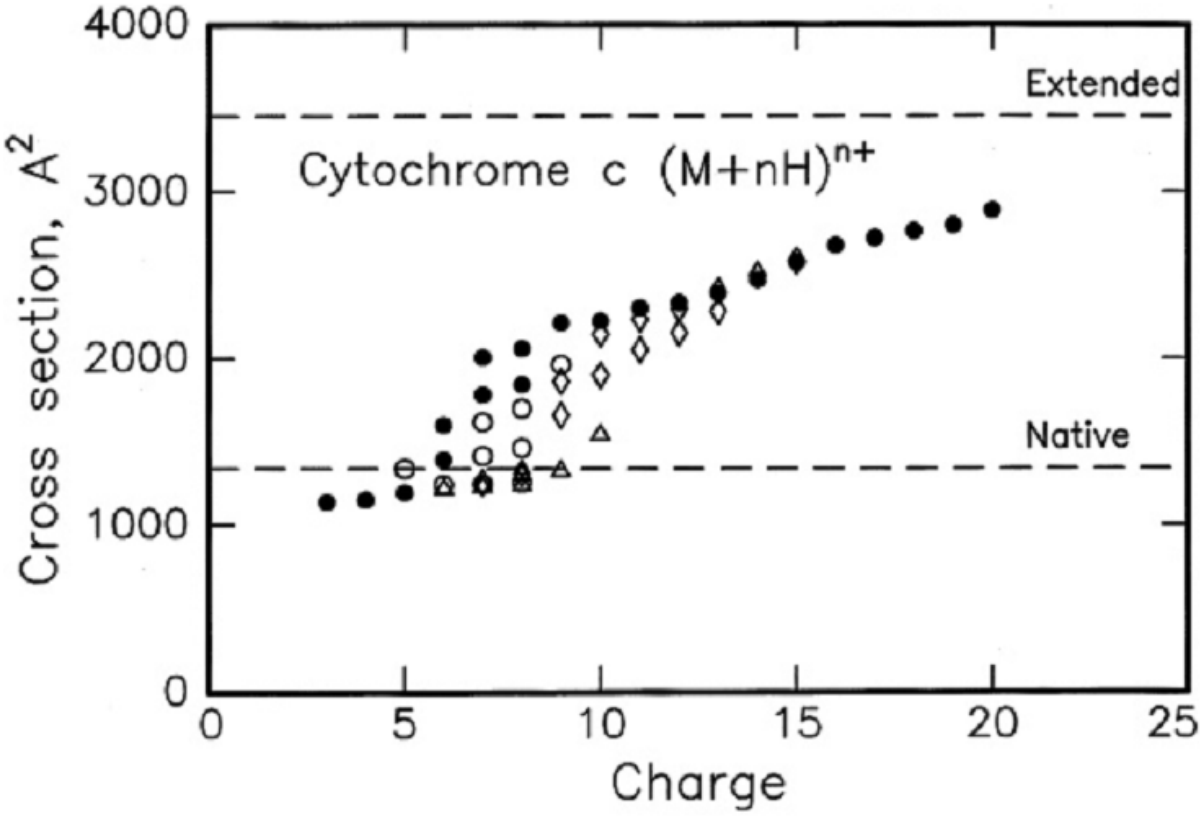

Figure 3 Plot of the cross sections of the main features resolved in the drift time distributions of the +3 to +20 charge states of bovine cytochrome *c*. Cross sections are shown for features observed on an injected ion drift tube apparatus at high injection energies (*closed circles*) and for metastable conformations observed at lower injection energies (*open circles*). Features observed on a high-resolution apparatus (with no injection energy) are also shown. Here the cross sections depend on the electrosprayed solution. Results are shown for an unacidified aqueous solution (*open triangles*) and for an acidified solution (*open diamond*). (*Dashed lines*) The cross sections calculated for the crystal structure coordinates and for a fully extended string.

Annu. Rev. Phys. Chem. 2000. 51:179–207

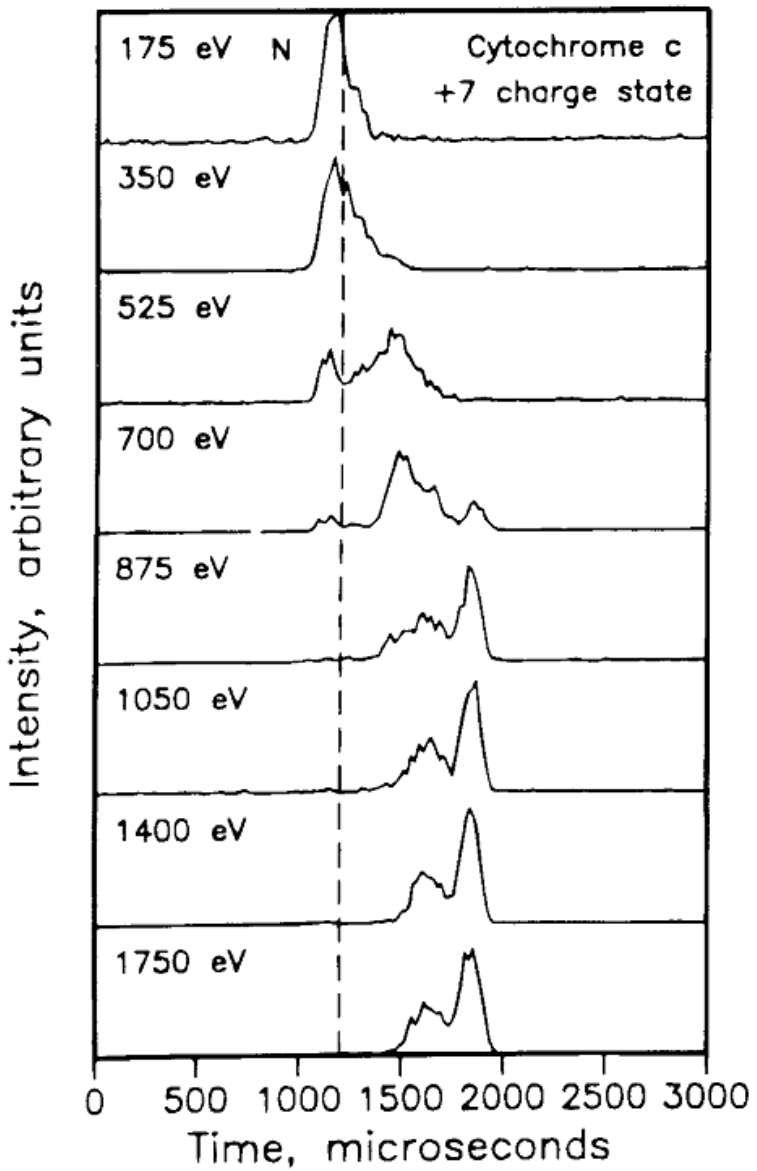

Figure 7. Drift time distributions for the +7 charge state of bovine cytochrome *c* measured as a function of injection energy. The dashed line shows the drift time expected for the native conformation of cytochrome *c*.

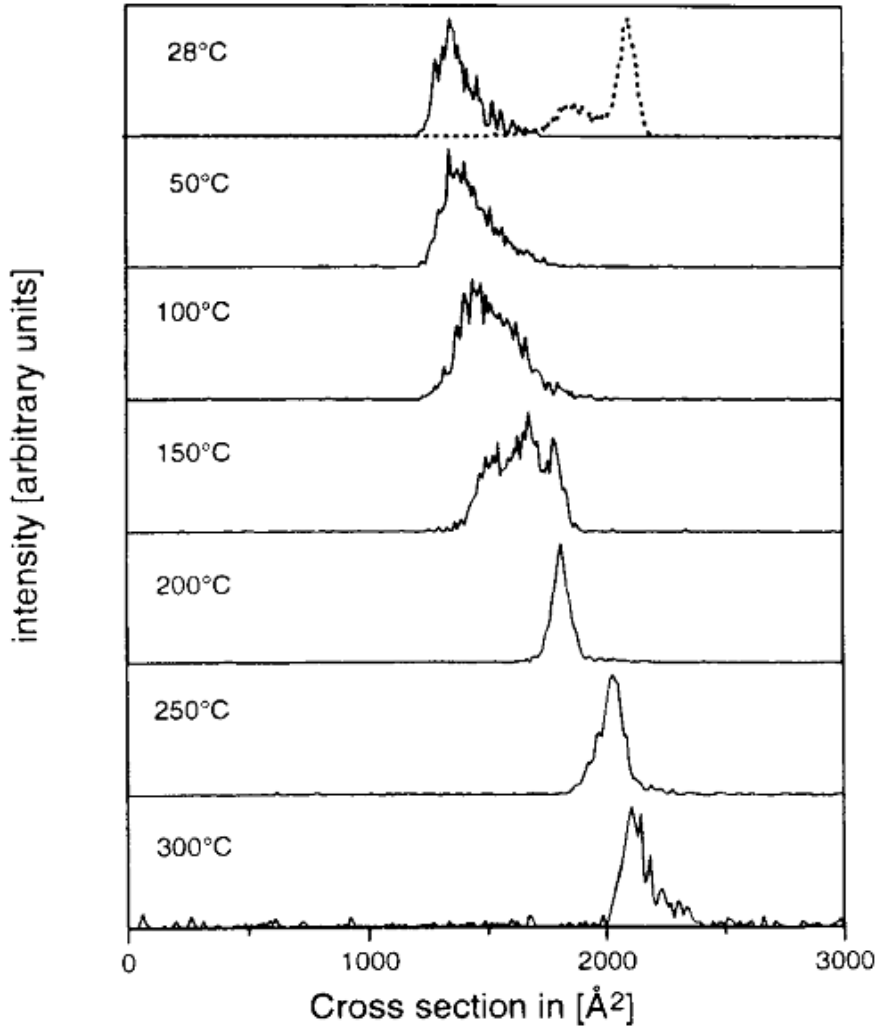

Figure 9. Drift time distributions recorded for the +7 charge state of cytochrome *c* as a function of drift tube temperature. The drift time-scale has been converted into a cross-section scale so that distributions recorded at different temperatures can be easily compared. The dashed line shows the distribution measured at high injection energy (2100 eV). The other distributions were recorded with a low injection energy (350 eV).

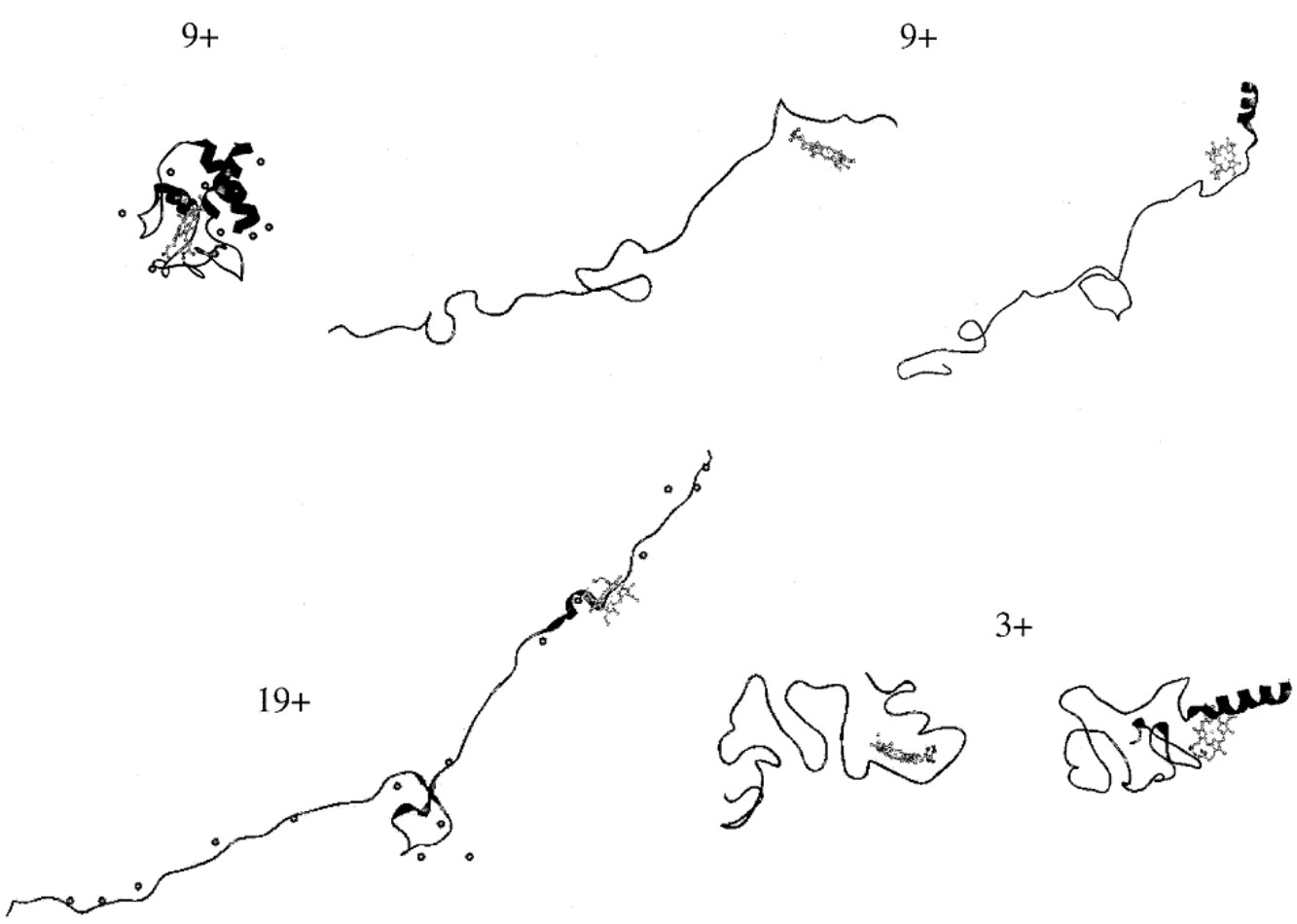

Figure 6 Representative conformations from the molecular dynamics simulations of cytochrome *c* ions in vacuo; (*Left*) The folded +9 and unfolded +19 are from simulations started from the crystal structure. (*Dots*) The location of the charges. The partially refolded +9 conformations were produced by removing 10 protons from the unfolded +19. They are more compact than the +19 and are much less compact than the folded +9 prepared from the crystal structure, although the partially refolded and folded +9 have similar energies. The +3 conformations were prepared by removing an additional six protons from the +9. These are less compact than the folded +3 generated from the crystal structure and are significantly higher in energy.

Annu. Rev. Phys. Chem. 2000. 51:179–207

Professor Martin F. Jarrold

INDIANA UNIVERSITY
BLOOMINGTON

Disulfide-Intact and -Reduced Lysozyme in the Gas Phase: Conformations and Pathways of Folding and Unfolding

Stephen J. Valentine, Jennifer G. Anderson, Andrew D. Ellington, and David E. Clemmer*

Department of Chemistry, Indiana University, Bloomington, Indiana 47405

J. Phys. Chem. B **1997,** *101,* 3891−3900

The conformations of gaseous lysozyme ions (+5 through +18) produced by electrospray ionization have been studied in the gas phase using ion mobility mass spectrometry techniques. When solutions containing the disulfide-intact and disulfide-reduced lysozyme are electrosprayed, the gas-phase ions that are produced have distinctly different collision cross sections. Disulfide-intact ions favor two conformer types: a highly folded conformer with a cross section near that calculated for the crystal structure and a partially unfolded conformer that is formed when the ions are injected into the drift tube at high injection voltages. Ions formed from the disulfide-reduced solution have collision cross sections that are much larger than any observed for the disulfide-intact protein, showing that these ions are largely unfolded. Gas-phase proton-transfer reactions in the ion source can be used to favor lower charge states for both solutions. When protons are removed from disulfide-intact lysozyme ions, highly folded compact conformations are favored. Exposing the disulfide-reduced lysozyme ions to proton-transfer reagents causes the protein to fold up, and several of the new conformations have cross sections that are indistinguishable from those measured for the disulfide-intact protein. It appears that an array of gas-phase folding intermediates or misfolded metastable states are stable because of the well-defined interplay between attractive−folding and repulsive−Coulombic interactions

Secondary Structure of Intact Lysozyme

Length; 129 residues

Secondary structure;

41% helical (7 helices; 54 residues)

10% beta sheet (9 strands; 14 residues)

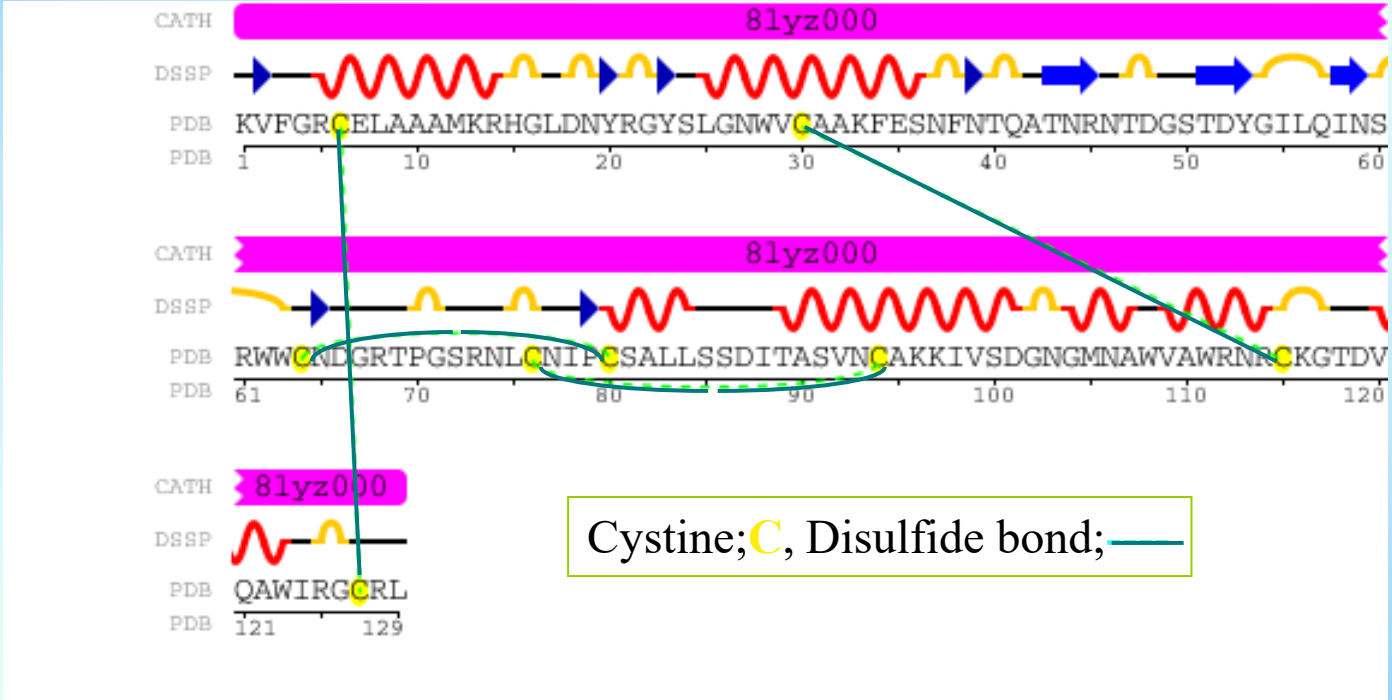

Before measurements, the disulfide bonds are reduced by adding DTT to sample solution.

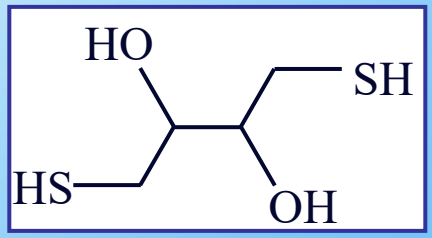

Dithiothreitol(DTT)

Reference; Protein Data Bank (http://www.rcsb.org/pdb)

Reduction of S-S bonds with DTT

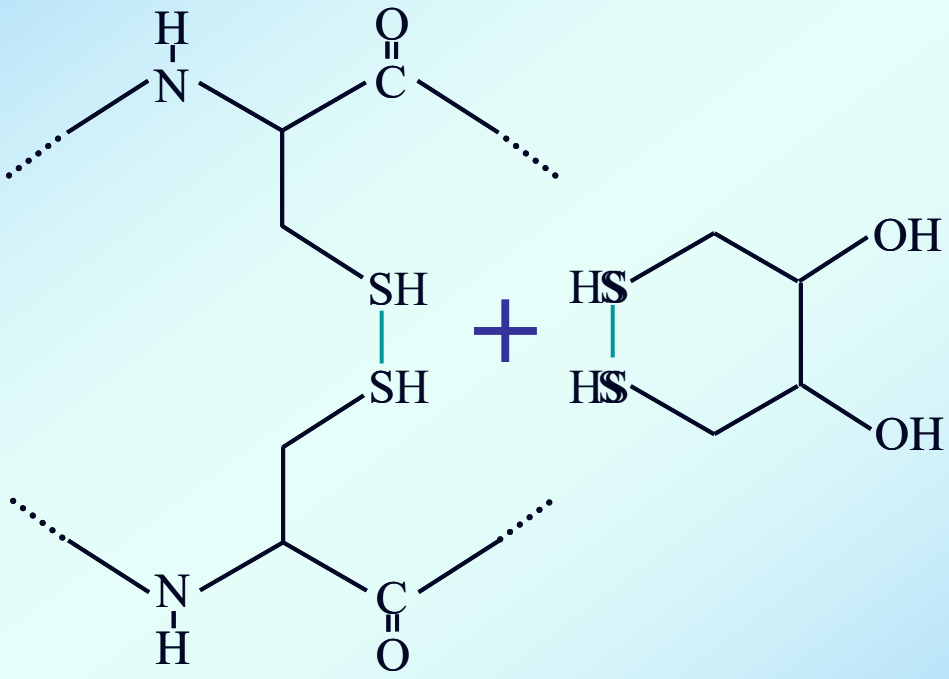

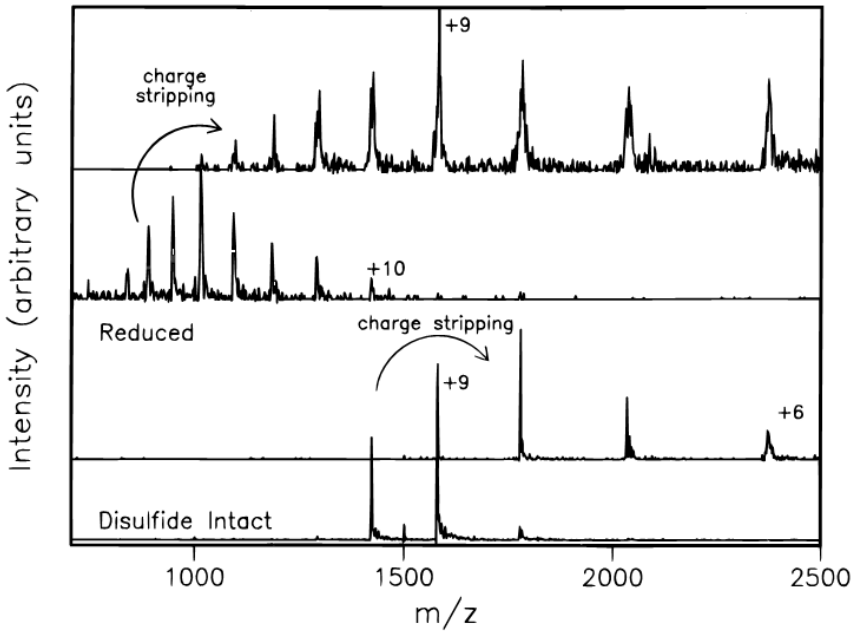

Figure 2. Mass spectra for disulfide-intact and -reduced lysozyme solutions as described in the text. Also shown are the mass spectra obtained when these solutions are exposed to gas-phase charge-stripping reagents in the source.

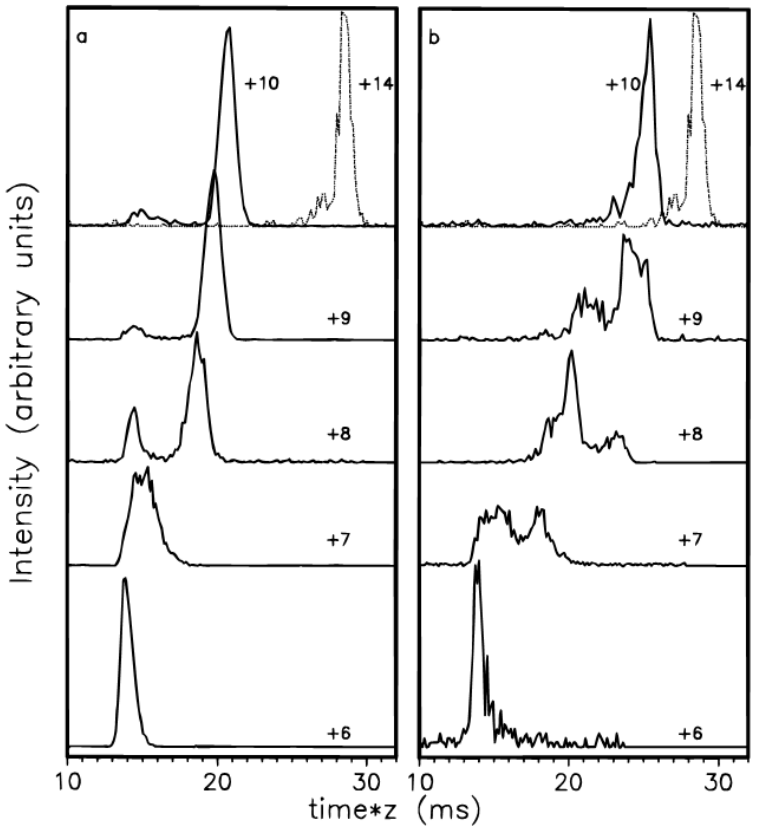

Figure 5. Charge-normalized drift time distributions for the +6 to +10 charge states of disulfide-intact (part a) and -reduced (part b) lysozyme. All data were recorded at an injection voltage of 120 V and have been scaled to a buffer gas pressure of 2.000 Torr. Ion-mobility distributions for the low charge states (+6 and +7 disulfide-intact, and +6 to +10 of the disulfide-reduced protein) were recorded after ions were exposed to proton-transfer reagents in the source gas cell.

J. Phys. Chem. B, Vol. 101, No. 19, 1997 **3897**

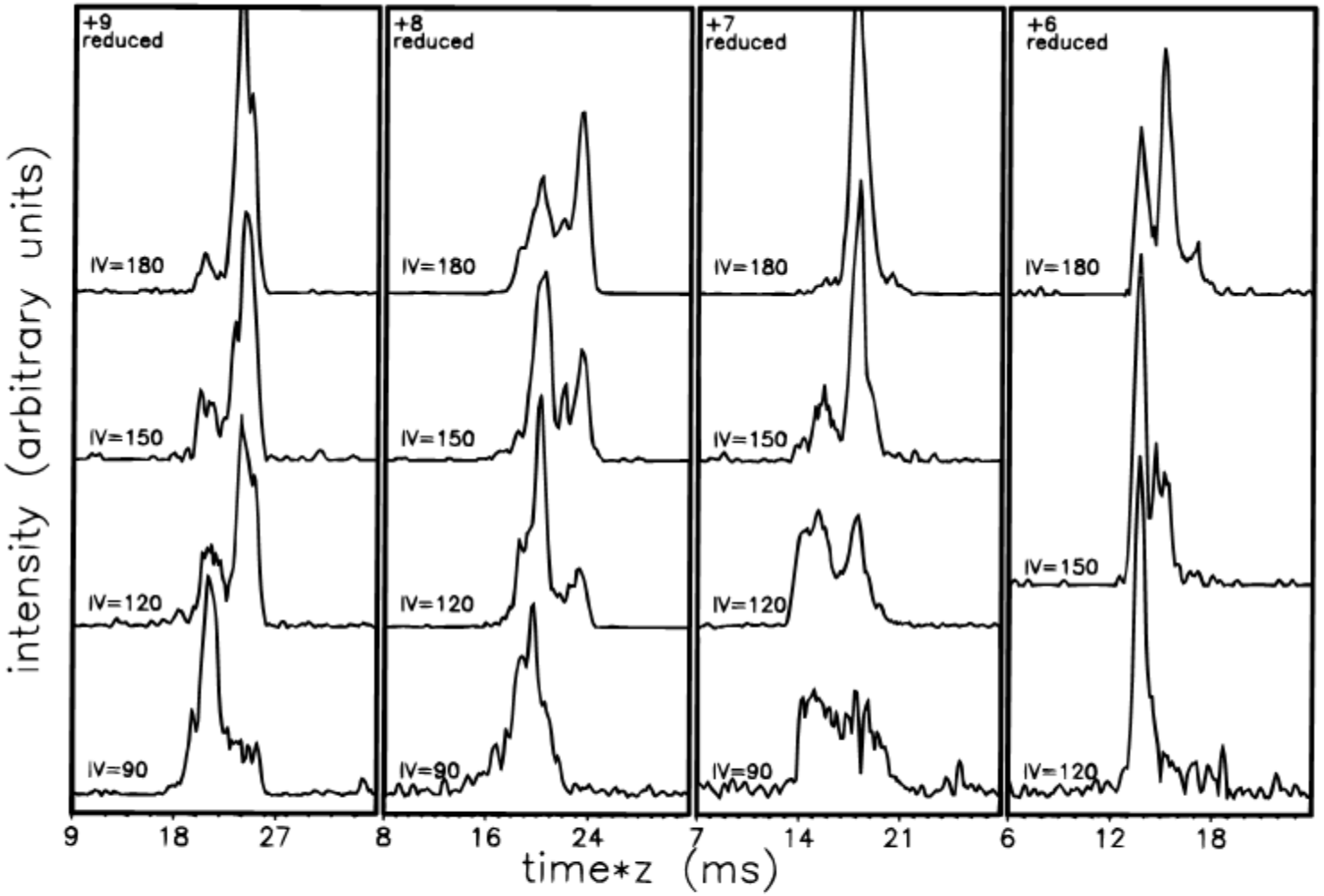

Figure 6. Charge-normalized drift time distributions as a function of injection voltage for the +6 through +10 charge states of disulfide-reduced lysozyme after it has been exposed to gas-phase proton-transfer reagents. The data have been scaled to a buffer gas pressure of 2.000 Torr.

J. Phys. Chem. B, Vol. 101, No. 19, 1997 **3897**

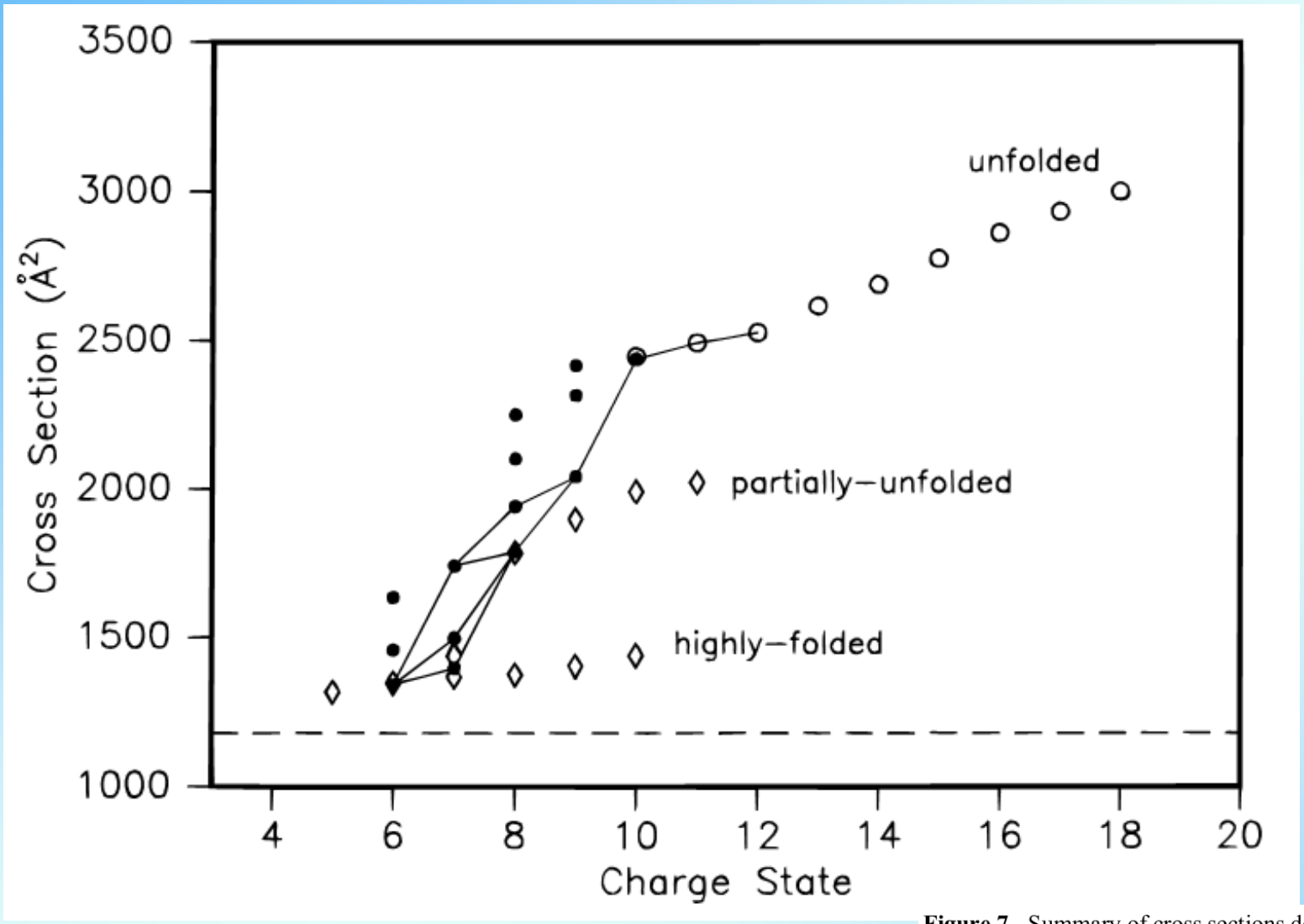

Figure 7. Summary of cross sections determined for all ions observed in these studies. The open diamonds correspond to disulfide-intact lysozyme ions and correspond to highly folded and partially unfolded conformations (see text). The open circles correspond to unfolded conformers that were formed by electrospraying a disulfide-reduced solution of lysozyme. The solid circles correspond to peaks observed after the disulfide-reduced peaks (open circles) are exposed to gas-phase charge-stripping reagents in the source gas cell. The solid line corresponds to those species that appear to be formed directly from proton-transfer reactions in the source (see text). The dashed line is the calculated cross section for the crystal coordinates of lysozyme.

Structural Stability from Solution to the Gas Phase:
Native Solution Structure of Ubiquitin Survives Analysis in a Solvent-Free Ion Mobility Mass Spectrometry Environment

T. Wyttenbach, M. T. Bowers
J. Phys. Chem. B 2011, 115, 12266.

Ubiquitin is a small (8.5 kDa) regulatory protein that has been found in almost all tissues (ubiquitously) of eukaryotic organisms.

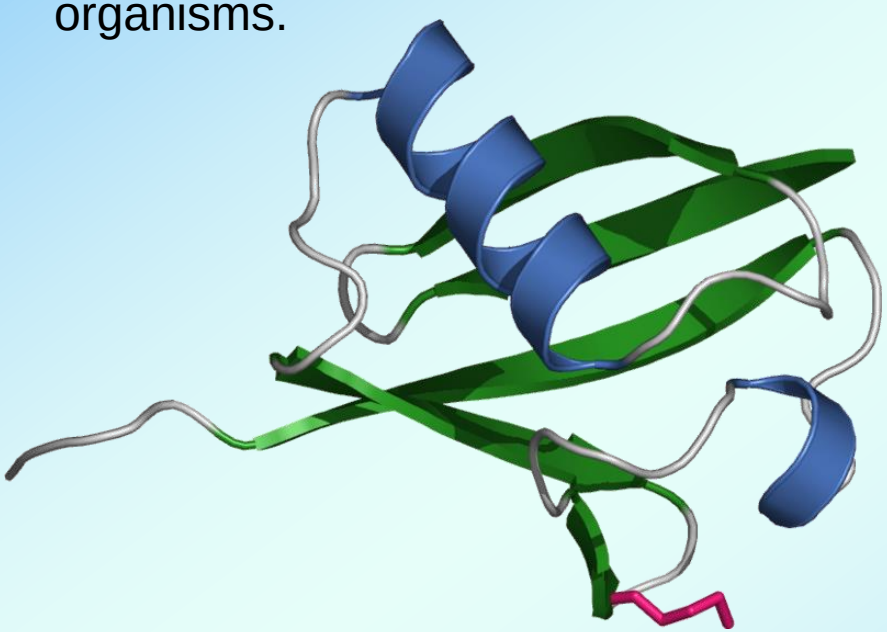

Ubiquitination is a post-translational modification (an addition to a protein after it has been made) where ubiquitin is attached to a substrate protein.

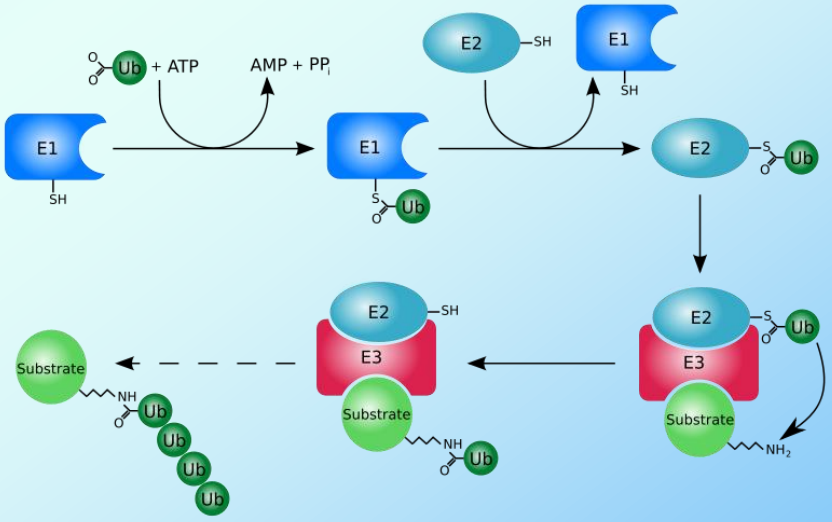

Wikipedia; ubiquitin

Ubiquitin

M. W. 8564.8 Da, 76 residues

25% helical (3 helices; 19 residues)

34% beta sheet (7 strands; 26 residues)

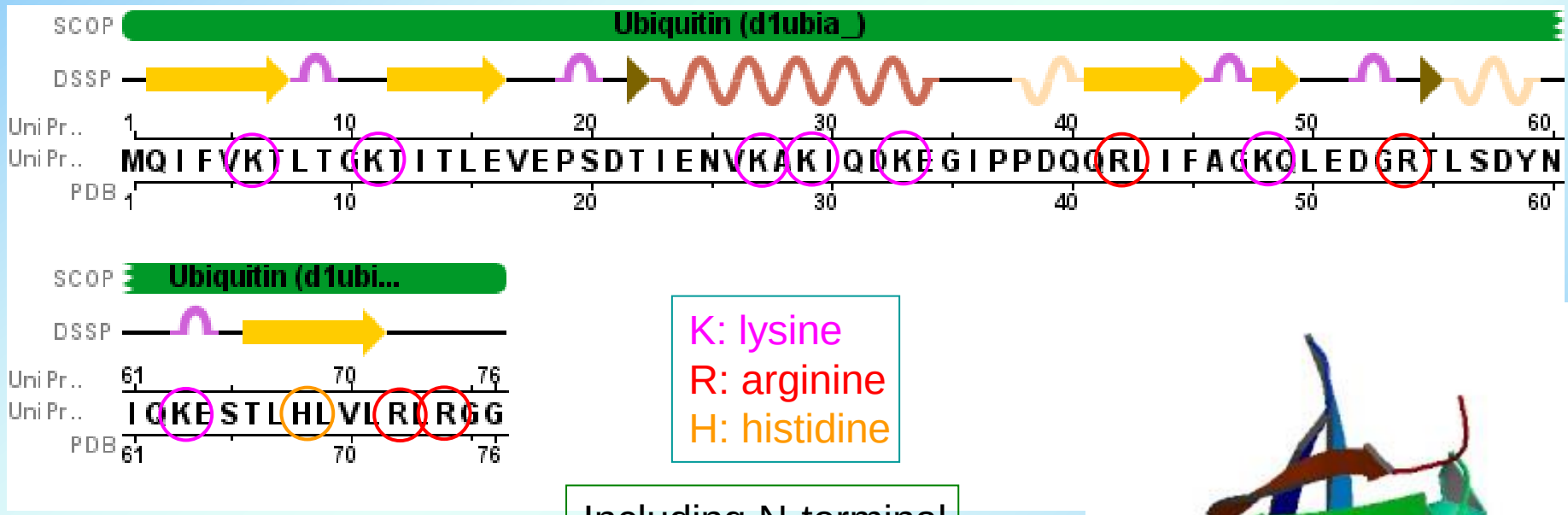

K: lysine
R: arginine
H: histidine

Including N-terminal,
13 protonated sites

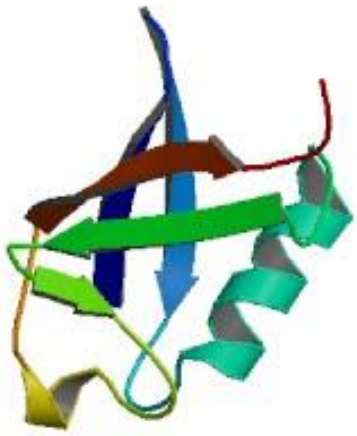

Ubiquitin from bovine erythrocytes (Sigma-Aldrich)

Reference; Protein Data Bank (http://www.rcsb.org/pdb)

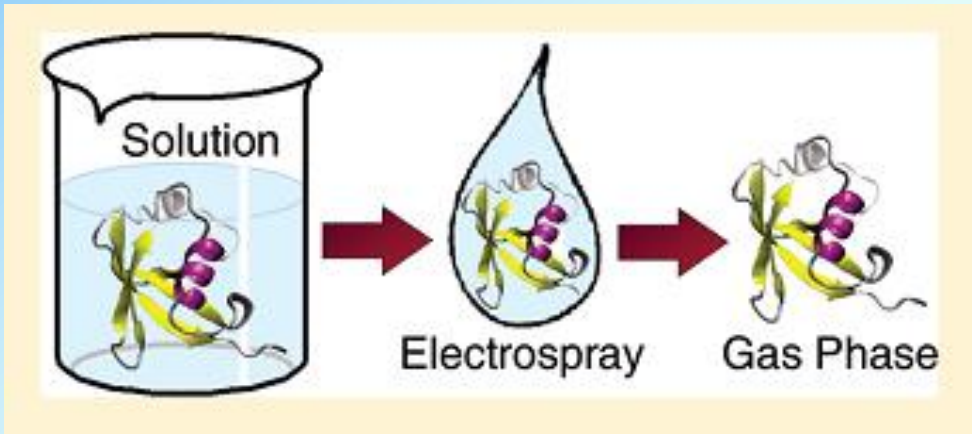

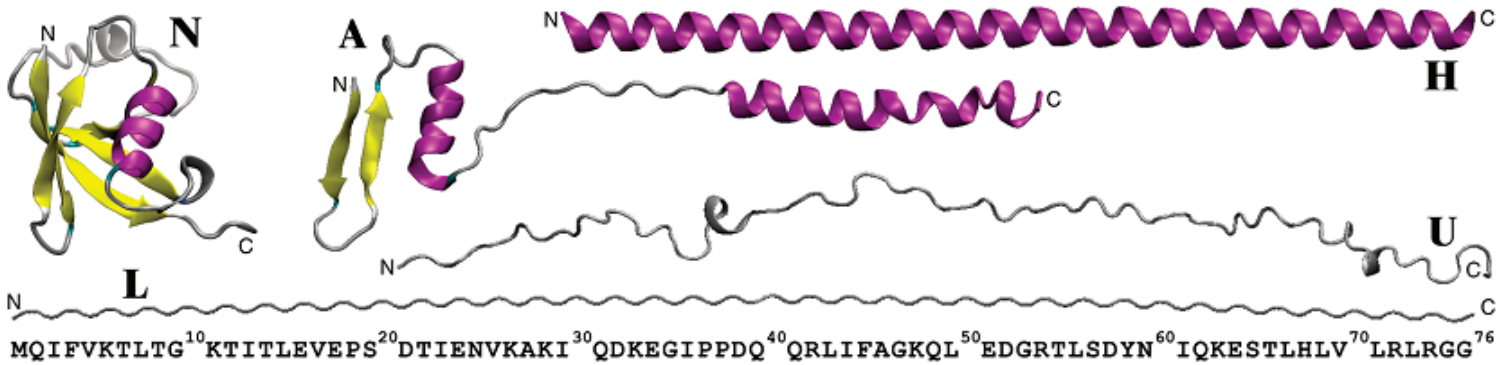

Figure 1. Various conformations and the human sequence of the 76 residue protein ubiquitin. **N** is the native state characterized by X-ray crystallography and NMR; **A** the *A* state found in acidic solutions containing high concentrations of methanol; **H** a hypothetical fully α-helical conformation (all backbone dihedral angles set to $\phi = -57°$ and $\psi = -47°$); **U** an unfolded conformation found in MD simulations of $[M + 13H]^{+13}$ in a solvent-free environment;[52] and **L** a hypothetical fully linear conformation ($\phi = \psi = 180°$). All structures are rotated such that their N terminus is on the left and their C terminus is on the right with the termini labeled by nonbold letters N and C, respectively.

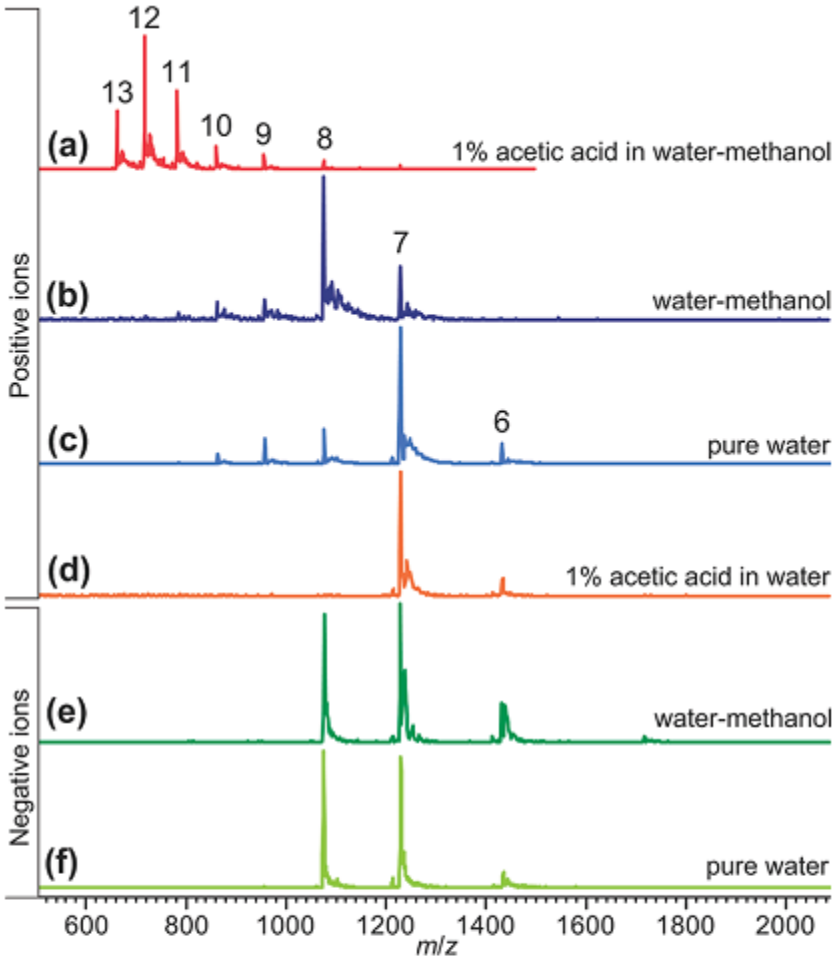

Figure 2. Positive and negative ion mass spectra of ubiquitin as a function of ESI solution condition. (a) Positive ion spectrum obtained under typical ESI conditions employing a solvent of 1% acetic acid in 1:1 water−methanol. In this solvent mixture ubiquitin is known to occur in the *A* state. The native state, on the other hand, is known to be stable under all other solvent conditions used here: In positive ion mode, (b) 1:1 water−methanol, (c) pure water, (d) 1% acetic acid in water; and in negative ion mode, (e) 1:1 water−methanol and (f) pure water. The numbers above the peaks indicate the charge state of ubiquitin.

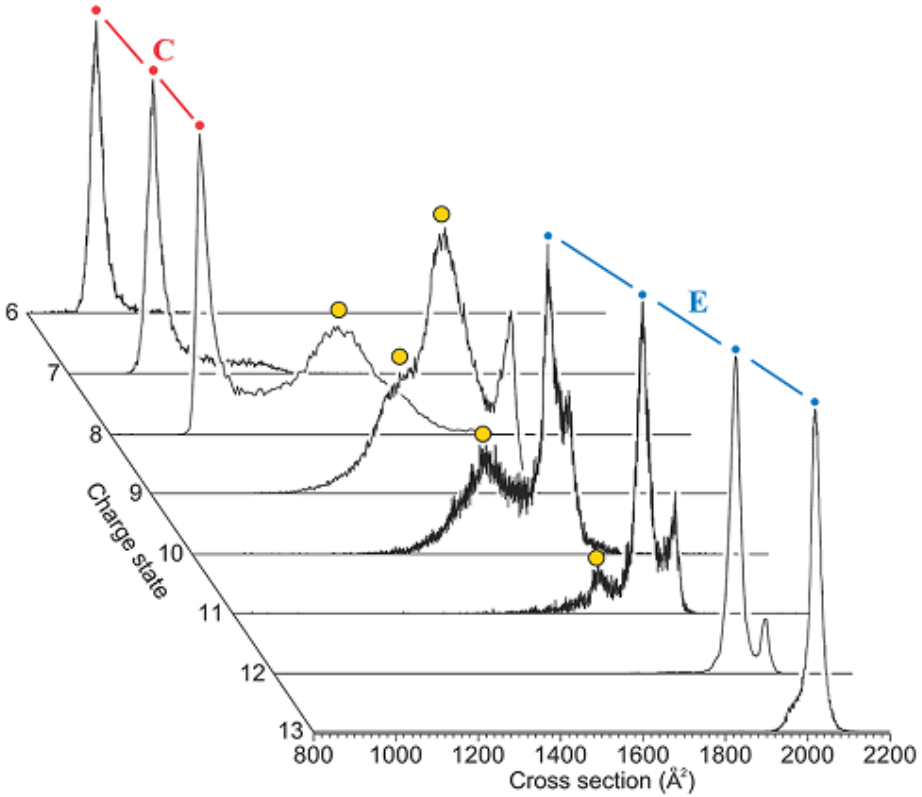

Figure 3. Ion mobility spectra of mass-selected positive ubiquitin ions as a function of charge state. Drift times (x-axis) are normalized by ion charge, helium pressure, and drift voltage in each case and are therefore proportional to cross sections indicated in units of Å^2. This representation allows direct comparison of features across spectra. Ion drift times are of the order of 40−100 ms in all spectra. Apparent are several sharp peaks (marked in red) corresponding to a family **C** of ions with a cross section of ~1000 Å^2 and a charge of 6−8. Another set of sharp intense peaks **E** (blue) occurs in the range of 1600−2000 Å^2 for charge states 10 and above. Broad features observed for ions of intermediate charge and intermediate cross section are marked with a large yellow dot. Solvents used for acquisition of the spectra are pure water for $z = 6$ and 7; 1:1 water−methanol for $z = 8$ and 9; and 1% acetic acid in 1:1 water−methanol for $z = 10-13$.

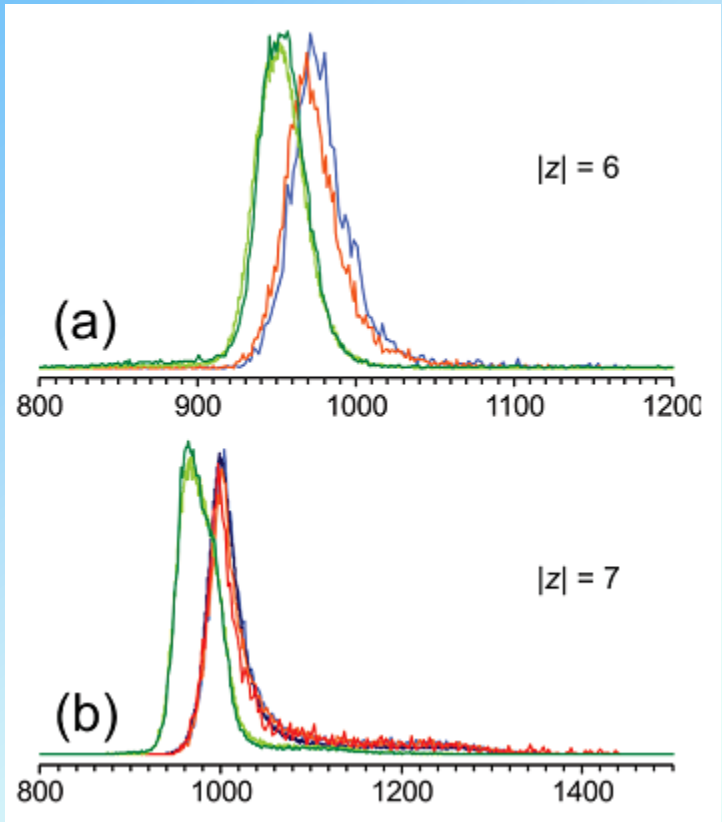

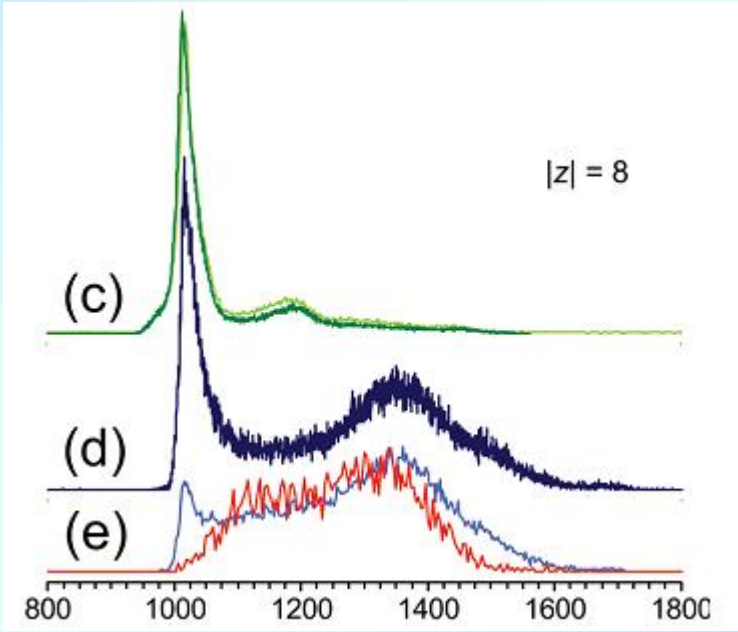

Figure 4. Ion mobility spectra of mass-selected ubiquitin ions as a function of ion mode (positive or negative) and ESI solvent composition for a selection of charge states: (a) ±6, (b) ±7, (c) −8, (d) and (e) +8, and (f) +11. Shown in blue are spectra for positive ions sprayed from pure water (light blue) or from a 1:1 water−methanol mixture (dark blue). Shown in green are spectra for negative ions sprayed from pure water (light green) or from a 1:1 water−methanol mixture (dark green). Shown in orange and red are spectra for positive ions sprayed from 1% acetic acid in water (orange) or 1% acidic acid in 1:1 water−methanol (red).

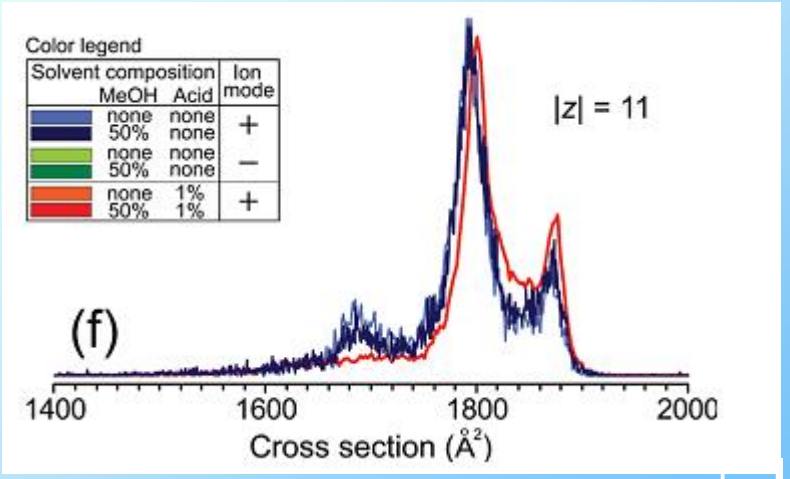

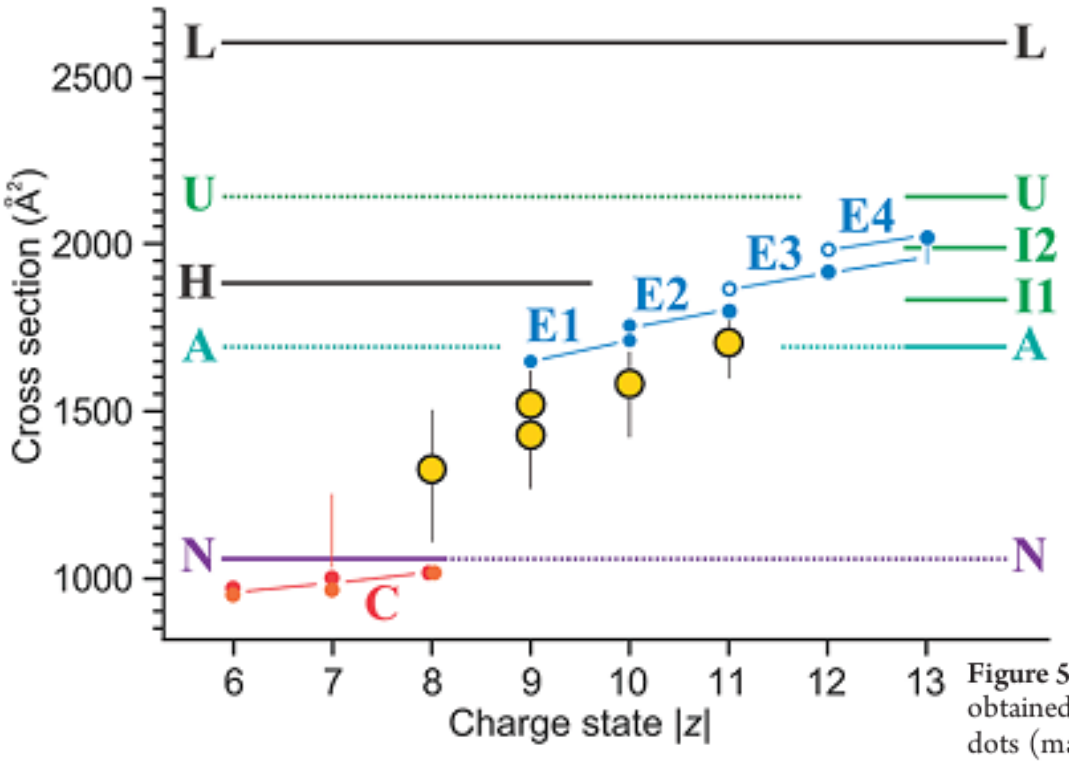

Figure 5. Ubiquitin cross section as a function of charge state $|z|$. Values obtained for sharp peaks in the ion mobility spectrum are shown as small dots (major peaks) or small circles (minor peaks). Weak shoulders on one side of the peak are indicated with a vertical bar spanning the width of the shoulder. Cross sections corresponding to the center of a broad IMS peak are shown as large yellow dots with a vertical bar indicating the width of the peak. There is a family of compact structures **C** with a cross section near 1000 $Å^2$ (red data for positive, orange for negative ions) and several families of well-defined extended structures above 1600 $Å^2$ (blue data). The blue data appear to increase in three steps from $z = 9$ to $z = 13$ indicating the presence of four distinct elongated families of structures **E1**−**E4**. The cross section of the native state ($z = 6-8$) is calculated (EHSS) to be ~1060 $Å^2$ (solid purple line) and that of the *A* state ($z = 13$) to be 1690 $Å^2$ (turquoise). Also shown are cross section data for theoretical structures obtained for a helical (**H**) and a linear (**L**) conformation (Figure 1) and for MD structures (metastable intermediates **I1** and **I2** and final unfolded state **U**) of $[M + 13H]^{+13}$ in a solvent-free environment (green).[52] The **U**, **A**, and **N** values are extended with dotted lines over the entire *z*-range for better comparison of the data.

Professor Michael T. Bowers

Department of Chemistry and Biochemistry
University of California
Santa Barbara, CA 93106 – 9510, USA

SYNAPT G2 HDMS

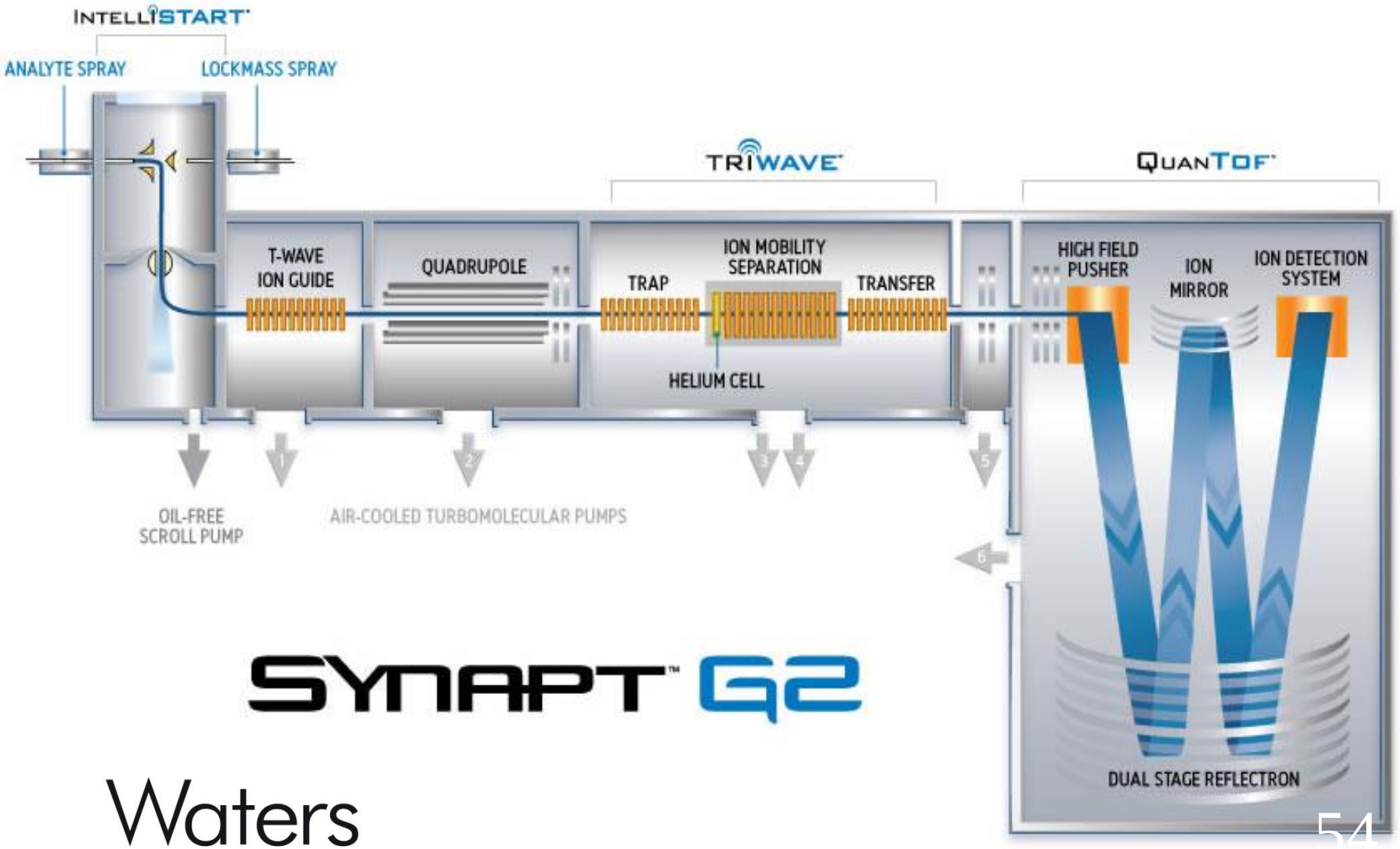

SYNAPT™ G2

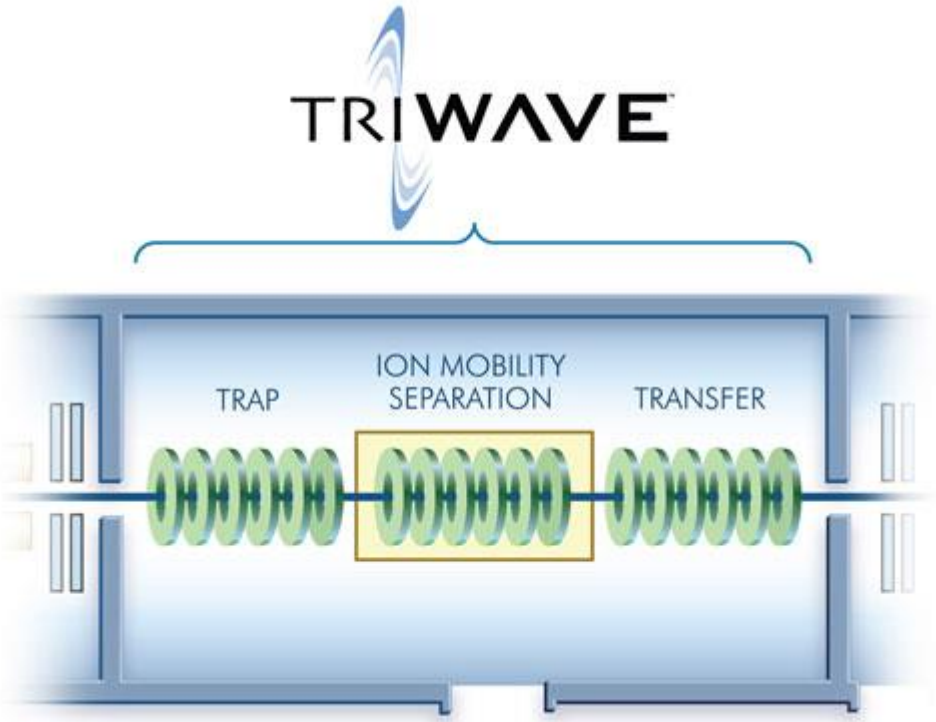

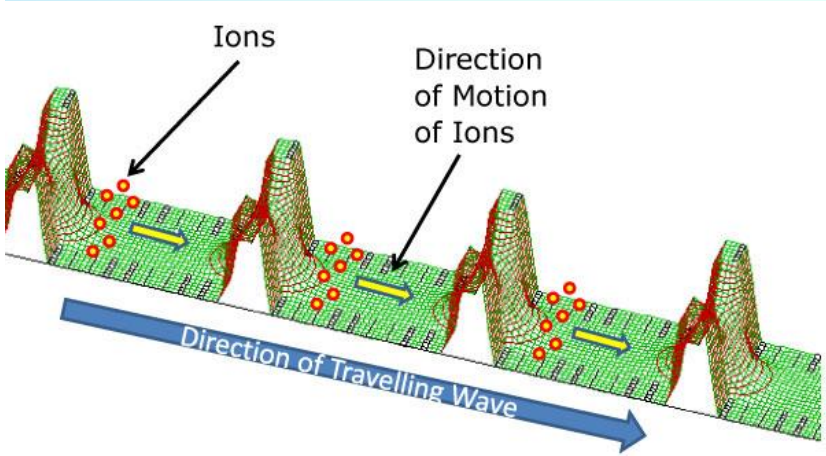

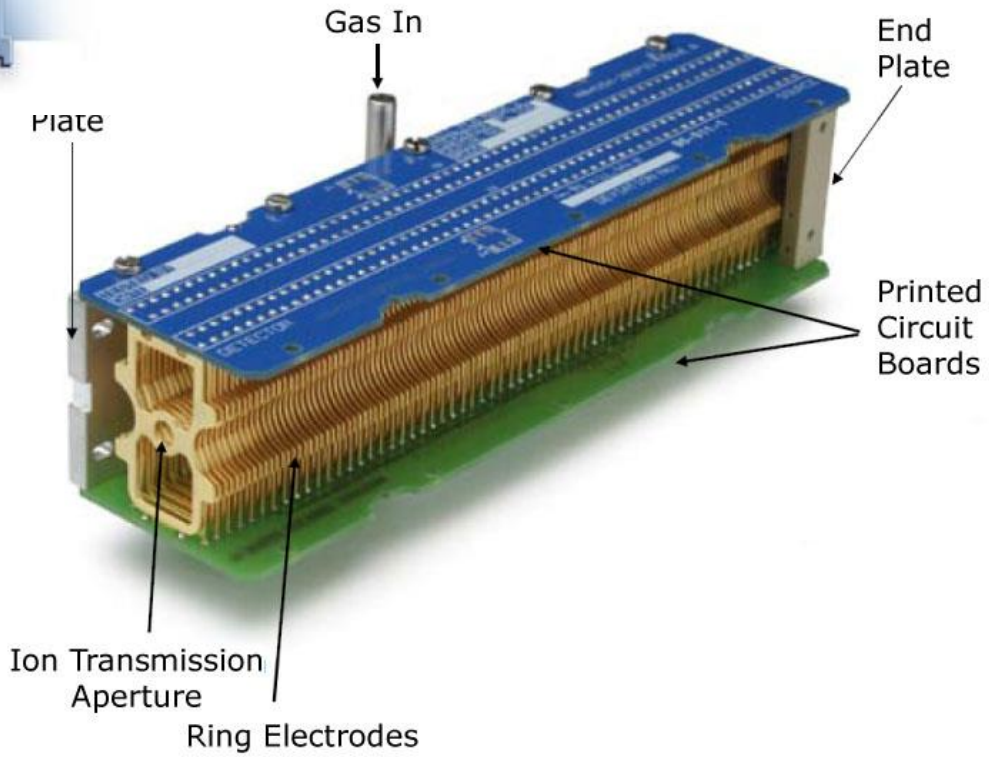

Waters

THE SCIENCE OF WHAT'S POSSIBLE.™

Ion mobility mass spectrometry (IMS–MS) of ubiquitin

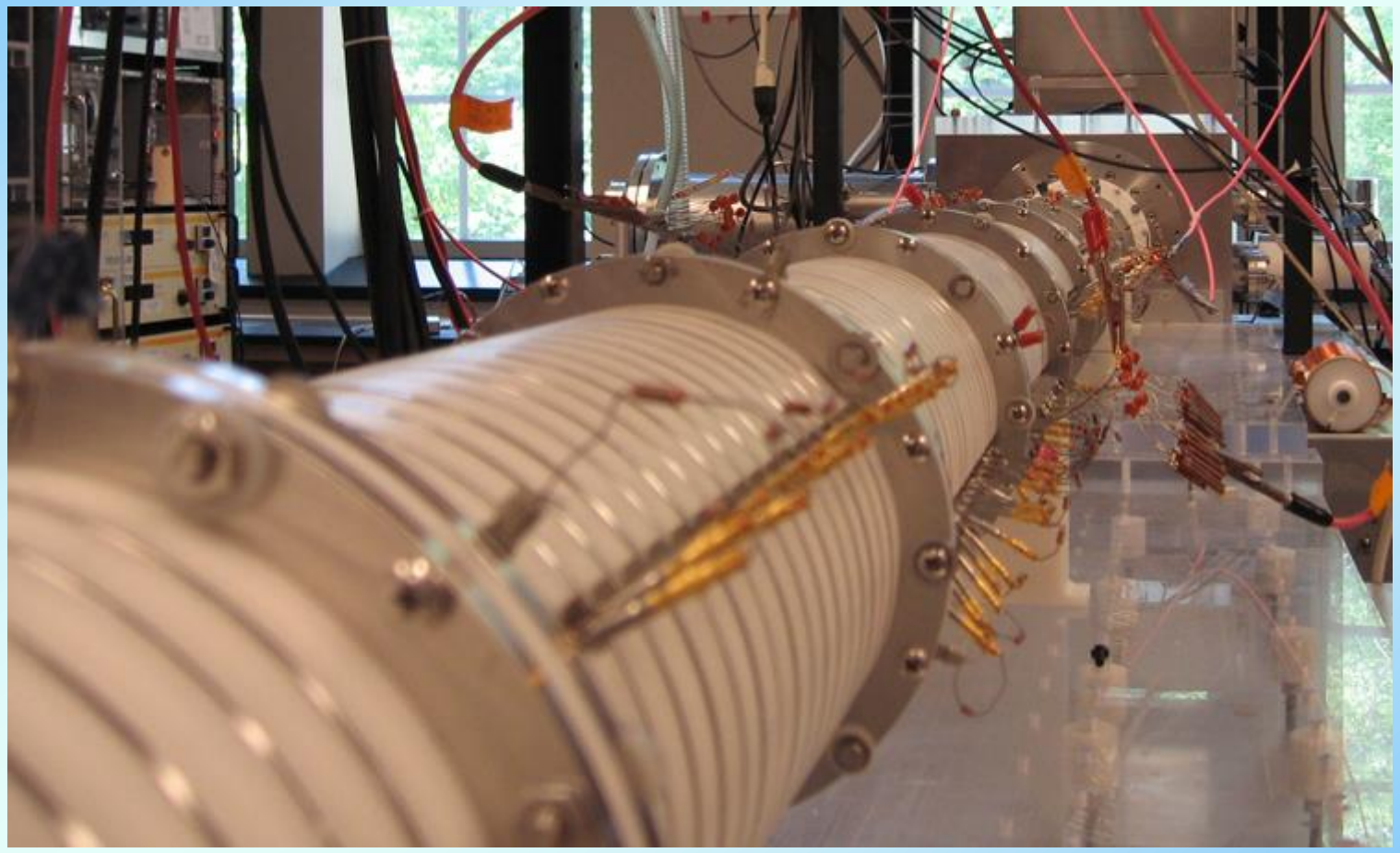

Prof. David E. Clemmer's group

Indiana University Bloomington

Figure 3. Collision cross sections for the +4 to +13 charge states of ubiquitin ions measured under several different experimental conditions, reported previously in refs 7 and 8. The open circles correspond to data recorded using a range of injection energies an injected ion drift tube (analogous to the instrument used in the present study). The +4 and +5 charge states were formed by proton transfer reactions using an instrumental design that incorporated a gas cell at the exit of the ESI source. The +6 to +13 charge states were formed directly by ESI. The original data (and subsequent studies) have been reanalyzed and it is now possible to resolve additional features in the distributions for +7 and +8 ions, which were not resolvable in the original report (refs 7 and 8). The vertical lines through the open circles show a range of cross sections that are associated with unresolved features in the ion mobility distributions. Also shown are cross sections for the +6 to +11 charge states, recorded at several source temperatures in a high-pressure drift tube, upon electrospraying a 49:49:2 water/aceteonitrile/acetic acid solution (solid diamonds) and a 89:9:2 solution (open diamonds). Overall trends in ion mobility peak shapes and cross sections as a function of charge state suggest that five different conformer types (A though E) are present, indicated by the gray regions in the figure. Finally, dashed lines indicate cross sections that are calculated from coordinates for the crystal structure by two methods (see text) as well as a nearly linear structure.

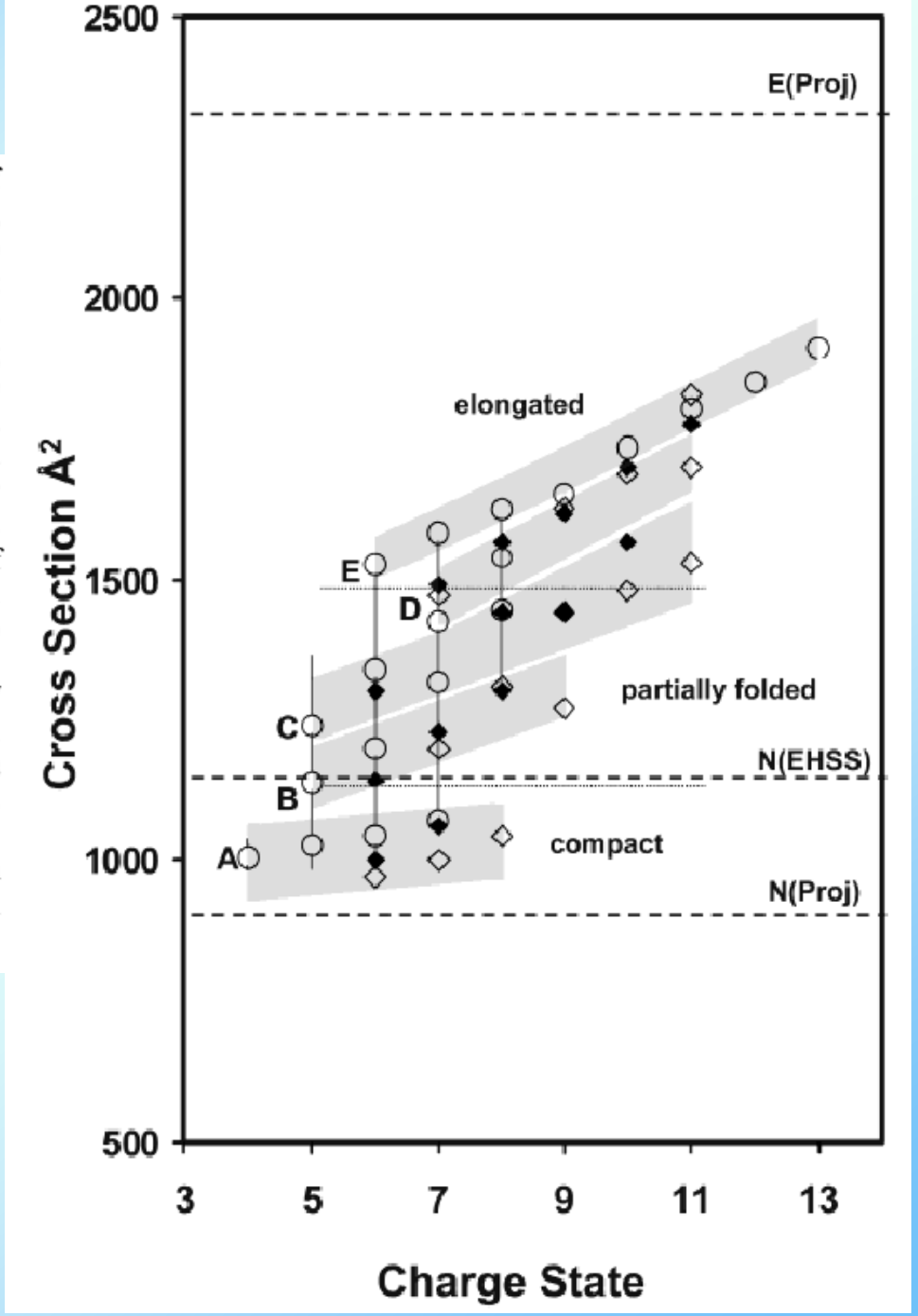

J. Phys. Chem. A **2002,** *106,* 9976−9982

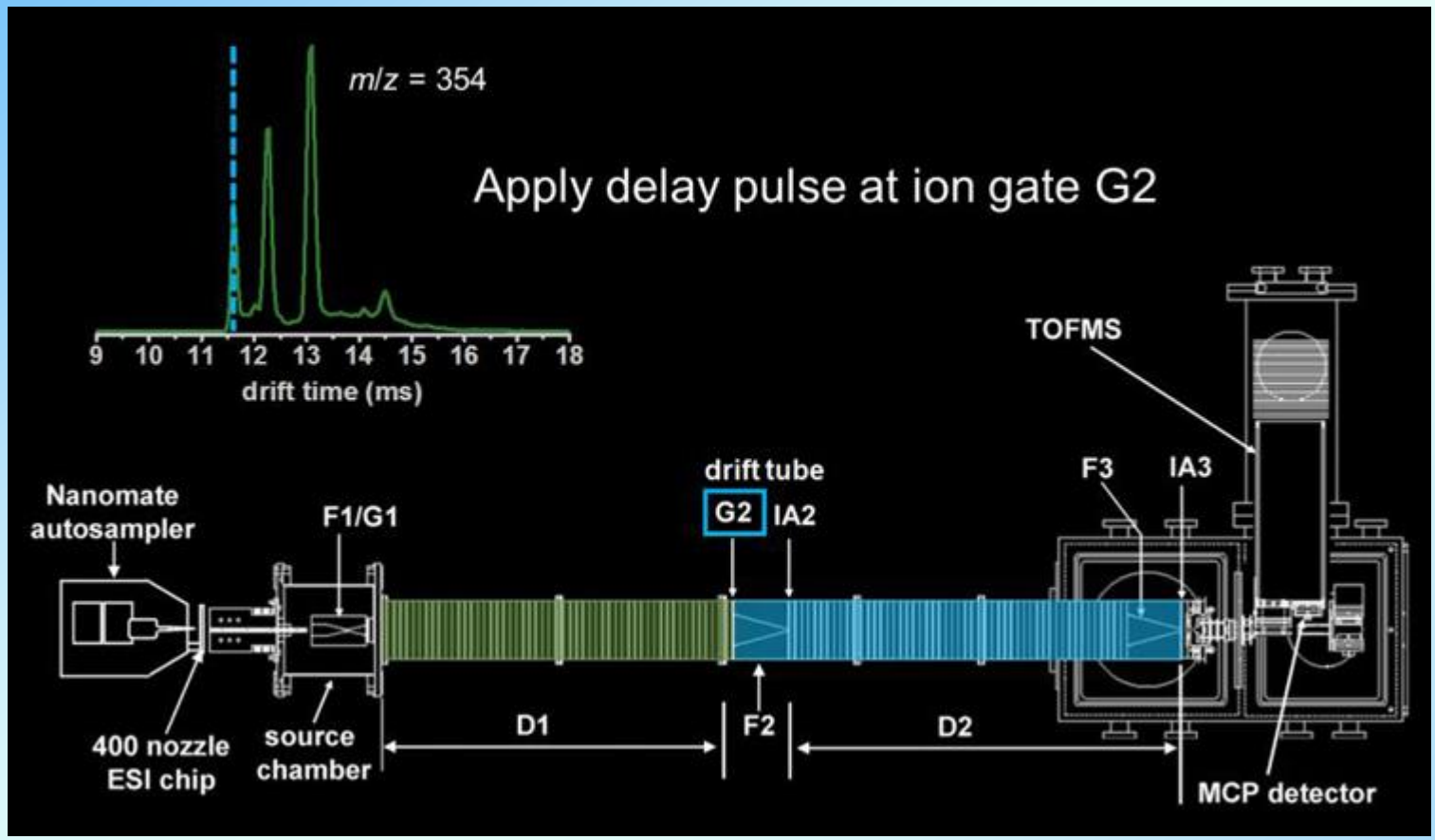

Following conventional IMS separation through a given drift region, a narrow packet of mobility-matched ions is isolated by momentarily lowering a repulsive potential at the electrostatic gate at a given delay time.

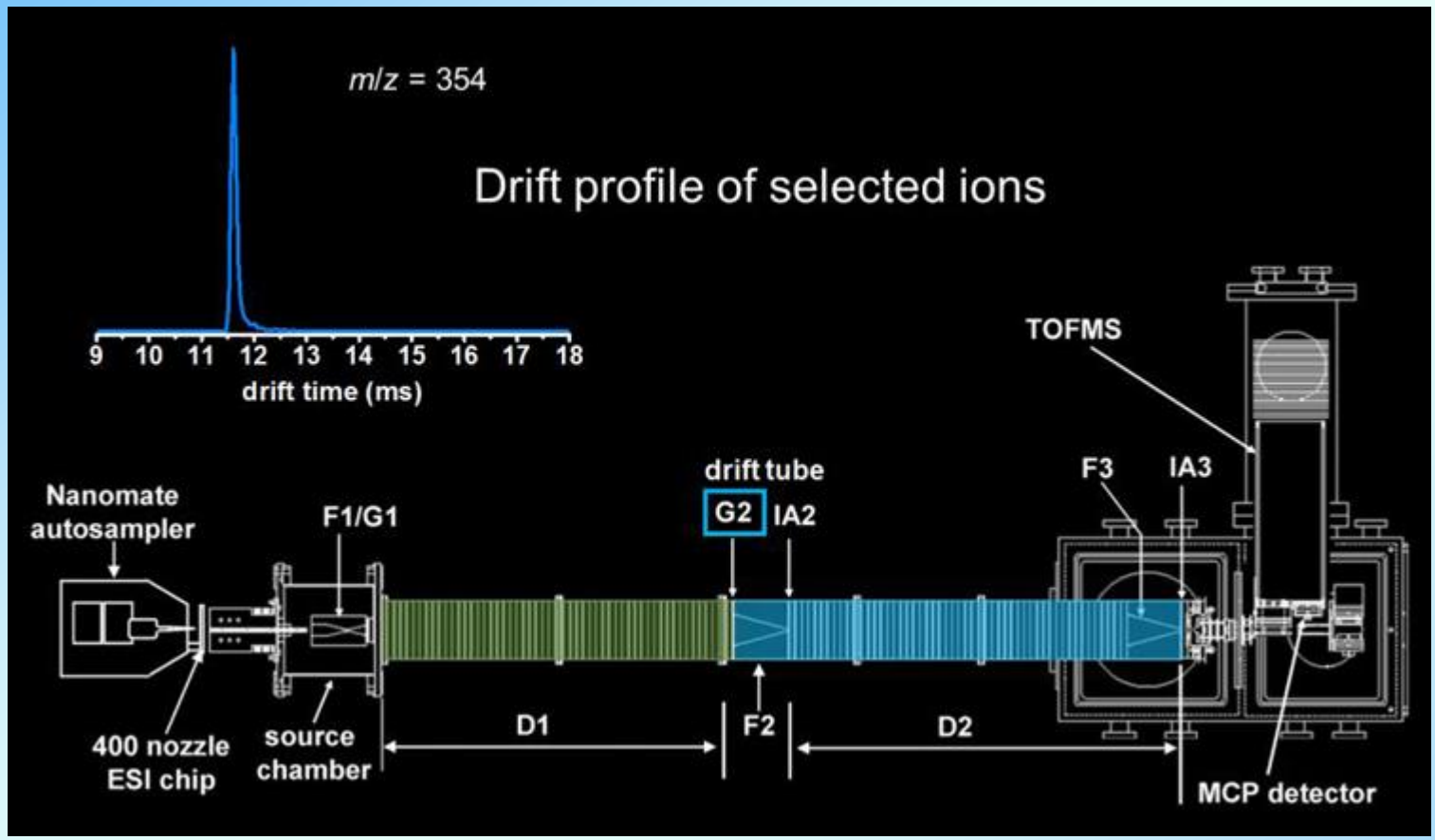

The selected ions are then subjected to collisional activation (ion–neutral collisions with the He buffer gas) by increasing the electric field in the ion activation region. This ion activation step can cause some of the ions to anneal to more compact structures, some of the ions to anneal to more elongated structures, and some of the ions remain the same. In addition to changing structure, higher activation voltages can be used to dissociate selected ions by CID.

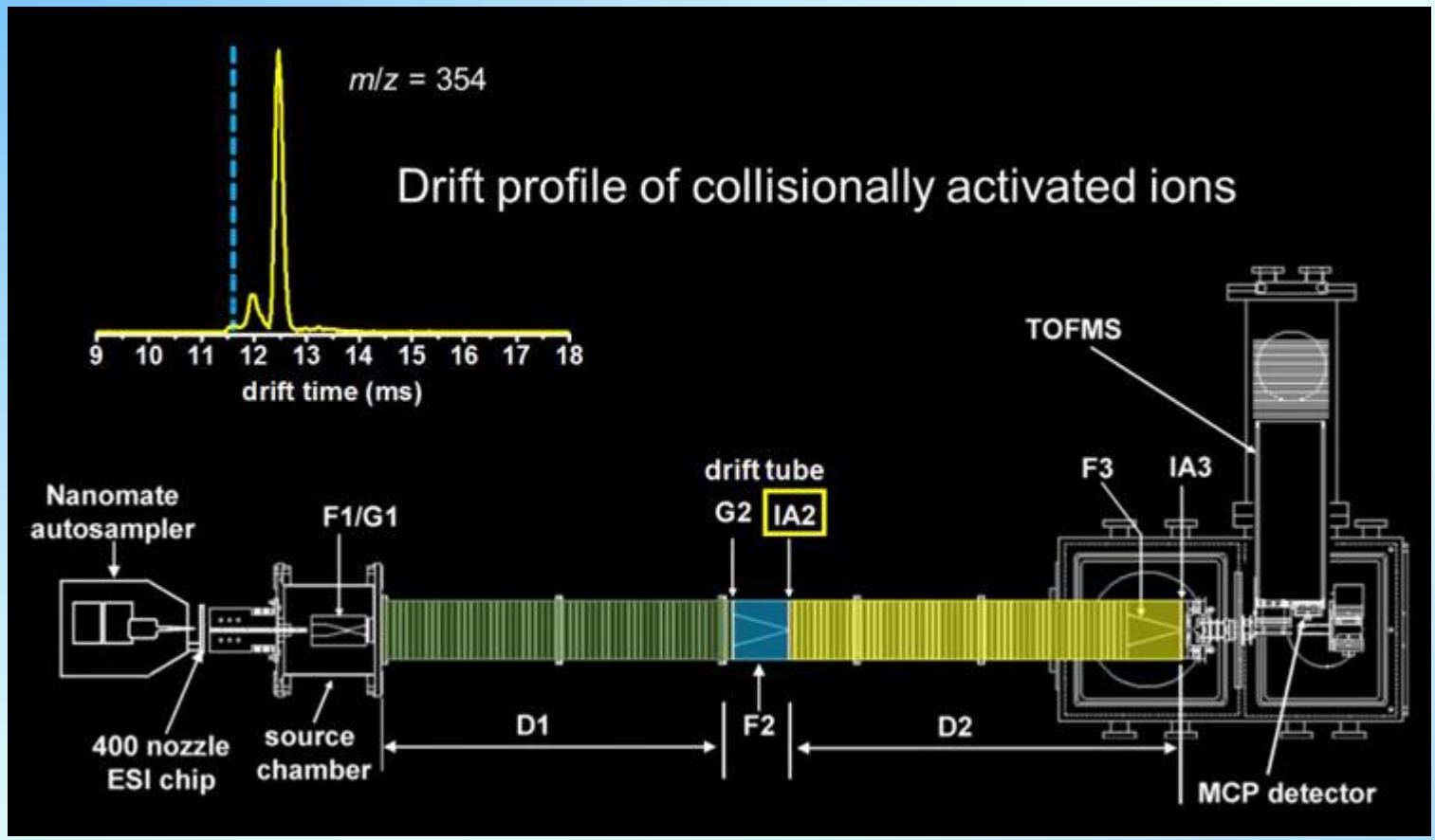
m/z = 354
Drift profile of collisionally activated ions
9 10 11 12 13 14 15 16 17 18
drift time (ms)
TOFMS
Nanomate autosampler
F1/G1
drift tube
G2
IA2
F3
IA3
400 nozzle ESI chip
source chamber
D1
F2
D2
MCP detector

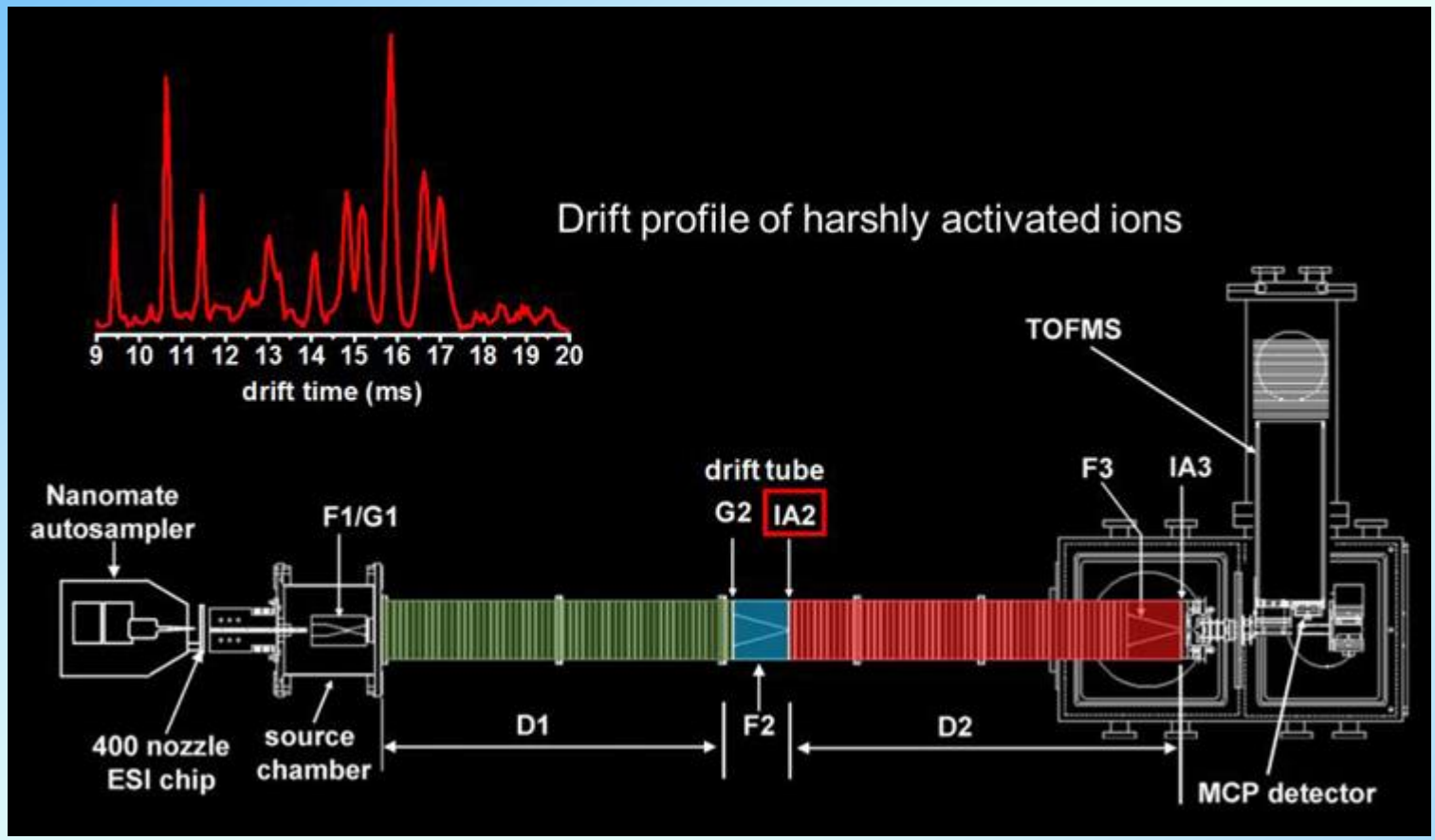

No longer uniformly mobility matched, the ions are then separated in the following drift region. We have demonstrated both two- and three-dimensional IMS. Higher-throughput multidimensional IMS can be achieved through a technique called combing.6 Pictures of the linear instruments typically used for these experiments can be found here for the 2m version and here for the longer 3m version.

2m IMS and IMS–IMS Instrument

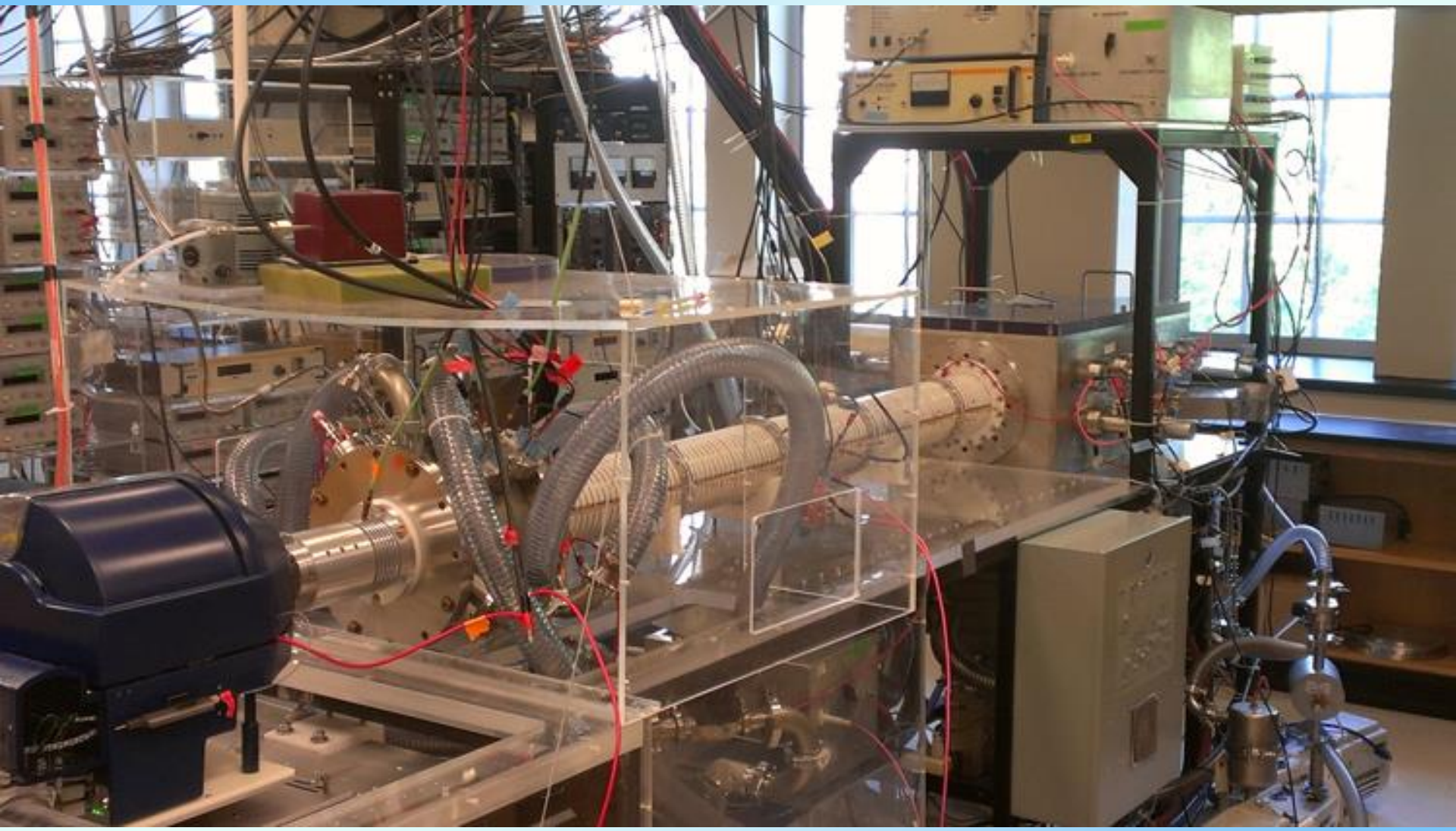

3m IMS, IMS–IMS, and IMS–IMS– Instrument

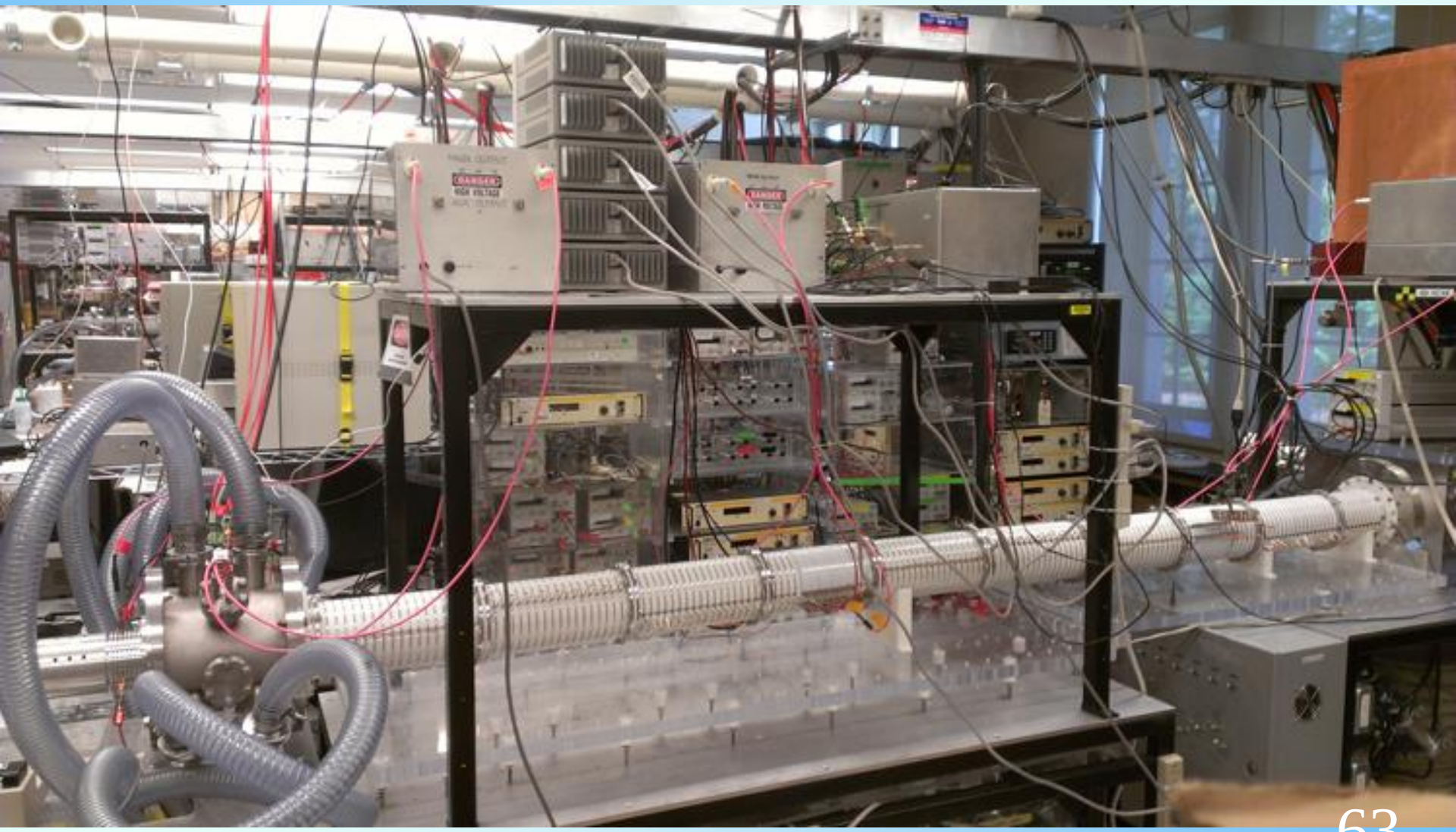

Transfer of Structural Elements from Compact to Extended States in Unsolvated Ubiquitin

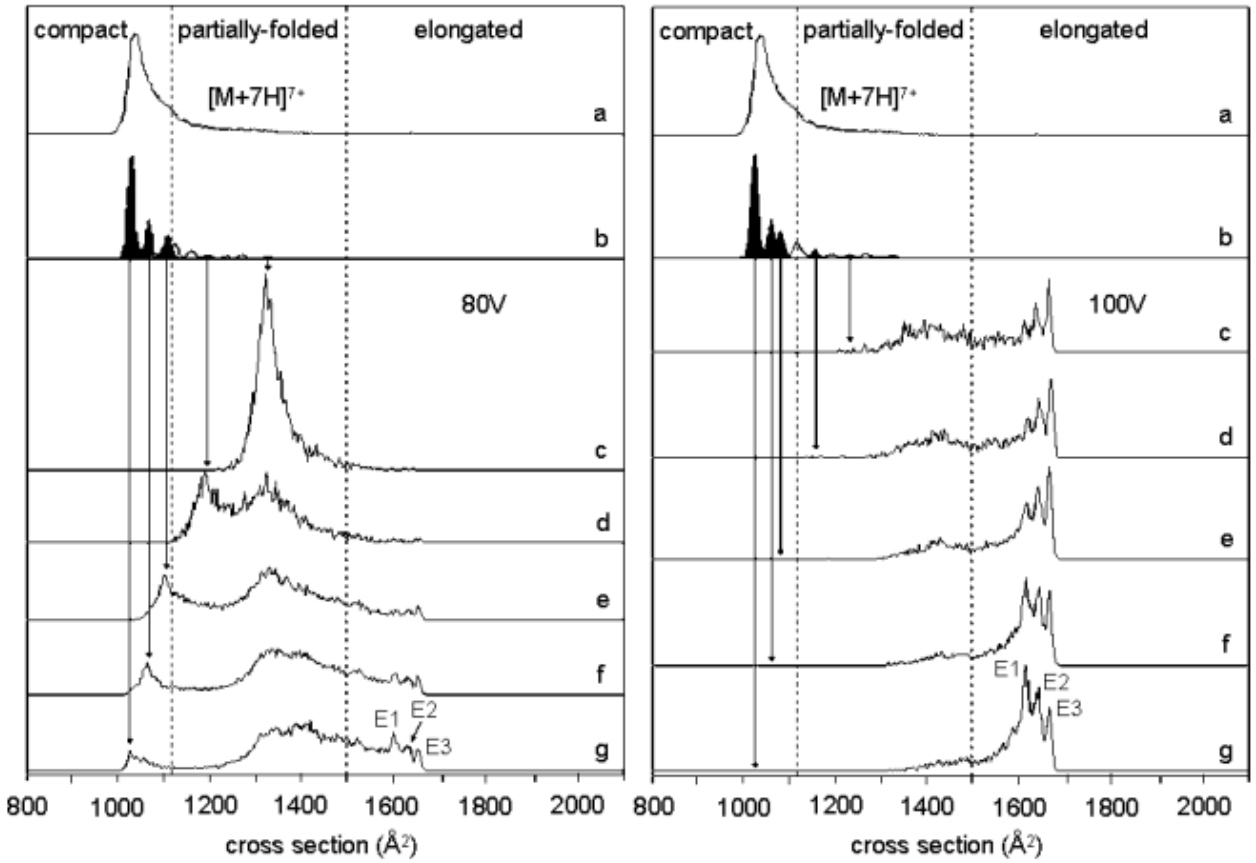

Figure 2. Ion mobility distributions of ubiquitin $[M + 7H]^{7+}$ ions, showing the initial distribution of ions formed by ESI (a) and nine narrow distributions of mobility-selected ions obtained by gating a 100 μs pulse of ions into D2 at various delay times (b). Activation of the selected ion distributions (shaded) at IA2 with a voltage of 80 V (left) and 100 V (right) produces distributions (c) through (g). The cross sections of the selected ions activated at 80 V were 1329 (c), 1196 (d), 1101 (e), 1063 (f), and 1025 Å^2 (g); and for 100 V were 1234 (c), 1158 (d), 1082 (e), 1063 (f), and 1025 Å^2 (g). The selection at 1063 Å^2 (shaded gray) shows a transition in the relative abundance of the three resolved elongated states (E1−E3) at 80 and 100 V. These distributions are obtained from nested $t_D(t_F)$ datasets by integration of a narrow range of *m/z* values for the $[M + 7H]^{7+}$ of ubiquitin. Dashed lines delineate the region in cross section for each conformer type. See text for discussion.

J. AM. CHEM. SOC. 2006, *128*, 11713−11719

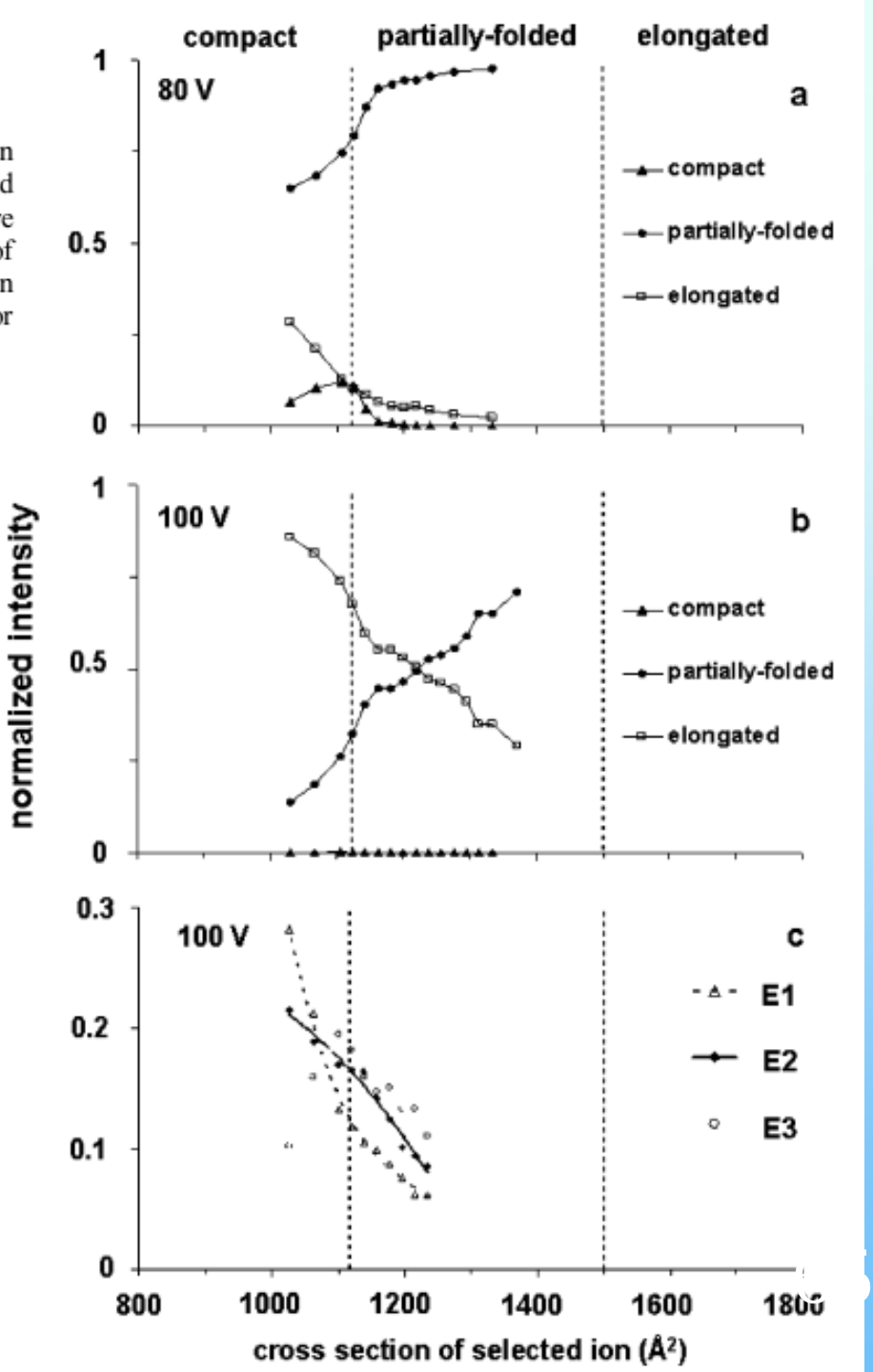

Figure 3. Relative populations of conformer types formed by activation of mobility-selected $[M + 7H]^{7+}$ ubiquitin ions as a function of the selected ion cross section. Populations represent the distributions shown in Figure 2 upon activation with 80 V (a) and 100 V (b). Relative populations of specific elongated structures (E1−E3) with respect to the total population are also shown (c). Dashed lines delineate the region in cross section for each conformer type.

J. AM. CHEM. SOC. 2006, *128*, 11713−11719

Figure 4. Ion mobility distributions of ubiquitin $[M + 7H]^{7+}$ ions obtained in IMS-IMS-IMS/MS experiments. Distribution **a** is the initial distribution consisting of primarily compact conformers. Upon selection of a narrow distribution of compact ions at G2 (100 μs), distribution **b** is obtained. Activation of the selected compact ions at IA2 produces distribution **c**. A second selection of an intermediate within the partially folded structures performed at G3 (150 μs) is shown in **d**, with the diffusion-limited peak width of the selected ion (gray line). Upon activation of the partially folded structures at IA3, distribution **e** is produced, consisting of a broader distribution of partially folded structures and a smaller distribution of elongated states (gray line). Distributions **f** and **g** are obtained upon higher-energy activation of the partially folded structures shown in **d**. These distributions are obtained from nested $t_D(t_F)$ datasets by integration of a narrow range of *m/z* values for the $[M + 7H]^{7+}$ of ubiquitin. See text for discussion.

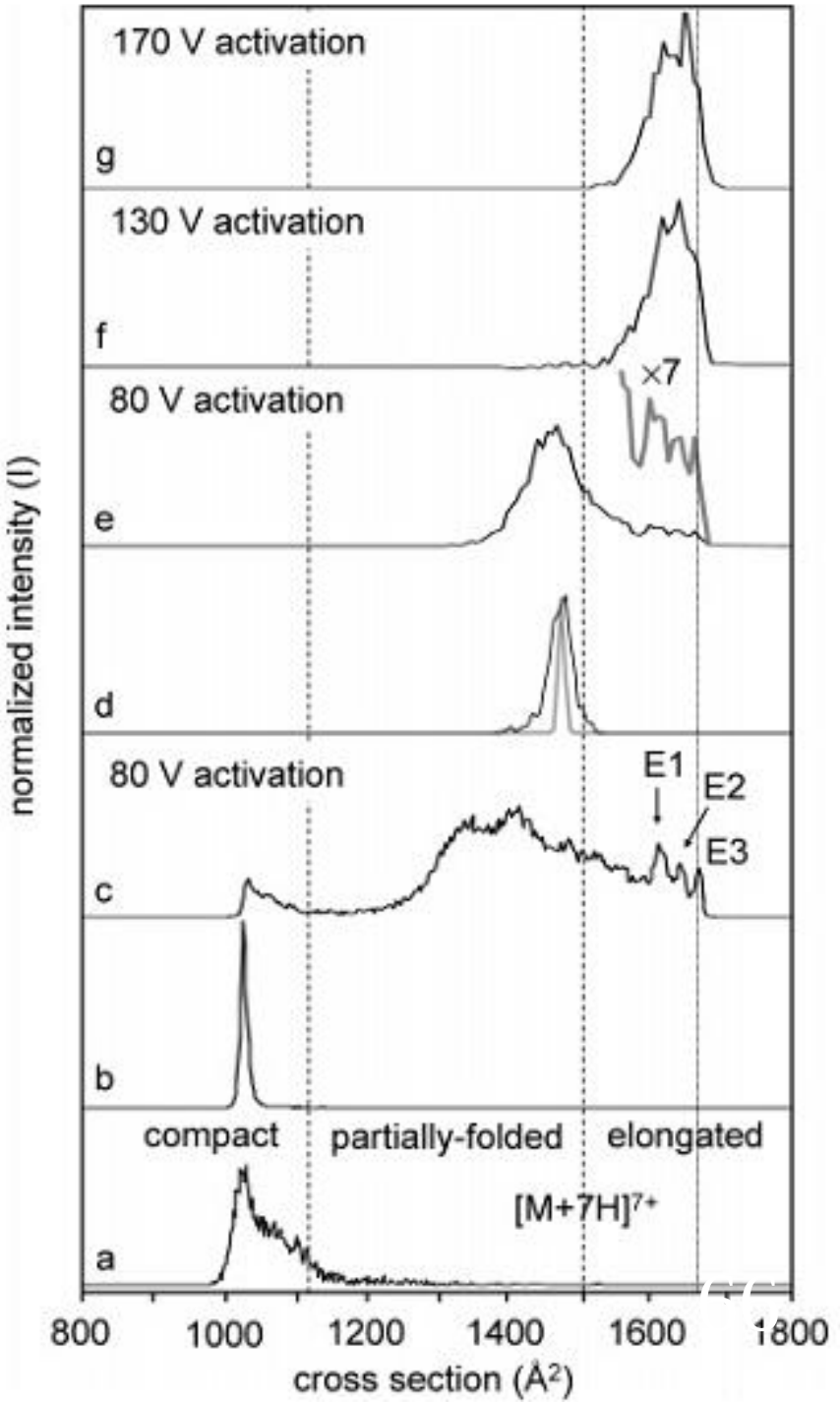

J. AM. CHEM. SOC. 2006, *128*, 11713−11719

Evidence for Many Resolvable Structures within Conformation Types of Electrosprayed Ubiquitin Ions

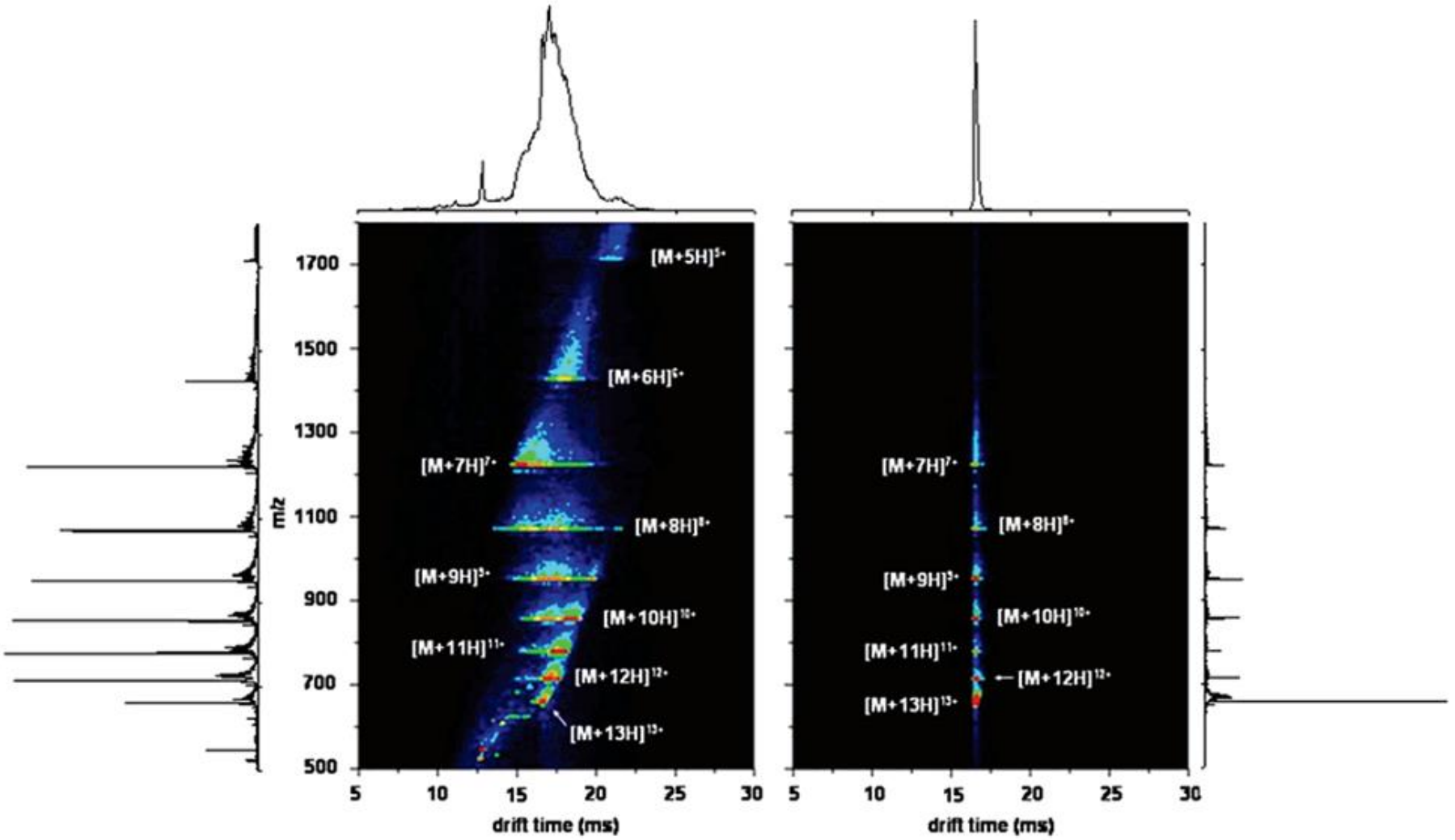

Figure 2. Nested drift(flight) time distributions showing the total distribution of electrosprayed ubiquitin ions (left) and a narrow distribution of mobility-selected ions that were gated into D2 at 7.8 ms (right). Also shown are the summed mass spectra (sides) and summed drift time distributions (top) obtained by integrating the two-dimensional data across all drift times and all *m/z* values, respectively. The drift time represents the total time required for the ions to travel through D1 to the TOF source.

J. Phys. Chem. B **2006,** *110,* 7017−7021

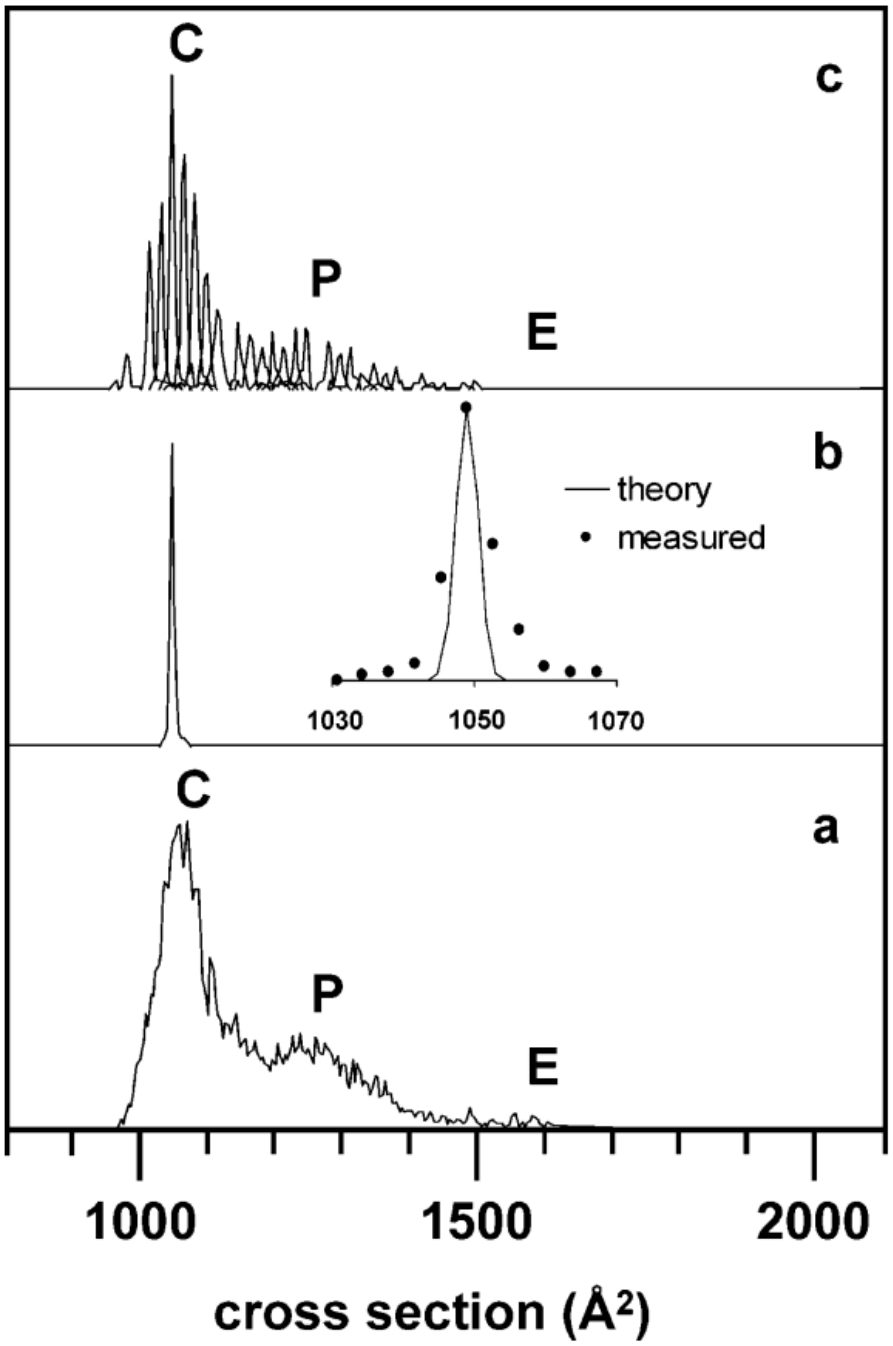

Figure 3. Drift time distributions of the $[M + 7H]^{7+}$ of ubiquitin. Mobility distributions were obtained by integrating drift time intensities over a narrow range of *m/z* values corresponding to the $[M + 7H]^{7+}$. (a) The total mobility distribution shows that the +7 charge state exists mostly as compact structures (C), some partially-folded structures (P), and minimal elongated structures (E). (b) A single peak is observed when a narrow distribution (50 μs) of the compact structure is isolated with mobility selection at 7.8 ms. The inset compares the theoretical to the experimentally measured peak shape (see text). (c) The total mobility distribution for the +7 is reconstructed with 28 mobility-selected distributions acquired every ~0.125 ms.

J. Phys. Chem. B **2006,** *110,* 7017−7021

Resolution and Structural Transitions of Elongated States of Ubiquitin

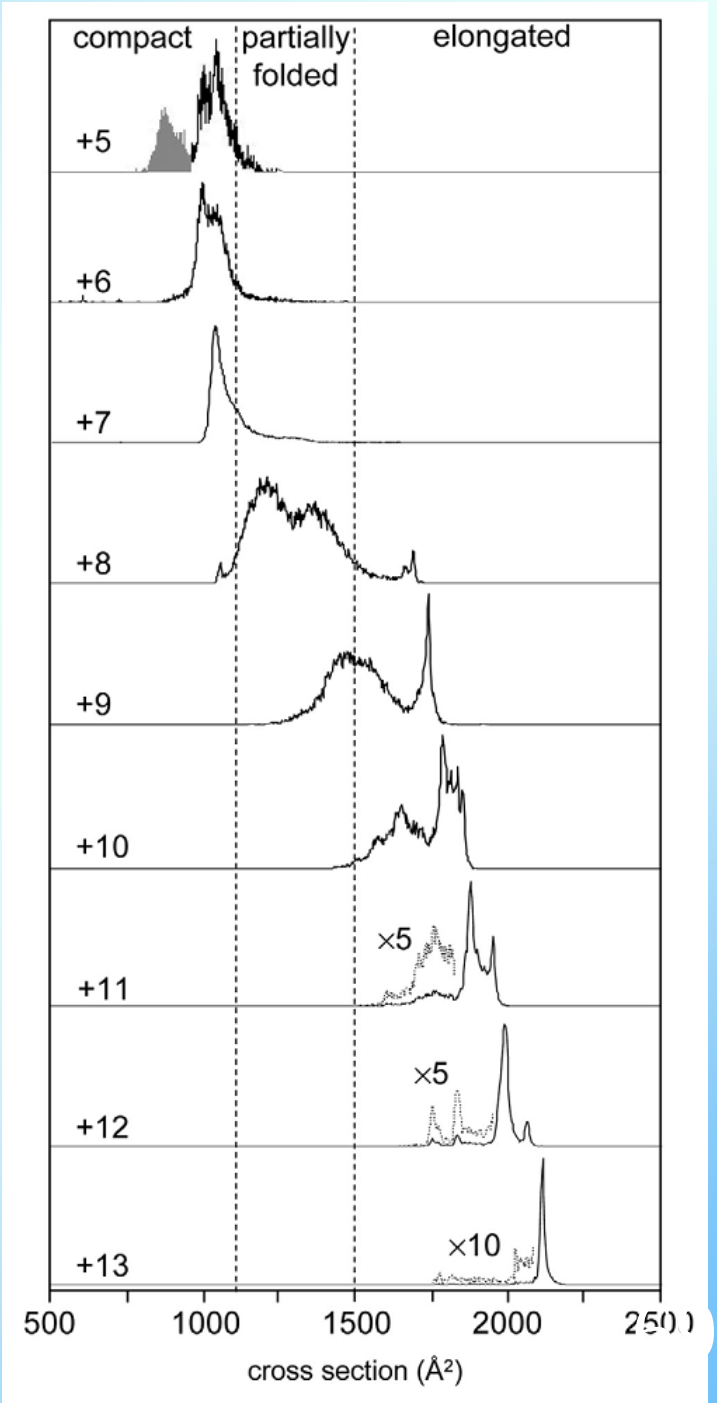

Figure 2. Cross section distributions for the +5 to +13 charge states of electrosprayed ubiquitin ions. Regions corresponding to compact, partially-folded, and elongated conformations are indicated. The $[2M + 10H]^{10+}$ (filled gray) for the +5 charge state is identified from a small family of dimers observed in the $t_D(t_F)$ distribution. Low intensity features of the +11 to +13 charge states are shown magnified (dotted lines). Distributions are obtained by taking slices from a $t_D(t_F)$ dataset.

J Am Soc Mass Spectrom 2007, 18, 322–331

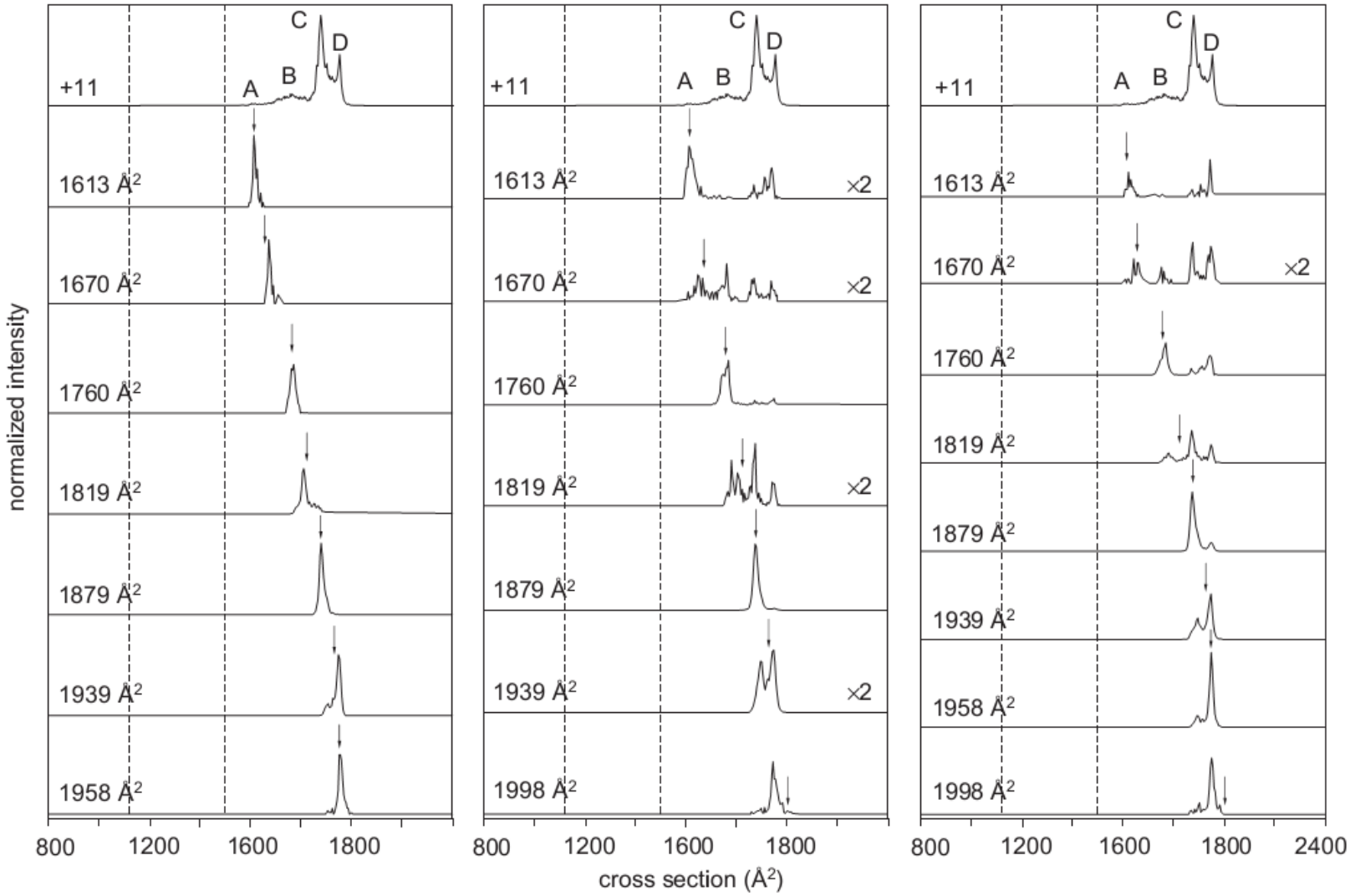

Figure 3. Cross section distributions for the +11 charge state of ubiquitin obtained upon selection and activation of specific mobility regions at G2 and IA2, respectively. Four stable conformations (labeled A–D) are observed within the initial distribution of ions produced by ESI (top). Mobility-selected ion distributions (with no activation) indicate the presence of stable and unstable ion populations (left). Activation of these ions with 80 V (middle) and 100 V (right) produces a new distribution that is unique to the selected ions. Distributions are labeled according to the cross section that was selected (indicated by the arrow in the distribution), and dashed lines delineate the regions corresponding to the compact, partially-folded, and elongated conformations. Distributions are obtained by taking slices from $t_D(t_F)$ data sets. See text for discussion.

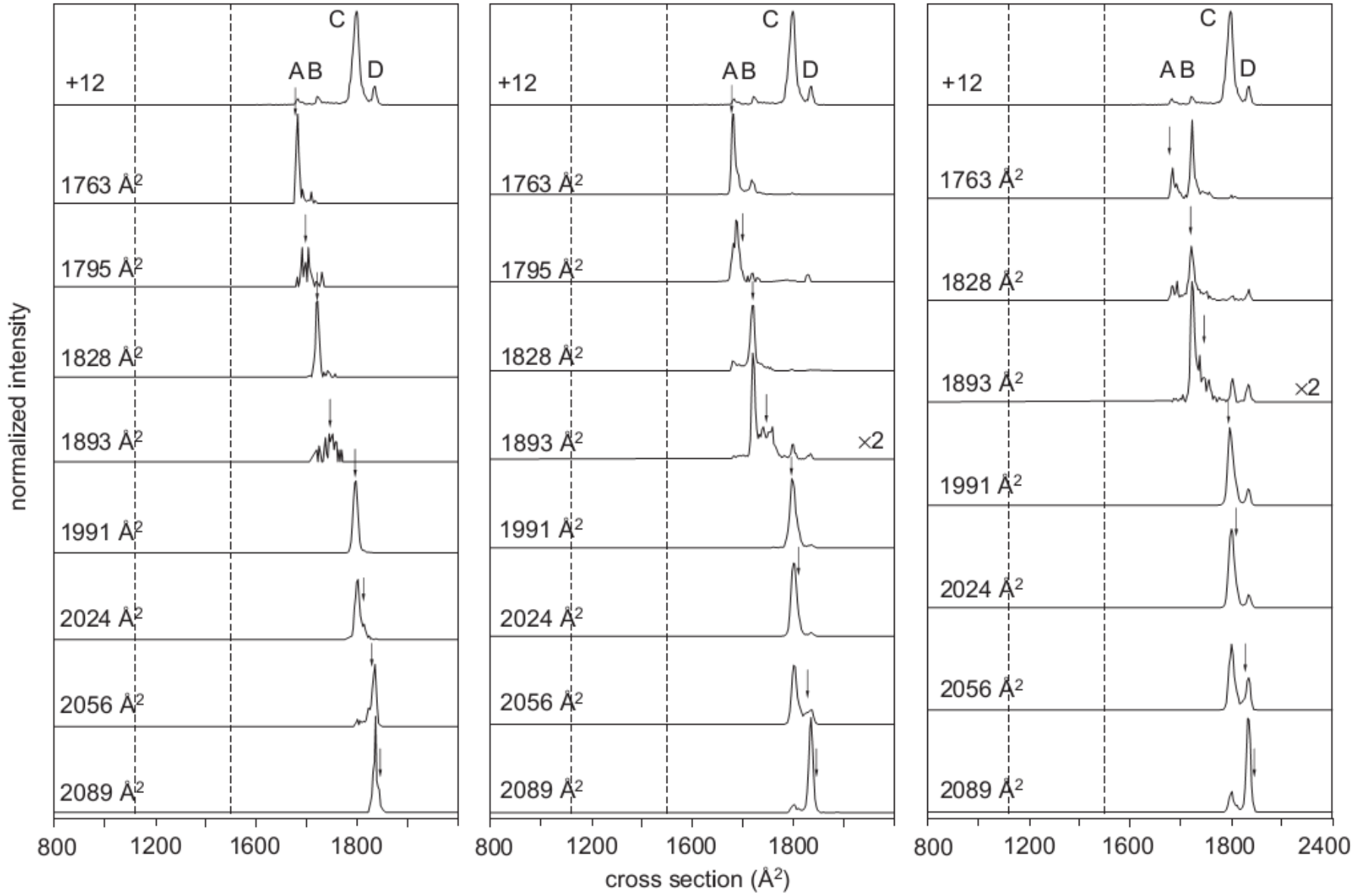

Figure 4. Cross section distributions for the +12 charge state of ubiquitin obtained upon selection at G2 (left) and activation at IA2 with 80 V (middle) and 100 V (right). Four stable conformations (labeled A–D) are observed within the initial distribution of ions produced by ESI (top). Details of the figure are the same as those in Figure 3. See text for discussion.

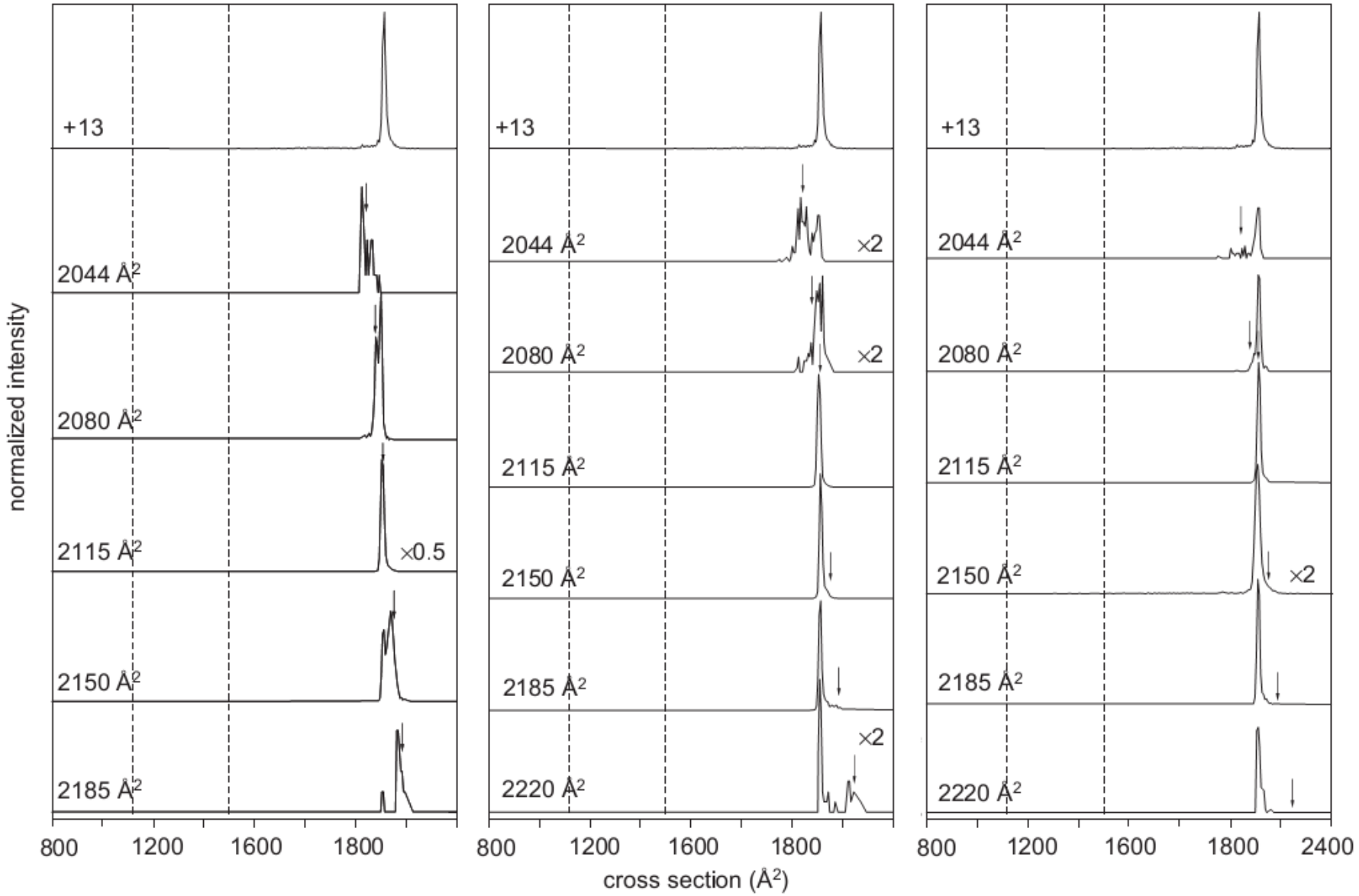

Figure 5. Cross section distributions for the +13 charge state of ubiquitin obtained upon selection at G2 (left) and activation at IA2 with 80 V (middle) and 100 V(right). The initial distribution of ions produced by ESI (top) is shown. Details of the figure are the same as those in Figure 3. See text for discussion.

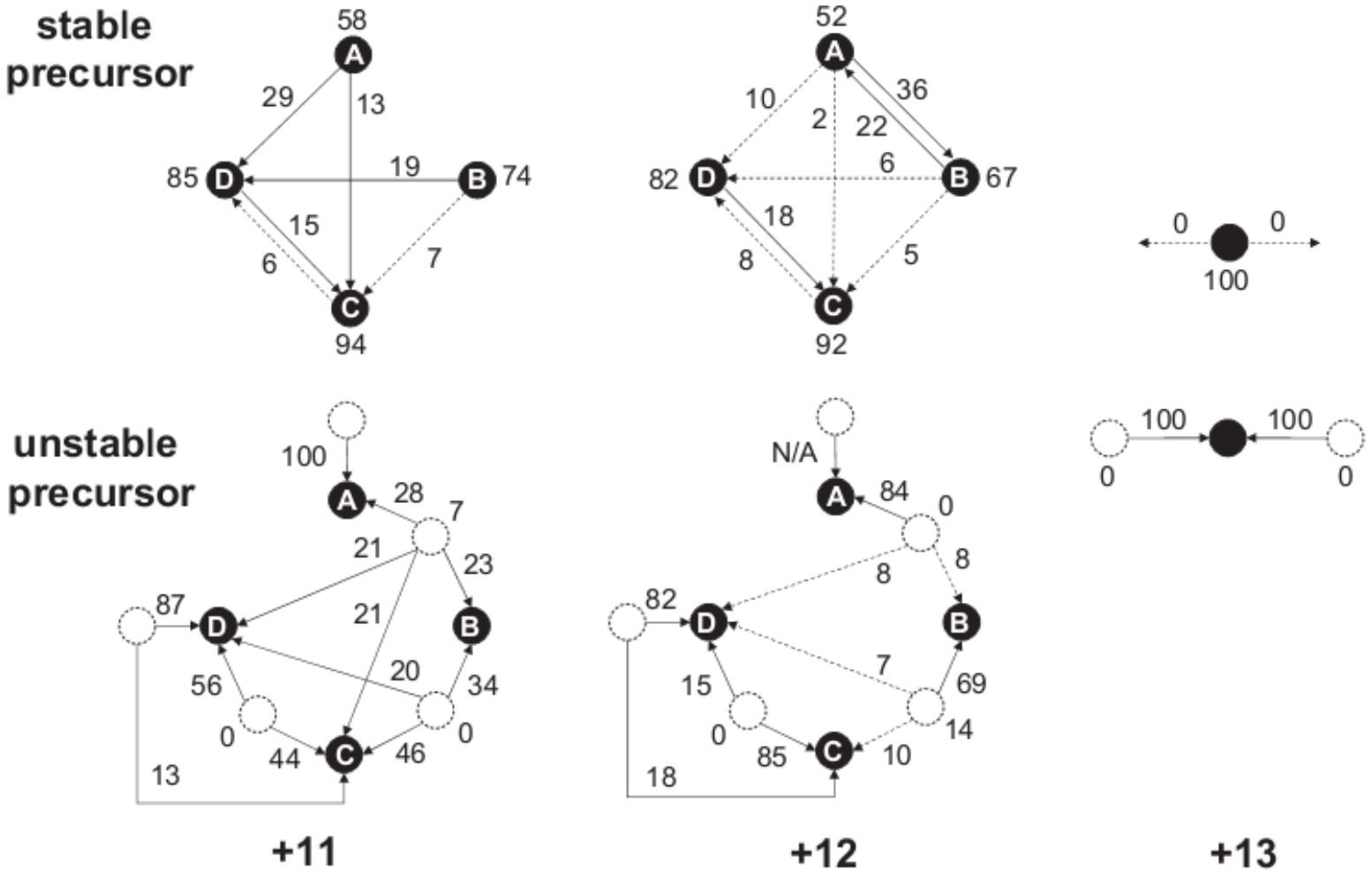

Figure 6. Transition diagrams showing the % efficiency of stable (top, labeled A–D) and unstable (bottom, dashed circles) precursor transitions upon activation at IA2. The % efficiency is the average of the relative abundance of each conformer formed (labeled A–D) upon activation at 80 and 100 V. Transitions of low efficiency (≤10%) are indicated by dotted lines. Unstable ion populations selected at higher mobility than conformer A and lower mobility than conformer D are shown above and to the left, respectively, of the solid circles A–D for the +11 and +12. Selection and activation of unstable ion populations at higher and lower mobility for the +13 are also shown. See text for discussion.

J Am Soc Mass Spectrom 2007, 18, 322–331

Conformation Types of Ubiquitin $[M+8H]^{8+}$ Ions from Water:Methanol Solutions: Evidence for the N and A States in Aqueous Solution

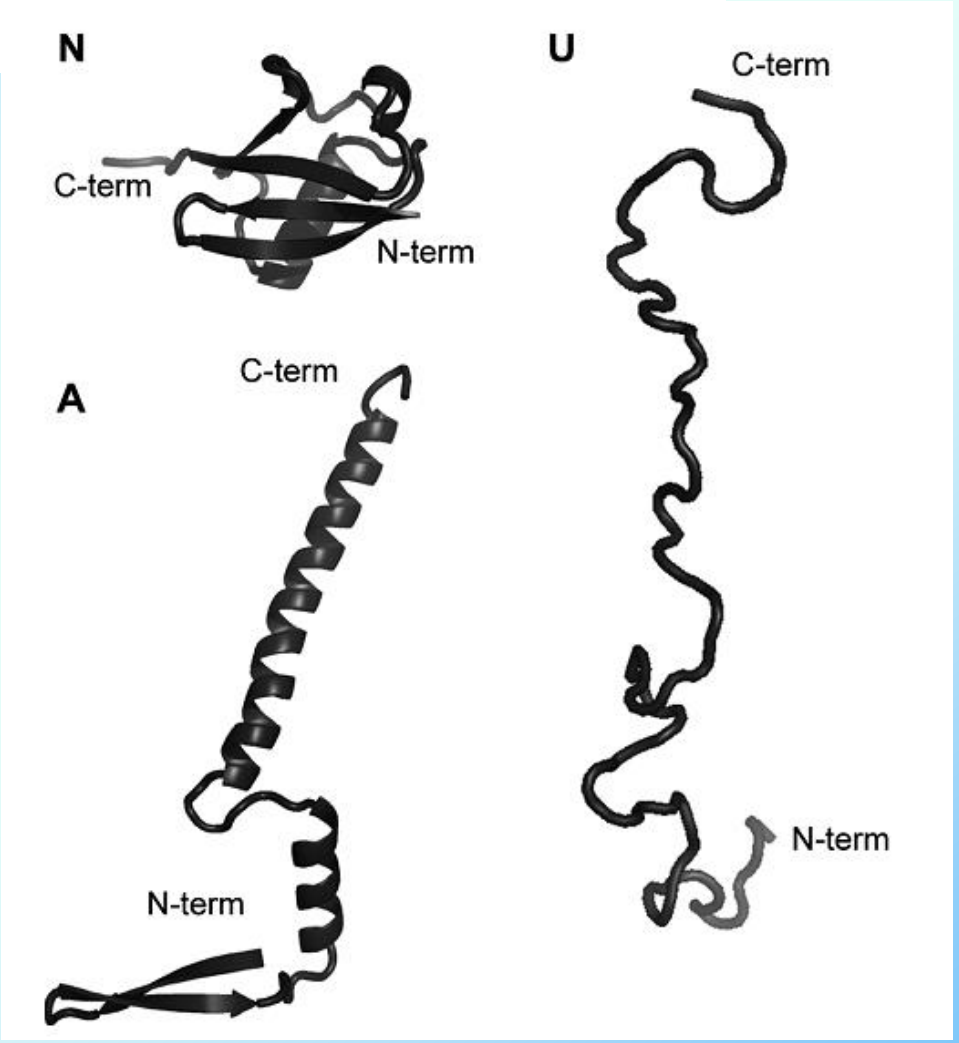

Figure 1. (N) Structure of the native state of ubiquitin.[10] (A) Structural model of the A state of ubiquitin (constructed based on the model proposed in ref 14). (U) Structural model of the unfolded state of ubiquitin.

J. Phys. Chem. B 2012, 116, 3344–3352

Figure 2. Collision cross section (ccs) distributions for $[M+8H]^{8+}$ ubiquitin ions from six different water:methanol solutions. The plots have been obtained from nested $t_D(m/z)$ data sets where all m/z bins over a narrow range (corresponding to $[M+8H]^{8+}$ ubiquitin ions) have been integrated for each t_D bin. Solution compositions (water:-methanol) are provided as labels for each of the distributions. The data sets have been normalized by using the integrated peak intensity. Dashed lines are drawn to indicate the calculated ccs for the N, A, and U state model structures shown in Figure 1.

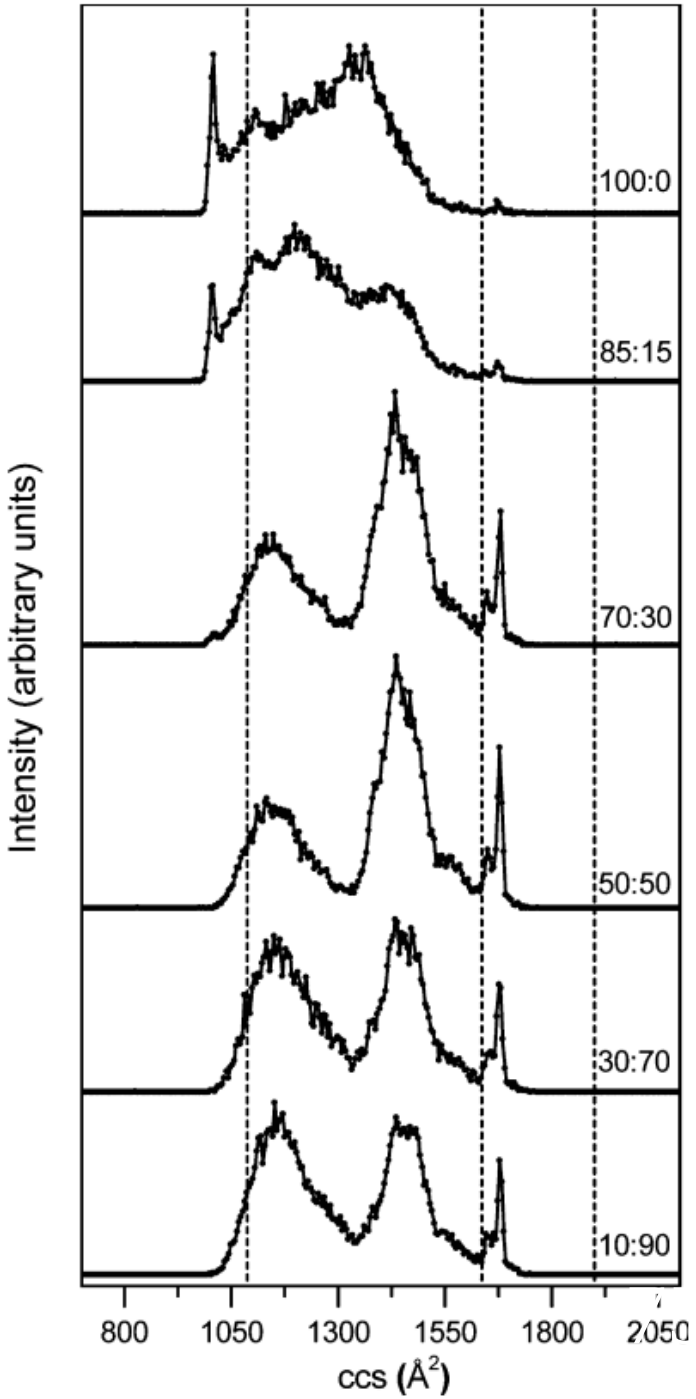

J. Phys. Chem. B 2012, 116, 3344–3352

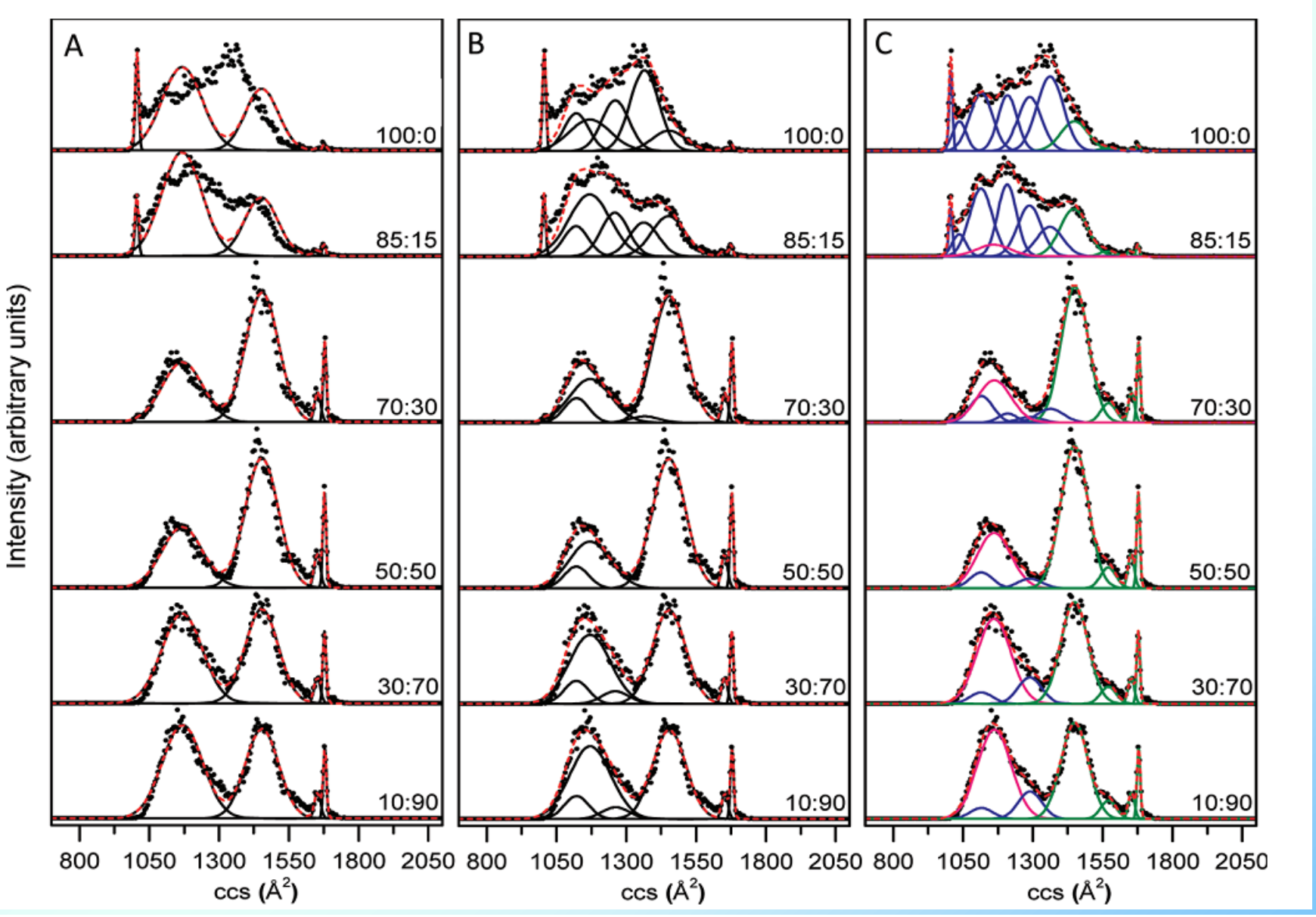

Figure 3. Gaussian models of collision cross section (ccs) distributions of $[M+8H]^{8+}$ ubiquitin ions electrosprayed from six different water:methanol solutions. Solution compositions (water:methanol) are provided as labels for each of the distributions. Panels A, B, and C have utilized 5, 8, and 11 Gaussian functions, respectively, to model the data sets. The experimental data (normalized) are plotted as solid circles, the Gaussian functions are plotted as black solid lines, and the sum of the Gaussian functions is plotted as a red dashed line. In panel C, conformer types that are assigned to the N, A and U states of ubiquitin are plotted in blue, green, and pink, respectively (see text for more details).

Figure 5. Plots of peak intensity as a function of solvent methanol percentage for different gas-phase conformation types. (A) Intensities for the three sharp conformer types having Ω = 1020 ± 6 (blue ▲), Ω = 1650 ± 11 (green ○), and Ω = 1680 ± 6 Å^2 (green ■). The most compact feature has been assigned to the N state and the more elongated features have been assigned to the A state. (B, C, D) Intensities for the gas-phase conformers that are assigned to the solution states of ubiquitin, N, A, and U, respectively. The labels N1−N6, A1−A4, and U correspond to the assignments in Table 1. N1 1020 ± 6 Å^2 (blue ▲), N2 1040 ± 25 Å^2 (blue ○), N3 1120 ± 41 Å^2 (blue ×), N4 1210 ± 34 Å^2 (blue ■), N5 1290 ± 42 Å^2 (blue ◇), N6 1360 ± 47 Å^2 (blue ⊕); A1 1450 ± 49 Å^2 (green ◆), A2 1570 ± 28 Å^2 (green △), A3 1650 ± 11 Å^2 (green ○), A4 1680 ± 6 Å^2 (green ■); U 1160 ± 60 Å^2 (pink ●). Intensity multiplication factors are listed for specific conformer types. (E) Sum of the intensities for different gas-phase conformation types that are assigned to the N, A and U states of ubiquitin. Conformer types that are assigned to the N, A, and U states of ubiquitin are plotted in blue, green, and pink, respectively.

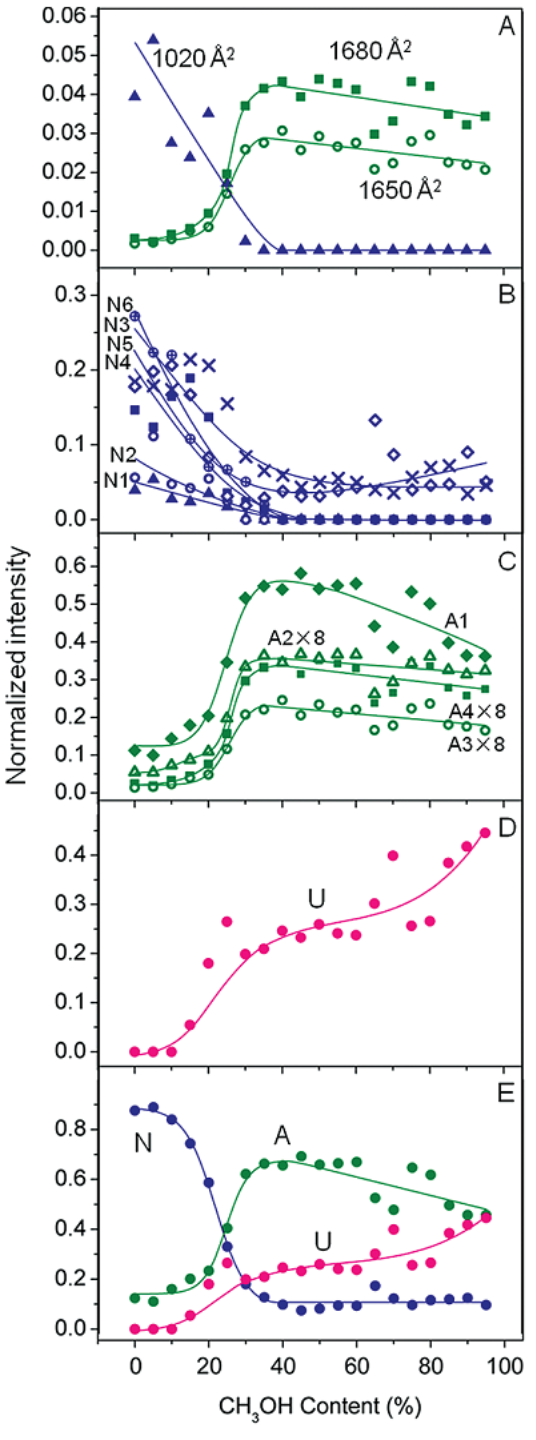

J. Phys. Chem. B 2012, 116, 3344−3352

Ion Trapping for Ion Mobility Spectrometry Measurements in a Cyclical Drift Tube

R. S. Glaskin, M. A. Ewing, D. E. Clemmer

Anal. Chem., **2013**, *85*, 7003–7008.

Circular Drift Tube

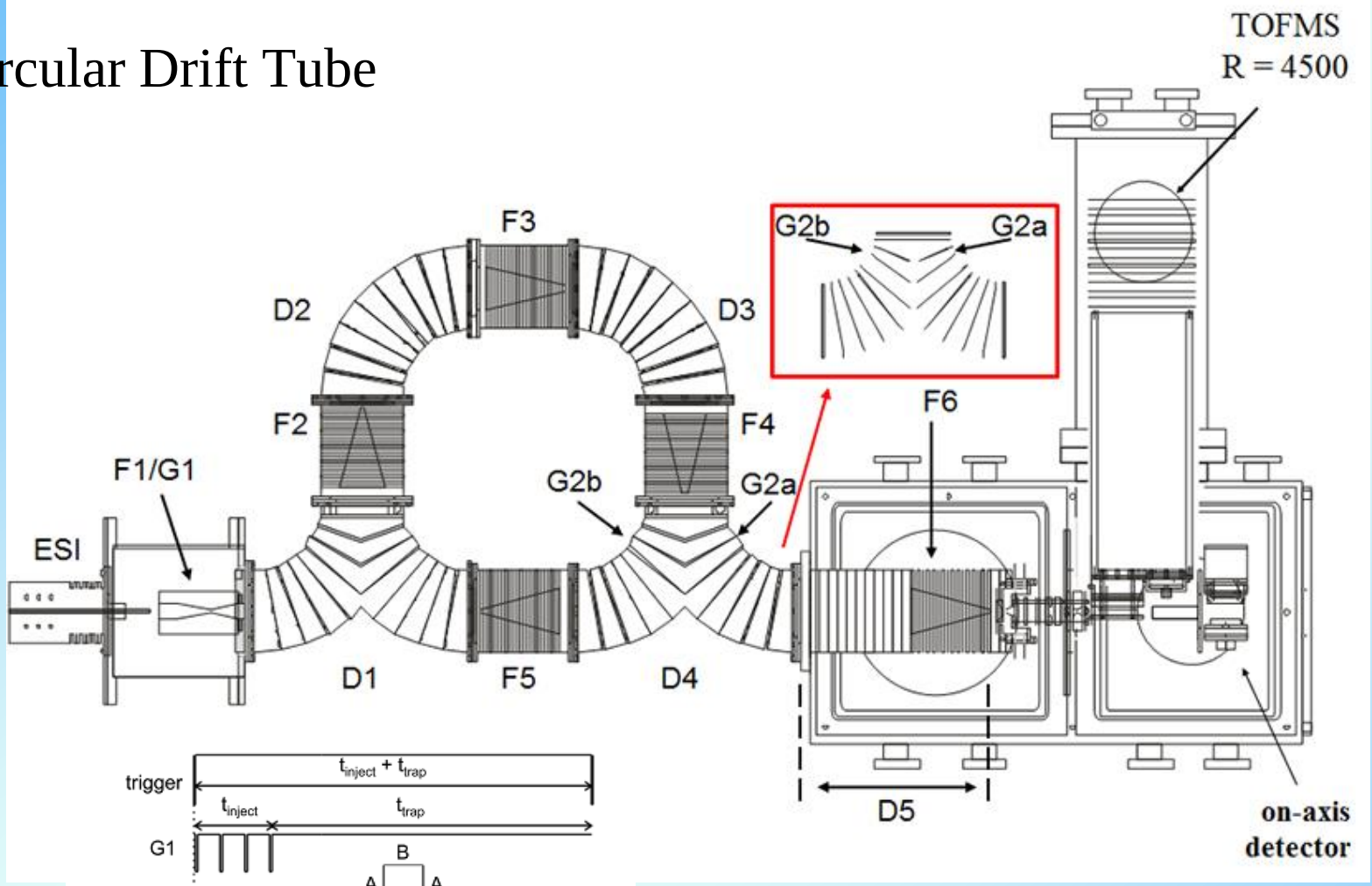

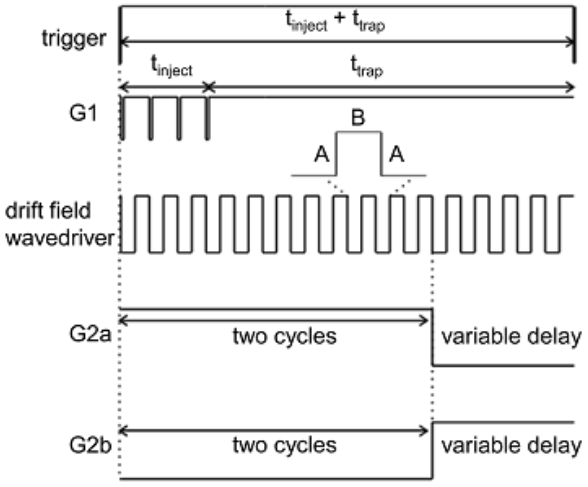

Figure 1. Schematic diagram of the ion cyclotron mobility spectrometer used in these studies. The inset displays a blowup of the Y-shaped fork region labeled as D4, where G2a and G2b are electrostatic gates used to direct ions either around the cyclotron for additional cycles or fixed to release the ions to the detector for analysis. Reprinted from ref 35. Copyright 2010 American Chemical Society. The sequence of pulses applied to the source funnel (G1), the drift field wavedriver, and the electrostatic gates G2a and G2b are shown below the schematic. This represents an example of one complete injection sequence for ions that have been trapped for 1 3/4 cycles after four source pulses were introduced into the cyclotron. A more detailed description is provided in the text.

Anal. Chem. **2009**, *81*, 1482–1487.

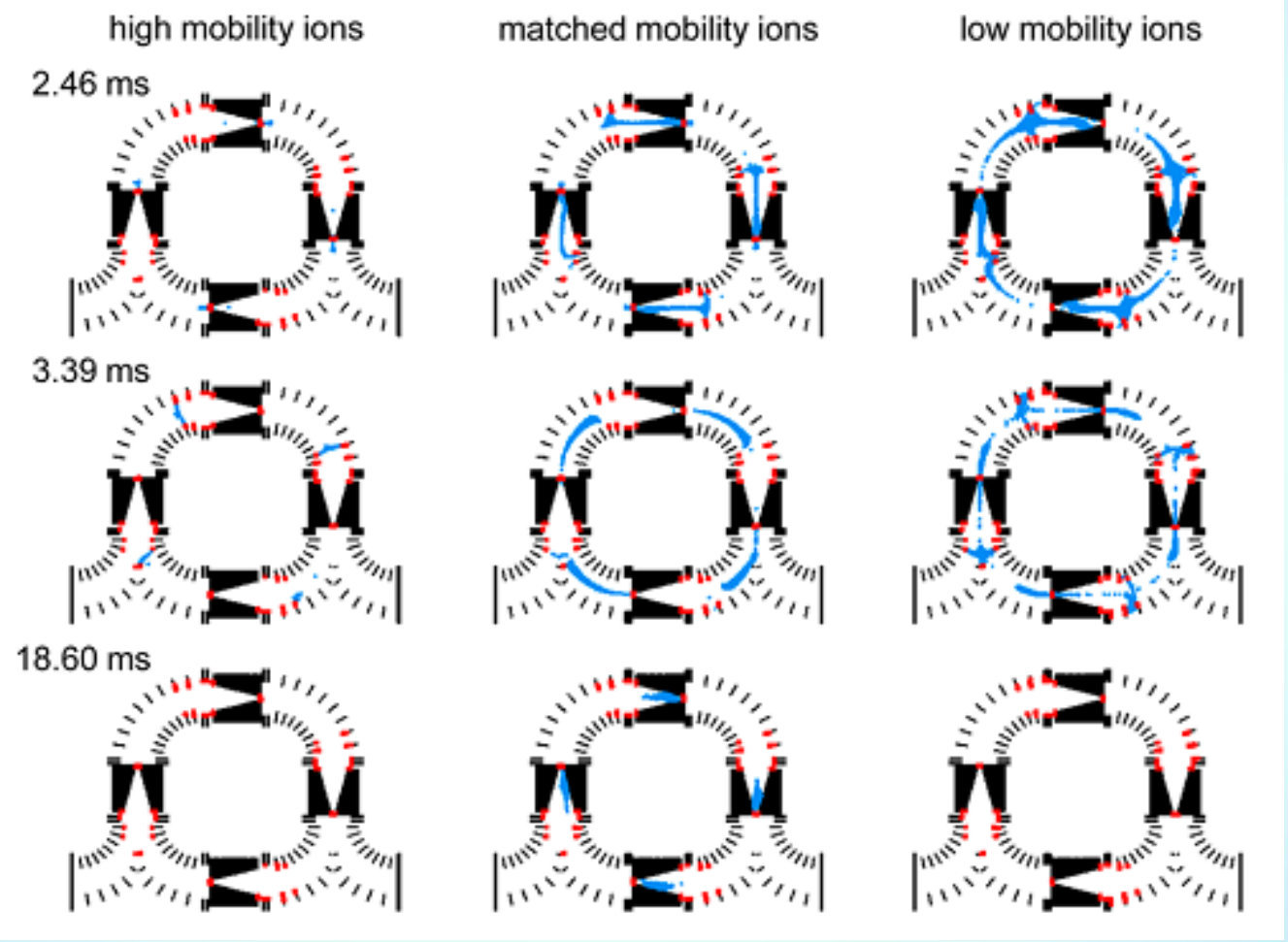

Figure 2. Snapshots of the trajectory of ions traveling two cycles around the cyclotron are plotted for three time points: 2.46, 3.39, and 18.60 ms. The left, center, and right columns correspond to ions with a 30% higher mobility than the compact $[M + 3H]^{3+}$ ions of substance P, matched mobility ions (compact $[M + 3H]^{3+}$ ions of substance P), and 30% lower mobility ions ($[M + 2H]^{2+}$ ions of substance P) at a drift field application period of 2.34 ms. Lenses of the cyclotron are shown in black, eliminated ions are in red, and transmitting ions are in blue.

Anal. Chem., **2013**, *85*, 7003–7008.

Circular Instrument

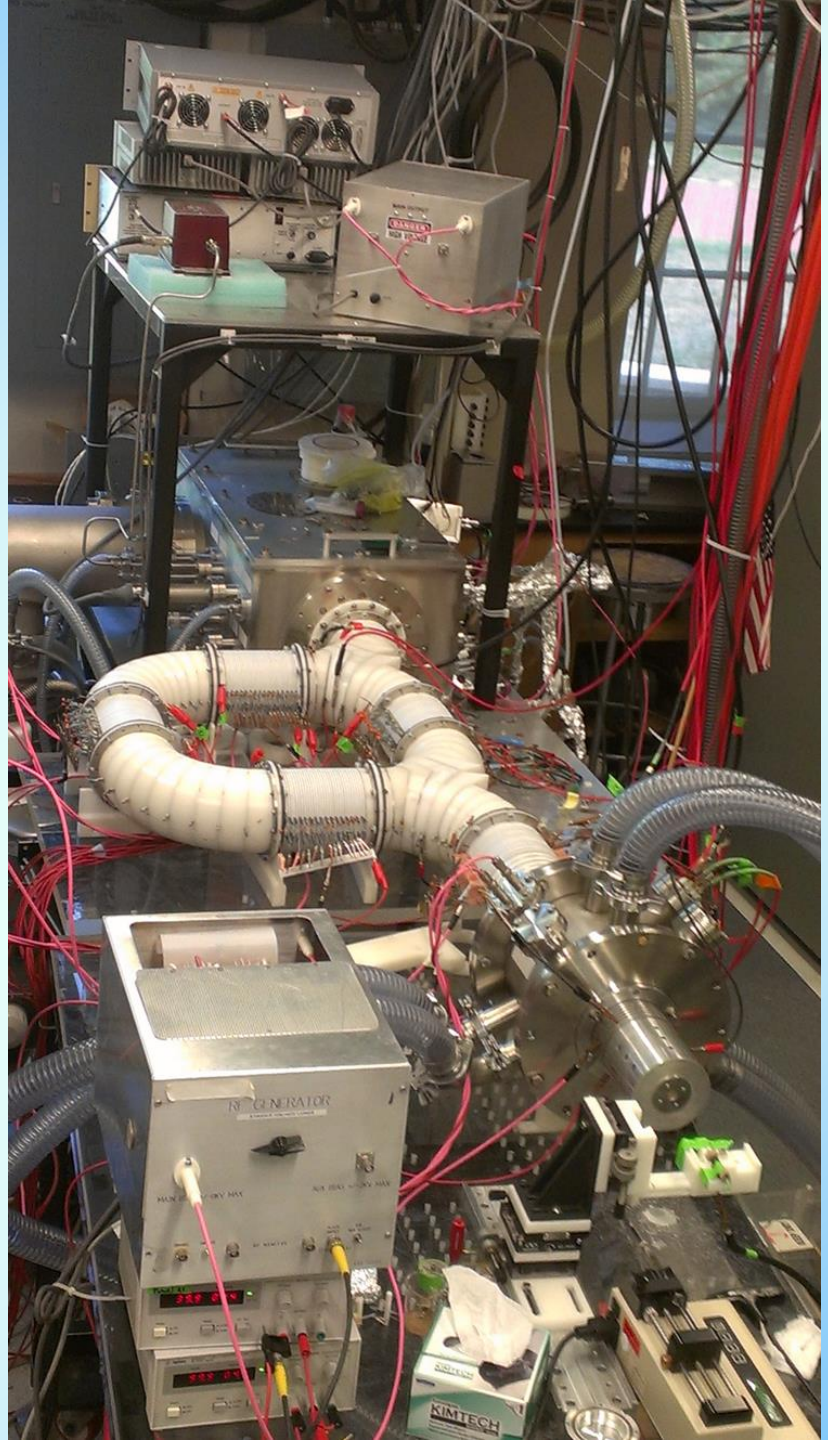

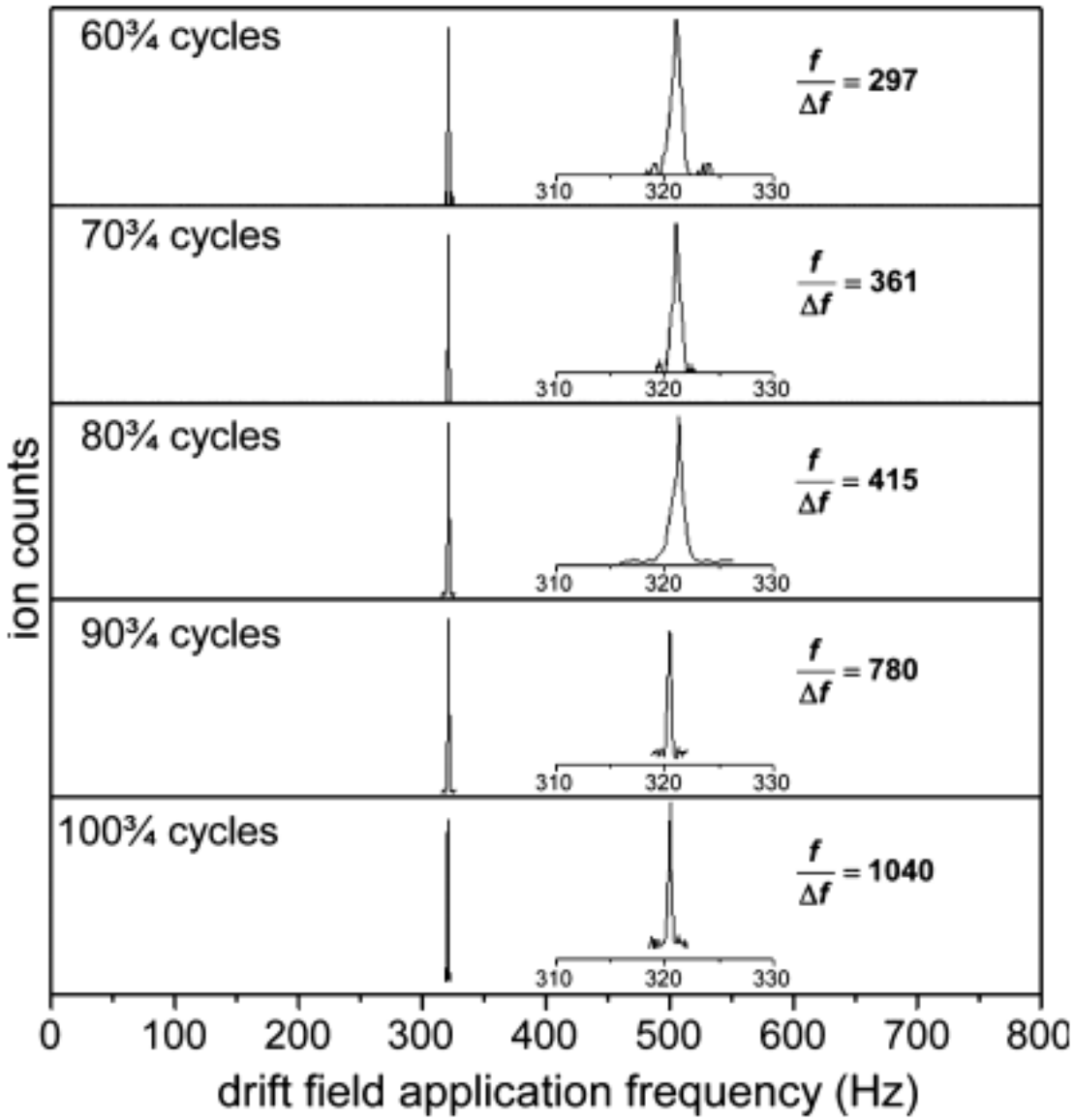

Figure 4. Drift field application frequency distributions are shown for the compact $[M + 3H]^{3+}$ ions of substance P that have traveled 60 3/4, 70 3/4, 80 3/4, 90 3/4, and 100 3/4 cycles around the cyclotron. A resolving power of approximately 1040 was obtained for ions that have traveled 100 3/4 cycles around the cyclotron, which corresponds to a total drift length of 182.86 m.

Anal. Chem., **2013**, *85*, 7003–7008.

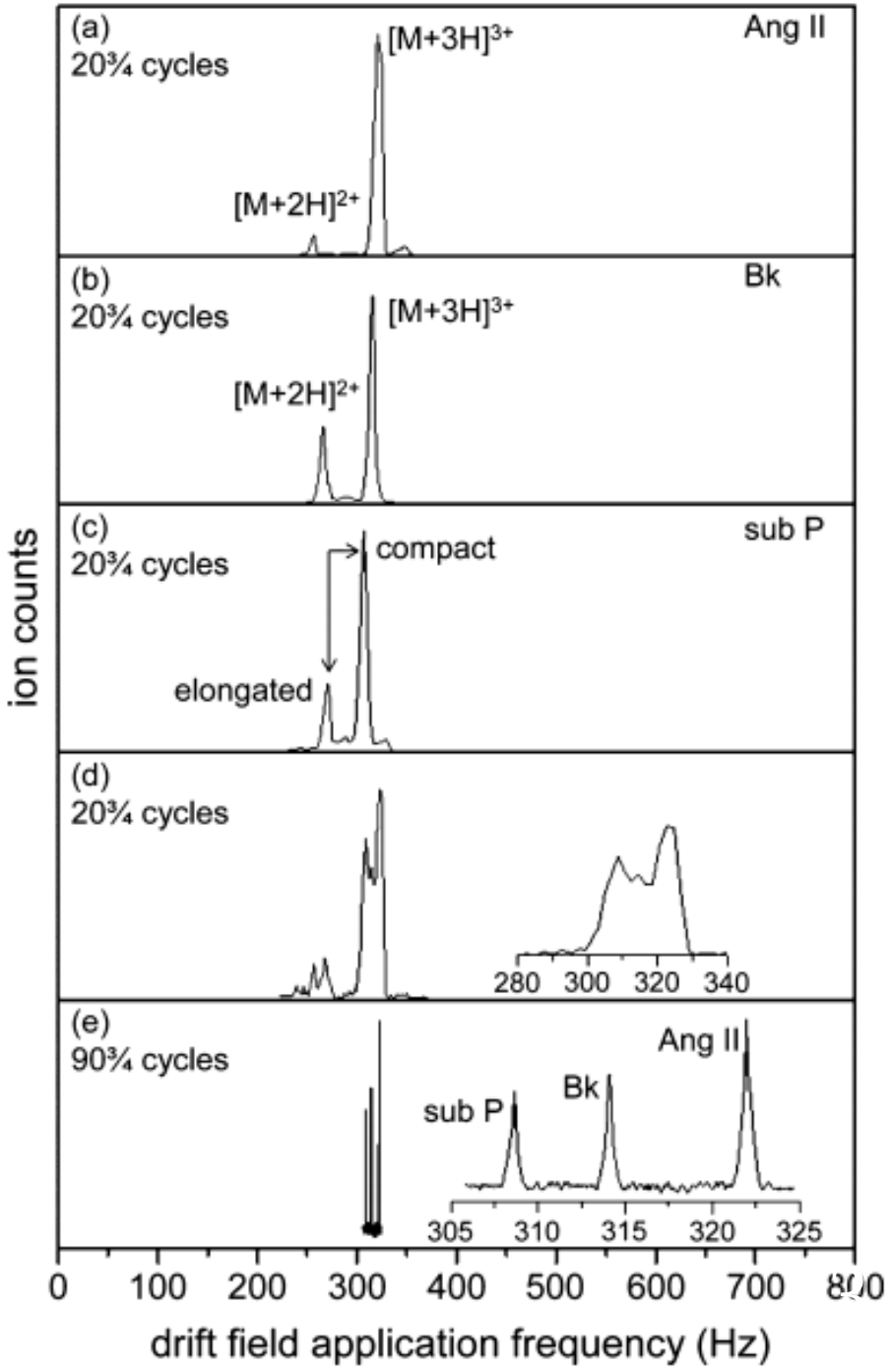

Figure 5. Drift field application frequency distributions for three individual peptides ((a) angiotensin II (Ang II), (b) bradykinin (Bk), and (c) substance P (sub P)) that have traversed 20 3/4 cycles around the cyclotron and for a 1:1:1 mixture of angiotensin II, bradykinin, and substance P ions that after (d) 20 3/4 and (e) 90 3/4 cycles of trapping. A regression of collision cross sections against the drift field application period for these three peptides was used to assign the main feature for the $[M + 3H]^{3+}$ ions of bradykinin to the conformation previously denoted as C. Three peak apexes can be observed in the inset at 20 3/4 cycles for the $[M + 3H]^{3+}$ ions of angiotensin II, conformation C $[M + 3H]^{3+}$ ions of bradykinin, and compact $[M + 3H]^{3+}$ ions of substance P occurring over a drift field application frequency range of 280 to 350 Hz. The inset at 90 3/4 cycles displays the resulting drift field application frequency distribution obtained from the same mixture, in which the species are resolved.

Anal. Chem., **2013**, *85*, 7003–7008.

Evidence for a Quasi-Equilibrium Distribution of States for Bradykinin $[M + {}^{3}H]^{3+}$ Ions in the Gas Phase
N. A. Pierson, S. J. Valentine, D. E. Clemmer
J. Phys. Chem. B 2010, 114, 7777–7783

Number of Solution States of Bradykinin from Ion Mobility and Mass Spectrometry Measurements
N. A. Pierson, L. Chen, S. J. Valentine, D. H. Russell, D. E. Clemmer
J. Am. Chem. Soc. 2011, 133, 13810–13813

Bradykinin

Bradykinin is a peptide that causes blood vessels to dilate (enlarge), and therefore causes blood pressure to fall.

M. W. 1060.2 Da

Arg-Pro-Pro-Gly-Phe-Ser-Pro-Phe-Arg-OH

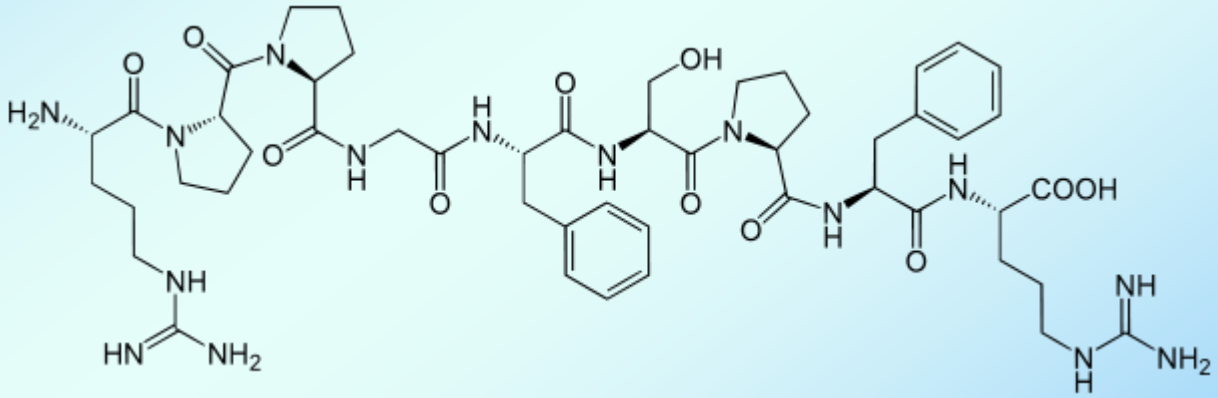

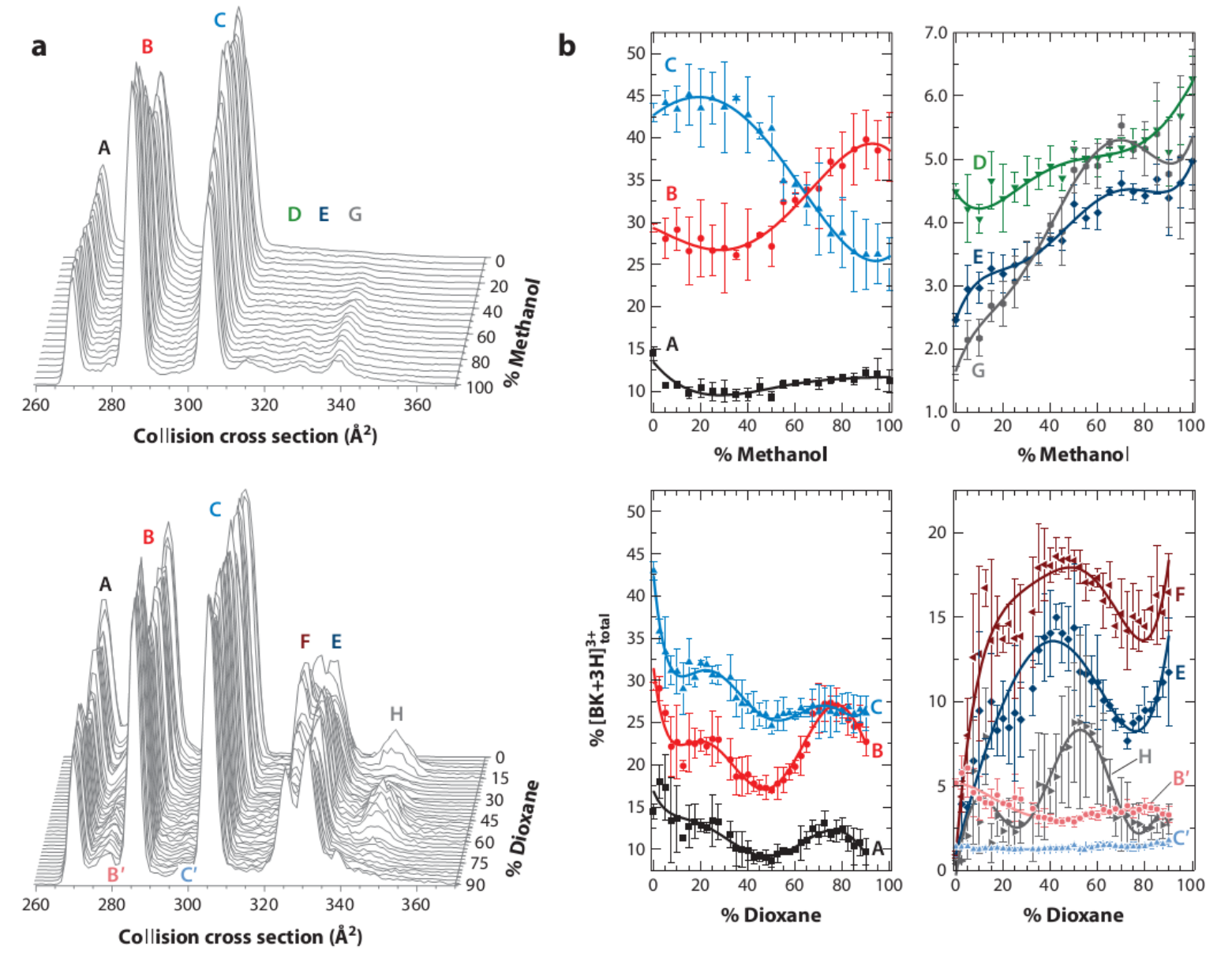

(*a*) Cross-sectional profiles of bradykinin $[BK+3H]^{3+}$ (each an average of three data sets) from 21 different methanol:water (*top*) and 37 different dioxane:water (*bottom*) solutions. Abundant conformers A–C and seven minor features are labeled. (*b*) Relative abundance (peak integration) of the 10 labeled features as a function of solution composition for methanol:water (*top*) and dioxane:water (*bottom*). Error bars represent the standard deviation from a triplicate analysis. A polynomial function is fit through each data set to guide the eye. Figure adapted from Reference 43. Copyright 2011 American Chemical Society.

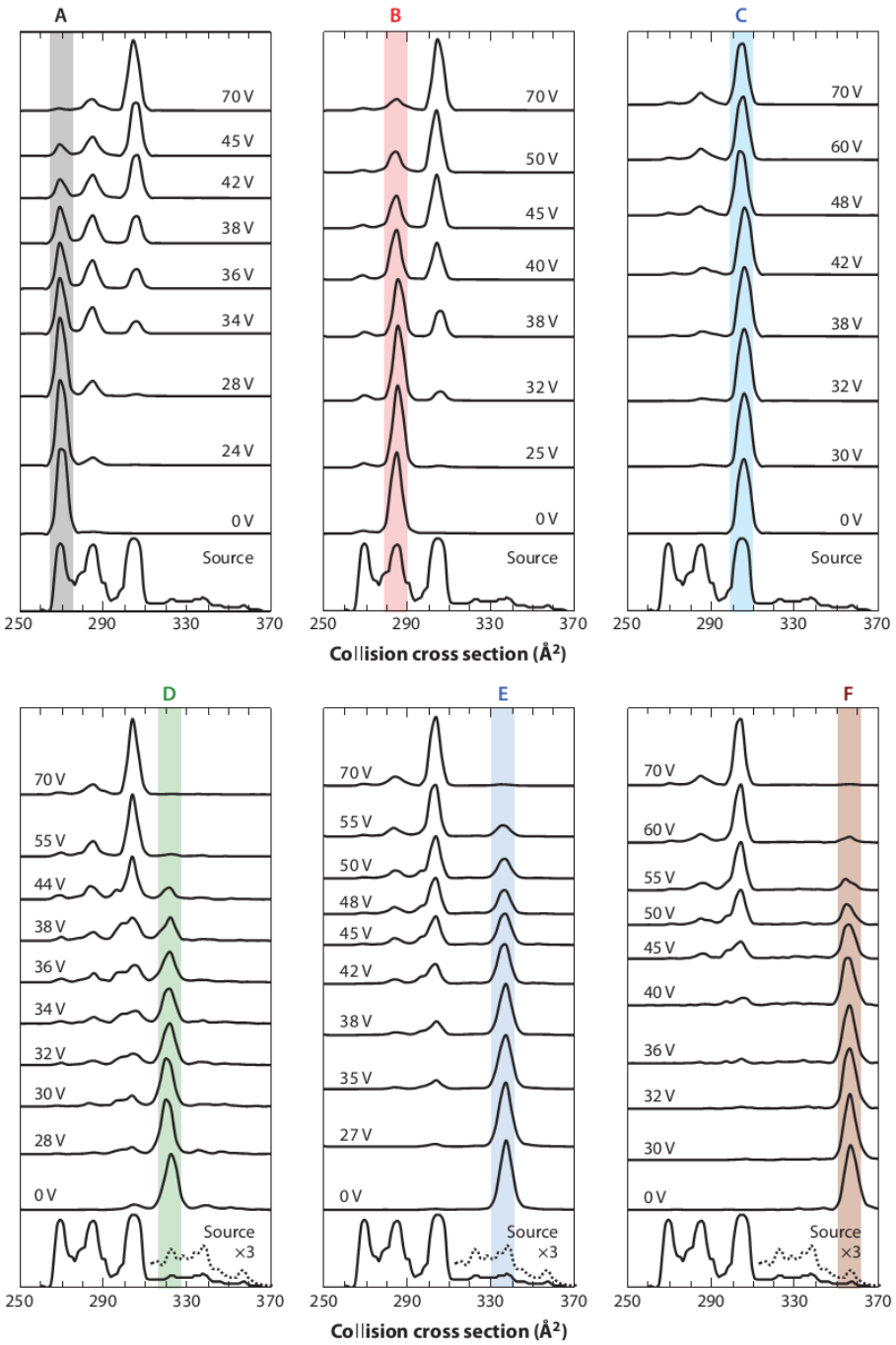

Cross-sectional profiles of bradykinin $[BK+3H]^{3+}$. The bottom trace in each panel shows the electrospray ionization source distribution (with a portion magnified by a factor of three to better show features D–F). Each panel shows one of six separate sets (A–F) of experiments, beginning within a set with the initial selection (no activation), followed by increasing activation voltages up to 70 V. The area under all peaks in a distribution is normalized to unity. Selections of conformations A–F all converge to the same quasi-equilibrium distribution at 70 V. Figure taken from Reference 42. Copyright 2010 American Chemical Society, reproduced with permission.

Prof. David E. Clemmer

Indiana University Bloomington

問.
ESIによって生成された気相タンパク質イオンの構造は、溶液中での状態との間に、どのような相関があるのだろうか？あなたが考えていることについて、簡単に述べなさい。

♣ 生体分子の質量分析における新技術

Charge Detection Mass Spectrometry

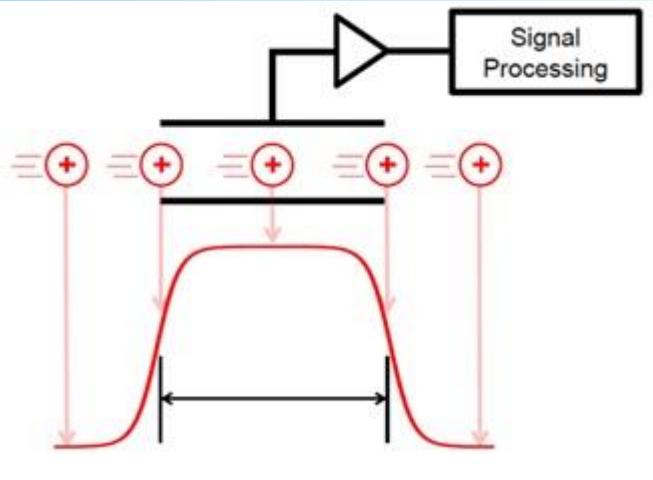

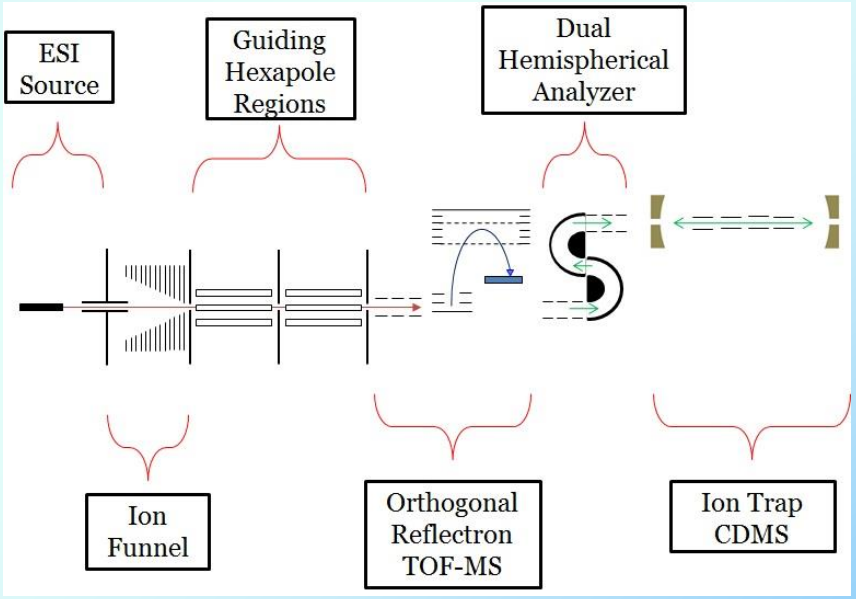

New CDMS Instrument

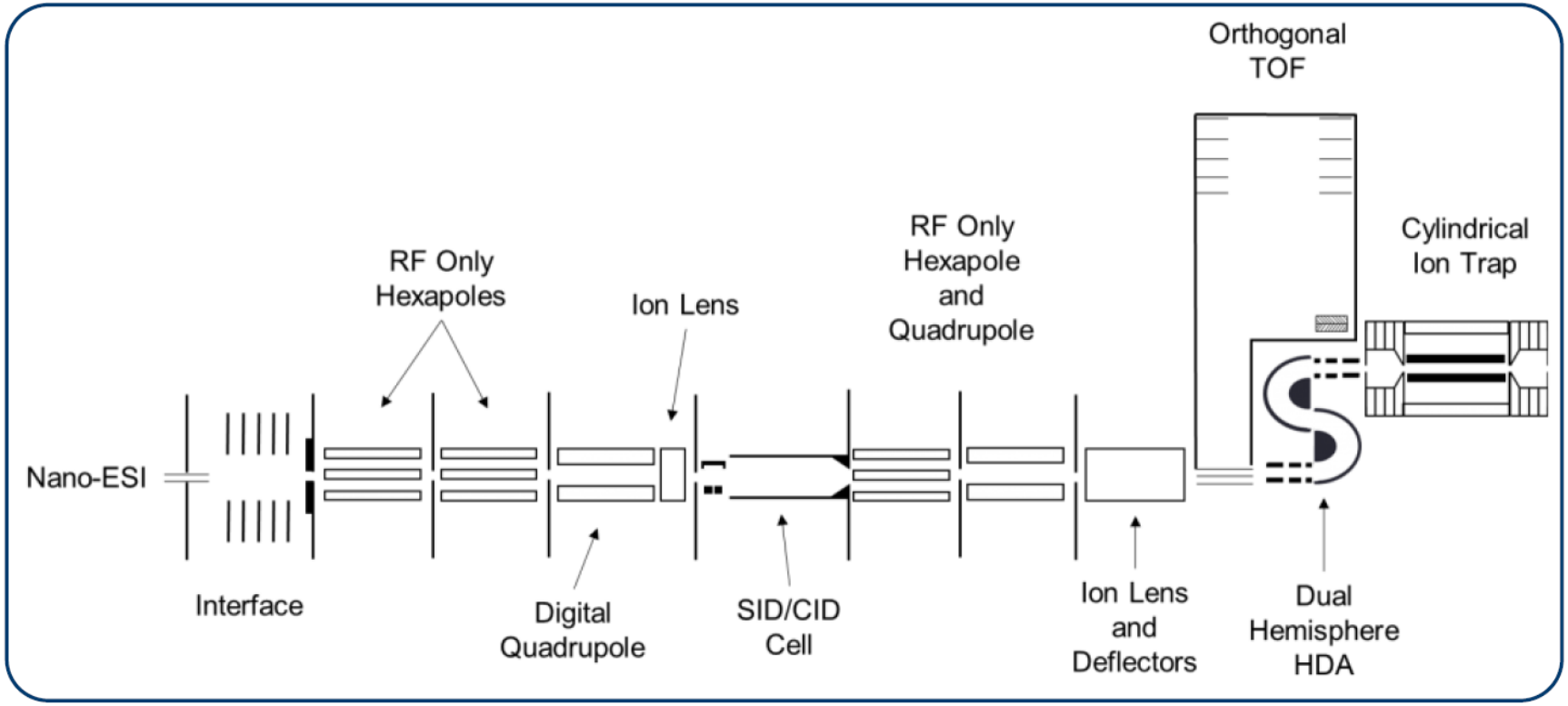

The Jarrold Group is currently constructing a new CDMS instrument implementing devices designed previously by the Jarrold Group: a DC ion carpet, digitally scanned quadrupole appropriate for high mass ions, and a cylindrical cone trap capable of charge measurement with almost perfect precision. The new instrument will also be capable of surface/collision induced dissociation of large peptides and virus capsids.

https://nano.lab.indiana.edu/instrumentation/

Hepatitis B Virus

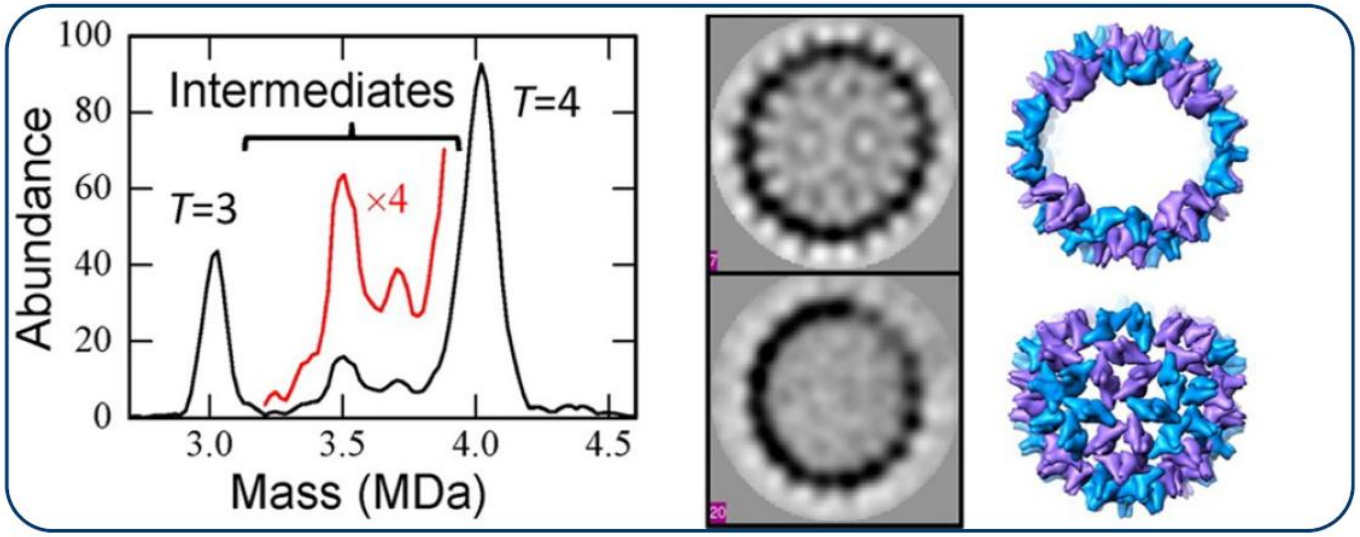

We are using CDMS to study the assembly of hepatitis B virus (HBV). HBV assembly is of particular interest because it is a devastating pathogen and is a target for the development of new assembly-directed antiviral molecules. Learning how to stop the virus from assembling requires knowledge of how it assembles. Unlike conventional MS, CDMS is capable of measuring the mass distribution of complex mixtures in the multi-MDa range and is therefore ideal for measuring the many assembly intermediates for HBV. We have already uncovered late intermediates in the assembly pathway and proposed structures for these species based on their stability and kinetic accessibility.

https://nano.lab.indiana.edu/applications/

Bacteriophage P22

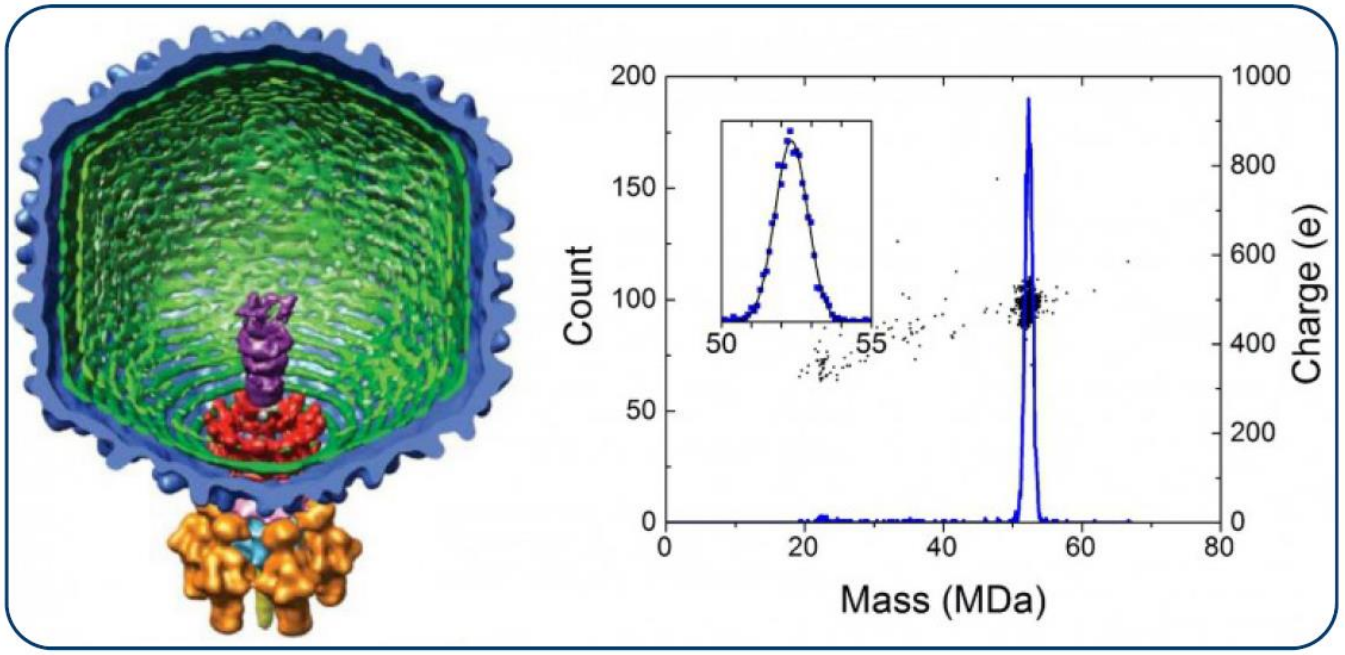

P22 protein shells can be used in materials applications to transport and protect foreign cargos, such as enzymes. There is typically a broad distribution in the number of cargo molecules encapsulated, and MS of these samples is very difficult. CDMS can easily measure the mass spectrum of mixtures and can be used to determine the distributions of cargo. We have already applied CDMS to P22 capsids to determine the distribution of internal scaffolding proteins.

https://nano.lab.indiana.edu/applications/

Adeno Associated Virus

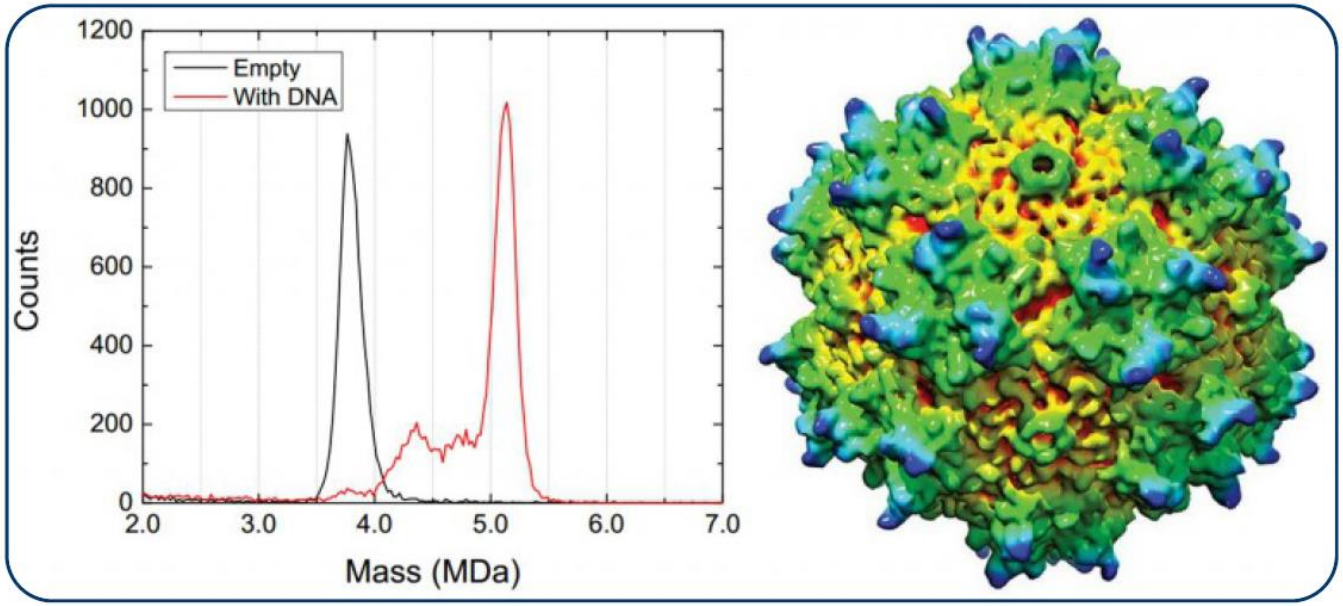

Adeno-associated virus (AAV) is a small DNA virus that is non-pathogenic and exhibits diverse tropism among human and animal tissues. As a result, AAV is a potential candidate as a vector for gene therapy of diseases affecting the eyes, liver, central nervous system, and more. With CDMS, we have obtained some surprising results about the purity and stability of AAV particles that are used in clinical trials for gene therapy.

https://nano.lab.indiana.edu/applications/

Professor Martin F. Jarrold

INDIANA UNIVERSITY
BLOOMINGTON

質量選別機能を備えた気相イオンNMR 分光法の開発

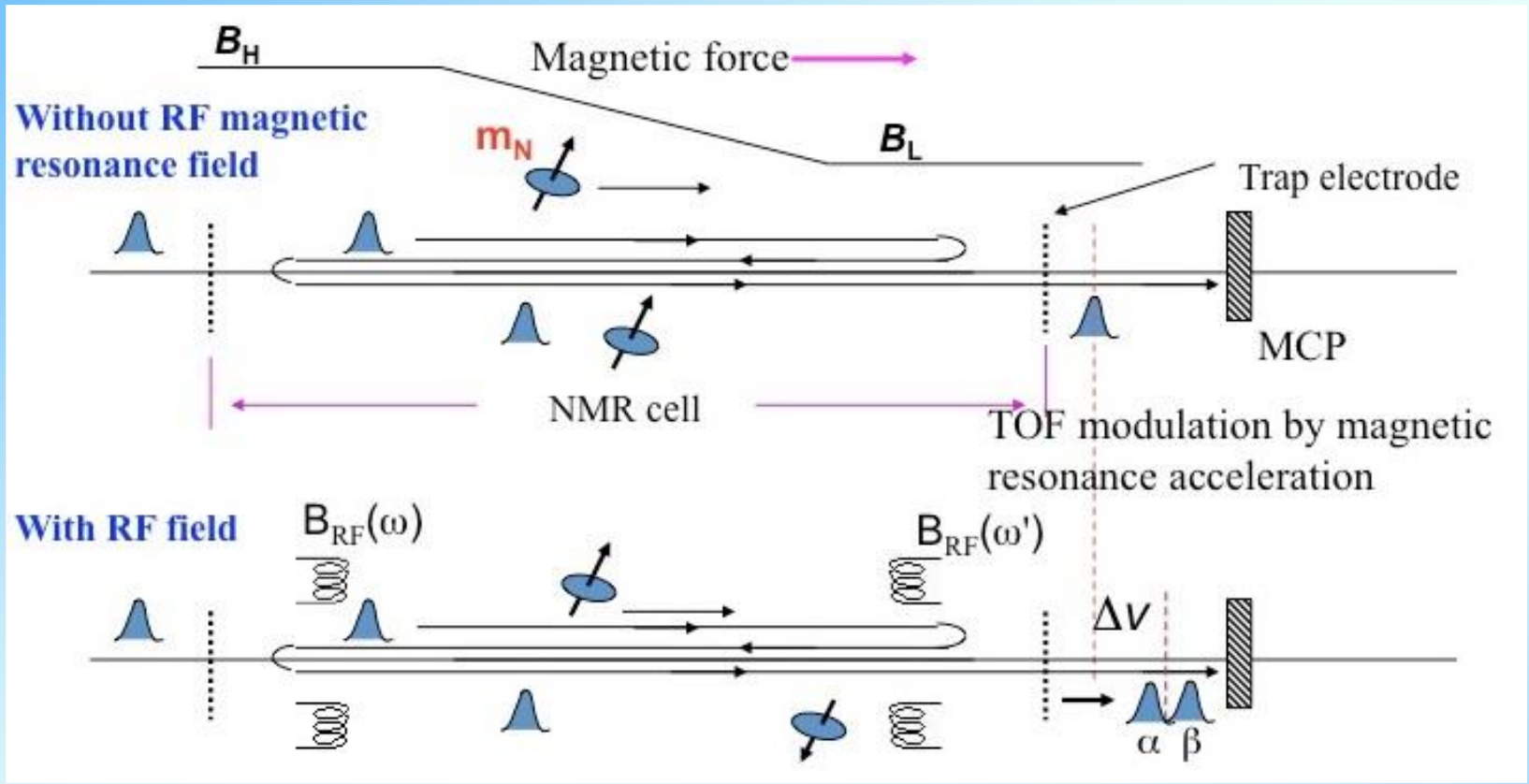

均一な高磁場と低磁場および、その間に大きな傾斜磁場をもつ磁石内に、フロントゲートとバックゲートに相当する捕捉電極で構成されたNMR セルを設置する。このセルは一種のPenning トラップに相当し、セル内に高磁場側からイオン束（例としてプロトン）を注入すると、イオンはサイクロトロン運動による磁気モーメントおよび核磁気モーメントと磁場勾配の相互作用で発生する磁気力のため加減速を伴いながらセル内を往復する。セル両端の均一磁場部にRF コイルを設置し、セル内を通過するイオンにπパルス（共鳴周波数をもつ弱磁場）を照射すると、核スピンは反転する。気相での磁気緩和は遅いためαおよびβスピンは連続的に加速または減速され、往復運動の回数が増えるに従って、核スピン状態の分極が起こる。一定時間後にバックゲートを開けて、MCP 検出器により飛行時間（TOF）の変調として観測する。この測定で得られる速度増分（Δv）を周波数に対してプロットすることにより、NMR スペクトルが得られる。実際の装置では、NMR セルの上流にイオンサイクロトロン共鳴セルを設置し、イオン源で発生したイオンの捕捉と質量選別および速度選別を行う。

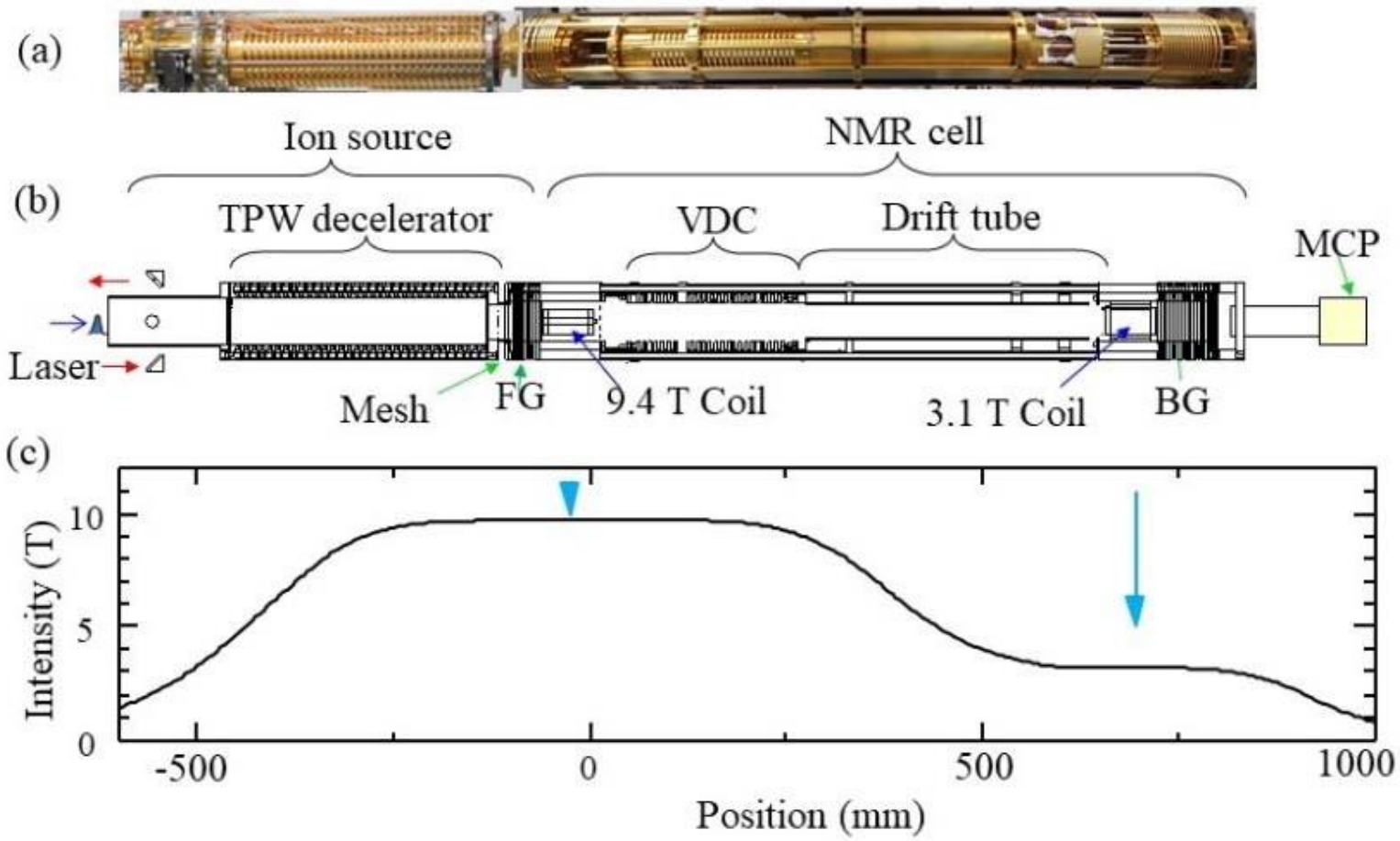

Fig. 3. (a) Photographs and (b) schematics of ion optics in the gas-phase NMR apparatus. (c) Magnetic field distribution of superconductive magnet.

富宅喜代一, 分子科学アーカイブス, AC0017, 2022.
Kiyokazu Fuke, Int. J. Mass Spectrom 490 (2023) 117068.

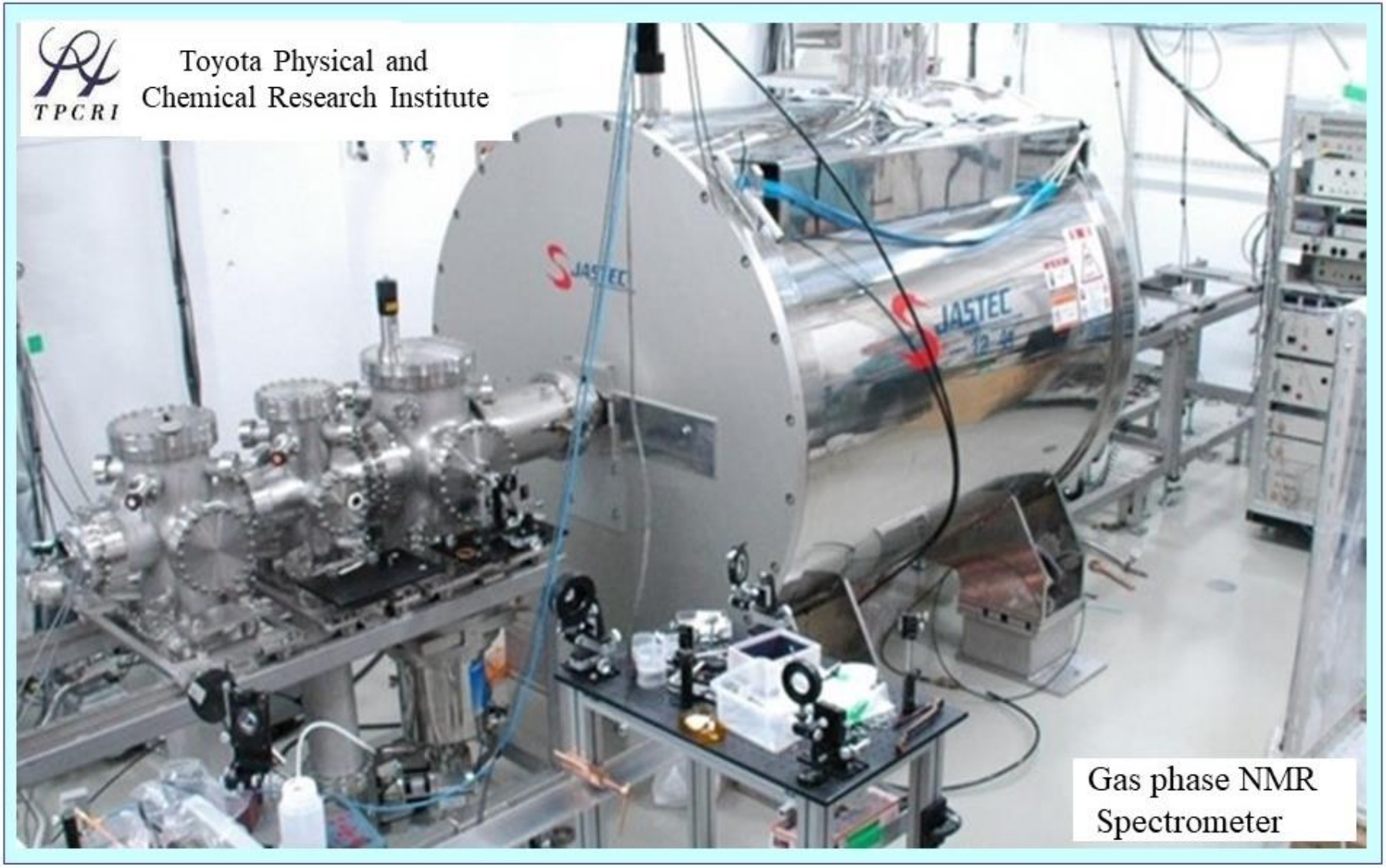

Fig. 17. Gas-phase NMR apparatus (Installed at Institute for Molecular Science; Photo by Nobuo Mizutani; 2014.06)

Kiyokazu Fuke

富宅喜代一　神戸大学名誉教授

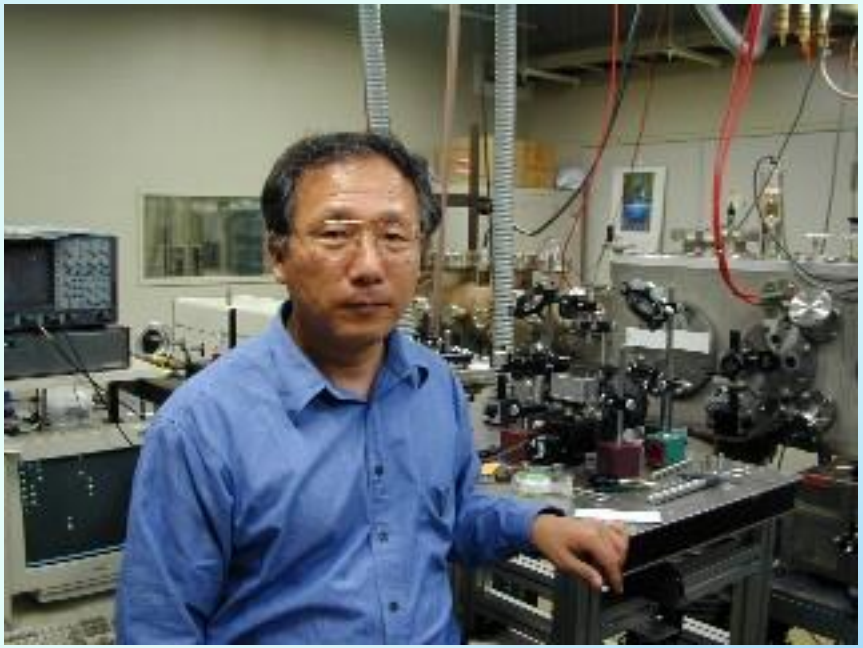

Kobe University

Direct Analysis of Biological Tissue by Paper Spray Mass Spectrometry

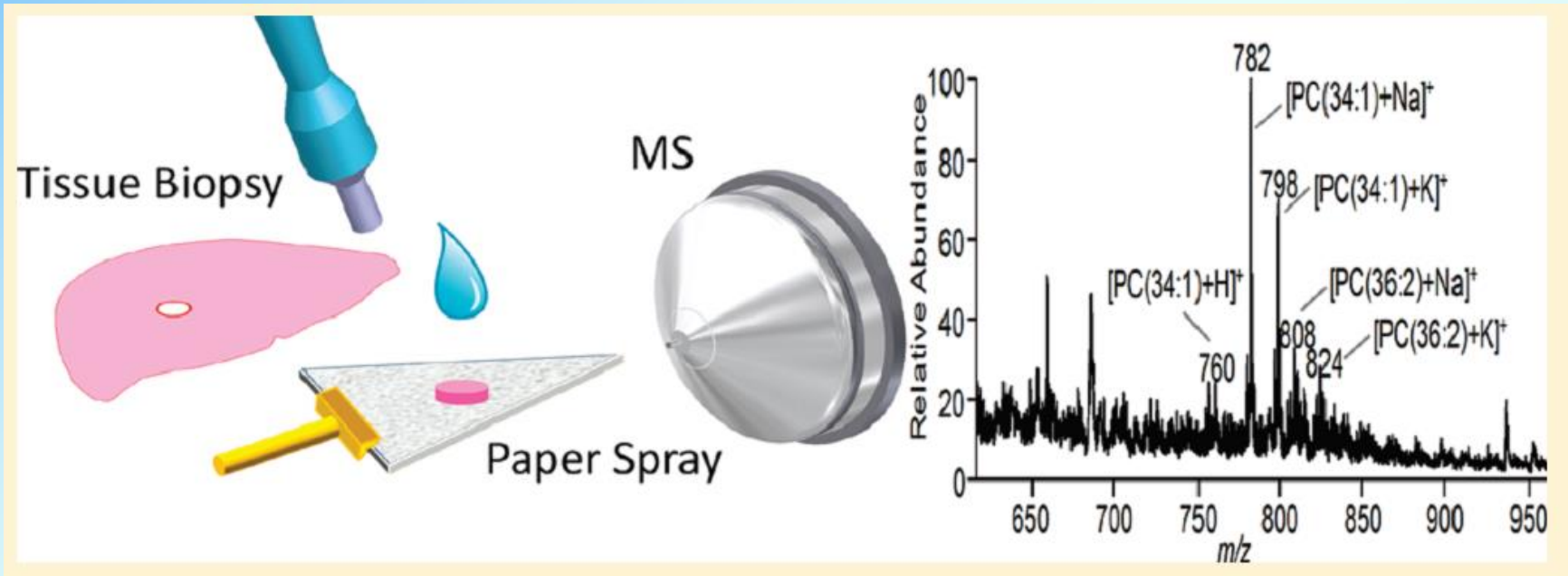

Anal. Chem.2011, 83, 1197–1201

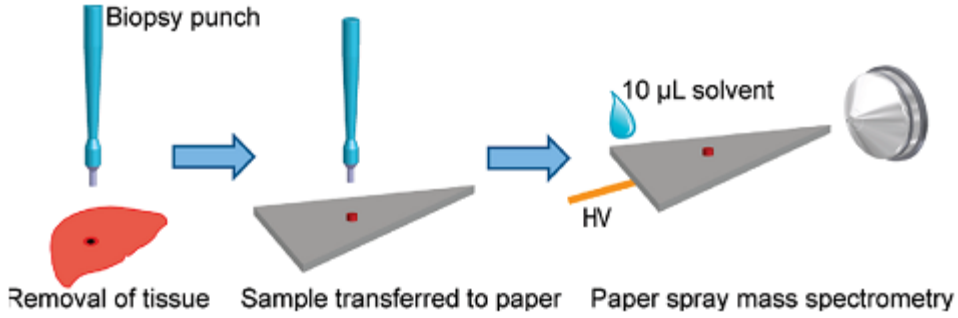

Figure 1. Procedure for combining tissue biopsy with paper spray mass spectrometry.

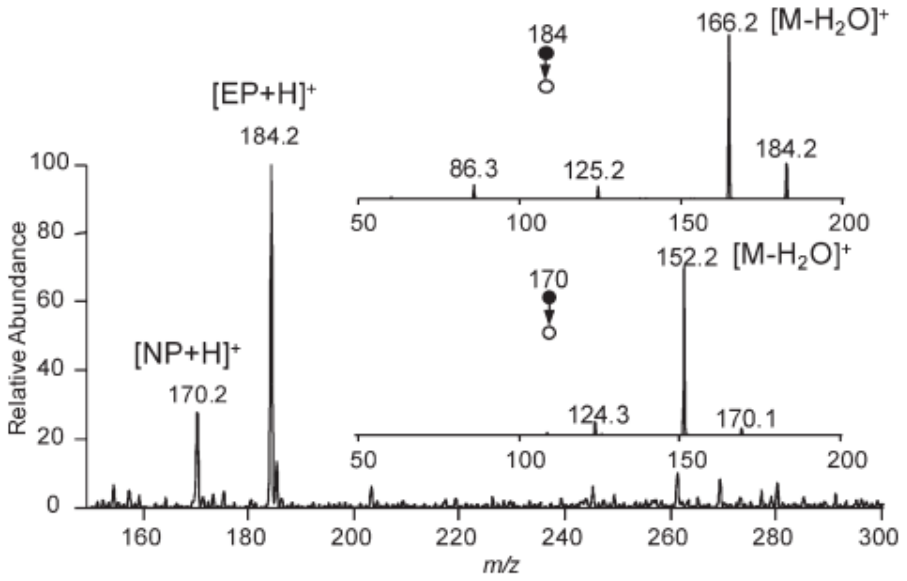

Figure 2. Direct analysis of hormones in animal tissue by PS-MS after needle aspiration biopsy. Porcine adrenal gland tissue (1 mm^3) was placed on the paper surface; MeOH/water (1/1 v:v; 10 μL) was added, and a DC potential of 4.5 kV was applied to the paper to produce a spray. Hormones epinephrine and norepinephrine were identified and confirmed with MS/MS (spectra shown as insets). Spectra recorded using LTQ ion trap mass spectrometer.

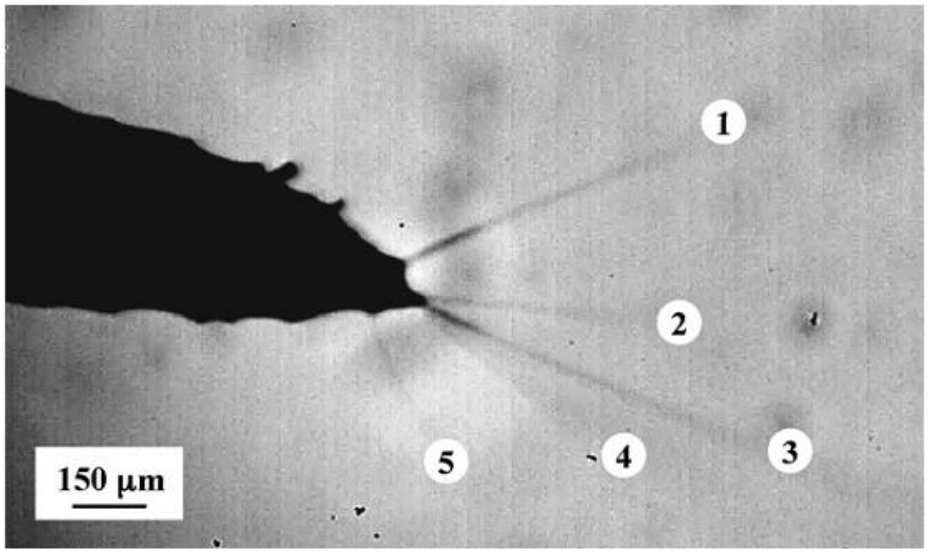

Fig. 1. Image of paper spray taken using a FASTCAM 1024 PCI with back-lit fiberoptic illumination. Substrate is Whatman 1 filter paper, solvent is 80/20 MeOH:H_2O, spray voltage is +4500 V. The spray is operating in Mode 1.

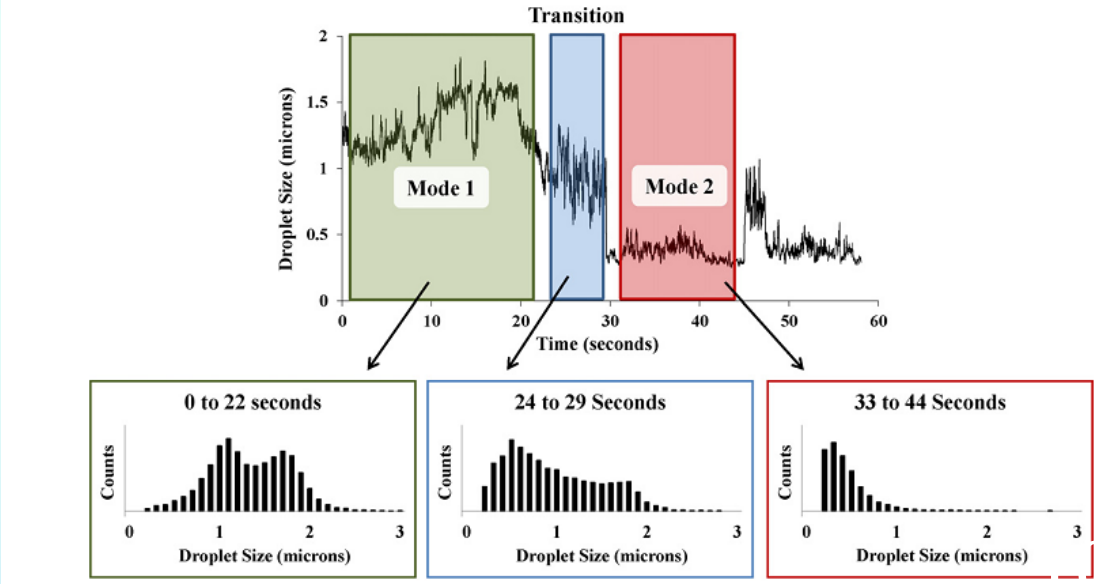

Fig. 2. Droplet size measurements taken by a PDPA during one experiment where 10 µL of 80/20 methanol:water and 4500 V was applied to a paper substrate and the solvent allowed to deplete over time. The time course displays a 50-point moving average of droplet measurements taken at 1000 Hz.

Direct Plant Tissue Analysis and Imprint Imaging by Desorption Electrospray Ionization Mass Spectrometry

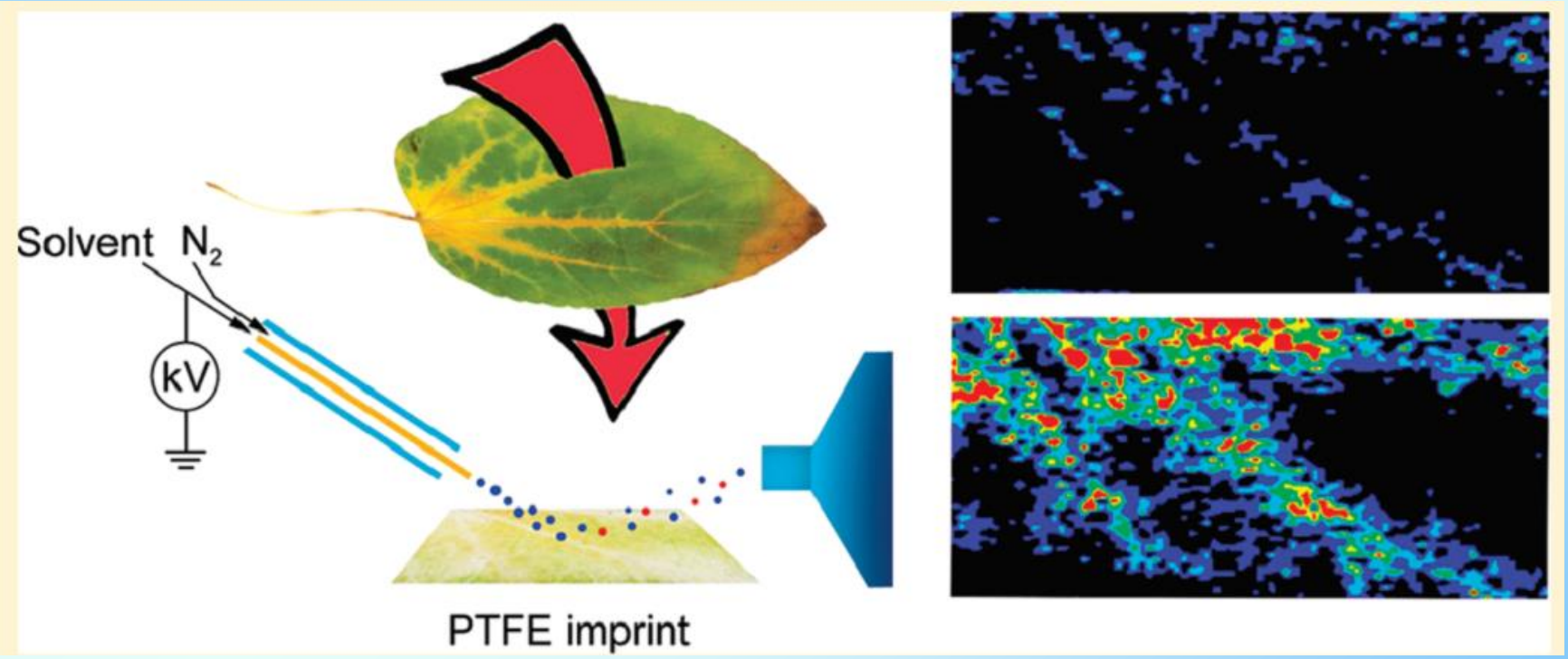

Anal. Chem.2011, 83, 5754–5761

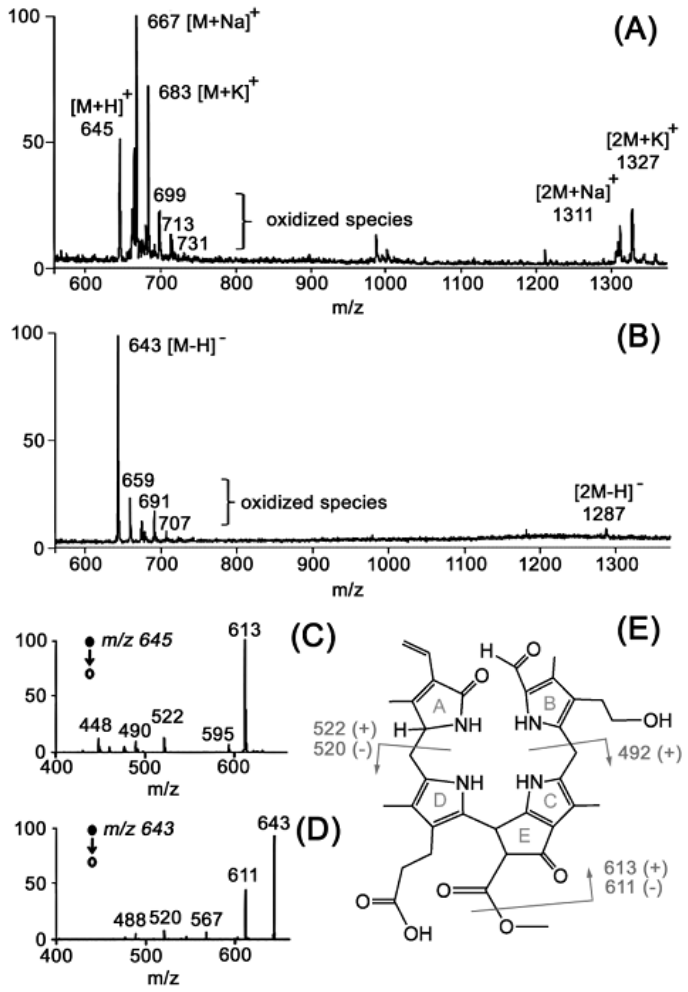

Figure 1. (A, B) DESI-MS spectra of a 3 mm spot of *Cj*-NCC-1 standard on a PTFE surface. Spray solvent was methanol/water (20:80) at a flow rate of 3 μL/min. (A) Positive ion mode DESI-MS spectrum. Protonated, sodiated, and potassiated molecules were detected at m/z 645, 667, and 683, respectively; the dimer, at m/z 1311. (B) Negative ion mode DESI-MS. Ions corresponding to deprotonated molecules were observed at m/z 643, and its dimer, at m/z 1287. (C) Positive ion mode DESI-MS/MS spectrum of the protonated molecule, m/z 645. (D) Negative ion mode DESI-MS/MS spectrum of the deprotonated molecule, m/z 643. (E) Constitutional formula of *Cj*-NCC-1,[45] characteristic CID fragmentations observed in positive ion mode (+) and negative ion mode (−) are highlighted in gray.

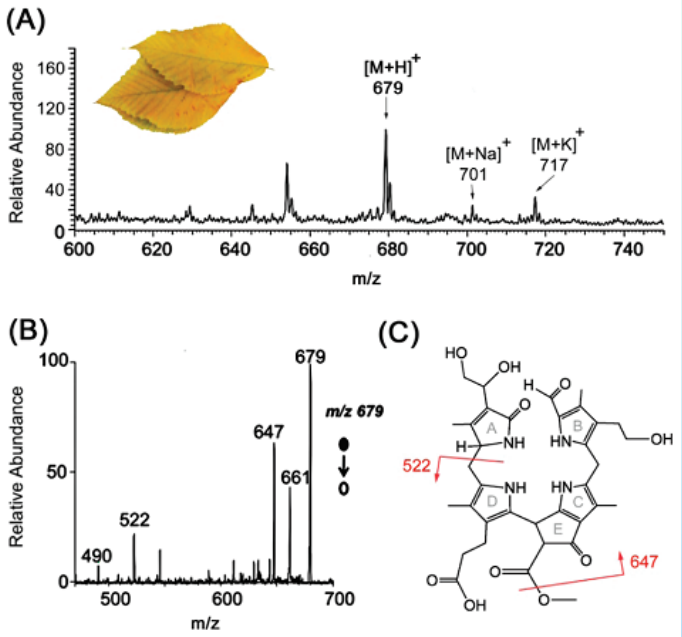

Figure 2. (A) Positive ion mode DESI-MS spectrum of the direct analysis of a hophornbeam (*O. virginiana*) leaf. Spray solvent was methanol/water (80:20) at a flow rate of 3 μL/min. Protonated, sodiated, and potassiated molecules were detected at m/z 679, 701, and 717, respectively. (B) DESI-MS/MS spectrum of the isolated protonated molecule, m/z 679. (C) Proposed structure of the chlorophyll catabolite corresponding to the ion at m/z 679, the *Ov*-NCC-1. The structure shown is proposed considering previous data.[3,48] Characteristic fragmentations due to the losses of methanol (fragment at m/z 647) and ring A (fragment at m/z 522) are marked.

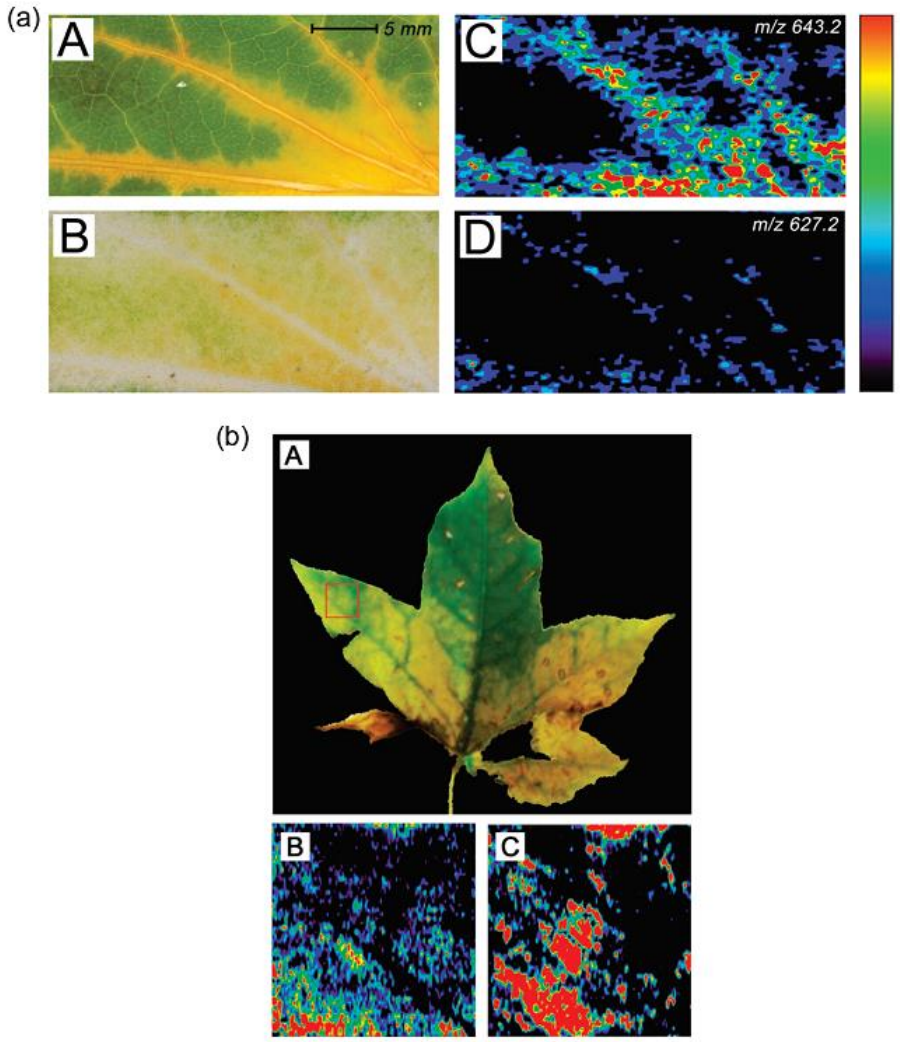

Figure 5. (a) Negative ion mode DESI imaging of a senescent Katsura tree leaf imprint on porous PTFE substrate. Spray solvent was 1% concentrated aqueous ammonia in methanol at a flow rate of 1.5 μL/min. Imaging parameters: 1.17 s/scan; 98 scans/horizontal row; 56 rows; pixel size was 310 × 250 μm; total acquisition time was 107 min. (A) 30.7 × 13.9 mm section of a photographic image taken from a senescent Katsura leaf. (B) 30.7 × 13.9 mm porous PTFE substrate with Katsura leaf imprint. (C, D) Ion images of the two chlorophyll catabolites[7,45] in Katsura leaves at m/z 643.2 and 627.2. Both images are plotted on the same color scale, which is depicted on the right-hand side of the figure to visualize relative ion intensities from 0 (black) to 100 (red). (b) Negative ion mode DESI imaging of a senescent American sweetgum leaf imprint on porous PTFE substrate. Spray solvent was 1% concentrated aqueous ammonia in methanol at a flow rate of 1.5 μL/min. Imaging parameters: 0.72 s/scan; 119 scans/horizontal row; 50 rows; pixel size was 130 × 300 μm; total acquisition time was 71 min. (A) Photographic image taken from a senescent American sweetgum leaf. The rastered 15 × 15 mm section is highlighted in red. (B, C) Ion images of the two chlorophyll catabolites found in American sweetgum[46] at m/z 643.2 and 627.2. Both images are plotted on the same color scale, which is depicted on the right-hand side of panel a to visualize relative ion intensities from 0 (black) to 100 (red).

Mass Spectrometry in the Ambient Environment

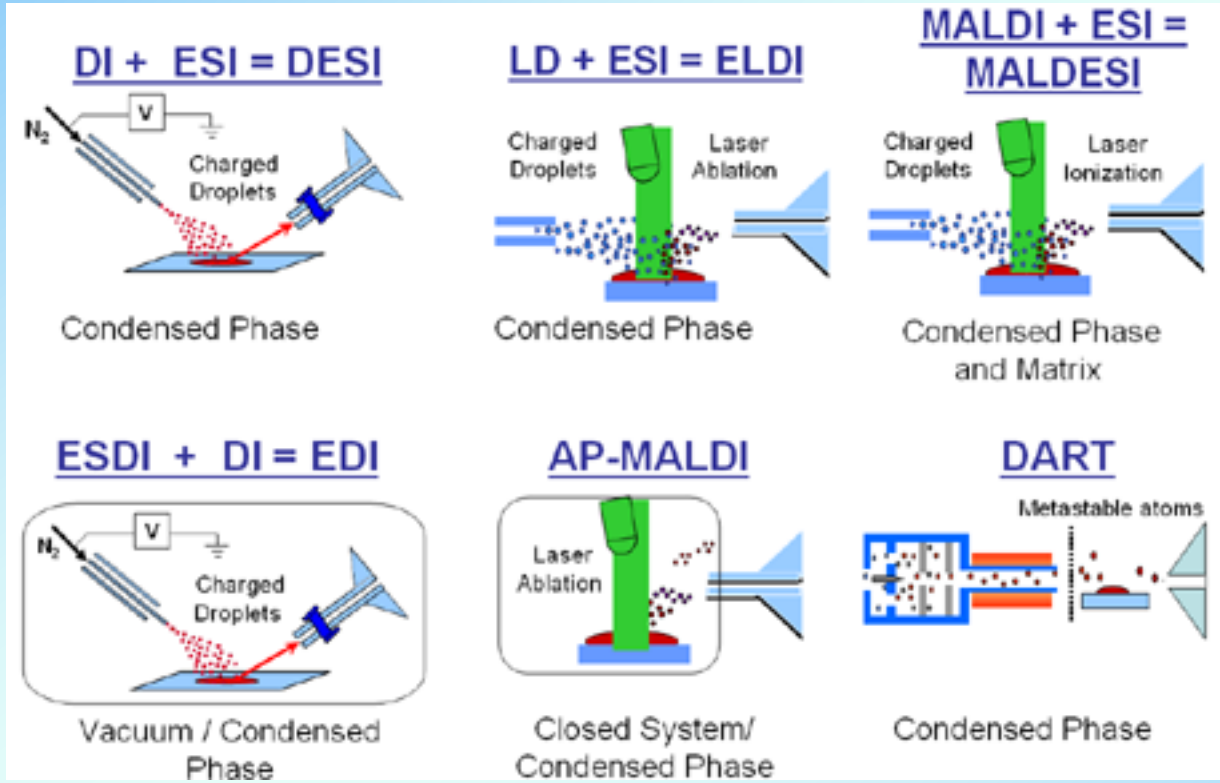

DESI: Takats et al, *Science*, 2004, 306, 471
ELDI: Shiea et al, *RCM*, 2005, 19, 3701
MALDESI: Muddiman, *JASMS*, 2006, 17, 1712
EDI: Hiraoka et al, *JMS*, 2006, 41, 894
AP-MALDI: Dororshenko et al, *IJMS*, 2002
DART: Cody et al, *Anal. Chem*, 2005, 77, 2297

Miniature Mass Spectrometers

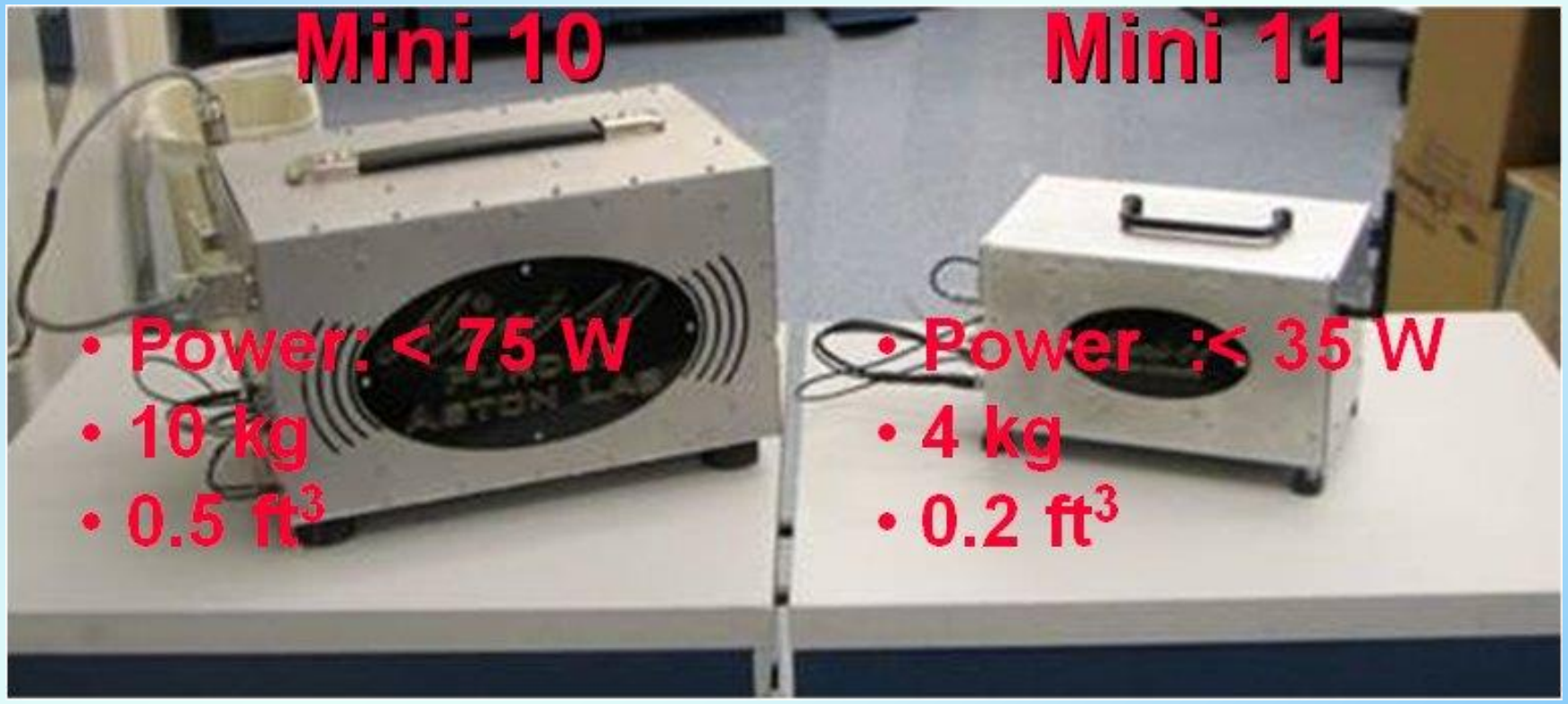

Prof. R. Graham Cooks

Aston Labs of Mass Spectrometry
Pudue University

MULTUM
マルチターン飛行時間型質量分析計

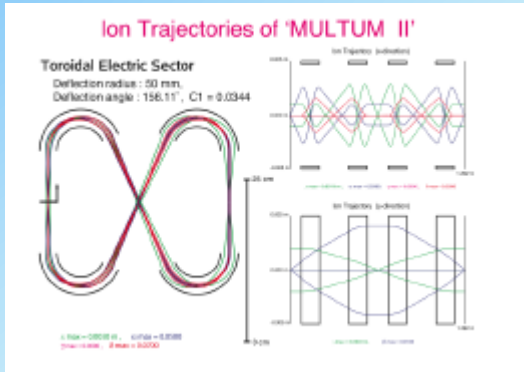

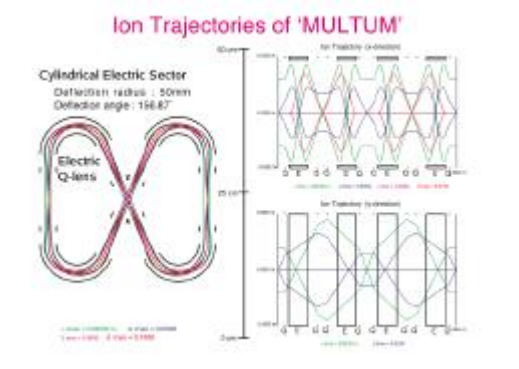

マルチターン飛行時間型質量分析計
MULTUM Linear plus

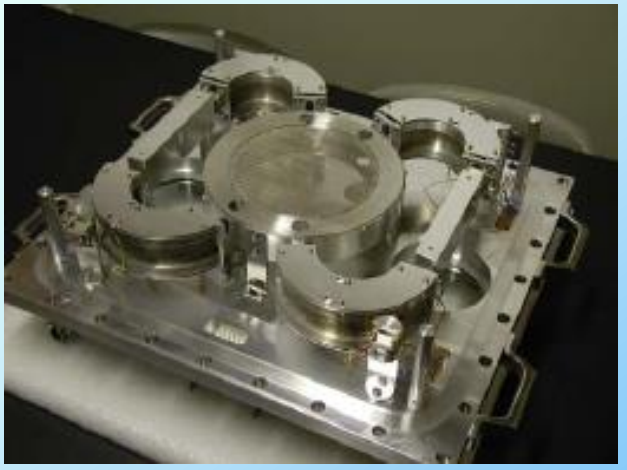

マルチターン飛行時間型質量分析計
MULTUM II

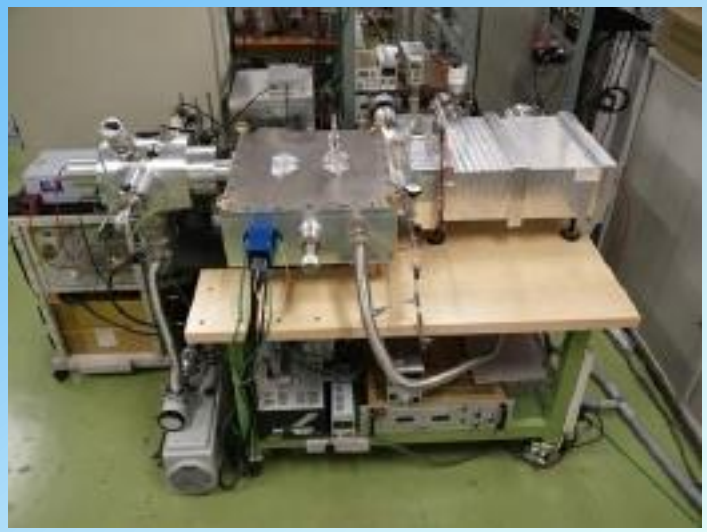

マルチターン・タンデム飛行時間型質量分析計
MULTUM-TOF/TOF

像投影型イメージング質量分析計
MULTUM-IMG

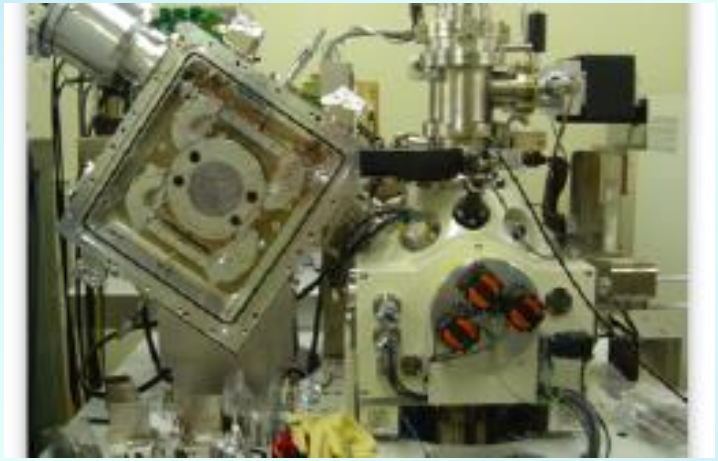

イメージング質量分析計
MULTUM-SIMS

小型マルチターン飛行時間型質量分析計
MULTUM-S

イメージング質量分析とは

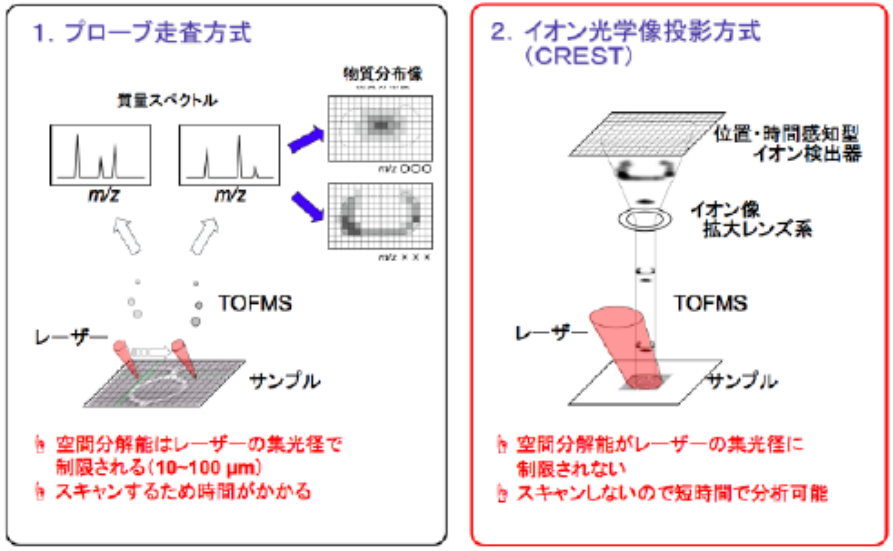

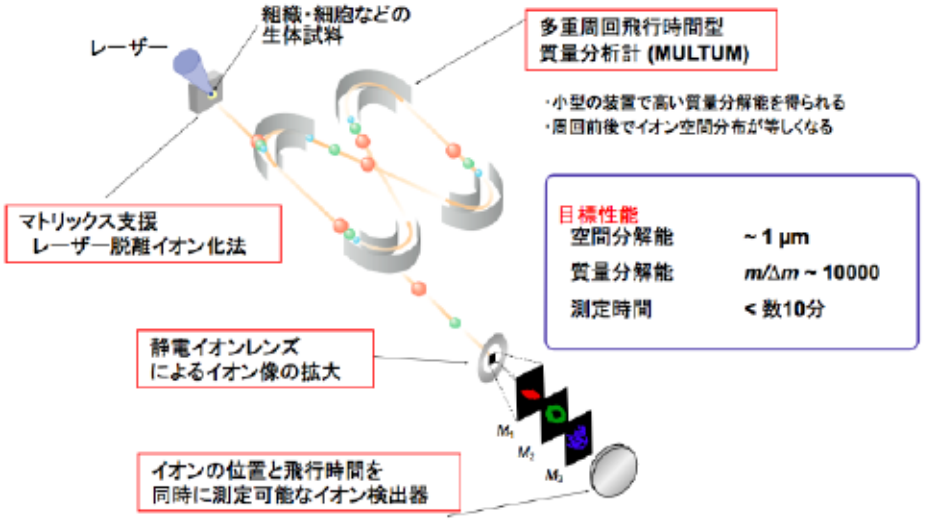

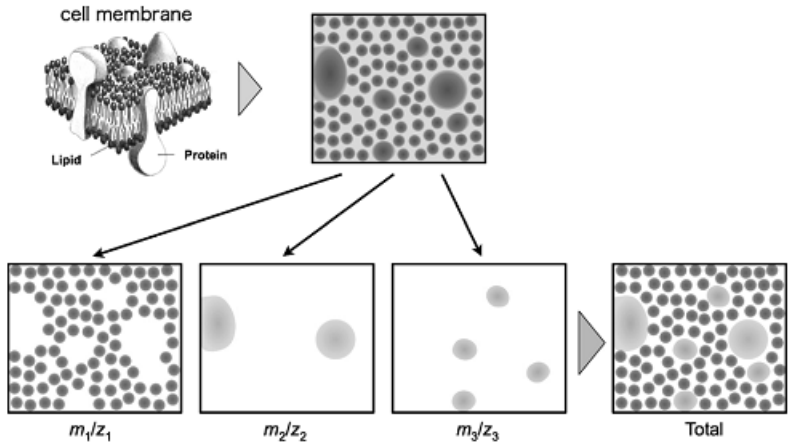

Fig. 1. Overview of imaging mass spectrometry.

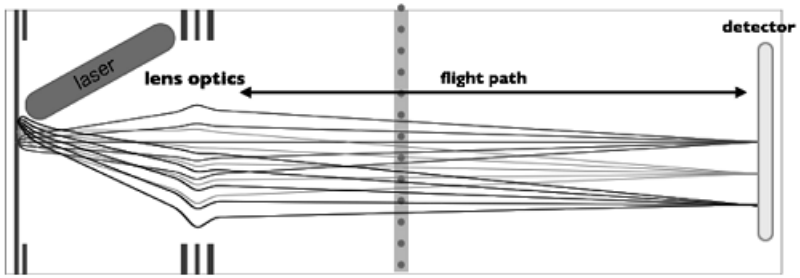

Fig. 3. Schematic of ion trajectory of a stigmatic time-of-flight imaging mass spectrometer.

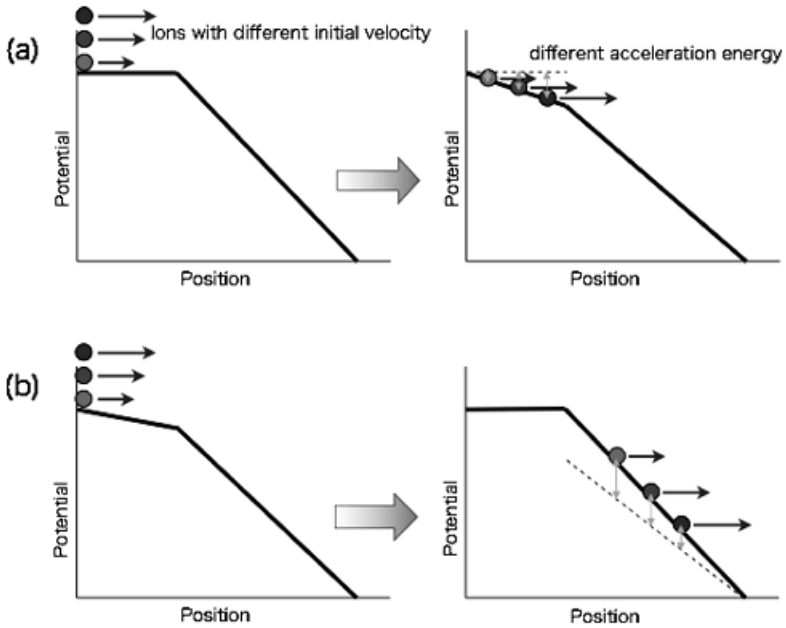

Fig. 4. Mechanism of delayed extraction method (a) and post extraction differential acceleration method (b).

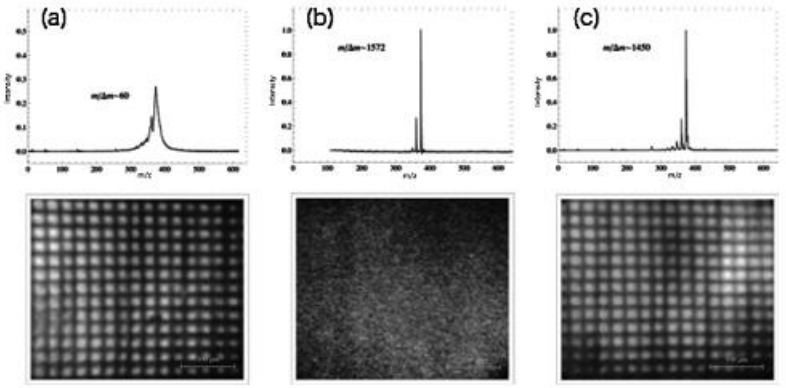

Fig. 5. Time-of-flight spectrum (upper half) and ion images (lower half) of different ion extraction methods; (a) normal extraction, (b) delayed extraction, (c) post extraction differential acceleration.

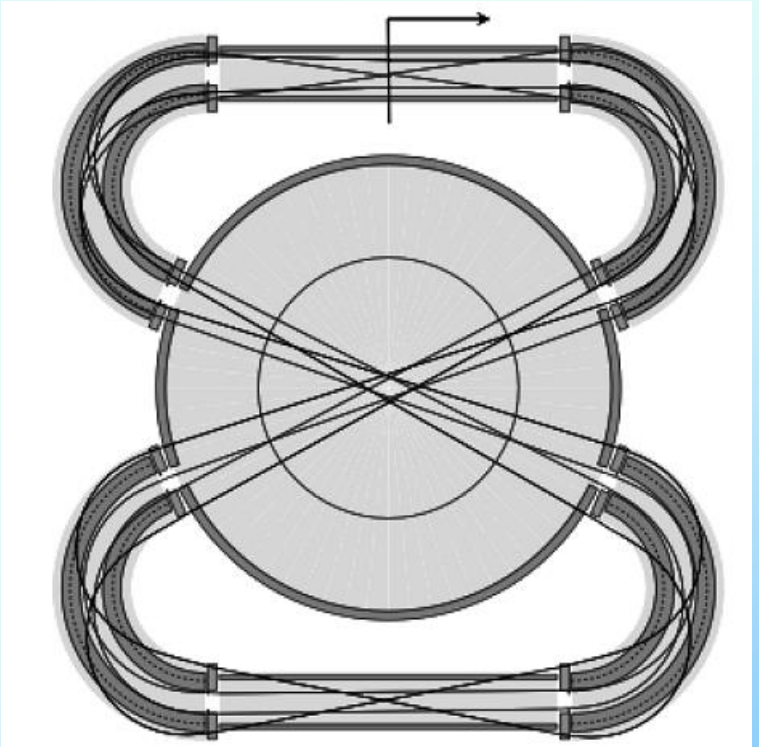

Fig. 6. Ion trajectory of multi-turn orbit.

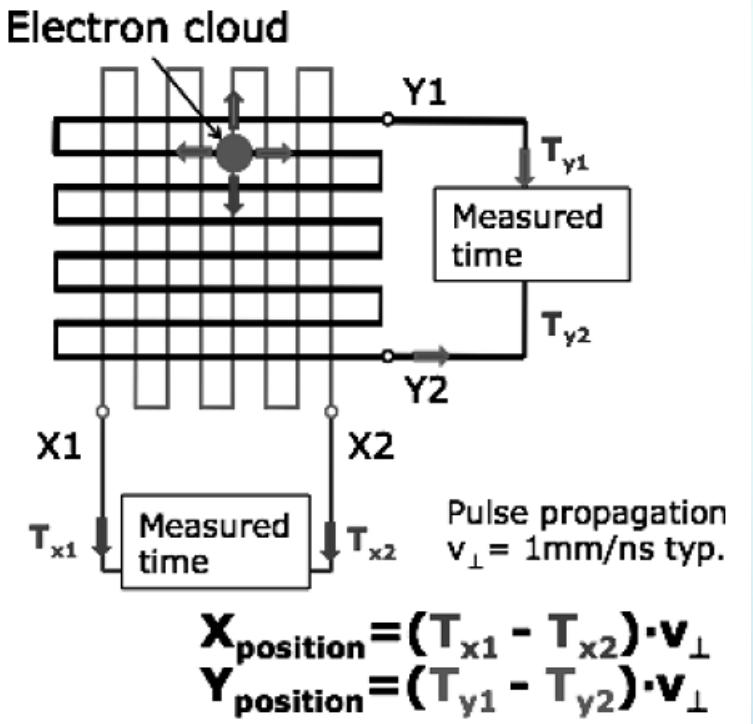

Fig. 9. Schematics of delay line detector.

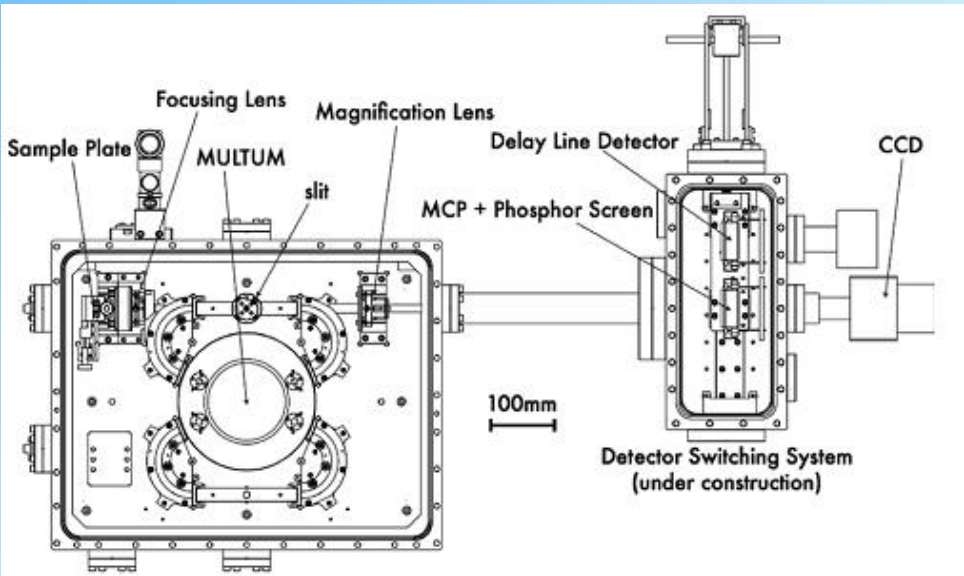

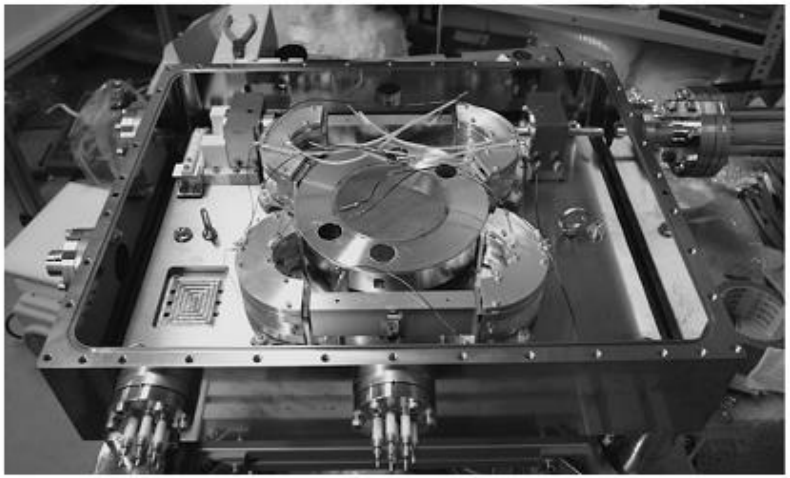

Fig. 15. MULTUM-IMG 2.

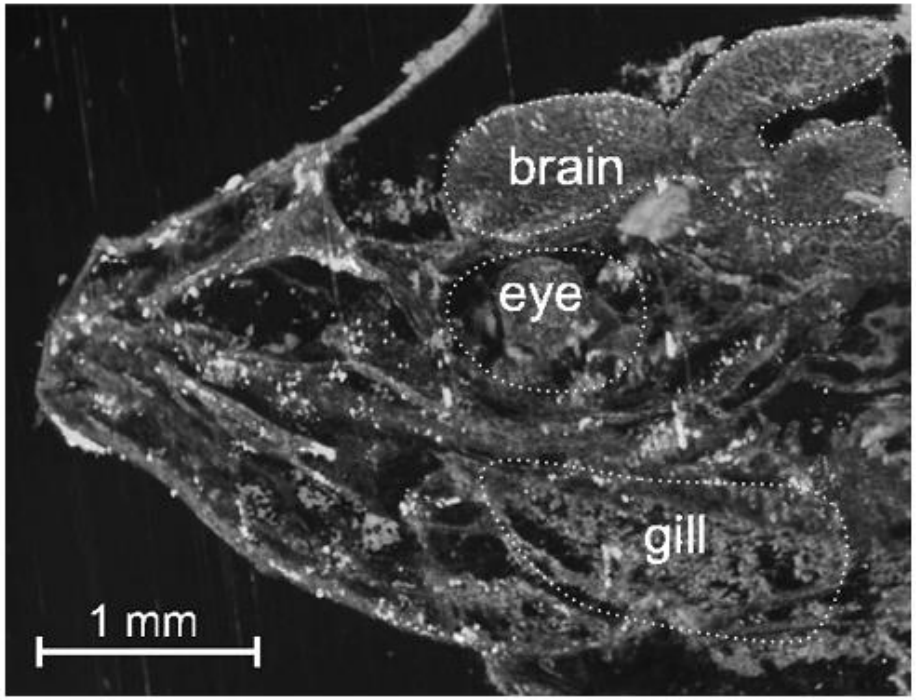

Fig. 21. Observed ion image of medaka tissue (Red:Sr/Green: K/Blue:Cs).

豊田岐聡
大阪大学理学部物理学科

質量分析の歴史

世界の動向		阪大質量分析グループの歴史
放物線型質量分析器（J.J. Thomson, 1912） 方向収束質量分析器（Dempster, 1918） 速度収束質量分析器（Aston, 1919）	1910年代	 国内初の質量分析装置 (Bainbridge-Jordan型) マグネットは国立科学博物館に寄贈 日本初の質量分析装置 Bainbridge-Jordan型 (浅田, 奥田, 分解能8000, 1939）
装置の改良，同位体測定（Aston）	1920年代	
二重収束質量分析器（Dempster, 1935）	1930年代	 緒方・松田型 終戦後~1951年, 分解能90万, 61年の第二室戸台風時に中之島で水没, 64年に豊中に移動して改良型を再製作, 分解能40万-50万をつねに発揮 緒方ー松田型 (緒方, 松田, 分解能90万, 1951）
原子質量の精密測定， 同位体分離・濃縮， 地質年代測定法の確立， 炭化水素混合物の測定	1940年代	
飛行時間型質量分析計（Stephens, 1946）		
高精度原子質量測定，高分解能装置の開発：Bainbridge (10万)，Nier (6万)など	1950年代	 r-1 磁場型の世界最高分解能120万を達成 阪神大震災で崩壊，国立科学博物館に寄贈    おろち 原子質量を10^{-6}のオーダーまで正確に決める目標をもって開発された超大型 装置. 大分散質量分析器 r-1 (松田, 世界最高質量分解能120万, 1968）
四重極，イオントラップ（Paul, 1953）		
スパッター源， CI，FDなどのイオン化法 GC/MS 有機化合物の測定	1960年代	
SIMS フーリエ変換イオンサイクロトロン共鳴質量分析計 (Marshall, 1976)	1970年代	おろち(緒方, 分解能80万, 1969） CQH(松田, 分解能24万, 1972） 三次近似イオン軌道計算ソフトTRIO (松尾, 1976）
生体高分子の測定 ESI (Fenn, 山下, 1984） LD	1980年代	六重収束飛行時間型質量分析計 (桜井, 1985） GEMMY (松田, 1988）
MALDI (Hillenkamp, 田中, 1991）	1990年代	 CQH 短寿命核の測定用に開発，その後，生体高分子やクラスターの測定に活用  GEMMY マグネットが9kgある大型装置，蛋白質の測定を狙って開発  六重収束飛行時間型質量分析計 直径40cmで飛行距離1.7m，六重収束のイオン光学系，分解能2000.
プロテオーム，メタボローム オービトラップ (Makarov, 1999)	2000年代	MULTUM (豊田, 1998）

FT-ICR 質量分析計

高い質量分解能（$R = 10^5 \sim 10^6$）
高い質量確度（$\Delta m = 10^{-4} \sim 10^{-3}$ u）
高い検出限界（10^{-18} mol）

$$r_\mathrm{m} = \frac{m_\mathrm{i} v}{qB}$$

$$v = r_\mathrm{m} \omega_\mathrm{c}$$

$$\omega_\mathrm{c} = \frac{qB}{m_\mathrm{i}}$$

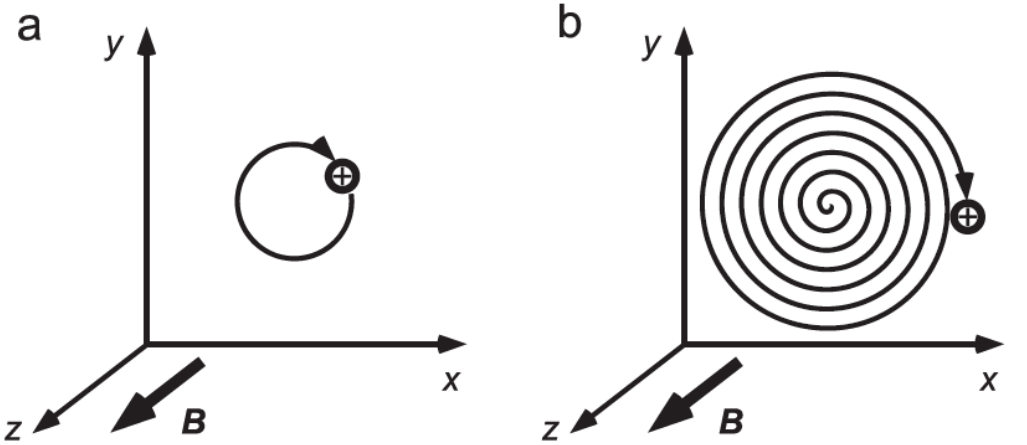

図 **4.49**：均一な磁場 B での正イオンの運動．(a) 円運動の半径はイオン速度に依存するが，回転周波数 f_c はイオン速度に依存しない．(b) イオン固有のサイクロトロン共鳴周波数と一致する高周波電場によるイオンの励起．

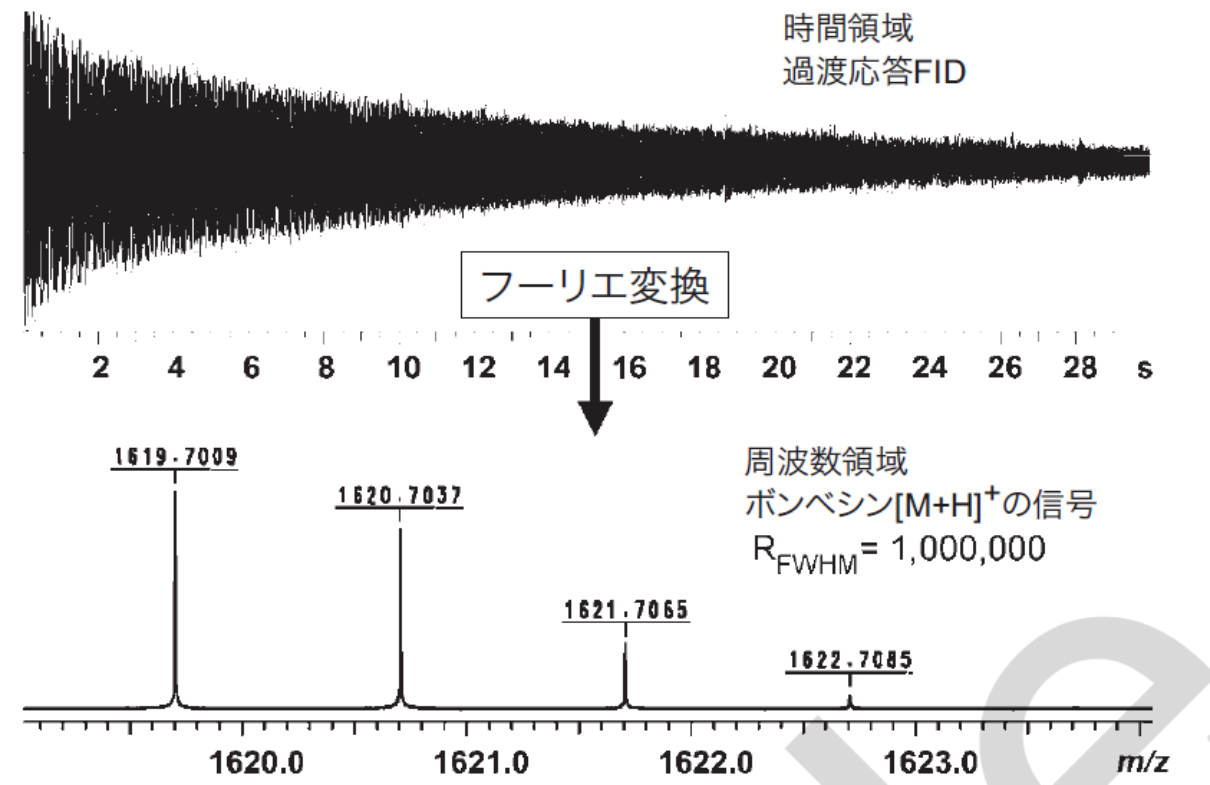
時間領域
過渡応答FID
フーリエ変換
2 4 6 8 10 12 14 16 18 20 22 24 26 28 s
1619.7009
1620.7037
1621.7065
1622.7085
周波数領域
ボンベシン[M+H]+の信号
RFWHM= 1,000,000
1620.0 1621.0 1622.0 1623.0 m/z

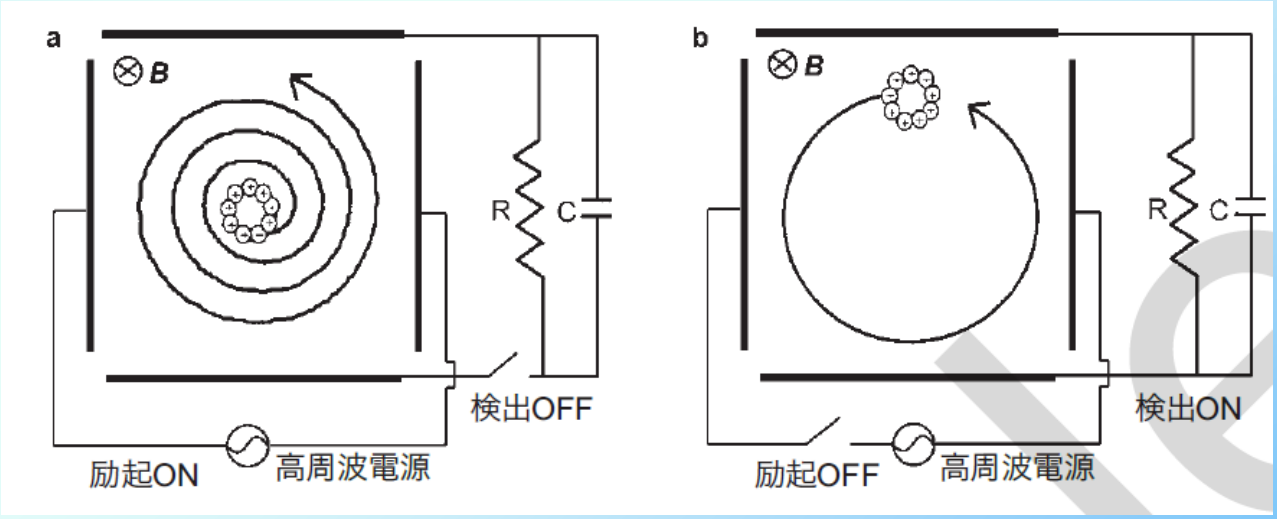
a
B
R
C
検出OFF
励起ON
高周波電源
b
B
R
C
検出ON
励起OFF
高周波電源

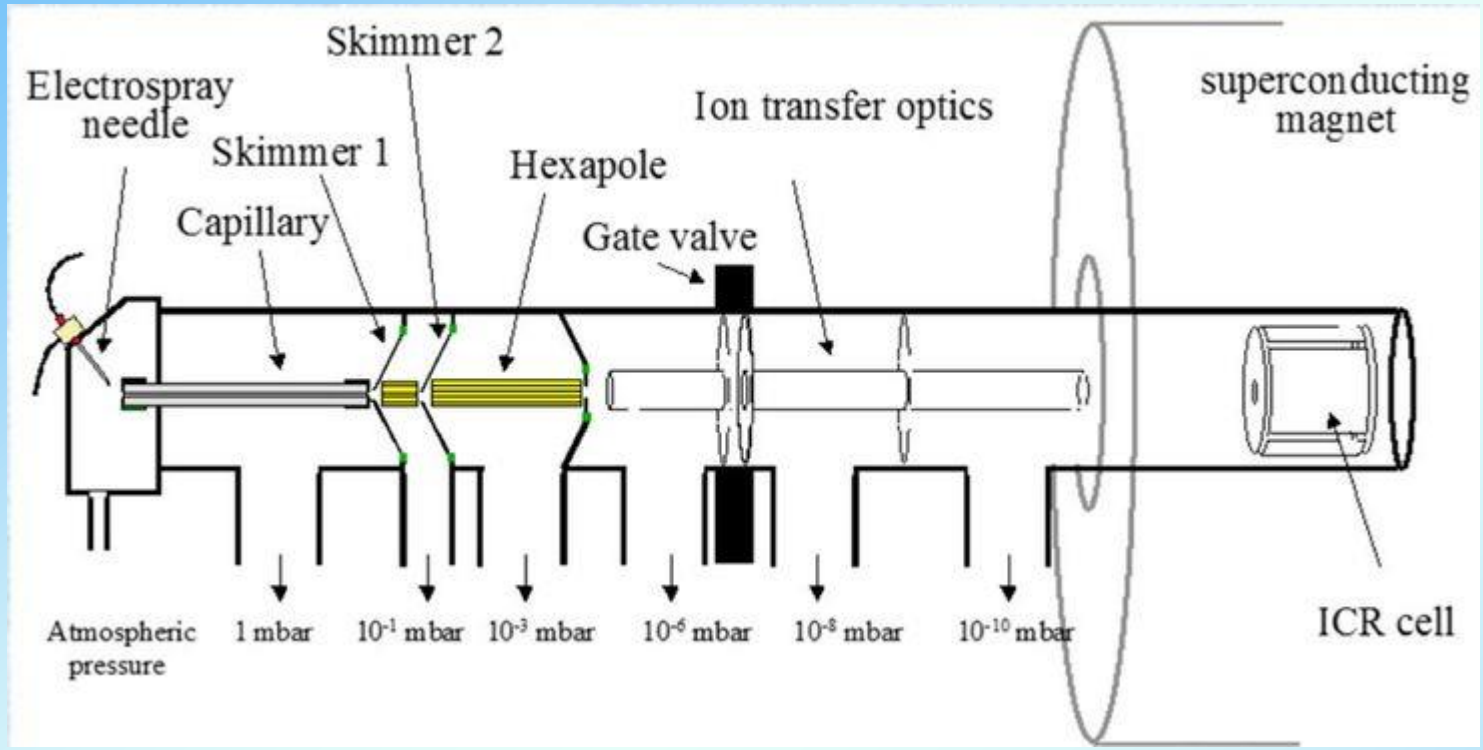
Skimmer 2
Electrospray needle
Ion transfer optics
superconducting magnet
Skimmer 1
Hexapole
Capillary
Gate valve
Atmospheric pressure
1 mbar
10^{-1} mbar
10^{-3} mbar
10^{-6} mbar
10^{-8} mbar
10^{-10} mbar
ICR cell


BRUKER
solarix

Orbitrap

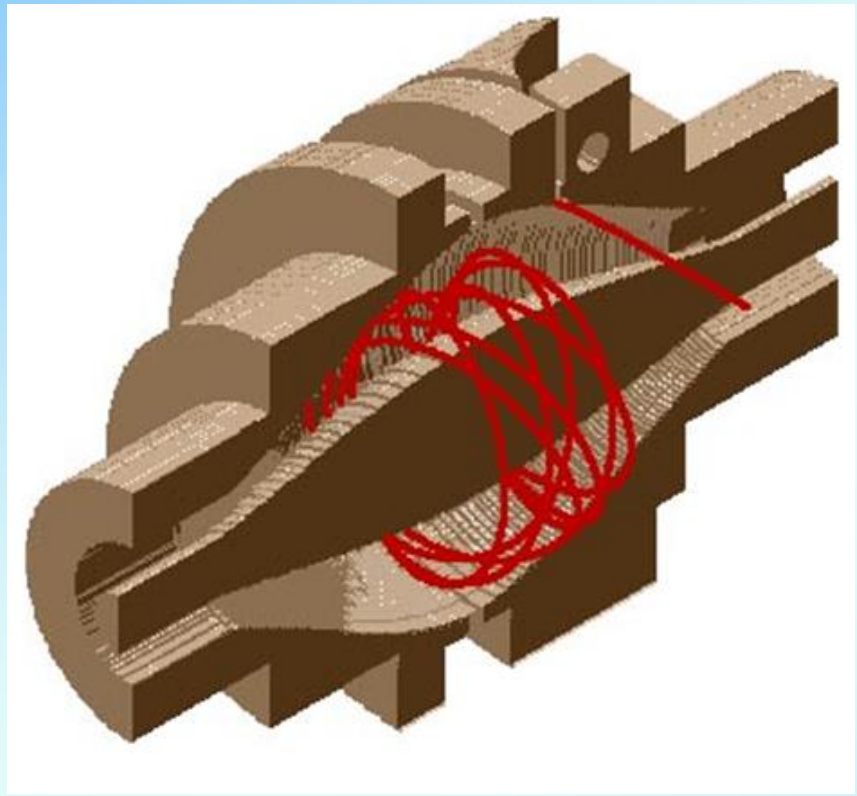

An orbitrap is a type of mass analyzer invented by Alexander Makarov.

It consists of an outer barrel-like electrode and a coaxial inner spindle-like electrode that form an electrostatic field with quadro-logarithmic potential distribution.

Image current from dynamically trapped ions is detected, digitized and converted using Fourier transform into frequency and then mass spectra.

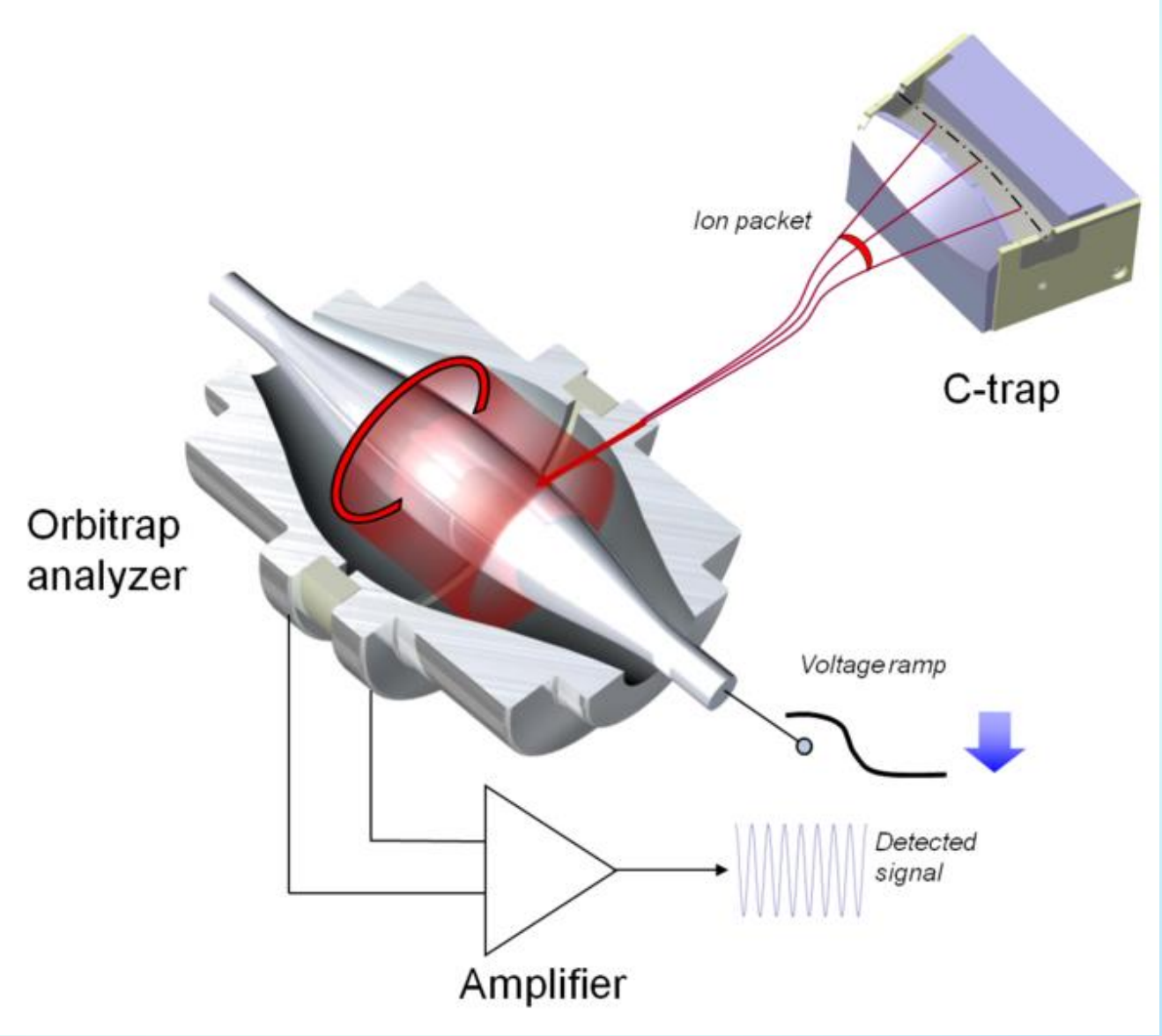

Cross-section of the C-trap and Orbitrap analyzer (ion optics and differential pumping not shown). Ion packet enters the analyzer during the voltage ramp and form rings that induce current detected by the amplifier.

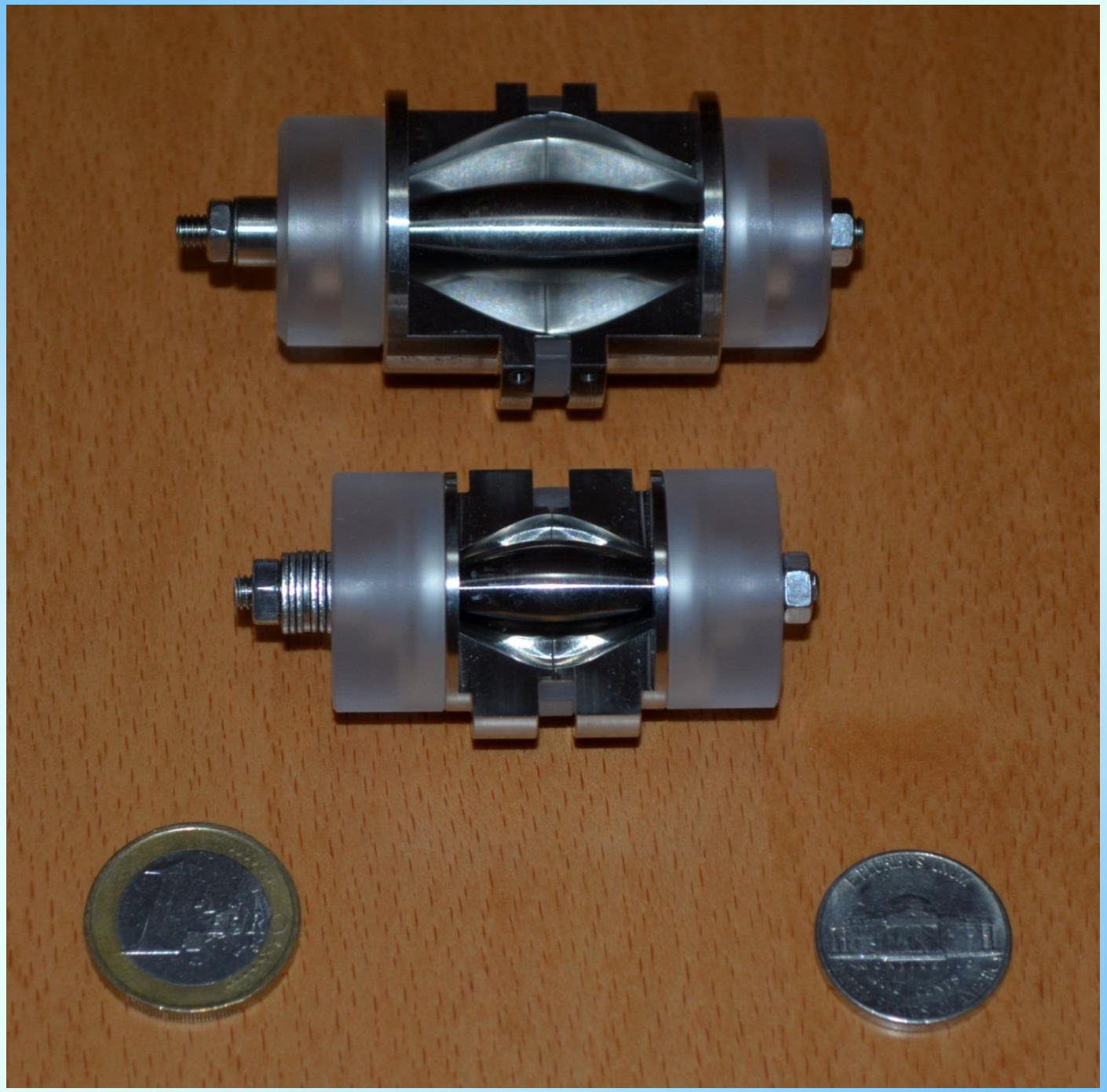

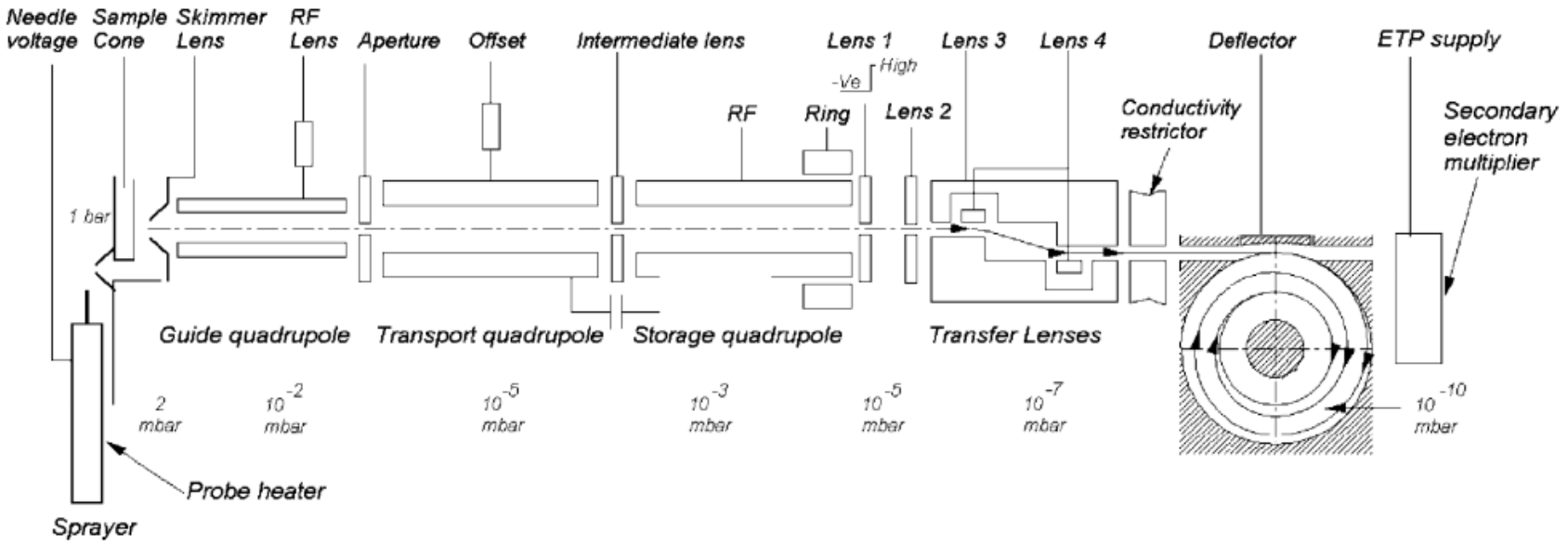

Figure 2. The experimental Orbitrap mass spectrometer. Ions are produced by the electrospray ion source at the extreme left. Ions then proceed through the source, collision quadrupole, selection quadrupole and then pass into the storage quadrupole. The storage quadrupole serves as an ion accumulator and buncher, allowing a pulsed mass analyzer such as the Orbitrap to be coupled to a continuous source like an electrospray ionization source. After accumulation and bunching in the storage quadrupole, the exit lens ('Lens 1') is pulsed low, the ion bunches traverse the ion transfer lens system and are injected into the Orbitrap mass analyzer (shown end-on).

J. Mass Spectrom. 2005; **40**: 430–443

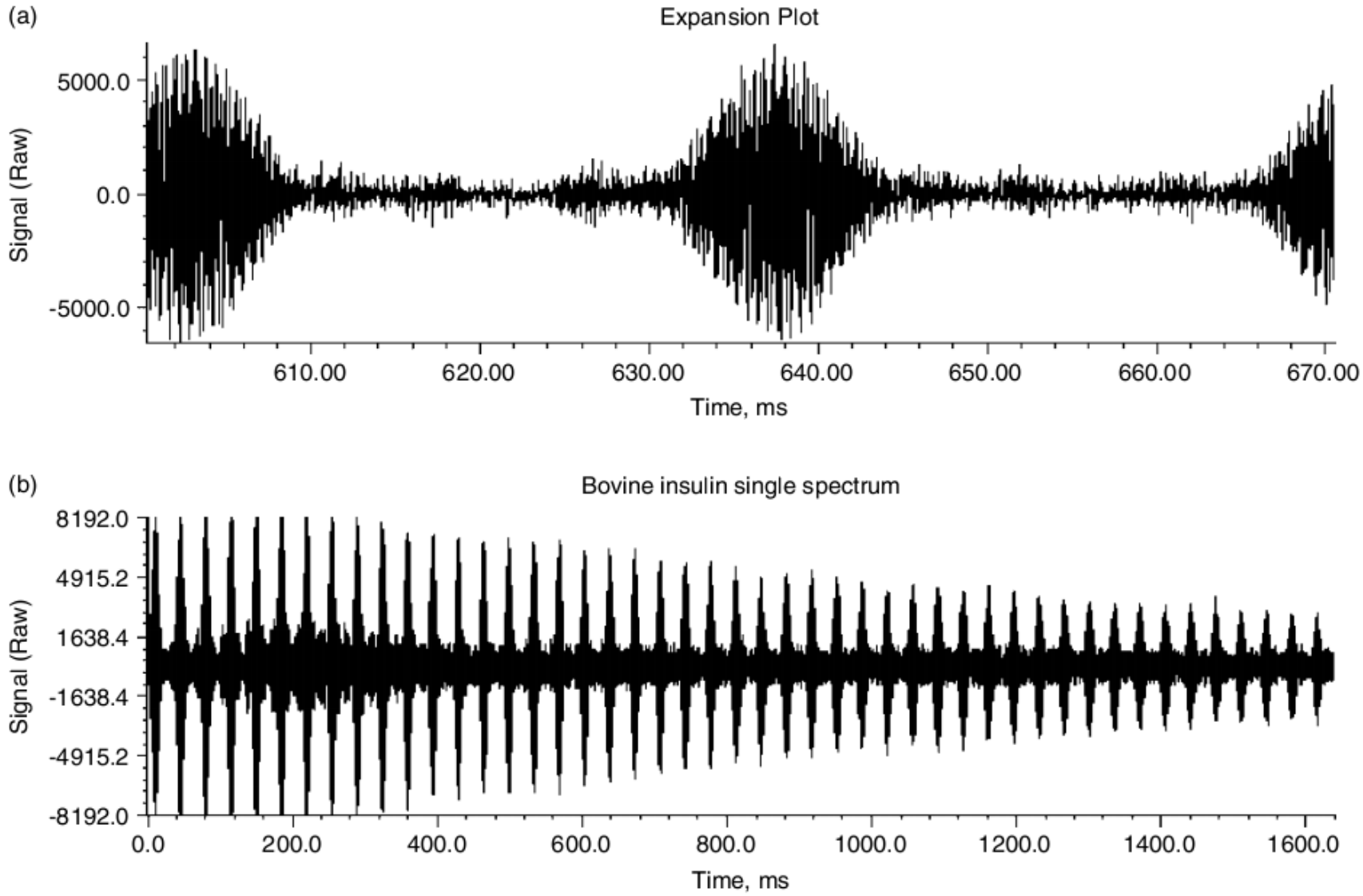

Figure 3. (a) Typical transient acquired to record the mass spectrum of bovine insulin. The transient acquired is equivalent to the free induction decay of FT NMR experiments. Top shows an expanded portion of the transient.

J. Mass Spectrom. 2005; **40**: 430–443

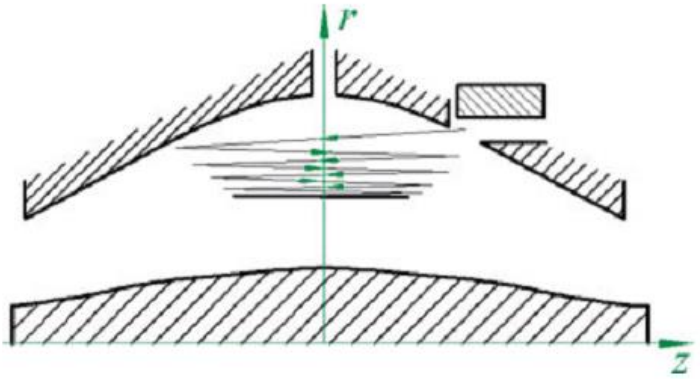

Figure 5. Principle of electrodynamic squeezing of ions in the orbitrap as the field strength is increased.

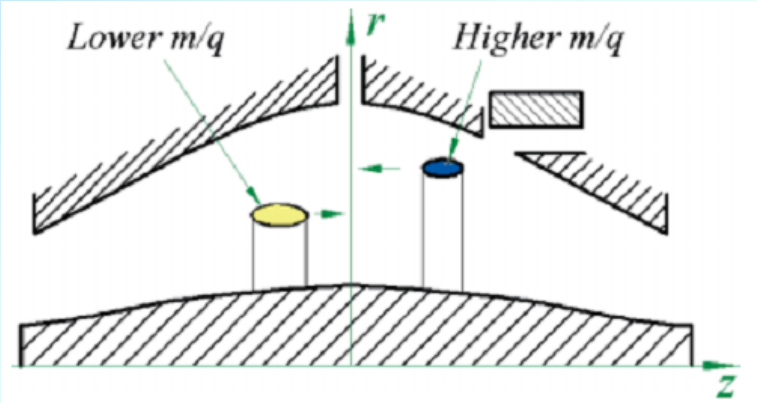

Figure 7. The approximate shape of ion packets of different *m/z* after stabilization of voltages. The Orbitrap is shown in cross-section along the *z*-axis. Ovals represent cross sections for thin rings of ions of different *m/z*. The cross-sectional area is exaggerated for illustration purposes.

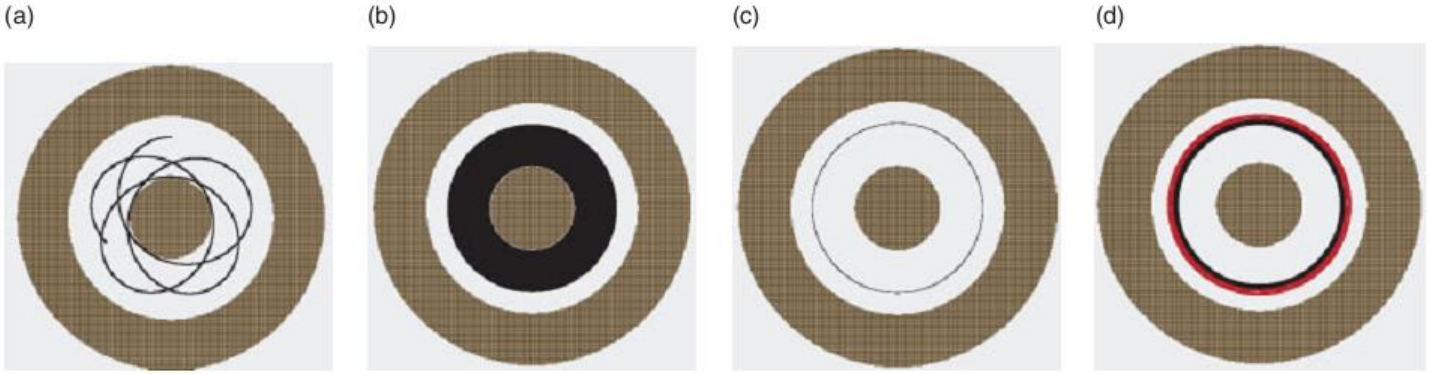

Figure 6. Matching of incoming ion kinetic energy to the radial component of the Orbitrap electric potential. Ion trajectories are shown for $z = 0$. (a) Incoming ion kinetic energy poorly matched to the radial component of the electric field, resulting in a highly eccentric, non-circular orbit. A few periods of the orbit, showing the rapid precession of perigee, are shown. (Trajectory trace line thickened to aid visibility). (b) Same incoming ion kinetic energy as in (a) but with hundreds of periods shown. Because of the large eccentricity and precession of the orbit, the locus of orbits appears as a 'fat doughnut'. (c) Ion kinetic energy (1620 eV) well matched to radial component of the electric field. This orbit is nearly circular, resulting in a locus of orbits that appears as a thin ring. Thousands of periods are shown superimposed and a thin trajectory trace line used. (d) Locus of orbits of two ion kinetic energies, 1570 and 1670 eV. Nearly circular orbits demonstrate the kinetic energy acceptance range of the Orbitrap.

J. Mass Spectrom. 2005; **40**: 430–443

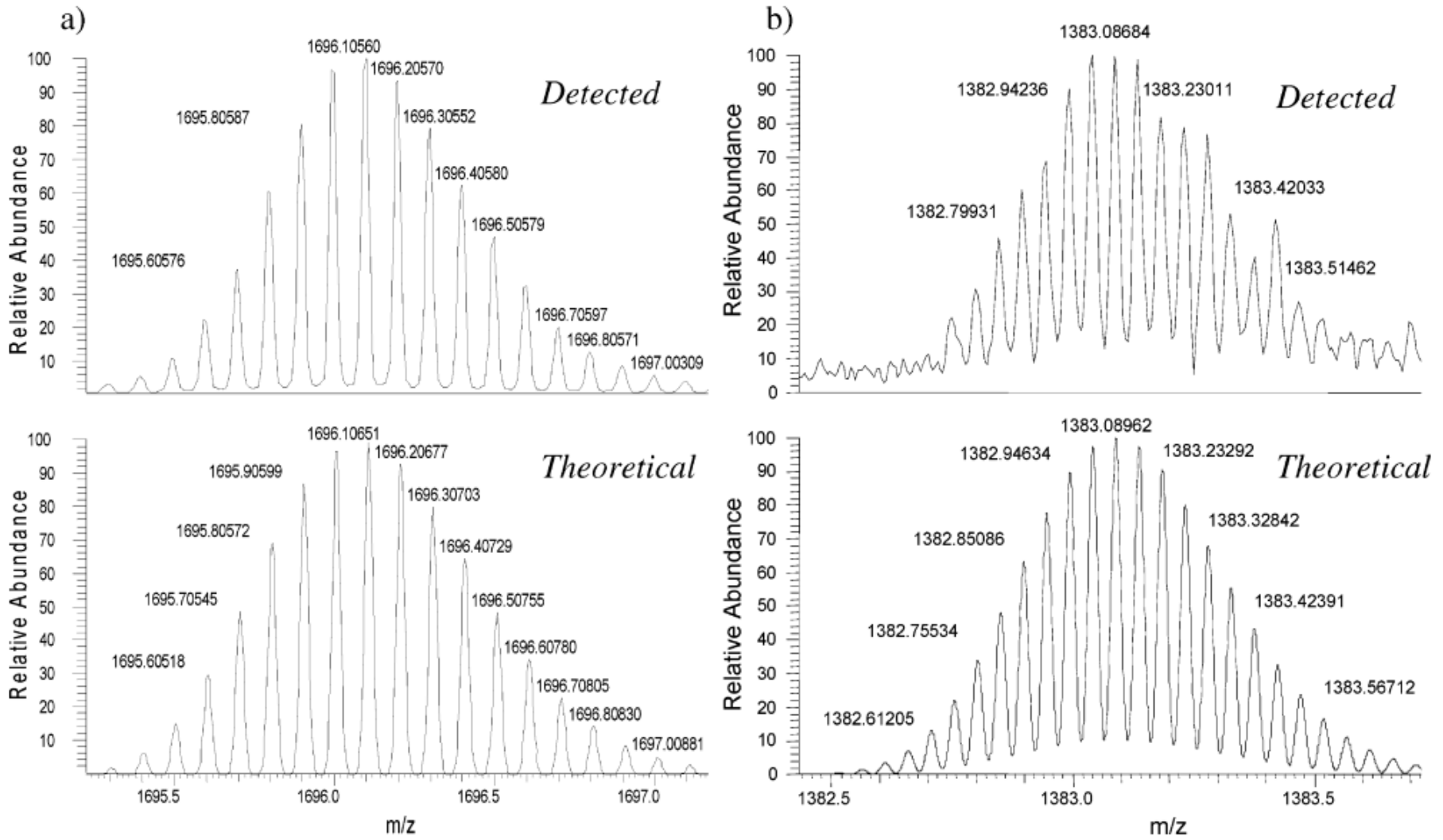

Figure 3. Measured and theoretical isotope distributions of proteins at setting $R = 100\,000$ (100 scans averaged, external calibration): (a) horse heart apomyoglobin, $m = 16\,940.965$ Da (monoisotopic, neutral), $z = +10$; (b) carbonic anhydrase, $m = 29\,006.683$ Da (monoisotopic, neutral), $z = +21$.

Thermo Fisher Orbitrap Elite

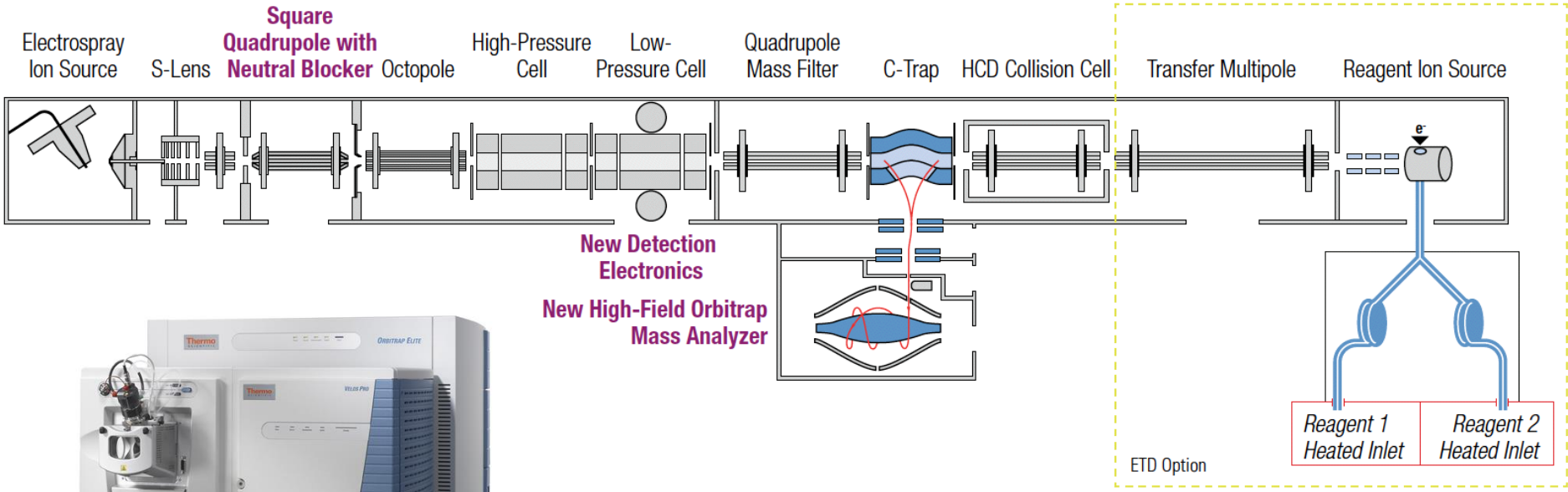

Mass Range

m/z 50 - 2,000, m/z 200 - 4,000

Resolution

60,000 at m/z 400 at a scan (FWHM) rate of 4 Hz

Minimum resolution 15,000

Maximum resolution > 240,000 at m/z 400

Thermo Fisher LTQ Orbitrap XL

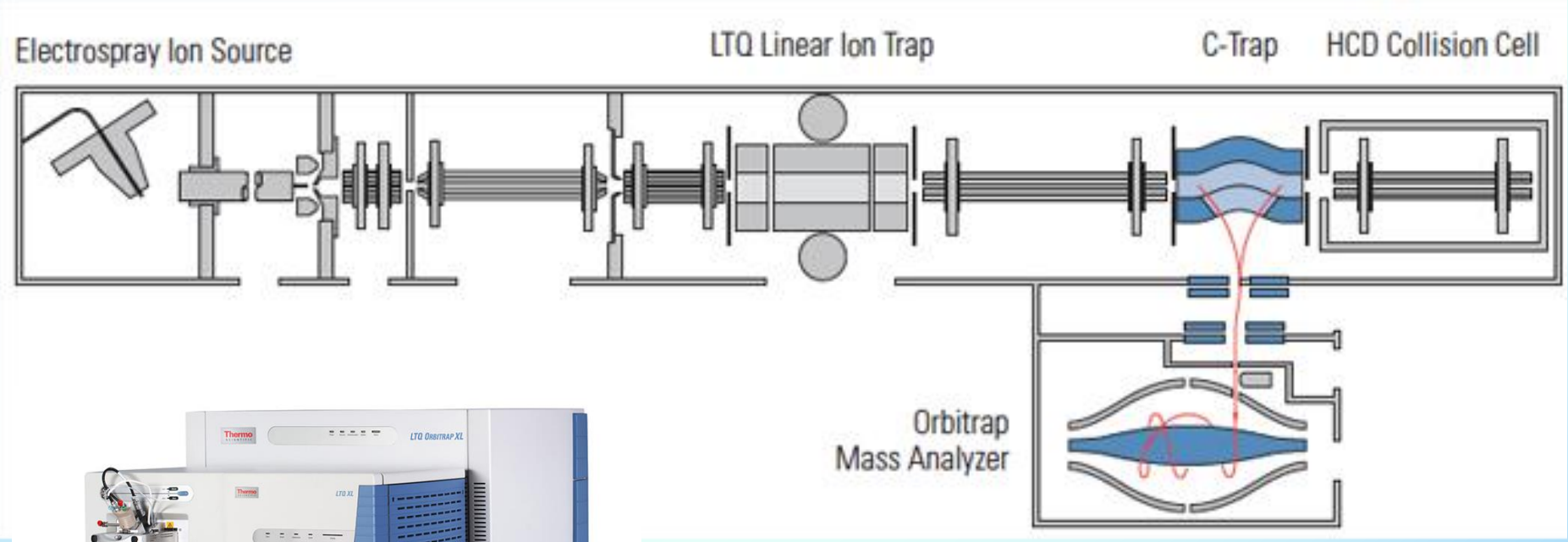

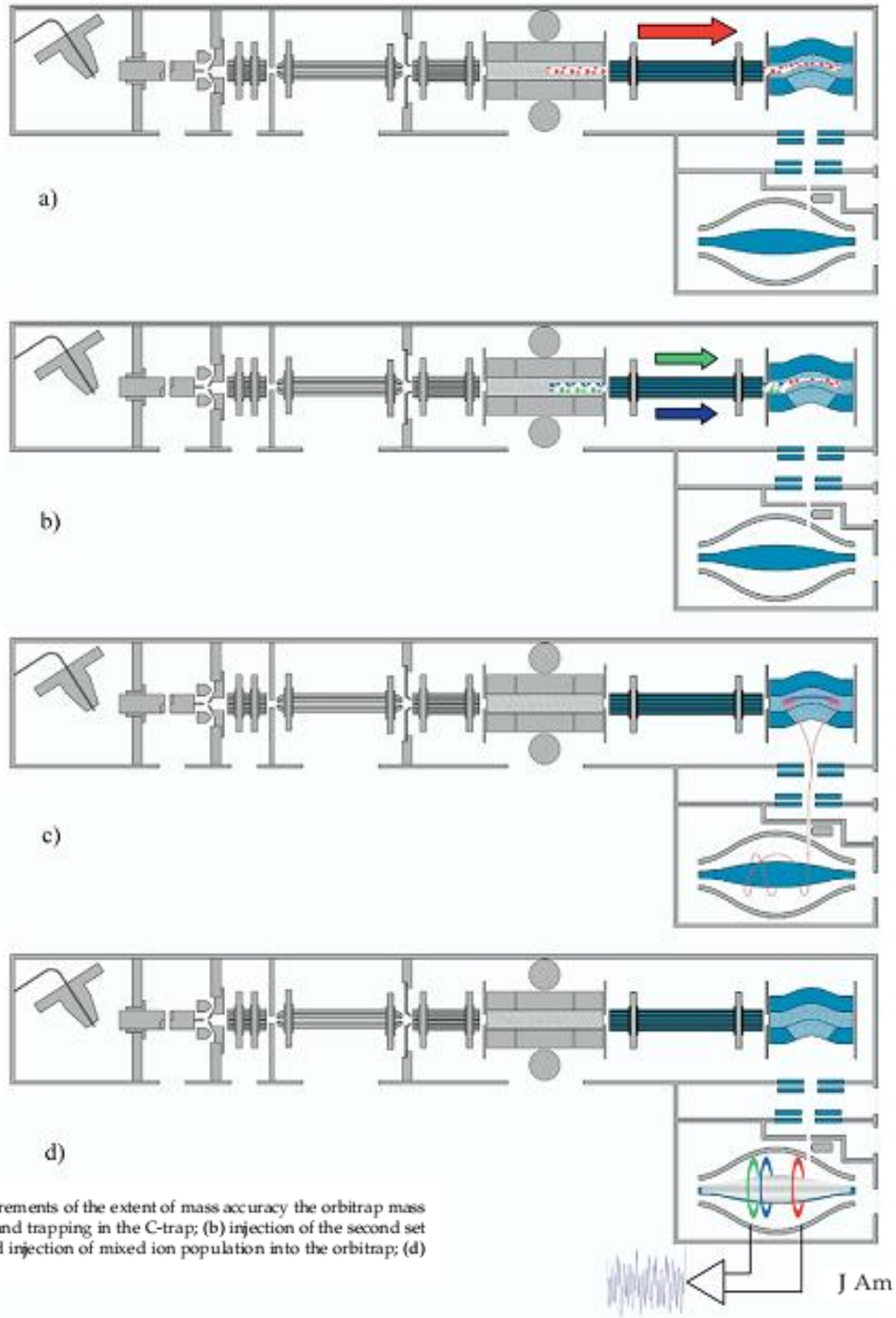

Figure 1. Experimental sequence for measurements of the extent of mass accuracy the orbitrap mass analyzer: (a) Injection of the first set of ions and trapping in the C-trap; (b) injection of the second set of ions and trapping in the C-trap; (c) pulsed injection of mixed ion population into the orbitrap; (d) ion detection in the orbitrap.

J Am Soc Mass Spectrom 2006, 17, 977–982

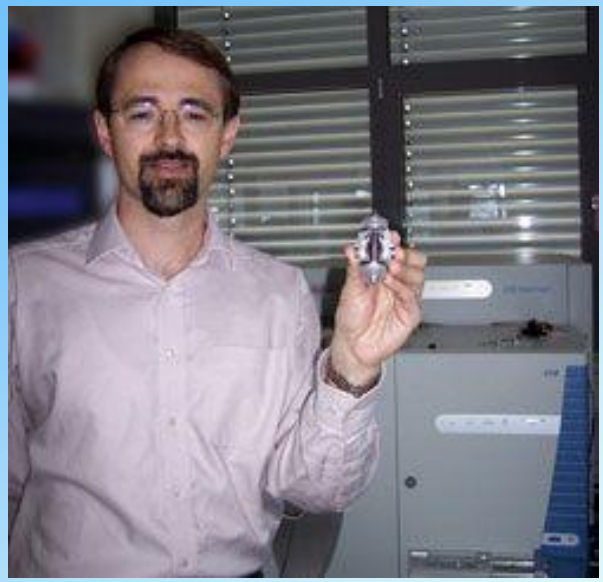

Dr. Alexander Makarov
Thermo Fisher Scientific scientist

Alexander Alexeyevich Makarov is a Russian physicist who led the team that developed the Orbitrap, a type of mass spectrometer.

Early life and education
1989 Moscow Engineering Physics Institute - M.S. Molecular Physics
1993 Moscow Engineering Physics Institute - Ph.D. Physics and Mathematics

Awards
2008 ASMS Distinguished Contribution in Mass Spectrometry Award
2012 Thomson Medal Award

問.
生体分子の質量分析における新技術の発展によって、どのような分野への応用が期待されるのだろうか？あなたが考えていることについて、簡単に述べなさい。

♣ Angiotensin I イオンと気体分子の温度変化によるプロトン移動反応

- S. Nonose et al., *J. Phys. Chem. B*, **118** 9651-9661 (2014).
- S. Nonose, *Mass Spectrometry*, **9**, A0083 (2020).
- 野々瀬真司, J. Mass Spectrom. Soc. Jpn. **70**巻, 51-57頁, 2022年.

孤立した状態において生体分子を研究する

有限な系
構造の揺らぎ
内部エネルギー
最も単純な反応

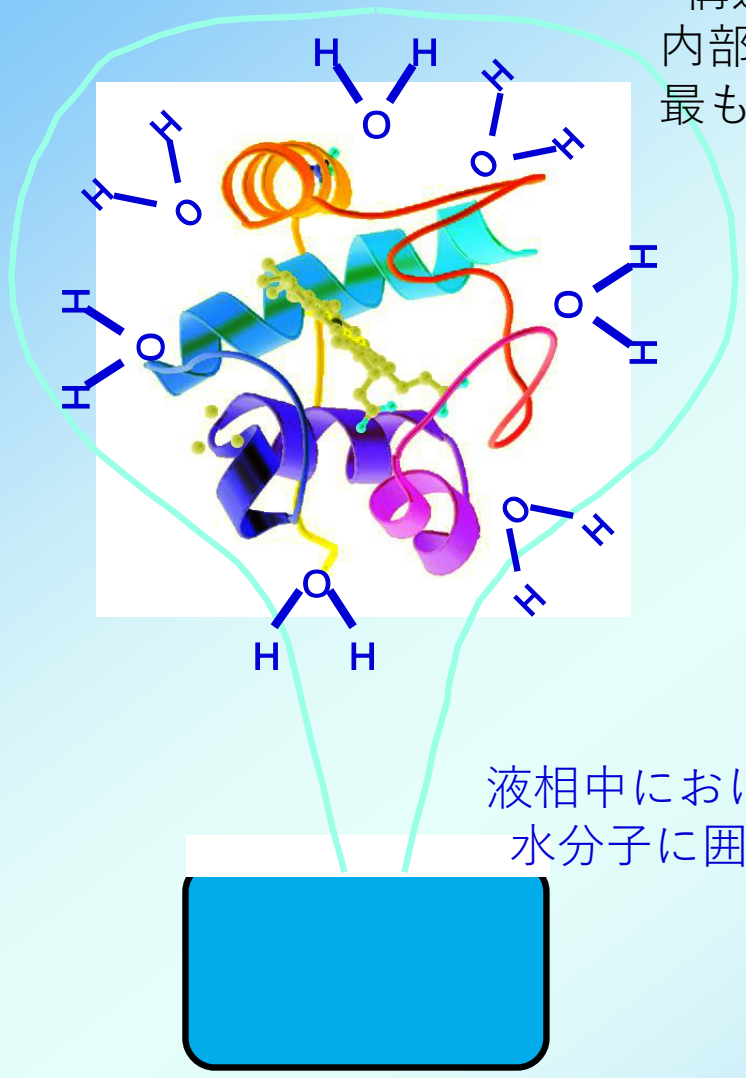

液相中における生体分子
水分子に囲まれている

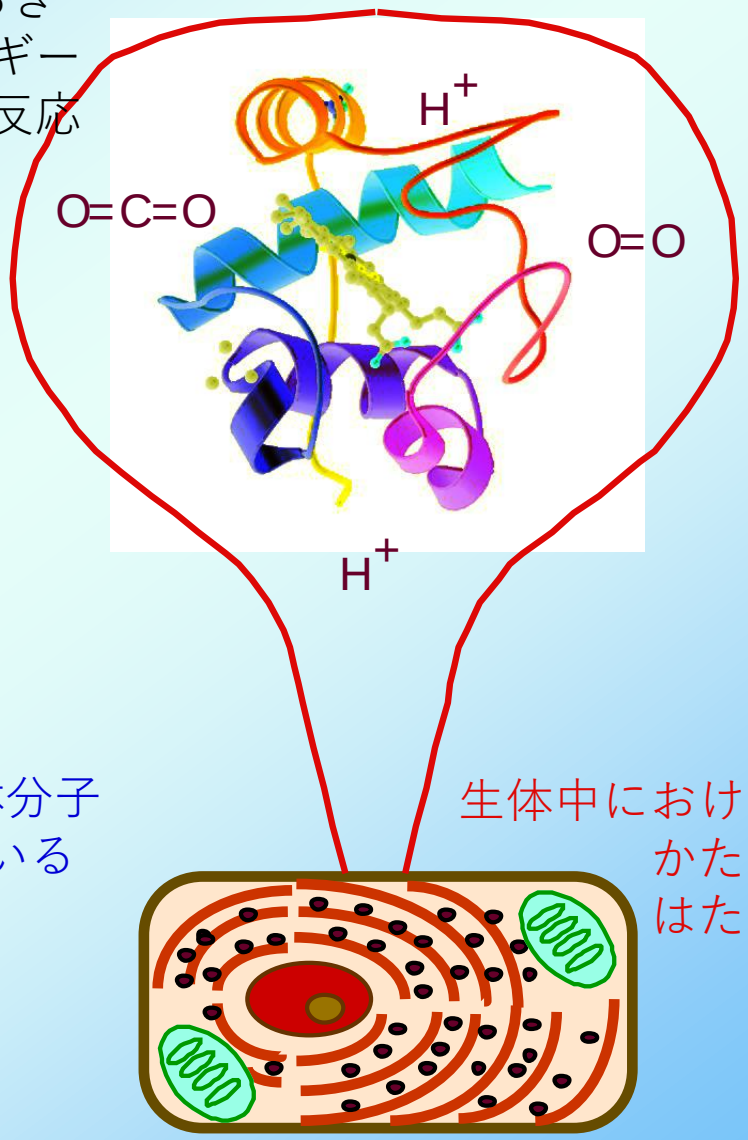

生体中における生体分子
かたち
はたらき

Abstract

- Biological Molecules in Gas Phase → Isolated finite systems
- Electrospray Ionization (ESI) → Non-destructive introduction of biomolecular ions into vacuum
- Production of Multiply-Protonated Biomolecular Ions with ESI

Angiotensin I

- Collisional Reactions of Charge-Selected Ions with Gaseous Molecules

→ Proton transfer from ions to target molecule

→ Measurement of absolute reaction rate and Distribution of product ions

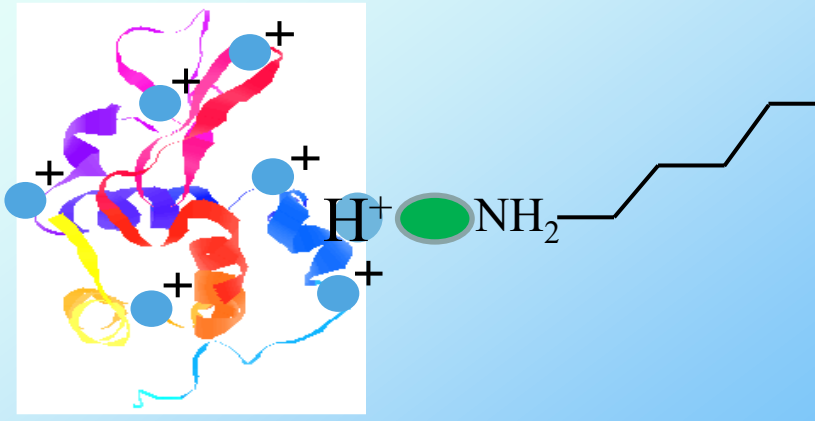

Proton affinity of residues in peptide
Intramolecular coulomb repulsion
Conformation of peptide in gas phase
  Folding vs unfolding
  Self solvation to charges
Charge delocalization

実験方法：気体分子との衝突反応

1.エレクトロスプレーイオン化法
によって真空中に
蛋白質イオンを生成

2.特定の電荷数
のイオンを選別

3.気体分子との
衝突反応

4. 反応生成物
を分析・検出

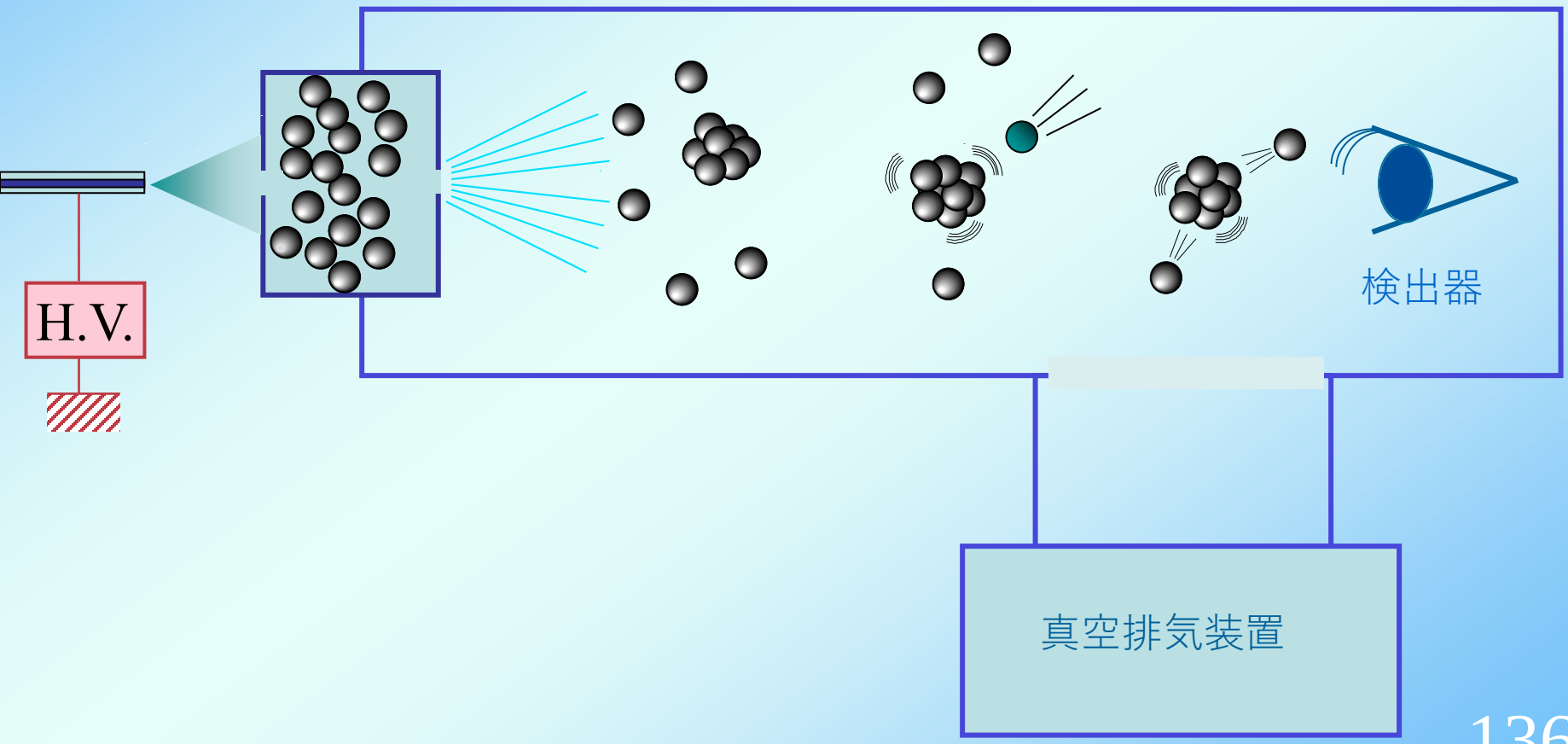

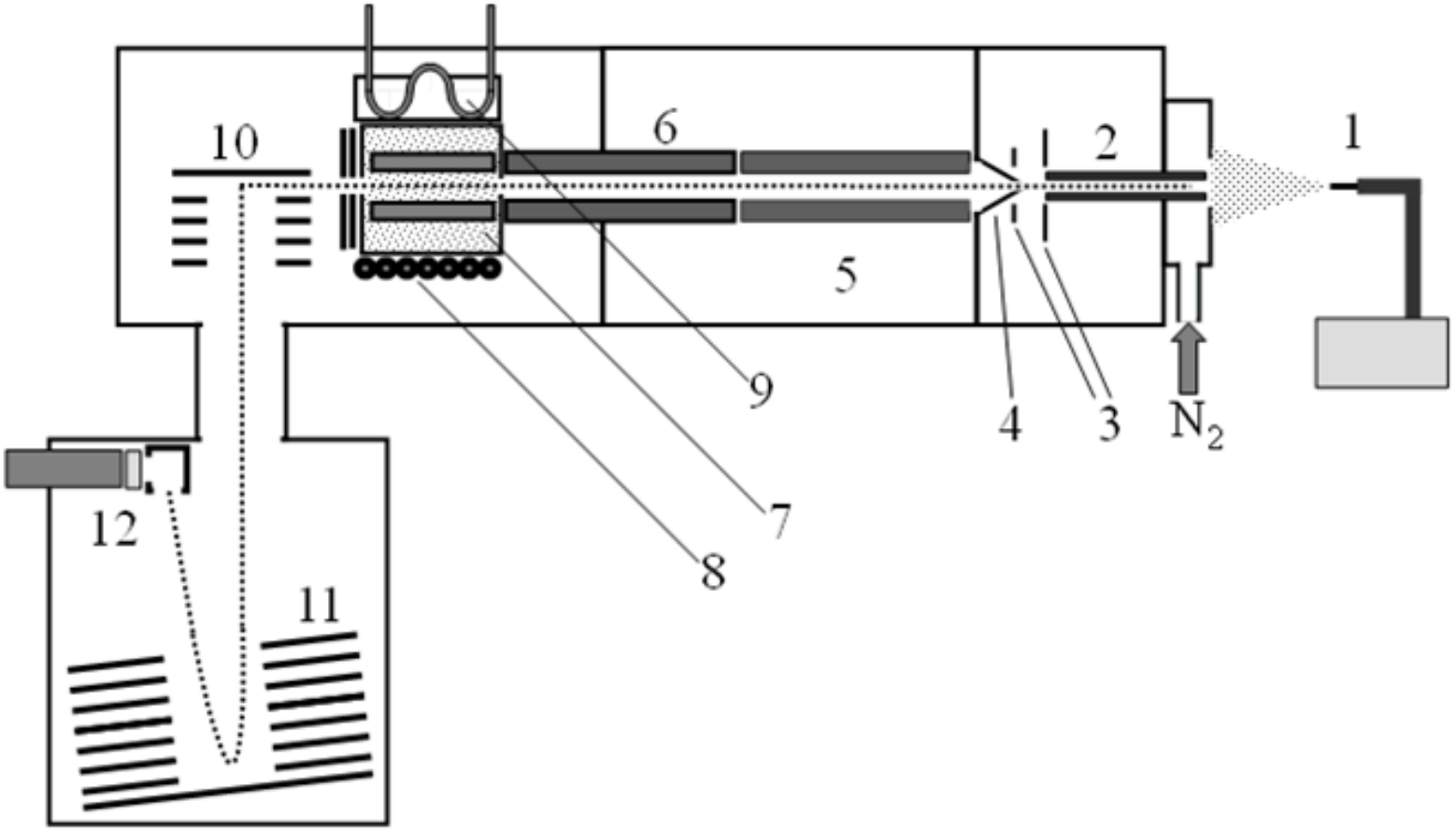

ESI源を備えたタンデム質量分析計の模式図。(1)エレクトロスプレーニードル、(2)ステンレスキャピラリー、(3)イオン光学系、(4)スキマー、(5)四重極イオンビームガイド、(6)四重極質量分析計、(7)八重極イオントラップ付きガスセル、(8)マイクロセラミックヒーター、(9)冷却器、(10)飛行時間型質量分析計用プッシャー、(11)リフレクトロン、(12)Daly検出器。

Angiotensin I の分子構造

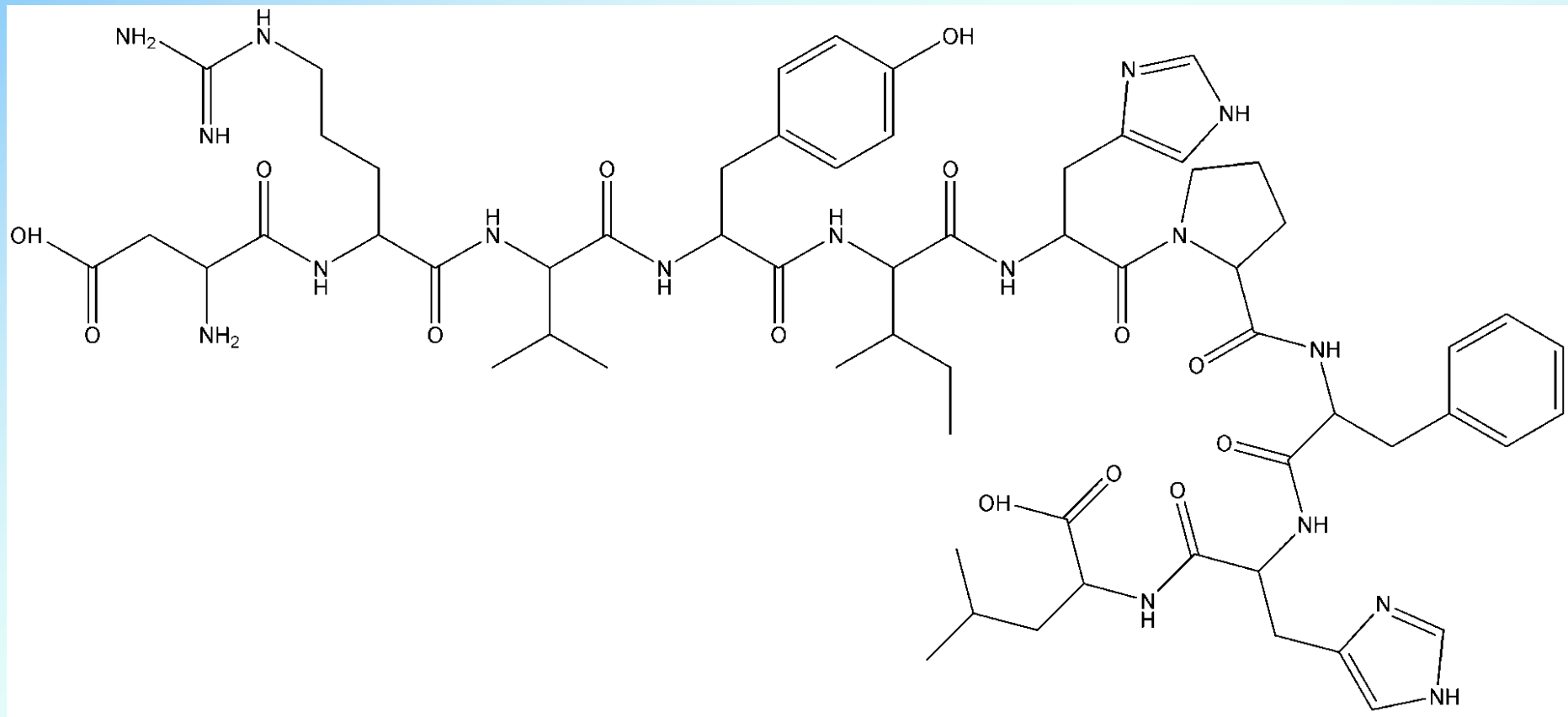

List of Target Molecules (Tm)

Proton Affinity: PA

Primary amines

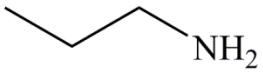

1-Propylamine (1-Pr)
(PA:917.8 [kJ/mol])

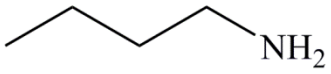

1-Butylamine (1-Bu)
(PA:921.5 [kJ/mol])

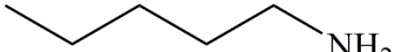

1-Pentylamine (1-Pe)
(PA:923.5 [kJ/mol])

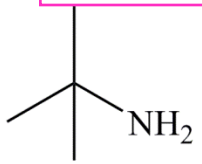

tert-Butylamine (t-Bu)
(PA:934.1 [kJ/mol])

Secondary amines

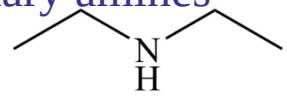

Diethylamine (Det)
(PA:952.4 [kJ/mol])

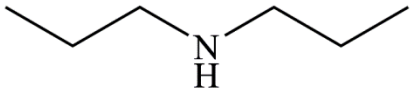

Dipropylamine (Dpr)
(PA:962.3[kJ/mol])

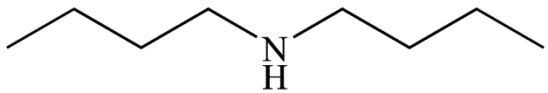

Dibutylamine (Dbu)
(PA:968.5[kJ/mol])

Aromatic amines

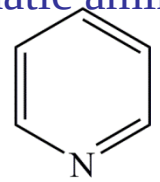

Pyridine (Py)
(PA:930.0[kJ/mol])

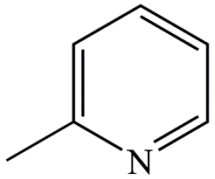

2-Methylpyridine (Mpy)
(PA:949.1[kJ/mol])

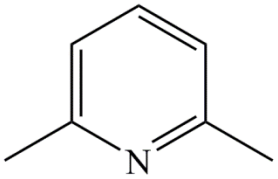

2,6-Dimethylpyridine (26Dmpy)
(PA:963.0[kJ/mol])

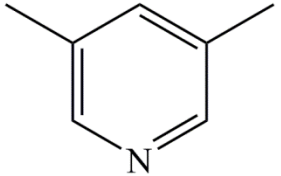

3,5-Dimethylpyridine (35Dmpy)
(PA:955.4[kJ/mol])

Diamines

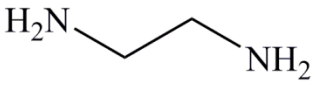

Ethylenediamine (Eda)
(PA:951.6[kJ/mol])

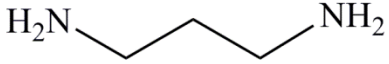

1,3-Propanediamine (Pda)
(PA:987.0[kJ/mol])

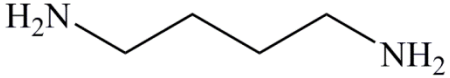

1,4-Butanediamine (Bda)
(PA:1005.6[kJ/mol])

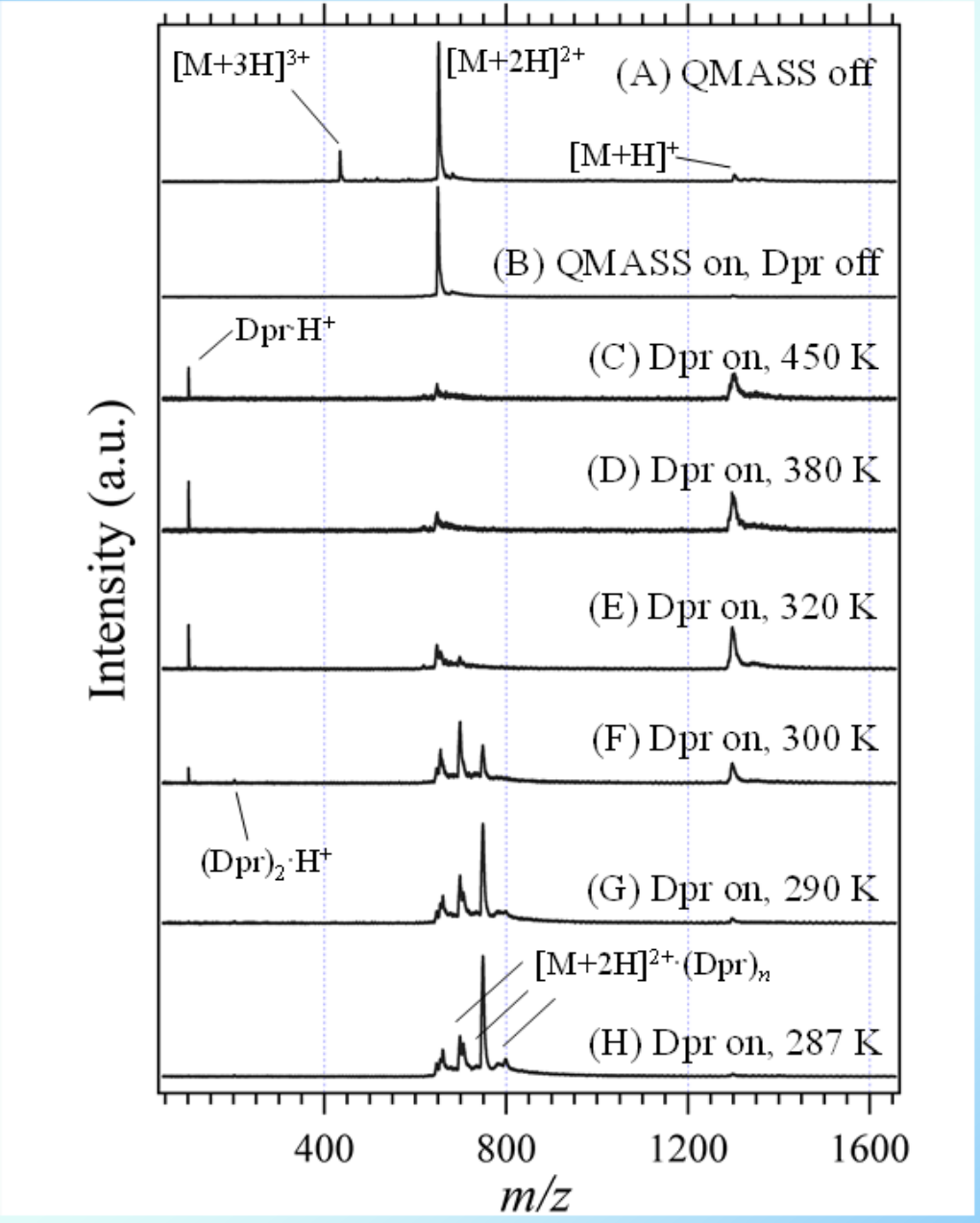

電荷数２のangiotensin Iイオン、$[M + 2H]^{2+}$、とDprとのプロトン移動反応の温度依存性に関する質量スペクトル。

Reaction Rate Constants of Angiotensin I(2+) with Secondary Amines

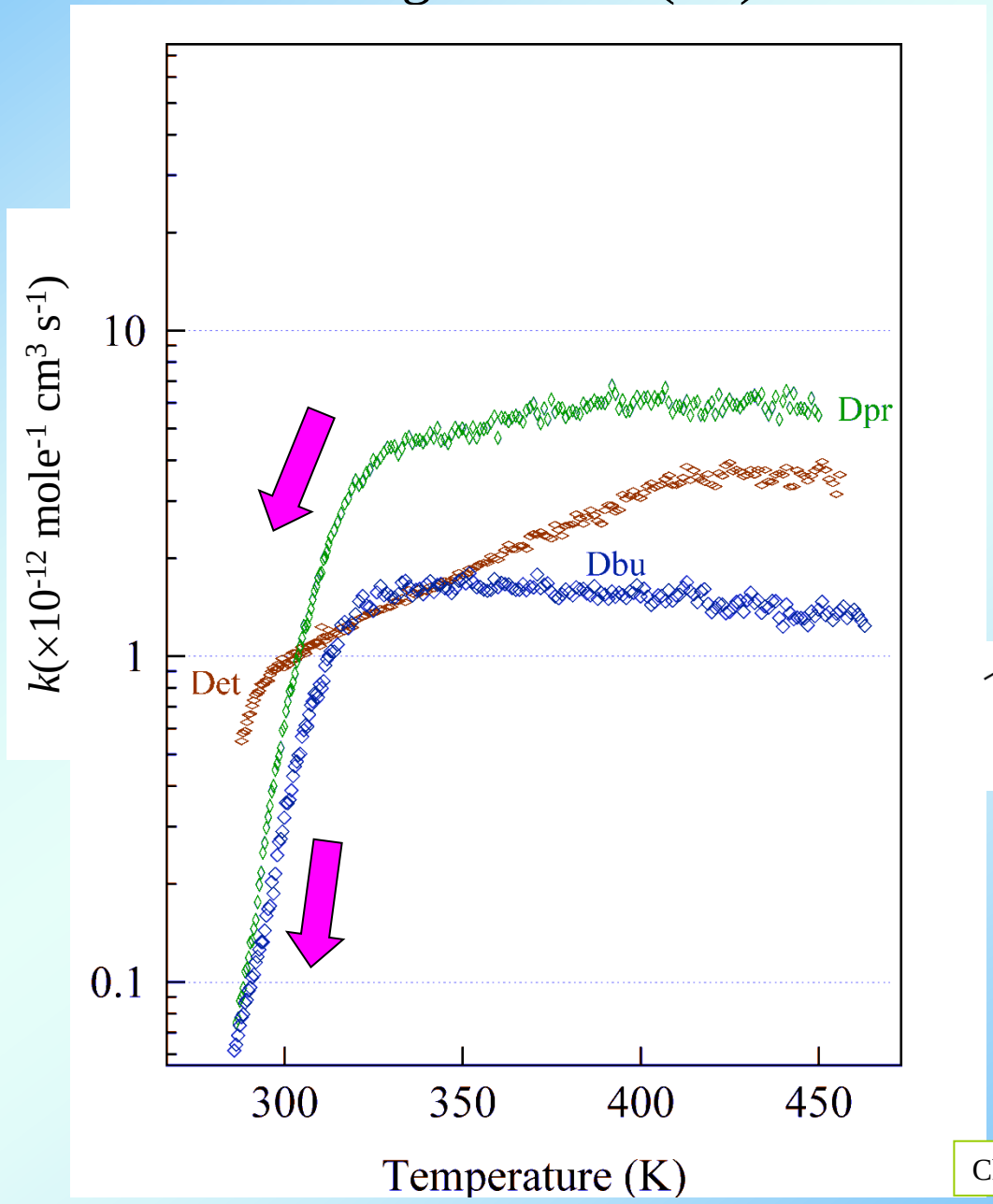

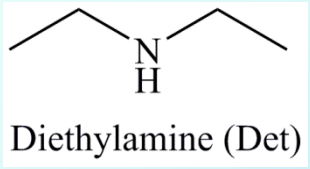

Diethylamine (Det)

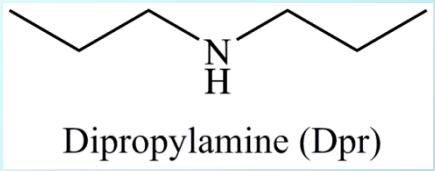

Dipropylamine (Dpr)

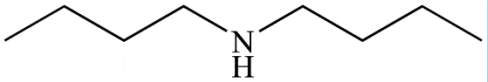

Dibutylamine (Dbu)

Chem. Phys., **423** 182–191 (2013).

Conformations Related to Internal Energy

Folding with decrease of energy

High energy
Extended conformation

Low energy
Compact conformation

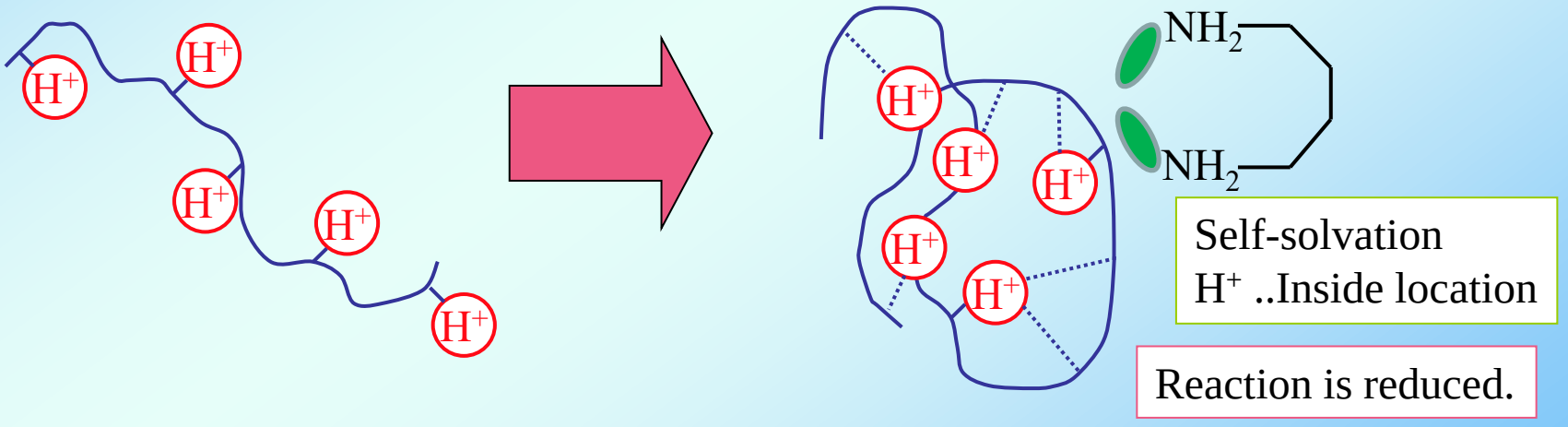

Self-solvation
H^+ ..Inside location

Reaction is reduced.

Reaction Rate Constants of Angiotensin I(2+) with Aromatic Amines

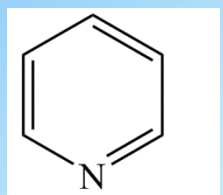

Pyridine (Py)

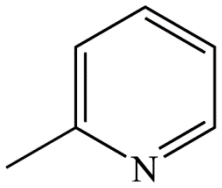

2-Methylpyridine (Mpy)

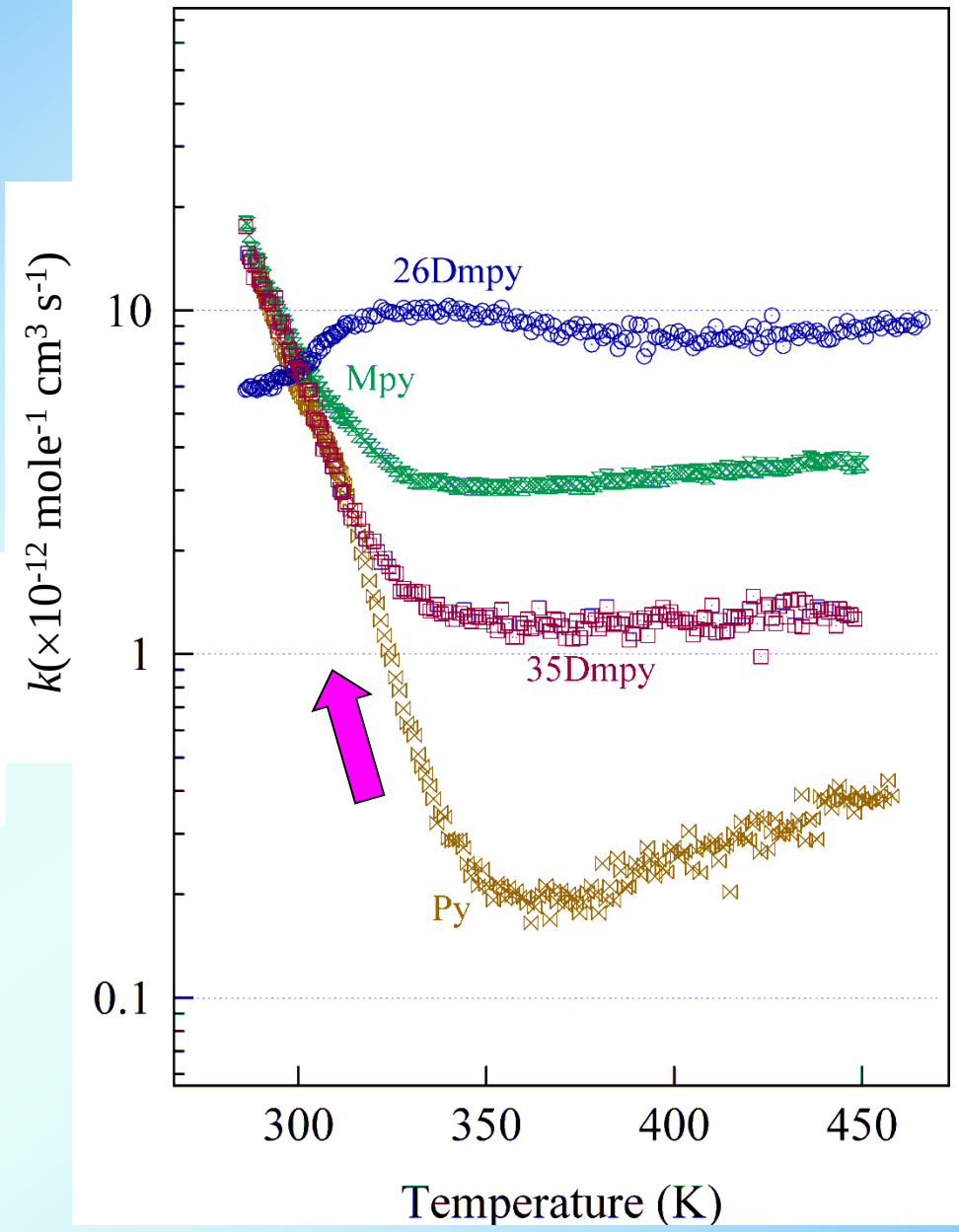

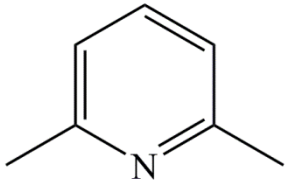

2,6-Dimethylpyridine (26Dmpy)

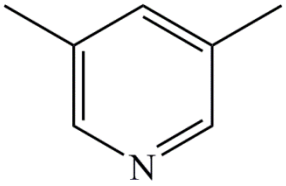

3,5-Dimethylpyridine (35Dmpy)

Chem. Phys., **423** 182–191 (2013).

Conformations Related to Internal Energy

Folding with decrease of energy

High energy
Extended conformation

Low energy
Compact conformation

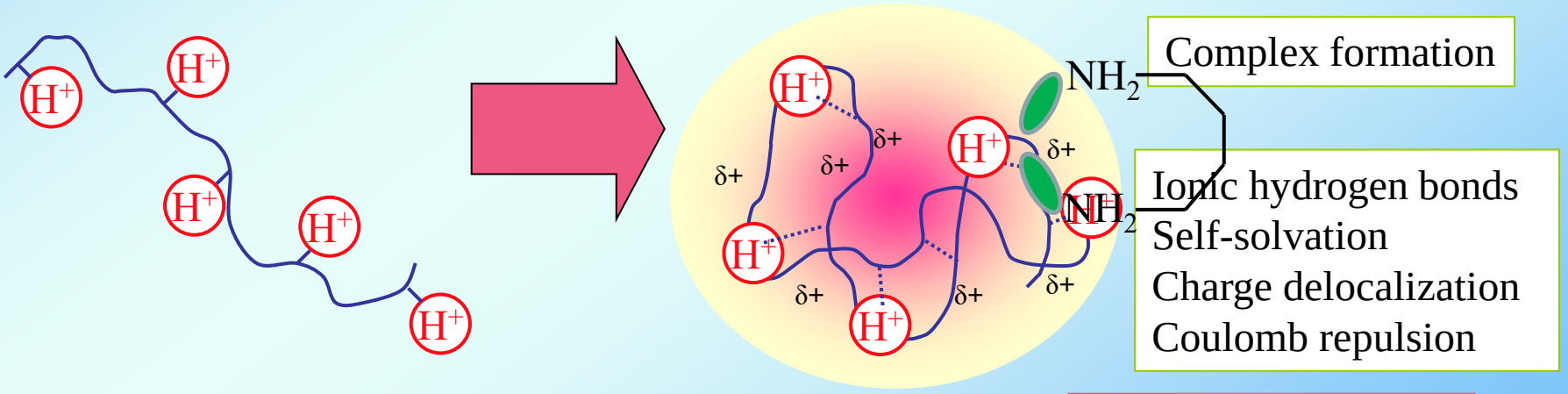

Complex formation

Ionic hydrogen bonds
Self-solvation
Charge delocalization
Coulomb repulsion

Reaction is enhanced.

26Dmpy

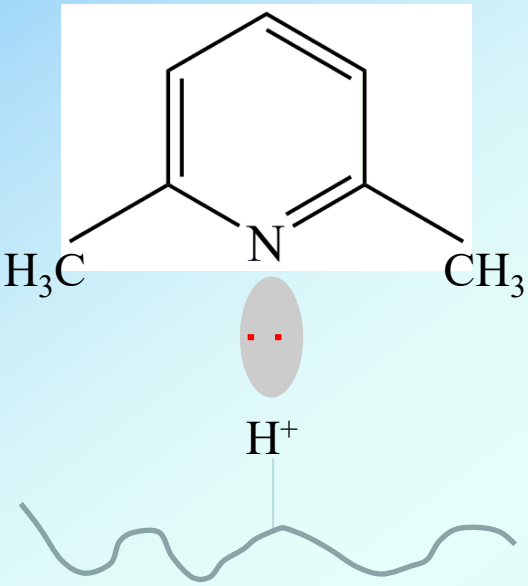

35Dmpy

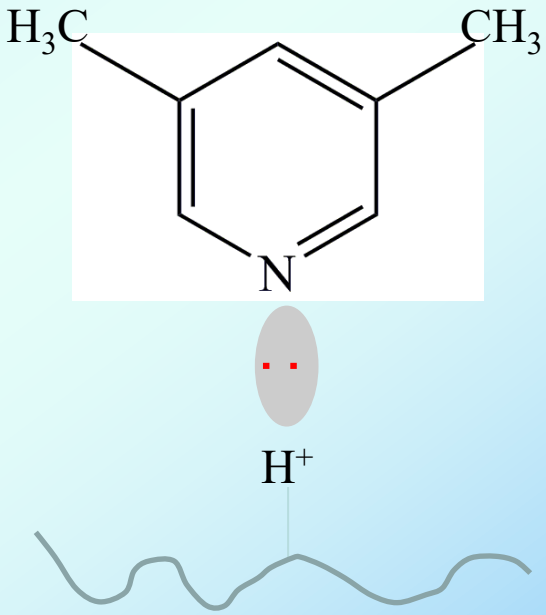

Steric hindrance at methyl groups

Reaction Rate Constants of Angiotensin I(2+) with 1-Bu

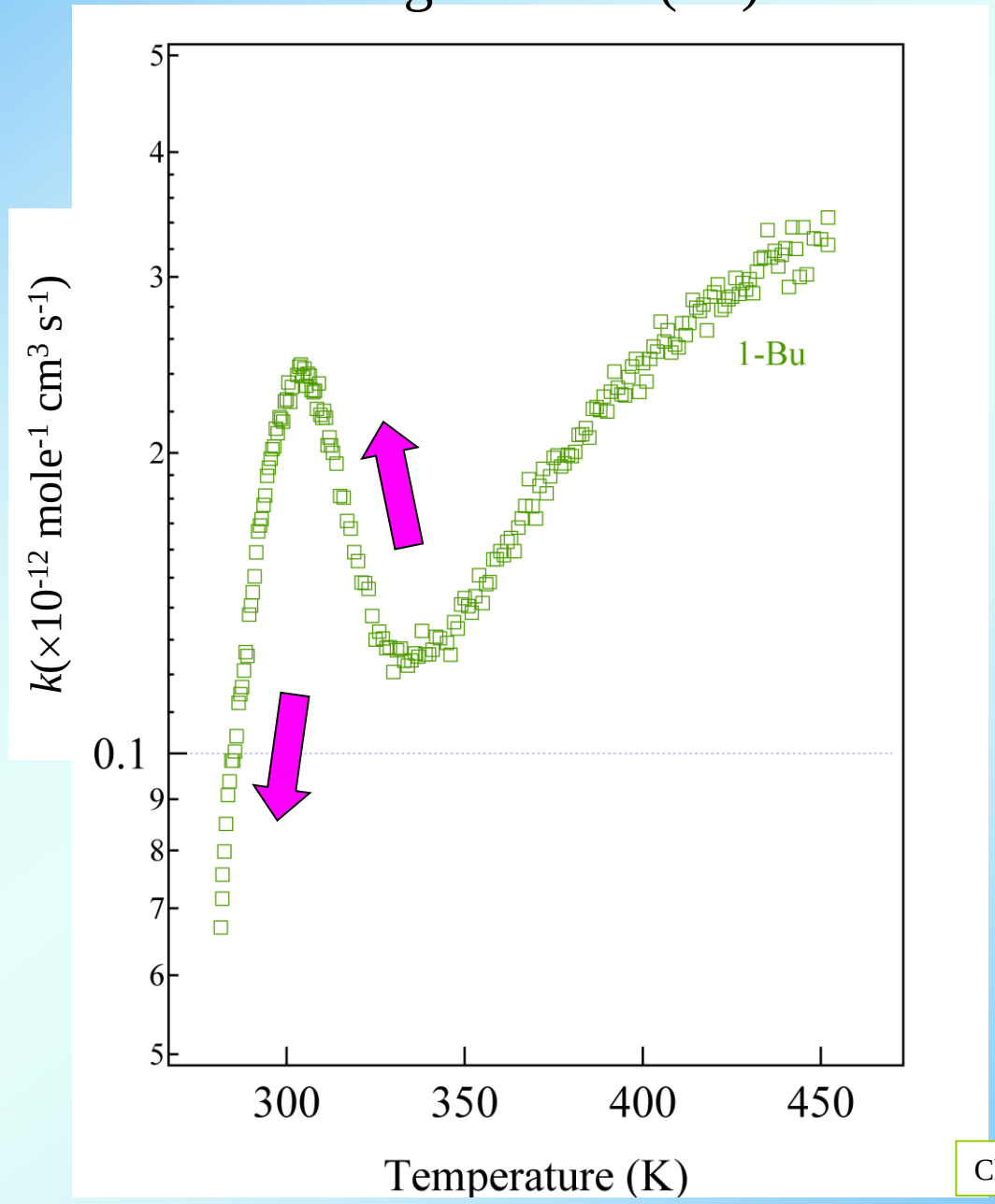

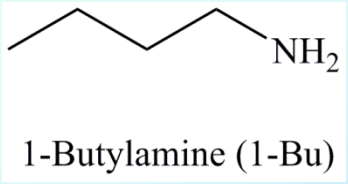

Chem. Phys., **423** 182–191 (2013).

Reaction Rate Constants of Angiotensin I(2+) with Primary Amines

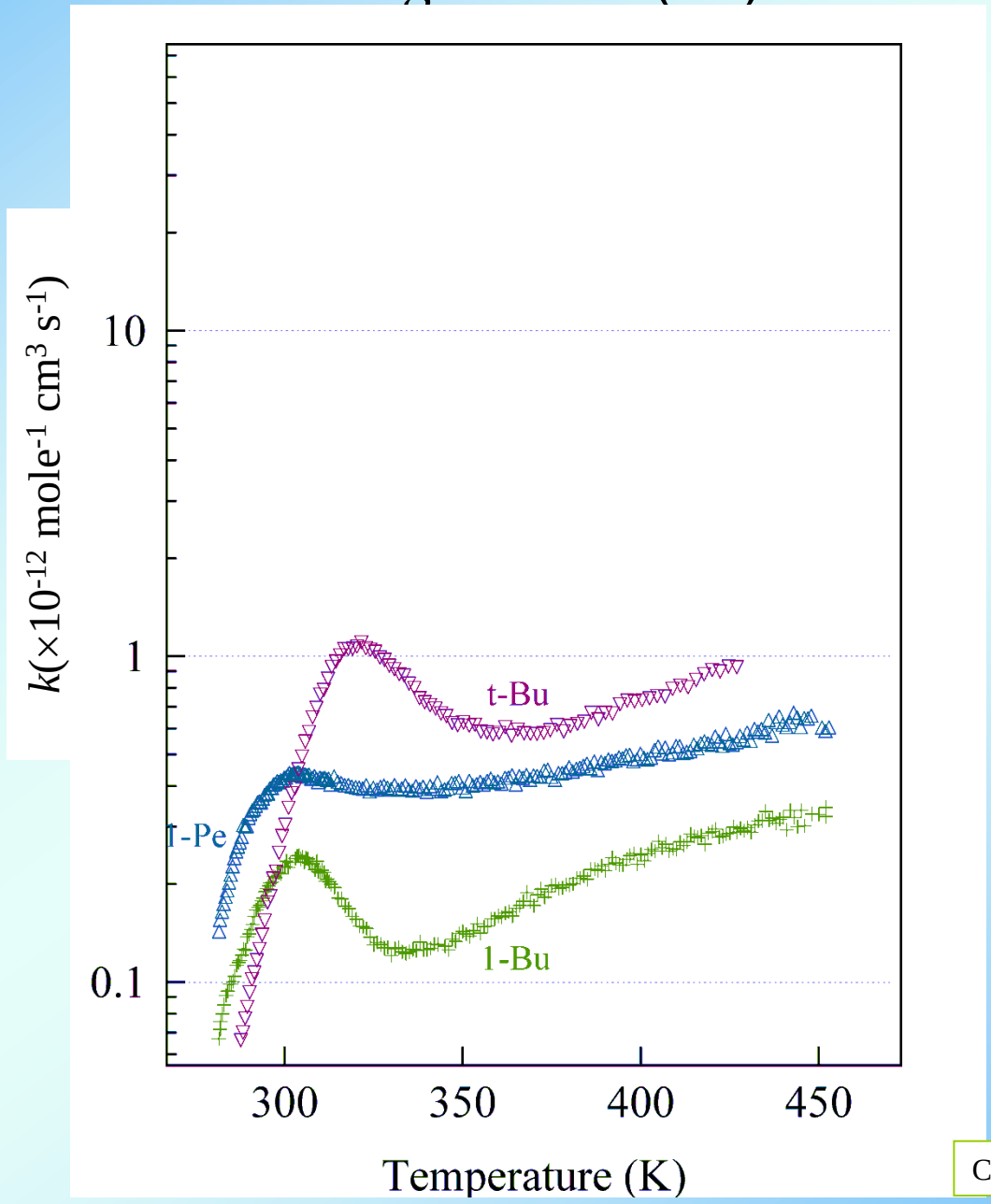

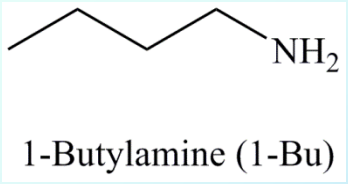

1-Butylamine (1-Bu)

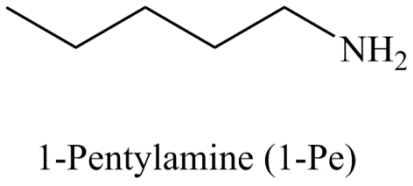

1-Pentylamine (1-Pe)

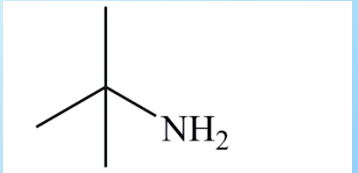

tert-Butylamine (t-Bu)

Chem. Phys., **423** 182–191 (2013).

Reaction Rate Constants of Angiotensin I (2+) with Diamines

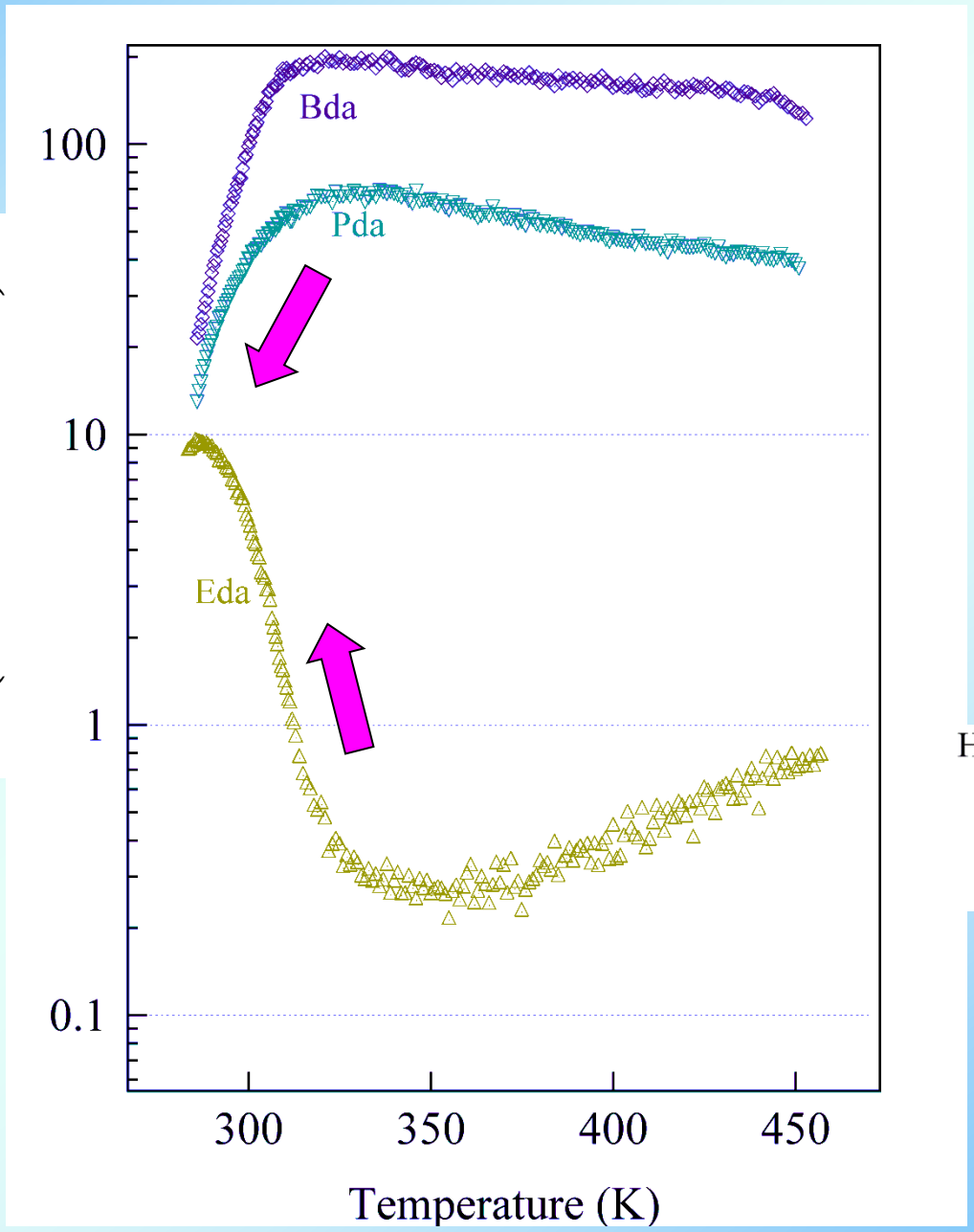

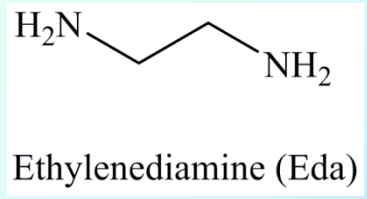

Ethylenediamine (Eda)

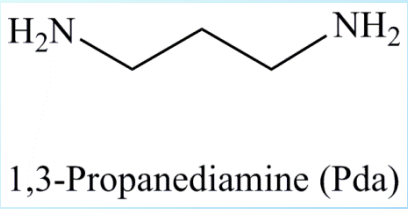

1,3-Propanediamine (Pda)

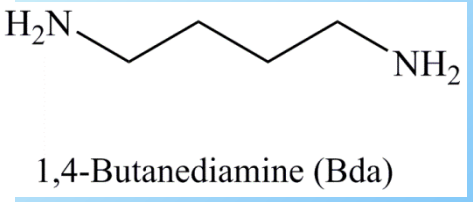

1,4-Butanediamine (Bda)

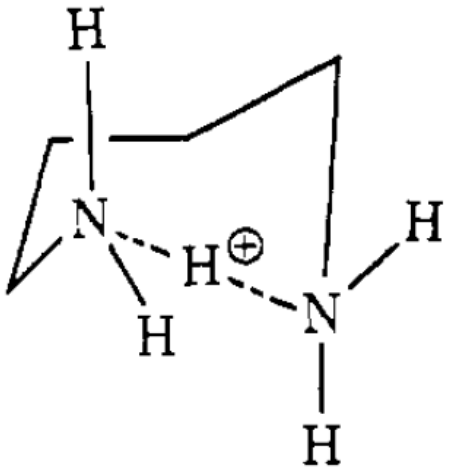

1

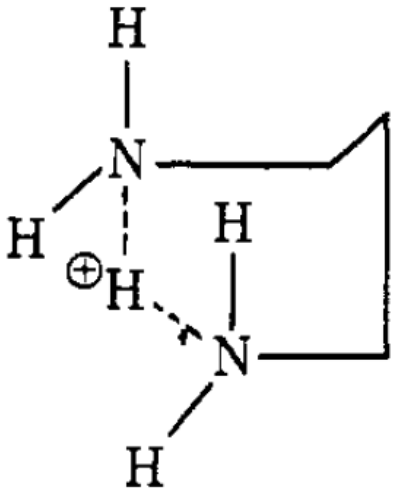

2

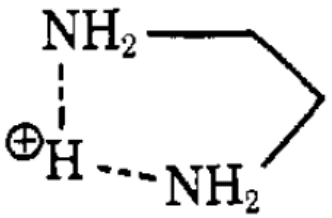

3

Table I. Gas-Phase Basicities of Diaminoalkanes[a]

	Compound	GB,[b] $-\Delta G°_{prot}$(g)	$-T\Delta S°_{prot}$[c]	PA,[b] $-\Delta H°_{prot}$(g)	$-\Delta H°_{ring\ form}$
3	$NH_2CH_2CH_2NH_2$	220.2	11.8	232.0	>9.7
	$NH_2CH_2CH_2CH_3$	213.7	8.6	222.3	
2	$NH_2CH_2CH_2CH_2NH_2$	225.7	12.6	238.3	>15.5
	$NH_2CH_2CH_2CH_2CH_3$	214.3	8.6	222.8	
1	$NH_2CH_2CH_2CH_2CH_2NH_2$	228.3	15.0	243.3	20.2
	$NH_2CH_2CH_2CH_2CH_2CH_3$	214.6	8.6	223.1	
	$NH_2CH_2CH_2CH_2CH_2CH_2NH_2$	226.6	14.7	241.3	18.1
	$NH_2CH_2CH_2CH_2CH_2CH_2CH_3$	214.7	8.6	223.2	
	$NH_2CH_2CH_2CH_2CH_2CH_2CH_2NH_2$	226.6	15.5	242.1	18.8
	$NH_2CH_2CH_2CH_2CH_2CH_2CH_2CH_3$	214.8	8.6	223.2	
	$CH_3OCH_2CH_2NH_2$	215.9	11.8	227.7	>4.9
	Morpholine	215.2	8.3	223.5	
	Piperidine	222.0	8.3	230.3	
	Piperazine	220	8.3	228	

[a] All values in kcal/mol. [b] Relative GB's are ±0.2 kcal/mol by multiple overlap of $\Delta G°$'s. [c] $T\Delta S$ term includes the entropy of free proton, the entropy from symmetry change, and the entropy of ring closure approximately estimated from the alkane ⇄ cycloalkane equilibrium for analogous hydrocarbons: D. R. Stull, E. F. Westrum, Jr., and G. C. Sinke, "The Chemical Thermodynamics of Organic Compounds," Wiley, New York, N. Y., 1969. T = 298 °K.

K. B. Sharpless, R. F. Lauer, J. Am. Chem. Soc., **95**, 2699 (1973).

Eda

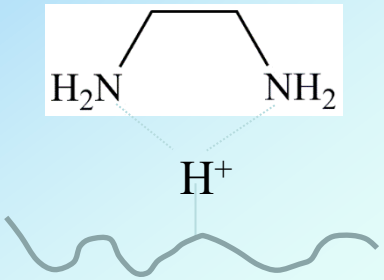

Pda

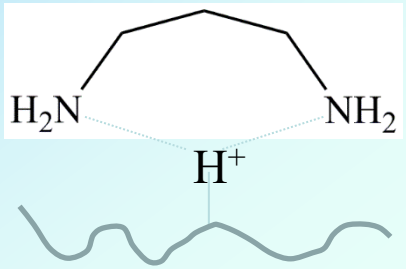

Nearly linear hydrogen bonds
can be accommodated in a ring.

Bda

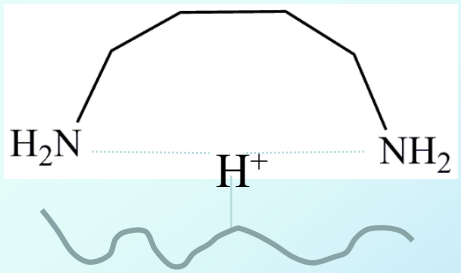

Linear hydrogen bonds
can be accommodated in a ring.

Proton Transfer of Angiotensin I Ion (2+) Reacted with Butanediamine (Bda) at Various Reaction Time

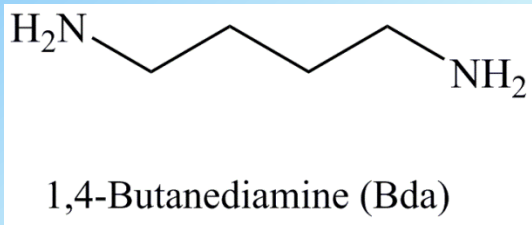

1,4-Butanediamine (Bda)

Reaction temperature; 288 (K)
Reaction time; 1 - 87 (ms)
Molecular density of Bda;
2.6×10^{11} (molecule cm^{-3})

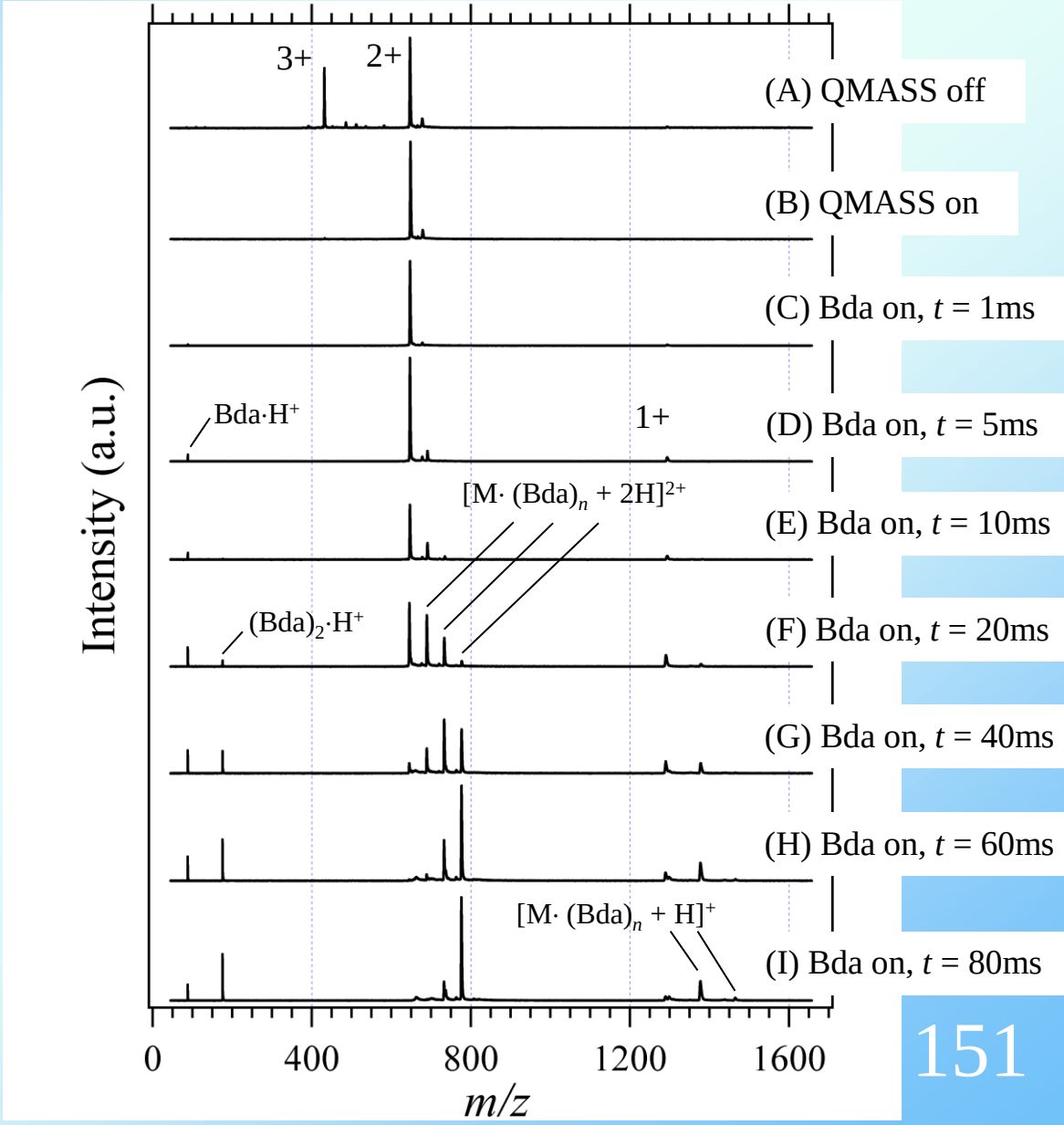

Branching Fractions of Angiotensin I Ion (2+) Reacted with Butanediamine (Bda) at Various Reaction Time

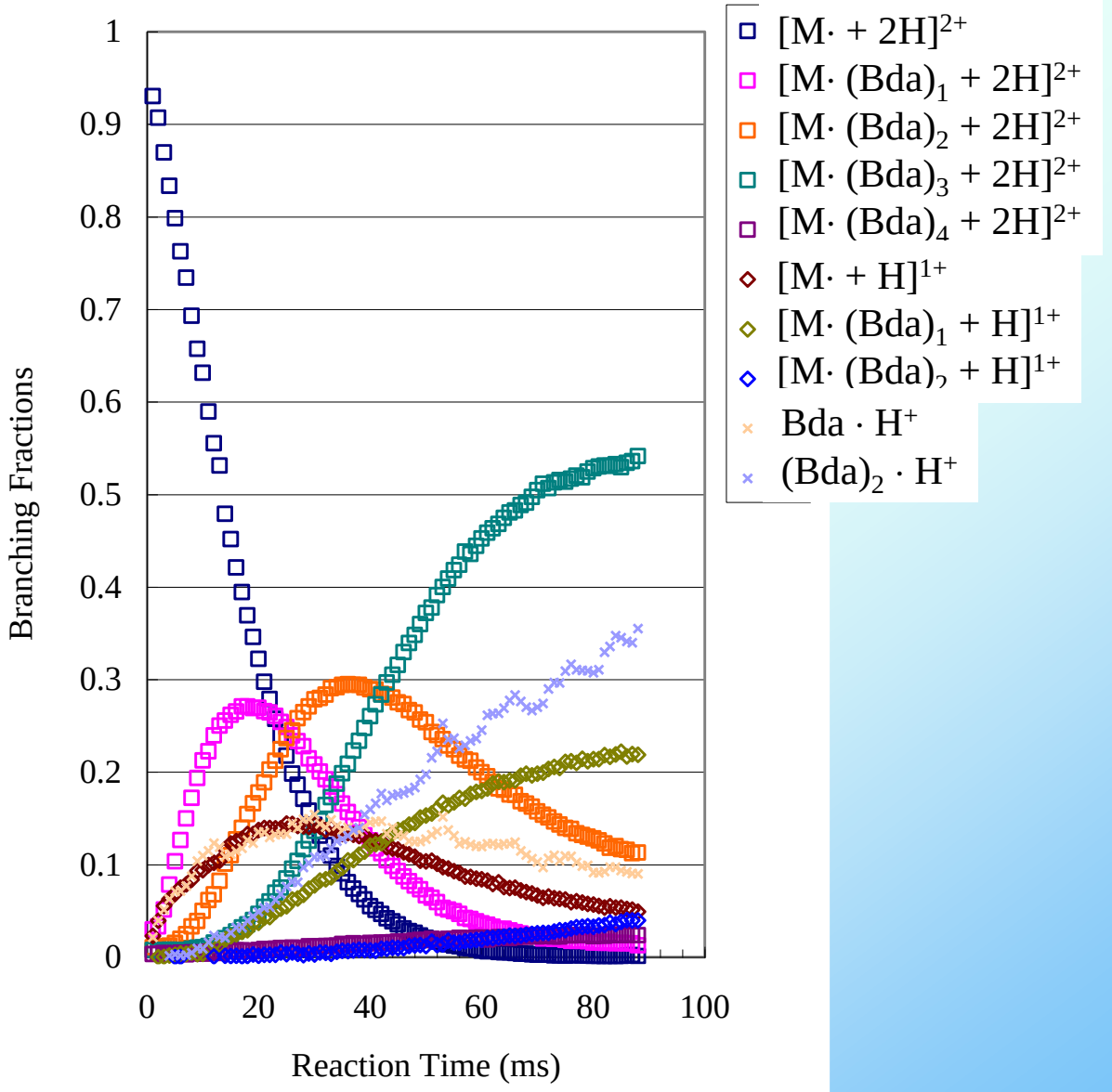

Reaction Kinetics of Proton Transfer

Two-step process by way of long-lived complex formation

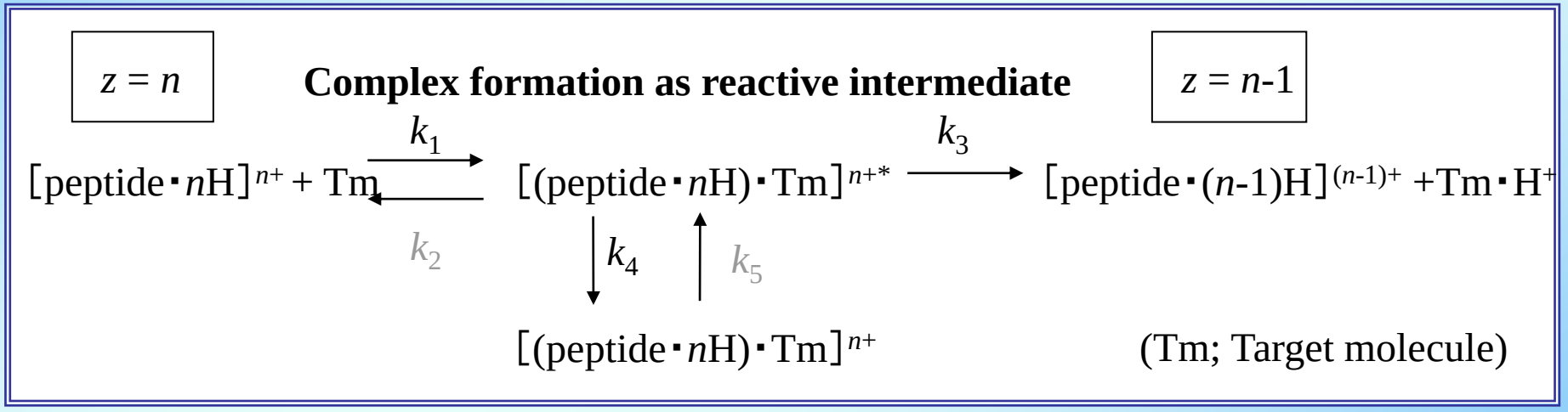

$$-\frac{d[\mathrm{A}]}{dt} = k'[\mathrm{B}][\mathrm{A}] = k[\mathrm{A}]$$

$$(k'[\mathrm{B}] = k)$$

$$\frac{d[\mathrm{A}]}{[\mathrm{A}]} = -k\,dt$$

$$\int_{[\mathrm{A}_0]}^{[\mathrm{A}]} \frac{d[\mathrm{A}]}{[\mathrm{A}]} = -k\int_0^t dt$$

$$\ln\frac{[\mathrm{A}]}{[\mathrm{A}_0]} = -kt$$

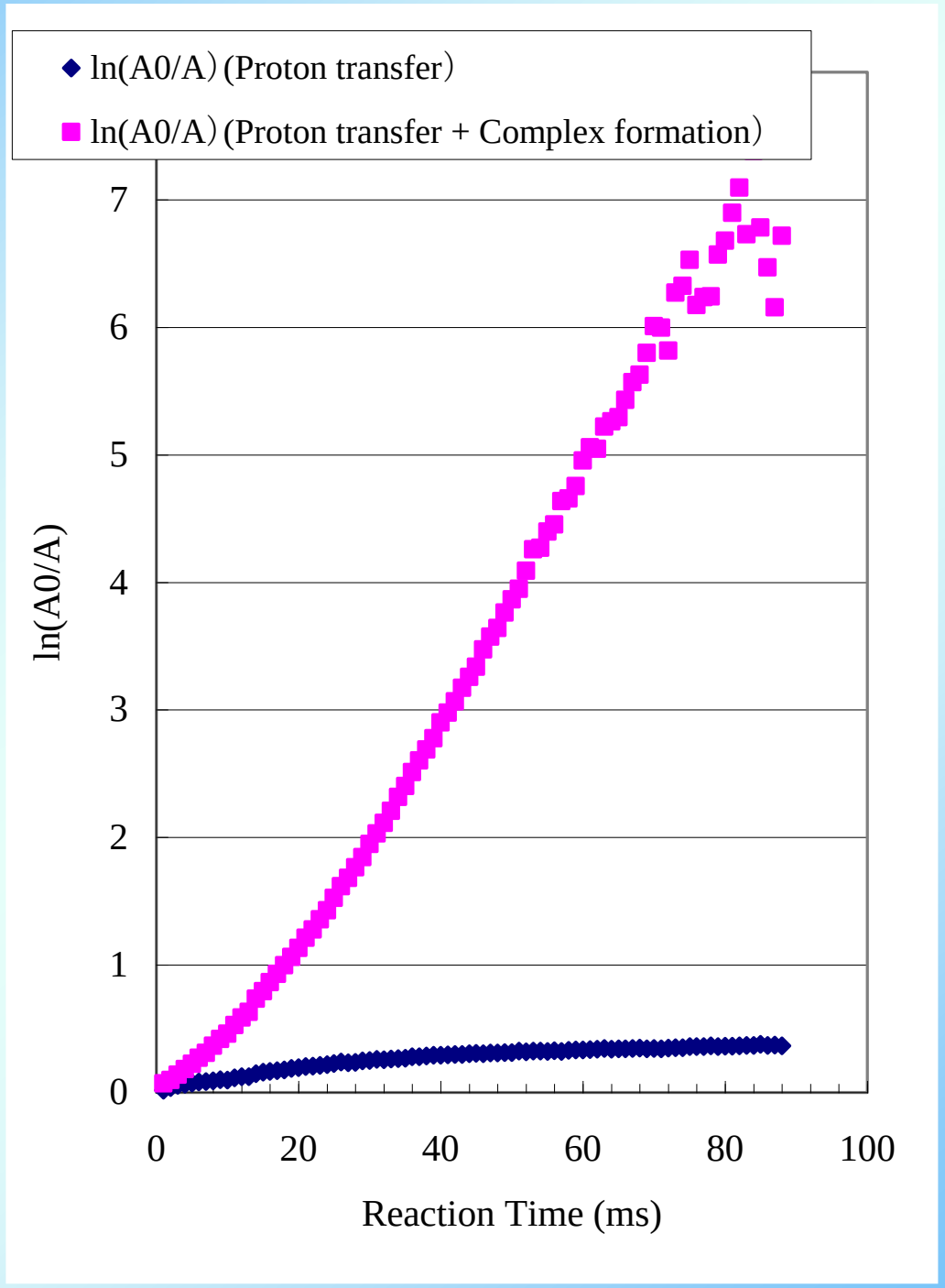

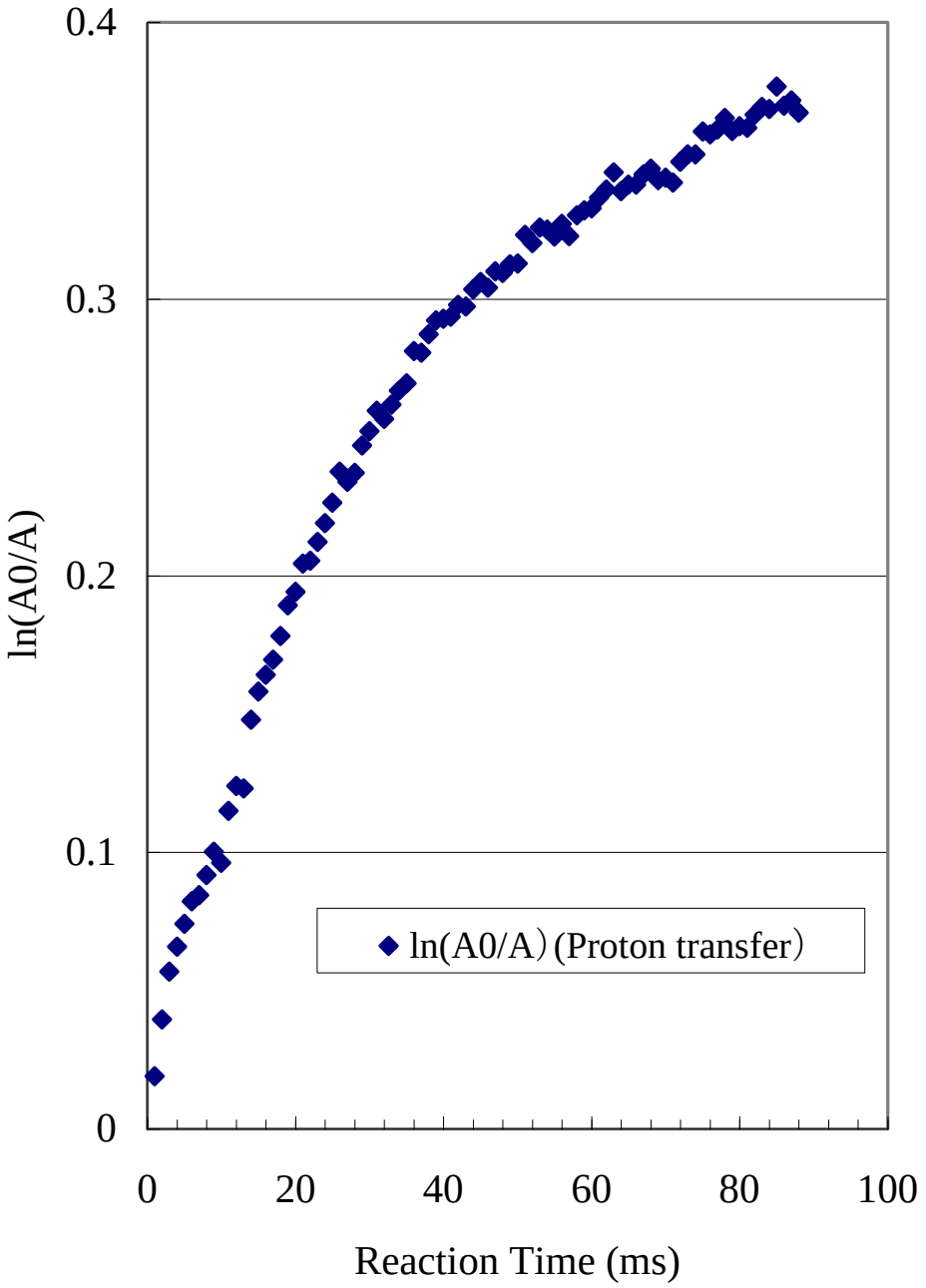
0.4
0.3
0.2
0.1
0
ln(A0/A)
0
20
40
60
80
100
Reaction Time (ms)
ln(A0/A)(Proton transfer)

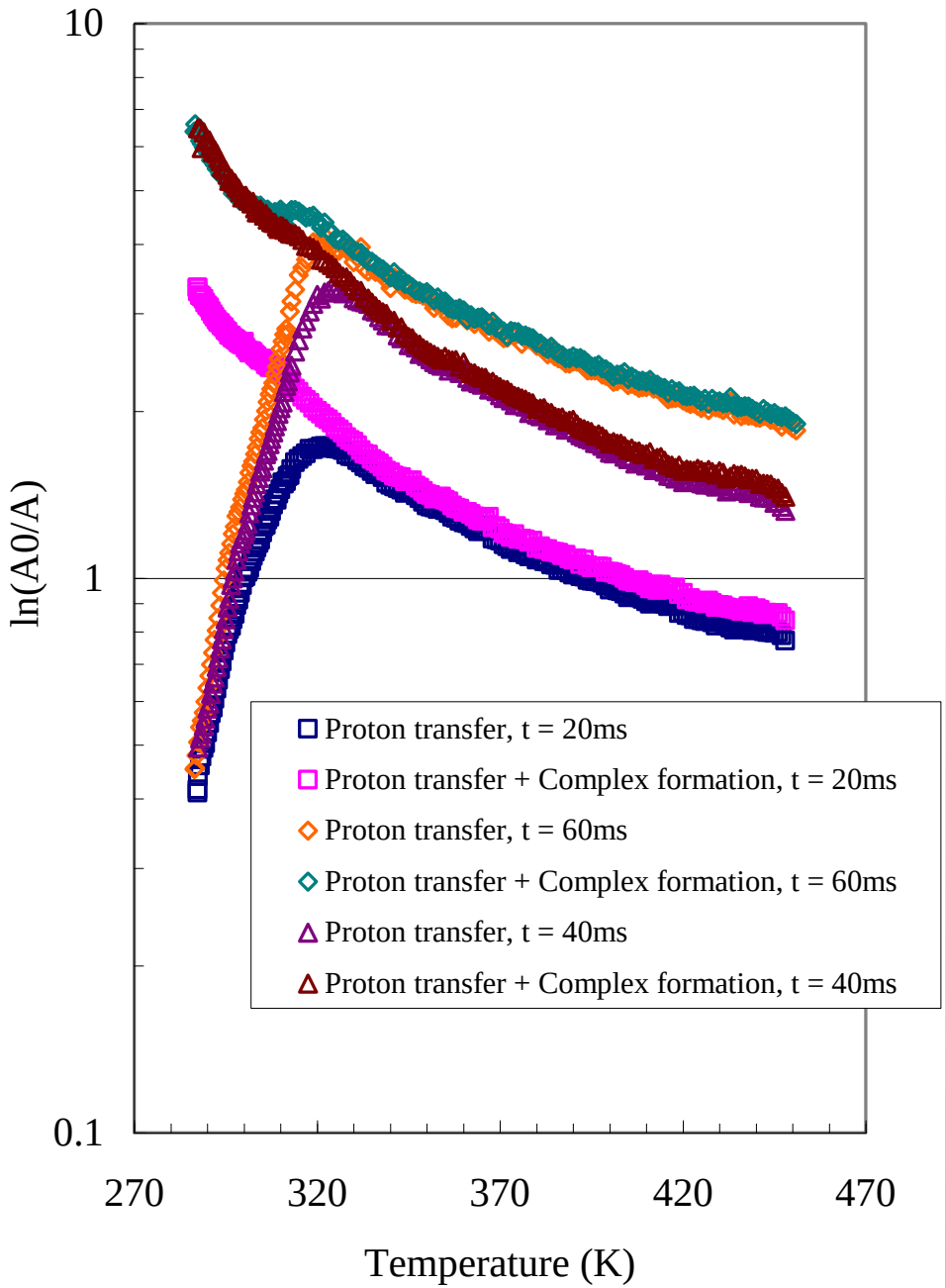
10
1
0.1
ln(A0/A)
270
320
370
420
470
Temperature (K)
Proton transfer, t = 20ms
Proton transfer + Complex formation, t = 20ms
Proton transfer, t = 60ms
Proton transfer + Complex formation, t = 60ms
Proton transfer, t = 40ms
Proton transfer + Complex formation, t = 40ms

Reaction Kinetics of Proton Transfer

Two-step process by way of long-lived complex formation

$z = n$

Complex formation as reactive intermediate

$z = n\text{-}1$

$$[\text{peptide}\cdot n\text{H}]^{n+} + \text{Tm} \underset{k_2}{\overset{k_1}{\rightleftharpoons}} [(\text{peptide}\cdot n\text{H})\cdot\text{Tm}]^{n+*} \xrightarrow{k_3} [\text{peptide}\cdot(n\text{-}1)\text{H}]^{(n-1)+} + \text{Tm}\cdot\text{H}^+$$

$$[(\text{peptide}\cdot n\text{H})\cdot\text{Tm}]^{n+} \quad (k_4,\ k_5)$$

(Tm; Target molecule)

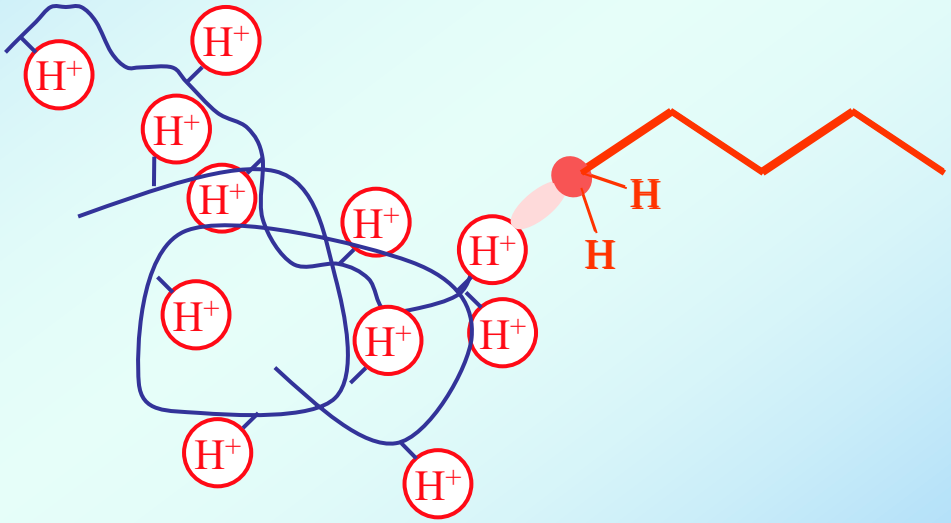

Temperature decreases → k_2 decreases → proton transfer is enhanced

k_5 decreases → proton transfer is reduced

Summary

- Construction of tandem mass spectrometer with electrospray ionization (ESI)
- Production of multiply-protonated biomolecular ions with ESI

- Collisional reactions of charge-selected biomolecular ions

- Proton transfer from angiotensin I ion to target molecules

  $[M \cdot 2H]^{2+} + Tm \rightarrow [M \cdot H]^{+} + Tm \cdot H^{+}$

  for reaction rate and distribution of product ions

High *T* ⇨ Unfolding

Low *T* ⇨ Folding

Self-solvation to H^+

Coulomb repulsion of charges

Delocalization of charges

本講義の課題

問1. 水銀クラスターの構成原子数が増大するに伴って、クラスターの電子構造が非金属から金属状態へ遷移する。その理由について、簡単に説明しなさい。

問2. アルカリ金属クラスターと原子核との類似性と異質性について、簡単に説明しなさい。

問3. Levinthalのパラドックスについて、簡単に説明しなさい。また、10個のアミノ酸から構成されるポリペプチド鎖が全てのコンフォーメーションを探索するのにかかる時間を求めなさい。

問4. 本講義の感想を記して下さい。
（批判的な内容の記述でも構いません。）